

Dissertation ETH Number 16939

# Dynamically Enhanced Membrane Foaming

A dissertation submitted to the  
Swiss Federal Institute of Technology Zurich

for the degree of  
Doctor of Sciences

presented by

Nadina Müller-Fischer

Dipl. Lm.-Ing. ETH, ETH Zürich

born November 18, 1977

citizen of Switzerland

accepted on the recommendation of  
Prof. Dr.-Ing. E.J. Windhab, examiner  
Dr. Martin E. Leser, co-examiner

2007

Copyright © 2007 Nadina Müller-Fischer  
Laboratory of Food Process Engineering (ETH Zurich)  
All rights reserved.

## **Dynamically Enhanced Membrane Foaming**

ISBN-10: 3-905609-32-0  
ISBN-13: 978-3-905609-32-5

*Published and distributed by:*

Laboratory of Food Process Engineering  
Institute of Food Science and Nutrition  
Swiss Federal Institute of Technology (ETH) Zurich  
ETH Zentrum, LFO  
8092 Zurich  
Switzerland  
<http://www.ilw.agrl.ethz.ch/vt/>

*Printed in Switzerland by:*

ETH Reprozentrale Höggerberg  
HIL C45  
8093 Zurich  
Switzerland

- *To Matthi* -



---

*Die Wissenschaft von heute ist die Technologie von morgen;  
Die Technologie von morgen ist das Brot von übermorgen.*

frei nach Richard von Weizsäcker

---

# Tankeschöön

Di vorliggendi Dissertation isch s'Resultaat vo drüehalb üsserscht spannende, lehrliche und unvergässliche Jahr won ich i dr Lääbäsmittelverfahrestechnikgruppe vo dr ETH Züri verbraacht han. Die Arbet hetti nöd chönne i dem Umfang entstaa, wänn nöd zahlrichi Lüüt mitghulfe und miich understützt hetted. All dene möcht ich a dere Stell tanke:

Ganz en bsundere Tank gaat an Prof. Dr.-Ing. E.J. Windhab, wo di ganzi Tokterarbet überhaupt erscht möglich gmacht hätt, mit siine unerschöpfliche, kreative Vorschlääg und siinere enorme Positivität und Begeischerigsfähigkeit en super Toktervatter gsi isch, miir aber au de nöötig wüesseschaftliche Freyruum zuegschtande hätt zum miini eigne Ideeä entwickle. Ich han enorm Fröid gha, i ängem Kontakt zu dr Induschtrii ä son äs aawändigsnöchs Projäkt durezfüere - so öppis wäri nie möglich gsi ohni di hervorragende Firmäkontakt vom Herr Windhab.

Em Dr. Martin Leser (Nestlé Research Center Lausanne) möcht ich ganz herzlich für d'Übernaam vom Korreferat und siini offni, fründliche Art tanke.

Wiiterhin tank ich öisne Induschtriipartner ganz herzlich für d'Finanzierig vo dem usserordentlich interessante Projäkt und di aagregte Diskussione a dä regelmässige Träffe. Kinematica AG tank ich für ali apparatetechnische Informatione wo öis wänn immer nötig zur Verfügung gschellt worde sind.

Es ganz groosses Tankeschöön gaat a di ganzi VT-Gruppe wo miini Ziiit im LFO mit villne luschtige gmeinsame Stunde und interessante Diskussione ebefalls unvergässlich gmacht hätt. De Natalie Dürr-Auster wett ich für di frööliche und gueti Zämenarbet tanke. Bisch e würkli gueti Teamkollegin, Lili! Em Tim Althaus, Paul Beck und em Res Baumann, de Muriel Graber, em André Braun und em Christoph Denkel möcht ich na im Bsundere für iri immer uufgschtellti Art und iri unkomplizierteri Fründschaft tanke - miir händ öis sicher nöd s'letschti Maal gsee! En ganz spezielle Tank gaat au a miin Bürokolleg, de Peter Bigler, wo jede Taag a de ETH mit siine fründschaftliche Hänseleye und Witz aagriicheret hätt. Eer hät miich grad scho am Aafang vo miinere Dissziit under siini Fittich gno und miir s'allermeischi Praktischi biibracht, won ich hütt chann. Eer isch au i de Freyziit immer für e Velotour oder e Wiideguschttation z'begeischtere gsii. Em Rescht vom Werchschtatt-Team, em Jan Corsano, em Dani Kiechl und em Bruno Pfister möcht ich für di gueti Zämenarbet und de enormi Iisatz tanke, wo si gleischtet händ zum all die ville Neukonstruktione für mich z'entwerfe und aazfertige - ohni sii wäri miini Arbet nöd möglich gsi. De Bernie Koller hätt miin Computer immer guet im Schuss ghalte, au das en Arbet, wo s'zügigi Schaffe erscht möglich gmacht hätt,

tanke! Em Rok Gunde tank ich für ali Gränzflächespannungsmässige.

Usserdem wett ich all miine Diplom- und Semeschterarbeiter und miine Hilf-sassischtente für ire tolli Iisatz tanke: nämli de Natalie Dürr-Auster, em Andreas Fleckenstein, em Dani Suppiger, de Carissa Kamarys, de Helen Bleuler, em Dario Cavegn, em Philip Tobler, de Corinne Rust und de Lea Gasser. Öii Ideeä und super Leischtige händ d'Experimänt i dem Umfang überhaupt erscht möglich gmacht, iir händ miini Ziiit da a de ETH aber au mänschlich sehr beriicheret und d'Betreuig hätt miir immer riisig Spass gmacht.

Miine Fründe und mim Schwager Christoph möcht ich für di ville beriichernde Stunde näbed de Arbet tanke, wo miir immer vill Fröid gmacht händ und en super Uusgliich zum Schaffe gsi sind. Miine beide Eltere Katja und Werner Fischer und miinere Schwöschter Carrie möcht ich ganz herzlich für de super Rückhalt wäred miim ganze bisherige Läbe tanke wo nur e Familie i dere Art chann gää - ich gnüüsse di gmüetliche und luschtige gmeinsame Stunde mit öi immer sehr. Und zum Schluss möcht ich miim Maa für di wunderschöni gmeinsami Ziiit und sini Underschtützig wäred dere ganze Arbet tanke. Biispiilswiis wär ich ohni siini Schuum-Uuswertigs-Software na hütt draa, Blaase vo Hand uf eme Touchscreen z'umchreise, hetti underdesse öppe zää Minusdioptrie und hetti nie son e riisigi Mängi a Date chönne verarbeite. Tanke villmaal, Matthi!

Männidorf, im Novämber 2006  
Nadina Müller-Fischer



# Contents

<b>Tankeschöön</b>	<b>vii</b>
<b>List of Figures</b>	<b>xiii</b>
<b>List of Tables</b>	<b>xix</b>
<b>Notation</b>	<b>xxi</b>
<b>Abstract</b>	<b>xxvii</b>
<b>Zusammenfassung</b>	<b>xxix</b>
<b>1. Introduction</b>	<b>1</b>
1.1. Foamed food products . . . . .	1
1.2. Aim of the presented work . . . . .	2
<b>2. Background</b>	<b>5</b>
2.1. Foam properties . . . . .	5
2.1.1. Foam stability . . . . .	6
2.1.2. Interfacial tension . . . . .	7
2.2. Foam generation . . . . .	14
2.2.1. Rotor-stator whipping device (R/S) . . . . .	16
2.2.2. Static membrane setup . . . . .	16
2.2.3. Dynamically enhanced membrane foaming . . . . .	17
2.3. Bubble deformation and breakup in laminar flow . . . . .	18
2.3.1. Parameters describing bubble deformation and flow stresses	18
2.3.2. Breakup of single bubbles in 2-dimensional shear and elon-	
gational flow . . . . .	22
2.4. Bubble formation at pores . . . . .	25
2.4.1. Dripping and jetting . . . . .	26
2.4.2. Bubble formation into stagnant continuous phase . . . . .	28
2.4.3. Bubble formation into flowing continuous phase . . . . .	32
2.4.4. Bubble detachment from pores of a dynamically enhanced	
membrane into a flowing continuous phase . . . . .	34
2.5. Flow characteristics . . . . .	35

2.5.1.	Power characteristics . . . . .	35
2.5.2.	Laminar flow . . . . .	38
2.5.3.	Turbulent flow . . . . .	39
2.5.4.	Taylor vortex flow . . . . .	40
2.5.5.	Power and energy input . . . . .	43
2.6.	Rheology . . . . .	45
2.6.1.	Rheological tests . . . . .	47
2.6.2.	Empirical modeling of non-Newtonian flow functions . . . . .	50
2.6.3.	Structure - Rheology Relationships . . . . .	51
<b>3.</b>	<b>Materials and Methods</b>	<b>55</b>
3.1.	Devices . . . . .	55
3.1.1.	Overview of the used devices . . . . .	55
3.1.2.	Parallel band apparatus . . . . .	58
3.1.3.	TECC device . . . . .	60
3.1.4.	Rotor-stator foaming device . . . . .	61
3.1.5.	Dynamically enhanced membrane foaming (DEMF) devices . . . . .	62
3.1.6.	Membranes . . . . .	70
3.2.	Analytical characterization of fluid and foam . . . . .	74
3.2.1.	Density measurements . . . . .	74
3.2.2.	Rheological measurements . . . . .	74
3.2.3.	Surface tension measurements . . . . .	76
3.2.4.	Determination of gas volume fraction . . . . .	77
3.2.5.	Foam microstructure . . . . .	77
3.3.	Processing methods . . . . .	80
3.3.1.	Mix production . . . . .	80
3.3.2.	Bubble deformation and break-up in simple shear . . . . .	81
3.3.3.	Rotor-stator foaming . . . . .	83
3.3.4.	Dynamically enhanced membrane foaming device . . . . .	87
3.4.	Materials . . . . .	94
3.4.1.	Materials used for single-bubble deformation and break-up . . . . .	95
3.4.2.	Materials used to obtain power characteristics . . . . .	97
3.4.3.	Materials used for foaming . . . . .	97
<b>4.</b>	<b>Results and Discussion</b>	<b>103</b>
4.1.	Single bubble deformation and breakup . . . . .	103
4.1.1.	Parallel band apparatus . . . . .	104
4.1.2.	Transparent Enlarged Concentric Cylinder (TECC) device . . . . .	110
4.2.	Impact of static pressure on foam microstructure . . . . .	114
4.2.1.	Ambient pressure . . . . .	115
4.2.2.	Whipping at increased pressure or partial vacuum conditions . . . . .	116
4.3.	Rotor-stator whipping . . . . .	119

4.3.1. Power characteristics . . . . .	119
4.3.2. Process parameter impact . . . . .	120
4.3.3. Dispersing characteristics . . . . .	133
4.4. Bubble detachment from single pore membrane . . . . .	134
4.4.1. Visualization of bubble detachment . . . . .	136
4.4.2. Model describing bubble detachment . . . . .	140
4.4.3. Results of experiments and model X . . . . .	142
4.4.4. Results of refined model XY . . . . .	146
4.4.5. Sinter membrane . . . . .	147
4.4.6. Taylor vortices . . . . .	149
4.5. Dynamically enhanced membrane foaming . . . . .	150
4.5.1. Power characteristics . . . . .	151
4.5.2. Dispersing characteristics . . . . .	152
4.5.3. ROME versus DESM . . . . .	153
4.5.4. Gap size . . . . .	155
4.5.5. Mix . . . . .	156
4.5.6. Velocity field . . . . .	162
4.5.7. Pore size and pore distance . . . . .	163
4.5.8. Type of membrane . . . . .	165
4.5.9. Residence time . . . . .	168
4.5.10. Membrane area . . . . .	169
4.5.11. Scale-up calculations from lab- to pilot-scale DESM . . . . .	170
4.5.12. Results obtained with pilot-scale DESM device . . . . .	172
4.5.13. Comparison of lab- and pilot-scale device . . . . .	174
4.6. Comparison of R/S, ROME and DESM device . . . . .	176
4.6.1. Power characteristics . . . . .	176
4.6.2. Impact of gas volume fraction on mean bubble size . . . . .	176
4.6.3. Dispersing characteristics . . . . .	179
<b>5. Conclusions and Outlook</b>	<b>181</b>
5.1. Single bubble deformation and breakup . . . . .	181
5.2. Impact of static pressure on foam microstructure . . . . .	182
5.3. Bubble detachment from single pore of rotating membrane . . . . .	182
5.4. Dynamically enhanced membrane foaming . . . . .	183
5.5. Scale-up of DESM device . . . . .	184
<b>Bibliography</b>	<b>185</b>
<b>Appendix</b>	<b>201</b>

<b>A. Illustrations of devices and membranes</b>	<b>203</b>
A.1. Technical drawing of pilot-scale DESM device . . . . .	203
A.2. Fitting of open mesh fabrics to clamping fixture . . . . .	204
A.2.1. Open mesh fabrics and rotating membrane . . . . .	204
A.2.2. Open mesh fabrics and DESM device . . . . .	204

# List of Figures

2.1. Schematic drawing of spherical and polyhedral foam bubbles with lamellae and plateau border. . . . .	7
2.2. Schematic of air/water interface. . . . .	9
2.3. Interfacial tension and surface-excess concentration of species $i$ as function of bulk surfactant concentration. . . . .	10
2.4. Qualitative illustration of the dynamic surface tension and surface-excess concentration as function of surface age. . . . .	11
2.5. Wetting angle of liquid on solid surface. . . . .	13
2.6. Wetting angle of bubble at pore of membrane. . . . .	14
2.7. Blow-by. . . . .	15
2.8. Model of bubble and foam generation when using a static membrane.	17
2.9. Parameters describing bubble deformation. . . . .	19
2.10. Deformation parameter $D$ and dimensionless extension ratio $L/x_B$ versus $Ca$ for bubbles in simple shear flow. . . . .	21
2.11. Influence of viscosity ratio on critical Capillary number. . . . .	23
2.12. Types of breakup observed in simple shear flow. . . . .	25
2.13. Schematic drawing of bubble formation at capillary tip or pore: dripping and jetting. . . . .	26
2.14. Drop formation mechanism at a capillary tip: a) dripping and b) jetting. . . . .	27
2.15. Schematic drawing of bubble formation at capillary tip. . . . .	27
2.16. Forces acting on a bubble for dripping into stagnant fluid. . . . .	28
2.17. Forces acting on a bubble during its formation and detachment from a pore into a flowing continuous phase. . . . .	32
2.18. Forces acting on a bubble during its formation and detachment from a pore of the rotating membrane. . . . .	34
2.19. Rotor and stator blades with pins. . . . .	36
2.20. Schematic drawing of Taylor vortices appearing in the gap between a rotating and a static cylinder. . . . .	40
2.21. Regimes observed in flow between independently rotating concentric cylinders. . . . .	41
2.22. $Ta-Re$ plane. . . . .	42
2.23. Impact of Taylor vortices on drop detachment from rotating membrane in emulsification. . . . .	42

2.24. Energy density plot for O/W emulsions produced with different emulsification devices. . . . .	44
2.25. Representation of simple shear flow. . . . .	46
2.26. Representation of elongational flow. . . . .	46
2.27. Comparison of Newtonian and non-Newtonian plots. . . . .	47
2.28. Applied shear rate and flow curve. . . . .	48
2.29. Dynamic strain test. . . . .	49
2.30. Frequency sweep. . . . .	49
2.31. Schematic diagram of the range of the various flow models for viscosity functions. . . . .	51
2.32. Qualitative structure-rheology relationship in "structured" multiphase fluids. . . . .	52
3.1. Parallel band apparatus . . . . .	58
3.2. Diagramm of the shear cell. . . . .	59
3.3. Illustration of the TECC (Transparent Enlarged Concentric Cylinder Device). . . . .	60
3.4. Picture of the TECC (Transparent Enlarged Concentric Cylinder) device. . . . .	61
3.5. Rotor-stator geometries. . . . .	62
3.6. Axial and radial cross-section of ROME and DESM device. . . . .	63
3.7. Picture of the dynamically enhanced membrane foaming device and associated elements. . . . .	64
3.8. Foaming head of ROME device. . . . .	65
3.9. Assembly of the foaming head. . . . .	65
3.10. Pictures of the transparent outer cylinder. . . . .	66
3.11. Camera and lighting for transparent ROME. . . . .	67
3.12. CAD-drawing of the membrane device with Sefar Nitex membrane mounted to housing and inner, rotating cylinder made of compact metal. . . . .	68
3.13. Picture of the housing containing the membrane. . . . .	68
3.14. Picture of the pilot-scale DESM device. . . . .	69
3.15. Technical drawing of sinter membrane. . . . .	70
3.16. Structure of Sefar Nitex membranes. . . . .	71
3.17. Technical drawing of clamping fixture. . . . .	72
3.18. SEM pictures of the membrane pores. . . . .	73
3.19. Construction of the cylindrical module. . . . .	73
3.20. Computational image analysis. . . . .	79
3.21. TEC device with white box. . . . .	83
3.22. Flow sheet of the pilot plant for experiments conducted at either increased pressure (A), atmospheric pressure (B) or partial vacuum conditions (C). . . . .	84

3.23. Schematic drawing of the rotor-stator head: alignment of the rotor-stator pairs and flow direction. . . . .	85
3.24. Schematic drawings of the dynamically enhanced membrane device. . . . .	87
3.25. ROME setup to obtain power characteristics. . . . .	94
3.26. Haworth projection formulas of glucose and maltose. . . . .	96
3.27. General formula for silicone oil . . . . .	96
3.28. Viscosity and density of water and glucose syrup solutions. . . . .	98
3.29. Chemical structure of the basic unit of Guar Gum. . . . .	100
3.30. Viscosity of model mixes A, B, C and D. . . . .	100
4.1. Development of bubble deformation in simple shear flow. . . . .	105
4.2. Steady-state bubble shape and orientation at different deformations in simple shear. . . . .	106
4.3. $D$ as function of $Ca$ for bubbles in simple shear: measured values. . . . .	107
4.4. $D$ as function of $Ca$ for bubbles in simple shear flow: measured values and data by Rust and Manga [144 . . . . .	107
4.5. $L/x_B$ as function of $Ca$ for bubbles in simple shear: measured values and models. . . . .	109
4.6. Bubble orientation in simple shear flow as a function of $Ca$ . . . . .	109
4.7. Bubble shapes before and during tip breakup in simple shear, entire bubble. . . . .	110
4.8. Tip breakup in simple shear, bubble tip. . . . .	111
4.9. Bubble breakup in simple shear. . . . .	113
4.10. Bubble breakup in simple shear: power law fit. . . . .	113
4.11. Influence of air volume fraction on mean bubble size, $x_{50,3}$ . . . . .	115
4.12. Schematic drawing demonstrating the two cases of pressure impact investigation. . . . .	116
4.13. Impact of static pressure - gas volume fraction constant in whipping head. . . . .	117
4.14. Impact of static pressure - gas volume fraction constant in final product. . . . .	118
4.15. Power characteristics for Kinematica rotor-stator device. . . . .	120
4.16. Influence of gas volume fraction on mean bubble size $x_{50,0}$ . . . . .	121
4.17. Bubble size as a function of rotational speed. . . . .	123
4.18. Mean bubble size as a function of volumetric energy input, residence time and gas volume fraction. . . . .	123
4.19. Schematic graph showing the influence of volumetric energy input, residence time and gas volume fraction on the mean bubble size. . . . .	124
4.20. Influence of shear stresses acting in the flow field on energy density and resulting bubble size. . . . .	126
4.21. Bubble size as function gas volume fraction for different continuous phases. . . . .	127

4.22. Storage modulus $G'$ , loss modulus $G''$ and complex viscosity $\eta^*$ of foam A in first and second trial. . . . .	128
4.23. Frequency sweeps of mix and foam A for a wide range in gas volume fractions. . . . .	128
4.24. Frequency sweeps of foam A and E, each at two different gas volume fractions. . . . .	129
4.25. Impact of rotor-stator geometry on bubble size. . . . .	131
4.26. Influence of number of Radax rotor-stator pairs on resulting bubble size. . . . .	132
4.27. Energy density plot for turbulent rotor-stator device. . . . .	133
4.28. Possible types of bubble formation at rotating membrane. . . . .	135
4.29. Single pore experiments at high gas velocity and low circumferential velocity. . . . .	137
4.30. Single pore experiments at high gas velocity and high circumferential velocity. . . . .	138
4.31. Single pore experiments at low gas velocity and low circumferential velocity. . . . .	139
4.32. Single pore experiments at low gas velocity and high circumferential velocity. . . . .	139
4.33. Forces acting on bubble at pore. . . . .	141
4.34. Acting forces of model X. . . . .	142
4.35. Single pore membrane: comparison between bubble sizes resulting from modeling and visualization experiments. . . . .	144
4.36. Forces acting on bubble: model XY. . . . .	146
4.37. Bubbles in ROME gap, captured with CCD camera. Original and improved image quality. . . . .	148
4.38. Bubbles in ROME gap, captured with CCD camera. Evolution of bubbles in gap. . . . .	149
4.39. Taylor vortices observed through transparent housing of ROME device. . . . .	150
4.40. Power characteristics for DEMF device. . . . .	151
4.41. Energy density plot for laminar ROME device. . . . .	153
4.42. Comparison of the two types of membrane foaming device. . . . .	154
4.43. Impact of gap size on resulting mean bubble size for the DESM device. . . . .	155
4.44. Influence of continuous fluid phase on bubble size. . . . .	157
4.45. Viscosity as function of shear rate for foam E in first and second trial. . . . .	158
4.46. Viscosity $\eta$ of mix E and foam E with different gas volume fractions. . . . .	159
4.47. Dependency of mean bubble size $x_{50,0}$ on foam viscosity. . . . .	159
4.48. Master curve for flow curves. . . . .	161
4.49. Influence of mix viscosity on mean bubble size. . . . .	162
4.50. Impact of shear rate on mean bubble size for the DESM device. . . . .	163
4.51. Influence of pore size and circumferential velocity on bubble size. . . . .	164
4.52. Impact of pore size on bubble size for ROME and DESM. . . . .	166



4.53. Impact of type of membrane on bubble size for the ROME device, model mix C and 0.50 mm gap. . . . .	166
4.54. Impact of membrane and membrane module construction on bubble size for the ROME device, model mix E and 0.22 mm gap. . . . .	167
4.55. Clamping fixture and microturbulences. . . . .	167
4.56. Impact of residence time on mean bubble size for DESM device. . .	169
4.57. Impact of membrane area on mean bubble size for DESM device. .	170
4.58. Impact of shear rate and residence time on mean bubble sizes of foams obtained with pilot-scale device. . . . .	173
4.59. Mean bubble sizes as a function of the gas volume fraction for lab-scale ROME, lab-scale DESM and pilot-scale DESM device. . . . .	175
4.60. Impact of shear rate on mean bubble size for small and up-scaled device. . . . .	175
4.61. Power characteristics of the dynamically enhanced membrane foaming device and the rotor-stator device. . . . .	177
4.62. R/S versus ROME device for mix C. . . . .	177
4.63. R/S versus ROME and DESM device for mix E. . . . .	178
4.64. R/S versus ROME and SAMF device for mix E: distribution width. .	179
4.65. Dispersing characteristics and energy dissipation rates of the dynamically enhanced membrane foaming device and the rotor-stator device. . . . .	180
A.1. Technical drawing of pilot-scale DESM device. . . . .	203
A.2. Assembling of open mesh fabric to clamping fixture for ROME device. .	205
A.3. Assembling of open mesh fabric to head of DESM device. . . . .	206

*List of Figures*

---

# List of Tables

2.1. Interfacial properties of proteins and emulsifiers. . . . .	13
3.1. Membrane specifications. . . . .	70
3.2. Flow curve measurement parameters used for Newtonian fluids. . .	74
3.3. Temperature ramp parameters used for characterizing Newtonian fluids. . . . .	75
3.4. Parameters used for flow curve measurements. . . . .	75
3.5. Parameters used for oscillatory measurements. . . . .	76
3.6. Distribution parameters. . . . .	78
3.7. Newtonian fluids. . . . .	80
3.8. Concentrations of Ame-HV and Guar in model mixes A to D. . . .	81
3.9. Rotor-stator whipping: analyzed process parameter combinations. .	83
3.10. Specifications and free volume of the Radax and 12-HR geometry. .	87
3.11. Parameters used for foaming with ROME. . . . .	88
3.12. Parameters used for foaming with DESM device. . . . .	89
3.13. Parameters for scale-up experiments. . . . .	89
3.14. Formulas used for scale-up calculations. . . . .	90
3.15. Parameters for experiments with scaled-up device: impact of circumferential velocity, residence time and gas volume fraction. . . . .	91
3.16. Parameters used for experiments with single-pore membrane and for model calculations. . . . .	92
3.17. ROME device, single pore membrane and transparent outer cylinder.	92
3.18. ROME device, sinter membrane and transparent outer cylinder. . .	93
3.19. Viscosity, density and surface tension of glucose syrups. . . . .	96
3.20. Viscosity and surface tension of silicone oil. . . . .	97
3.21. Viscosity of water and glucose syrup. . . . .	98
3.22. Density of water and glucose syrup. . . . .	98
3.23. Viscosity of mixes A to D. . . . .	101
3.24. Density and surface tension of mixes A to E. . . . .	101
4.1. Rising velocity of bubbles in band apparatus. . . . .	104
4.2. Comparison of effect of decreased fluid flow rate on residence time and volumetric energy input. . . . .	125

4.3. Maximally achievable gas volume fractions for different geometrical set-ups. . . . .	132
4.4. Parameters used for model calculations applied to real foam system.	145
4.5. Multi pore membrane: comparison between modeling results and experiments. . . . .	145
4.6. Comparison of simplified and refined model. . . . .	148
4.7. Results of scale-up calculations DESM device. . . . .	171

# Notation

## Latin Letters

Symbol	SI Unit	Meaning
$a_L$	-	Langmuir parameter
$A$	$m^2$	area
$A_I$	$m^2$	interfacial area
$B$	m	minor axis
$c_d$	-	drag coefficient
$D_i$	m	rotor diameter
$D$	-	deformation
$e$	-	number of rotor and stator pairs
$f$	$s^{-1}$	frequency
$F$	N	force
$F_b$	N	buoyancy force
$F_c$	N	centrifugal force
$F_p$	N	pressure force
$F_{pa}$	N	pressure force in axial flow direction
$F_{pg}$	N	pressure force of gas
$F_{pm}$	N	pressure force of mix
$F_{pr}$	N	pressure force in rotational flow direction
$F_\tau$	N	drag force
$F_{\tau a}$	N	drag force in axial flow direction
$F_{\tau r}$	N	drag force in rotational flow direction

continued on next page

## Notation

---

Symbol (cont.)	SI Unit (cont.)	Meaning (cont.)
$F_\sigma$	N	surface tension force
$g$	$\text{m} \cdot \text{s}^{-2}$	gravity constant
$G$	$\text{s}^{-1}$	rate of deformation
$G'$	$\text{Pa} \cdot \text{s}$	storage modulus
$G''$	$\text{Pa} \cdot \text{s}$	loss modulus
$H$	m	height
$j_i$	$\text{mol} \cdot \text{m}^{-2} \cdot \text{s}^{-1}$	molar diffusion flux
$K$	m	Kolmogorov length
$l$	m	length
$l_{f,r}$	m	free radial distance
$L$	m	major axis
$m$	kg	mass
$n$	$\text{s}^{-1}$	rotational speed
$OR$	%	overrun
$p$	Pa	pressure
$p_{Ca}$	Pa	Capillary pressure
$P$	$\text{J} \cdot \text{s}^{-1}$	power
$P_V$	$\text{J} \cdot \text{s}^{-1} \cdot \text{m}^{-3}$	volumetric power input
$Q_m$	$\text{J} \cdot \text{kg}^{-1}$	mass specific heat quantity
$r$	m	radius
$r_{B,orbit}$	m	radius of bubble orbit
$\vec{r}_i$	$\text{mol} \cdot \text{s}^{-1}$	molar production rate vector of species i
$R$	-	gas constant
$R_i$	m	radius of inner cylinder
$R_o$	m	radius of outer cylinder
$s$	m	gap size
$\mathbf{s}$	m	thickness
$t$	s	time
$t_V$	s	residence time

continued on next page

---

---

Symbol (cont.)	SI Unit (cont.)	Meaning (cont.)
$T$	$^{\circ}\text{C}$	temperature
$v$	$\text{m} \cdot \text{s}^{-1}$	velocity
$v_{\text{cr}}$	$\text{m} \cdot \text{s}^{-1}$	creaming velocity
$v_{\text{St}}$	$\text{m} \cdot \text{s}^{-1}$	Stokes velocity
$\vec{v}$	$\text{m} \cdot \text{s}^{-1}$	velocity vector
$V$	$\text{m}^3$	volume
$V_{\text{B}}$	$\text{m}^3$	bubble volume
$\dot{V}$	$\text{m}^3 \cdot \text{s}^{-1}$	volume flow rate
$W$	J	work
$x$	m	diameter
$x_{\text{B}}$	m	bubble diameter
$x_{\text{P}}$	m	pore diameter
$x_{50,0}$	$\mu\text{m}$	mean bubble diameter of the cumulative number distribution
$x_{50,3}$	$\mu\text{m}$	mean bubble diameter of the cumulative volume distribution
$x_{3,2}$	$\mu\text{m}$	Sauter diameter
$z$	-	number of pores
$y$	m	distance between pins of rotor and stator blades

---

## Greek Letters

---

Symbol	SI Unit	Meaning
$\Delta$	-	difference
$\gamma$	-	deformation
$\dot{\gamma}$	$\text{s}^{-1}$	shear rate
$\dot{\dot{\gamma}}$	-	rate of strain tensor
$\Gamma_i^s$	$\text{mol} \cdot \text{m}^{-2}$	surface-excess molar density
$\Gamma_{i,\infty}$	$\text{mol} \cdot \text{m}^{-2}$	surface concentration limit of species i
$\eta$	$\text{Pa} \cdot \text{s}$	viscosity

---

continued on next page

---

## Notation

---

Symbol (cont.)	SI Unit (cont.)	Meaning (cont.)
$\eta_0$	$\text{Pa} \cdot \text{s}$	zero shear viscosity
$\eta_{\text{cont}}$	$\text{Pa} \cdot \text{s}$	continuous phase viscosity
$\eta_{\text{disp}}$	$\text{Pa} \cdot \text{s}$	disperse phase viscosity
$\eta^*$	$\text{Pa} \cdot \text{s}$	complex viscosity
$\Theta$	$^\circ$	rotation angle, contact angle
$\lambda$	-	viscosity ratio
$\nu$	$\text{m}^2 \cdot \text{s}^{-1}$	kinematic viscosity
$\phi_V$	-	gas volume fraction
$\rho$	$\text{kg} \cdot \text{m}^{-3}$	density
$\sigma$	$\text{N} \cdot \text{m}^{-1}$	interfacial tension
$\sigma_{\text{l,g}}$	$\text{N} \cdot \text{m}^{-1}$	interfacial tension between liquid and gas
$\sigma_{\text{s,g}}$	$\text{N} \cdot \text{m}^{-1}$	interfacial tension between solid and gas
$\sigma_{\text{s,l}}$	$\text{N} \cdot \text{m}^{-1}$	interfacial tension between solid and liquid
$\tau$	$\text{Pa}$	shear stress
$\omega$	$\text{s}^{-1}$	angular velocity
$\zeta$	-	number of resistance

---

## Indices

---

Symbol	Meaning
0	initial value
<i>b</i>	buoyancy
<i>B</i>	bubble
<i>c</i>	critical number
<i>char</i>	characteristic
<i>cont</i>	continuous phase
<i>Ca</i>	Capillary
<i>cr</i>	creaming
<i>d</i>	drag

---

continued on next page

---



---

Symbol (cont.)	Meaning (cont.)
<i>dyn</i>	dynamic
<i>disp</i>	disperse phase
<i>gap</i>	gap
<i>g</i>	gas
<i>i</i>	interfacial
<i>l</i>	liquid
<i>m</i>	mix
<i>P</i>	pore
<i>x, y, z</i>	x-, y- and z-direction

---

## Dimensionless Numbers

---

Symbol	Meaning
<i>Ca</i>	Capillary number
<i>Ca<sub>c</sub></i>	critical Capillary number
<i>Fr</i>	Froude number
<i>Ne</i>	Newton number
<i>Re</i>	Reynolds number
<i>Re<sub>gap</sub></i>	gap Reynolds number
<i>Ta</i>	Taylor number
<i>Ta<sub>c</sub></i>	critical Taylor number
<i>We</i>	Weber number
<i>We<sub>c</sub></i>	critical Weber number

---

## Abbreviations

---

Abbreviation	Meaning
DEMF	Dynamically enhanced membrane foaming
DESM	Dynamically enhanced static membrane (foaming)

---

continued on next page

---

## *Notation*

---

---

Abbreviation (cont.)	Meaning (cont.)
ROME	Rotating membrane (foaming)
LMVT	Laboratory of Food Process Engineering (Lebensmittelver- fahrenstechnik)
SEM	Scanning Electron Microscopy
R/S	Rotor-stator

---

# Abstract

Foamed food products like ice cream, chocolate mousse, fresh cheese or bakery products are increasingly popular due to their soft and creamy sensory properties. The perception, stability and flow behavior of food foams strongly depend on gas fraction and bubble size distribution. Ideally, foams contain smallest possible gas bubbles of equal size. If the gas bubbles are small enough, they can not be distinguished from fat particles in the mouth. Hence, fat can be replaced by gas, leading to a fat-free yet creamy product. A narrow size distribution slows destabilization mechanisms, and thus, the amount of stabilizers can be reduced or the shelf life prolonged. In numerous life science related application areas foams are manufactured using rotor-stator gas dispersing devices where gas is added to the fluid mix and dispersed by the flow forces (shear, elongation, inertia) acting in the whipping head. Improvements with regards to foam characteristics are often achieved by altering the ingredients composition but maintaining the same processing conditions. Contrary to this approach, the focus of this work was to understand and develop a new foaming process in which smaller and more narrowly distributed bubbles can be achieved without changing the recipe.

Fundamental insight into the mechanisms of bubble breakup in simple shear was sought. Experiments in a parallel band apparatus and a transparent concentric cylinder setup allowed the observation of bubble deformation and breakup, respectively. To date, no data regarding bubble breakup are found in literature. It was shown that no clear distinction between tip breakup and fracture can be made for bubbles. Critical Capillary numbers for bubble breakup between about 29 and 45 were found for viscosity ratios between  $3.1 \cdot 10^{-7}$  and  $6.7 \cdot 10^{-8}$ , respectively.

Another aim of this study was to determine the impact of reduced static pressure acting during the foaming process on the resulting foam microstructure. Since the gaseous disperse phase is compressible, static pressure plays a major role in foam production. Commonly, industrial foam production takes place in a pressure range of 2 - 4 bar absolute in order to reduce the effective gas volume fraction in the whipping device. However, the bubbles expand as soon as they are exposed to atmospheric pressure. To investigate the inverse effect, namely a bubble shrinkage during adaptation to atmospheric pressure, the static pressure in the whipping head was reduced to partial vacuum of 0.6 bar. The comparison of pressures between 0.6 and 4.0 bar, however, showed that best foaming results are achieved at atmospheric pressure compared to both increased and reduced static pressure. For foams whipped at increased pressure, the bubbles grew during expansion to

atmospheric condition while at reduced pressure coalescence probability was increased in the rotor-stator whipping device as a consequence of the enlarged gas volume fraction.

Furthermore, new types of foaming devices using either (i) a rotating membrane (ROME) or (ii) dynamically enhanced static membrane (DESM) were developed and characterized. The devices consist of two concentric cylinders, one forming the membrane: (i) rotor = membrane, (ii) membrane attached to housing. In (i) and (ii), the inner cylinder rotates with circumferential velocities up to 30 m/s. Air is pressed through the membrane into the narrow annular gap through which the continuous fluid phase passes. Bubbles are detached from the rotating membrane surface and further dispersed in the narrow annular gap due to the high acting shear stresses. Contrary to aeration with conventional non-rotating membrane devices, the shear stress is controlled by the circumferential velocity of the inner cylinder and is, thus, de-coupled from the volume throughput rate of the continuous fluid phase. The impact of shear rate, gas volume fraction, gap size, type of membrane, residence time and volumetric energy input was quantified for membranes of various types and pore sizes.

Foams produced with the newly developed devices were systematically compared to those whipped with an industrially commonly used rotor-stator device. The new ROME and DESM devices were shown to produce bubbles of about half the mean size for gas volume fractions  $> 0.5$  and with significantly narrower size distribution. The volumetric energy input  $E_V$  of the new devices is about one order of magnitude lower for the dynamically enhanced membrane device as a consequence of the reduced residence time necessary to disperse the gas bubbles. The DESM device was scaled up to pilot scale, built and tested. The results of laboratory and pilot scale DESM devices were comparable with respect to foam microstructure.

In order to get detailed information on the bubble formation mechanism in the dynamically enhanced membrane foaming device, bubble detachment from a single pore of a rotating membrane was visualized and systematically observed through a transparent housing construction. Based on a balance of forces valid for a bubble at the membrane surface, a simplified model was derived which allows the estimation of the mean size of the detached bubbles as a function of the acting shear rate. Experiments and model were in good agreement.

The combination of results on bubble breakup in simple shear, on detachment of bubbles from the pore of a rotating membrane and rheological and microstructural analysis of foams showed that the detachment of small bubbles from the membrane is the dominating bubble formation process in the dynamically enhanced membrane foaming process. An additional dispersing in the narrow annular gap is of minor importance.

# Zusammenfassung

Geschäumte Lebensmittelprodukte werden aufgrund ihrer angenehmen Textur immer beliebter. Dabei gibt es neben Desserprodukten wie Schokoladenmousse oder Eiskrem auch eine grosse Vielfalt an salzigen Produkten wie Frischkäse oder Lachsmousse. In geschäumten Produkten beeinflussen der Gasanteil und die Blasengrößenverteilung das Texturempfinden im Mund massgeblich. Idealerweise enthalten Schäume möglichst kleine Blasen, da sich diese im Mundraum nicht von Fettpartikeln unterscheiden lassen. Ein gänzlich fettfreies Produkt wird so trotzdem als cremig wahrgenommen. Eine enge Blasengrößenverteilung hingegen erhöht die Stabilität des Produktes, was dazu führt, dass dieses entweder länger haltbar ist oder Zusatzstoffe wie Verdickungsmittel und Stabilisatoren reduziert werden können. Vielfach werden Schäume industriell mit Rotor-Stator Aufschlagmaschinen hergestellt. Gas wird im Aufschlagkopf in vielen Schritten durch die wirkenden Fließkräfte (Scher-, Dehn- und Trägheitskräfte) in kleinere Blasen zerteilt. Produktverbesserungen werden oft durch eine Veränderung der Rezeptur bewirkt, während der Aufschlagprozess selten genauer betrachtet wird. Der Fokus der vorliegenden Arbeit war es hingegen, die Blasenentstehung besser zu untersuchen und einen neuen Aufschäumprozess zu entwickeln, mit dem kleinere und enger verteilte Gasblasen erzielt werden können.

In einem fundamentaleren Teil dieser Arbeit wurden Erkenntnisse zu Blasenauflbruchmechanismen in einfacher Scherströmung gesucht. Dazu wurden Versuche in einer durchsichtigen konzentrischen Zylinder-Konstruktion durchgeführt. Es gelang, bei tiefen Viskositätsverhältnissen Blasenauflbruch zu erzielen, wozu bislang keine Veröffentlichungen existieren. Für Viskositätsverhältnisse zwischen  $3.1 \cdot 10^{-7}$  und  $6.7 \cdot 10^{-8}$  wurden kritische Kapillarzahlen zwischen 29 und 45 ermittelt. Es konnte zudem gezeigt werden, dass es für Blasen keinen klar erkennbaren Unterschied zwischen gesamthaftem Auflbruch und Abscheren der Blasen Spitze gibt, so wie das für Emulsionstropfen bekannt ist.

Weiterhin wurde der Einfluss des statischen Druckes auf die resultierende Schaumstruktur untersucht. Da die gasförmige disperse Phase in Schäumen kompressibel ist, spielt der statische Druck während des Aufschäumprozesses eine bedeutende Rolle. In industriellen Herstellungsprozessen wird herkömmlicherweise bei absoluten Drücken zwischen 2 und 4 bar gearbeitet, um das Gasvolumen zu verkleinern. Sobald der Schaum aus der Anlage austritt und Atmosphärendruck ausgesetzt ist, wachsen die Blasen wiederum an, was für die Schaumstruktur unvorteilhaft ist. Innerhalb dieser Arbeit wurden deshalb Drücke bis hinunter zu 0.6 bar absolut un-

tersucht, um den gegenteiligen Einfluss eines Blasenschrumpfens bei Belüftung zu beobachten und analysieren. Der Vergleich dieser Schäume zeigte, dass sowohl ein erhöhter als auch ein reduzierter statischer Druck zu negativen Veränderungen der Schaumstruktur führt und dass die Schaumproduktion bei Atmosphärendruck zu den eindeutig kleinsten mittleren Blasengrößen führt. Es konnte weiterhin gezeigt werden, dass das Blasenvolumen sich entsprechend dem idealen Gasgesetz mit dem statischen Druck ändert.

In einem weiteren Teil dieser Arbeit wurde ein neuer Aufschäumprozess entwickelt, das sogenannte dynamische Membranschäumen. Die zugehörige Maschine besteht aus zwei konzentrischen Zylindern, von denen jeweils der eine aus kompaktem Metall besteht, während der andere die Membran ist. Der innere Zylinder kann mit Umfangsgeschwindigkeiten bis zu 30 m/s rotiert werden. Die disperse Gasphase wird durch die Membran in den engen Ringspalt gedrückt, durch den der Mix hindurchfließt. Die an den Poren der Membran gebildeten Blasen werden dank der hohen Schubspannung frühzeitig von der Membran abgelöst und erfahren im engen Ringspalt eine weitere Dispergierung. Anders als bei einer Schaumherstellung mittels einem statischen Membranaufbau ist die wirkende Spannung vom Durchsatz entkoppelt. Der Einfluss der Scherrate, des Gasanteiles, der Spaltweite, des Membrantyps, der Verweilzeit und des volumenspezifischen Energieeintrages wurden für Membranen mit verschiedenen Porengrößen quantitativ analysiert. Die so hergestellten Schäume wurden mit Schäumen verglichen, die mit einer herkömmlichen Rotor-Stator Anlage hergestellt wurden. Es konnte gezeigt werden, dass das dynamische Membranschäumen es ermöglicht, bei einem Gasanteil  $>0.5$  halb so grosse mittlere Blasengrößen mit engeren Blasengrößenverteilungen herzustellen. Der volumetrische Energieeintrag ins Produkt ist aufgrund der gleichermassen verkürzten Verweilzeit etwa eine Zehnerpotenz kleiner für Membrananlage. Die neue Membrananlage wurde in grösserem Massstab ausgelegt und gebaut. Vergleichende Versuche von Labor- und Pilotanlage zeigten, dass die resultierenden Blasengrößen praktisch identisch sind.

Ausserdem wurde der Blasenablösungsvorgang von den Poren der rotierenden Membran näher untersucht. Dazu wurde ein durchsichtiger Aussenmantel konstruiert und es wurden bei verschiedenen Drehzahlen mit einer Hochgeschwindigkeitskamera Filme aufgenommen. Die resultierenden Blasengrößen wurden analysiert und mit einem auf dem Kräftegleichgewicht basierenden Modell verglichen. Dabei wurde eine gute Übereinstimmung zwischen Modell und Visualisierungsexperiment gefunden.

Die Kombination der Resultate zu (i) Blasenaufruch in einfacher Scherströmung, zu (ii) Blasenablösung von der Pore einer rotierenden Membran und zur rheologischen und mikrostrukturellen Analyse von Schäumen (iii) hat gezeigt, dass die Blasenablösung der dominierende Blasenbildungsvorgang im dynamischen Membranschäumprozess ist. Die weitere Dispergierung im engen Ringspalt ist von untergeordneter Bedeutung.

# 1. Introduction

## 1.1. Foamed food products

Foamed products are of interest in many industrial fields such as those dealing with food, cosmetics, pharmaceutical and chemical products. In food applications, the interest in foamed products has been strongly growing for years since most consumers appreciate the soft and creamy mouth sensations triggered by the small gas bubbles. Beside the wide variety of traditionally aerated food systems like ice cream, whipped cream and mousse products, there is an ever-growing number of new aerated foods like spreads, cheese, butter, confectionery and bakery products. Some of the results of food aeration are [26]:

- a reduction in product density,
- a change in product texture and rheology resulting in a different mouthfeel and appearance,
- enhanced ability to take up sauces, due to the increased surface area,
- modification of digestibility,
- the possibility of a reduced shelf-life, as the finely dispersed air bubbles may enhance oxidation reactions and affect fat and flavor ingredients,
- a change in flavor intensity and delivery.

The effects of whipping can be of nutritional benefit since small enough gas bubbles can not be distinguished from fat globules in the mouth, thus, fat can be replaced by air bubbles [109] and a creamy, yet fat-free product created. Carbonation of soft drinks produces the tingling mouthfeel central to the appeal of these beverages, as well as contributing acidic preservative action. In some sparkling products like champagne, bubbles represent pure luxury, a trait much appreciated by the consumers. Historically, foamed food like souffles, mousses, champagne and cappuccino represent culinary art. This is the appeal of aerated foods to consumers and manufacturers. All in all, the positive benefits of aerated food products are primarily to do with texture. Fluid products such as whipped cream obtain smoothness and novelty, while solid products such as breakfast cereals and snacks

become light and crisp. Product rheology is altered by the air bubbles, allowing originally fluid ingredients to be molded into more attractive shapes such as meringue nests.

The instability of foamed systems is an issue for industrial foam production. Stability is largely correlated with the rheology of the system, the stabilization mechanisms can however vary. Bubbles are stabilized by surface active agents like proteins and emulsifiers (e.g. in mousse products) or solid crystals of fat in a liquid matrix phase (e.g. in whipped cream). Bubbles can as well be fixed by a semi-solid or solidified continuous matrix (e.g. fruit jellies). Often, a combination of stabilization mechanisms act together or consecutively (e.g. in ice-cream). The difficulty in describing foam formation in food products is that most of them are composed of different types of molecules like fats, proteins, emulsifiers, hydrocolloids and colloidal particles that interact in ways that are only partly understood to date [103].

Foam processing can be divided into three main categories:

- Processes in which the gas is actively dispersed in liquid, like whipping or shaking. Such methods are commonly used to produce cream and mousse products, frozen desserts and marshmallows.
- Sparging, where gas is injected into liquid. This type of aeration is commonly used in the chemical industry but is less known in food industry.
- In situ generation of gas, e.g. biological or chemical leavening, carbon dioxide release on pressure release. Typical examples found in food industry are fermentation, in which aeration is achieved due to carbon dioxide production by yeast or expansion extrusion, in which hot, pressurized product emerges suddenly from an extruder, such that moisture immediately vaporizes.

## 1.2. Aim of the presented work

This work deals with sparging and whipping of gas with the aim to generate foam products with a lifetime in the order of weeks. Foam structure and stability can always be improved by varying the surfactant or stabilizer composition. Within this thesis, foam stability was however addressed from the processing side, only. The focus was to understand and develop a new approach to foaming where smaller and more narrowly distributed bubbles can be achieved since foam microstructure determines its production behavior, stability, shelf life and mouthfeel.

In numerous life-science related application areas foams are manufactured using rotor-stator gas dispersing devices where gas is added to the fluid mix and dispersed by the acting flow forces (shear, elongation, inertia) in the whipping head. In comparison to rotor-stator whipping, the usage of static membranes for foam



production has been shown to allow dispersing at comparatively low energy input [10]. Gas is pressed through pores and resulting bubbles are detached from the membrane surface by the acting shear stresses. In non-rotating membrane set-ups, the shear stress is directly coupled with the volume flow rate of the continuous liquid phase. The resulting mean bubble sizes are large, up to one thousand times the pore size [11]. A new dynamically enhanced membrane foaming device was developed in this work where the shear stress no longer depends on the continuous phase throughput, but can be controlled by the circumferential speed of the inner cylinder which can be adjusted to values up to 30 m/s. The inner cylinder is either a cylindrical membrane (ROME device) or made of compact metal (DESM device). In the DESM device, the membrane is attached to the inner cylinder wall of the housing. The ROME type of dynamically enhanced membrane foaming device was also shown to be effective in the field of emulsification where it led to very small droplets and narrow drop size distributions, i.e. smallest mean droplet size equivalent to pore size [146]. For a better understanding of the dynamically enhanced membrane foaming process, bubble detachment from the pore of a rotating membrane was visually observed. Additionally, fundamental insight with respect to bubble breakup in simple shear was obtained using a transparent concentric cylinder construction.



## 2. Background

Food foams such as ice cream, protein-sugar foams like meringue, whipped cream, fresh cheese, fruit and chocolate mousse have become more and more popular in recent years. A number of fundamental investigations on complex foam structures can be found in literature, e.g. [2, 181, 145, 51, 177], and many publications concerning foam production and foam properties depending on ingredients like surface active molecules exist [18, 41, 175, 42]. In this chapter, the theoretical background is discussed which is mandatory to understand the performed experiments and find possible explanations of observed phenomena. The six main sections are: (i) foam properties, (ii) foam generation, (iii) deformation and breakup of single bubbles in laminar flow, (iv) bubble formation at pores, (v) flow characteristics, and, (vi) rheology.

### 2.1. Foam properties

Foams consist of gas (disperse phase) dispersed in a liquid (continuous phase). Depending on the volume ratio of gas to liquid, a distinction between spherical and polyhedral foam can be made. For gas volume fractions below 0.74, a monodisperse foam contains spherical bubbles between thick lamellae. Foams containing more than 74 % gas form polyhedral bubbles, their thin lamellae meet at an angle of  $120^\circ$  (Fig. 2.1). Pure liquids can not be foamed because soluble surfactants are required to stabilize the surfaces between air and liquid [182]. Foams are thermodynamically unstable due to their high free interfacial energy. The system is driven to minimize the interface by surface forces and to phase separate by gravitation forces. These effects can be reduced and even stopped by reducing the surface tension at the gas/liquid interface and by increasing the viscosity of the continuous liquid phase. For convenience, the instability has been classified into two extreme types according to the kinetics [133, 148]: (i) unstable or transient foams with lifetimes of seconds and (ii) metastable or so-called permanent foams with lifetimes which may be measured in days. There are several types of instabilities which will be discussed in more detail in the first part of this section [173, 131], i.e. Ostwald ripening, creaming, drainage and coalescence. The impact of surface tension on foam stability will then be discussed in a second part of the section.

### 2.1.1. Foam stability

#### Ostwald ripening

The growth of larger bubbles at the expense of smaller ones by diffusion is called Ostwald ripening. Gas diffuses from one bubble to another across the interfaces and through the continuous liquid phase. The driving force is the higher solubility of gas under higher pressure. According to Henry's Law, gas solubility is proportional to pressure and temperature. The Laplace pressure (see Eq. 2.3) is inversely proportional to the bubble radius. Thus, gas solubility is higher near small bubbles than near large ones and consequently gas is transported from smaller to bigger bubbles. This leads to disproportionation of the bubbles, i.e. small bubbles shrink, large ones grow.

In addition to the pressure difference, the extent of Ostwald ripening depends on gas solubility, temperature, lamella thickness and surface properties of the film. Shrinkage is rapid since the surface tension and the solubility of most gases in water-based solutions is high. Cooney [34] obtained highest foam stability and gas volume fractions with nitrogen, followed by oxygen, hydrogen and carbon dioxide. The higher foam stability with nitrogen can be explained by the fifty times lower solubility of nitrogen compared to carbon dioxide. Prins [131] discussed solubility, diffusion coefficient of nitrogen and carbon dioxide and the relation to foam stability in more detail.

#### Creaming

Creaming causes bubbles to rise to the product surface where bubbles build a close-packed layer. For dilute dispersions of spherical bubbles with diameter  $x_B$ , creaming velocity  $v_{cr}$  of single bubbles can be estimated by the Stoke's equation:

$$v_{cr} = \frac{1}{18} \cdot \frac{g \cdot \Delta\rho \cdot x_B^2}{\eta_{cont}}, \quad (2.1)$$

where  $g$  denotes gravity acceleration,  $\Delta\rho$  density difference between gas bubble and surrounding continuous phase and  $\eta_{cont}$  continuous phase viscosity.

#### Drainage

Drainage can be considered as the flow of liquid in a foam due to gravitational forces. The lamellae get thinner and a spherical foam turns into a polyhedral one. As a consequence of the pressure difference between plateau borders and lamellae an additional sucking of liquid from the lamellae to the plateau borders occurs in polyhedral foams.

The drainage rate of foams may be decreased either by increasing bulk liquid viscosity or by increasing the interfacial viscosity and elasticity. Comparison of pure

viscous liquids showed that the lifetime of foams was the same when the viscosities were made equal even though their surface tension differed [101]. Generally, the interfacial viscosity and elasticity can be increased by packing high surfactant or particle concentration in the interfacial film causing high adhesive or cohesive bonding. While surface viscosity reflects the speed of relaxation processes after imposing stress and, thus, is a measure of the energy dissipation in the surface layer, the surface elasticity is a measure of the energy stored in the surface layer as a result of an external stress [83]. Whereas bulk viscosity influences the thinning of thick films by fluid drainage, the interfacial viscosity has a stronger impact on thin film stability [133].

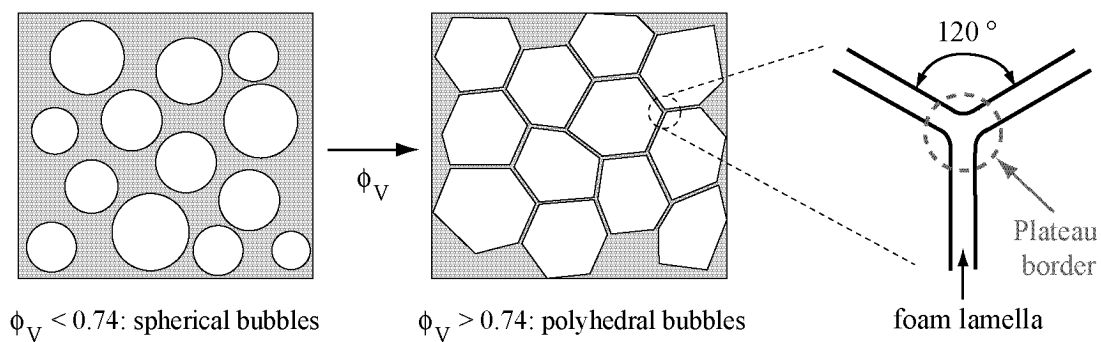


Figure 2.1.: Schematic drawing of spherical and polyhedral foam bubbles with lamellae and plateau border.

## Coalescence

Coalescence is the fusion of two bubbles into one due to the rupture of a lamella. If moving bubbles collide, they can either be repelled or they can coalesce. While bubbles converge, the continuous phase between them forms the lamella. The behavior of the lamella influences bubble coalescence. As soon as a critical film thickness is reached, the film gets unstable and ruptures. As a consequence, the number of bubbles decreases, their mean size increases, and the foam coarsens. Coalescence is a limiting factor in gas dispersing/whipping processes.

### 2.1.2. Interfacial tension

Interfacial tension plays a major role in bubble formation and deformation. It manifests itself as a normal stress jump at the interface between fluid and gaseous phase. The simple case described in Sec. 2.1.2 is a constant interfacial tension along the interface between e.g. air and pure water. Gas bubbles can not be stabilized in such a system.

The situation gets more complex if the liquid phase contains surfactant or interfacially active impurities: the adsorption kinetics of the surfactant molecules have to be taken into account and the interfacial tension exhibits a typical time-dependent behavior (see Sec. 2.1.2). Foam formation is possible using such a system. However, the interfacial area significantly grows during dispersion/foam formation. To create a stable foam, two time-scales have to be considered: time  $t_{\text{disp}}$  in which new bubbles are formed and time  $t_{\text{stab}}$  needed for interface stabilization by surfactants. If  $t_{\text{stab}} < t_{\text{disp}}$ , the conditions for the generation of finely dispersed foams is fulfilled. If  $t_{\text{stab}} > t_{\text{disp}}$ , the surfactant does not stabilize the interface fast enough leading to direct coalescence of newly formed bubbles.

### Interfacial tension of pure liquids

Molecules in a pure liquid are generally surrounded by similar neighbors. As a consequence, the molecules are not subject to any resulting force caused by molecular interactions. At air/liquid or liquid/liquid interfaces, respectively, this balance is no longer valid. As a consequence there is a net force acting normal to the interface causing the interfacial tension. The molecules at the interface have higher energy and, thus, the generation of interface requires work. The smaller the free surface energy per unit of area, the more surface can be generated for given energy input [78, 163]. The amount of work  $dW$  is directly proportional to the enlargement of the interfacial area  $dA_I$ :

$$dW = \sigma \cdot dA_I, \quad (2.2)$$

where  $\sigma$  denotes the interfacial tension. Interfacial tension represents a two-dimensional counterpart to the three-dimensional pressure. Young [190] and Laplace [100] derived the basic equation of capillarity describing the pressure difference between two fluids separated by a curved interface:

$$\Delta p_{\text{Ca}} = \sigma \cdot \left( \frac{1}{r_1} + \frac{1}{r_2} \right), \quad (2.3)$$

where  $\Delta p_{\text{Ca}}$  is the Capillary pressure difference and  $r_1$  and  $r_2$  represent the radii of the curved interface. For spherical bubbles with diameter  $x_B$ , the Laplace pressure is:

$$\Delta p_{\text{Ca}} = \frac{4 \cdot \sigma}{x_B}, \quad (2.4)$$

As a consequence of Eqs. 2.2 to 2.4, fluids tend to create smallest possible interfaces and a spherical shape is consequently preferred.

## Dynamic interfacial tension

Surface active compounds drastically reduce the interfacial tension. Due to their amphiphilic character, they are able to adsorb at gas-liquid interfaces and even tend to accumulate at the interface leading to higher surfactant concentration at the interface compared to the bulk liquid phase.

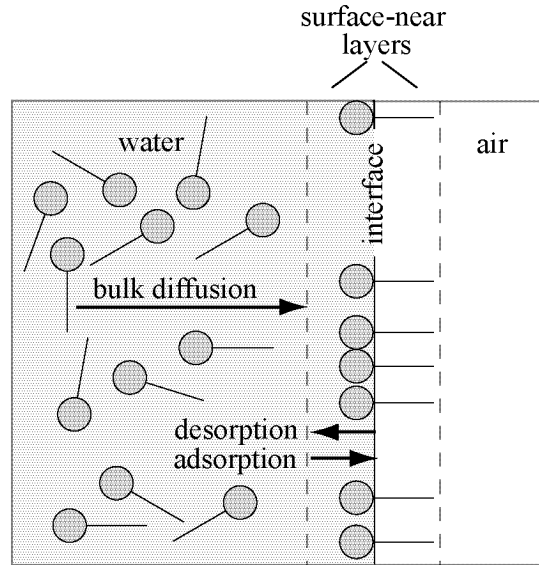


Figure 2.2.: Schematic of air/water interface and adsorption mechanism.

The adsorption process of surfactant  $i$  at the interface includes two mechanisms (see Fig. 2.2): (i) the bulk diffusion process where molecules are exchanged between bulk solution and surface-near layer, and (ii) the adsorption process, where surfactant is transferred between surface-near layer and surface layer. The interfacial tension is, thus, a function of bulk surfactant concentration  $c_i$  and the surface age. Ageing starts as soon as new interface is generated, e.g. by whipping. The molar transport equation (species  $i$ ) for an incompressible fluid is given as (see [49]):

$$\frac{\partial c_i}{\partial t} + (\vec{v}\nabla)c_i + \nabla \cdot \vec{j}_i = \vec{r}_i, \quad (2.5)$$

where  $c_i$  is the species concentration,  $\vec{v}$  represents the mass-average velocity,  $\vec{j}_i$  the molar diffusion flux and  $\vec{r}_i$  the molar production rate vector arising from internal processes. Eq. 2.5 states that a change in the concentration of species  $i$  may only be caused by convection flux, diffusive flux and by internal production processes.

Ignoring interactions of surfactant molecules and assuming monolayer adsorption and thermodynamically ideal bulk solutions, Langmuir [99] describes the relation-

## 2. Background

ship between surface-excess concentration,  $\Gamma_i^s$ , and bulk concentration,  $c_i$ , according to equation 2.6:

$$\Gamma_i^s = \Gamma_{i,\infty}^s \frac{c_i}{a_L + c_i}, \quad (2.6)$$

where  $a_L$  is the Langmuir parameter and  $\Gamma_{i,\infty}^s$  a theoretical surface concentration limit which is restricted in real systems due to coverage restraints such as critical micelle concentration and solubility.

In contrast to theories derived from a kinetic point of view, e.g. [99, 55], Gibbs equation [58] is derived from a purely thermodynamic basis and is given for a two-component system with the ideal dilute solution assumption (solute and solvent) as:

$$\Gamma_i^s = -\frac{1}{R \cdot T} \cdot \left( \frac{d\sigma}{d \ln c_i} \right)_T, \quad (2.7)$$

where  $R$  is the gas constant and  $T$  the temperature. The surface-excess concentration is not given as a direct function of the bulk concentration but in terms of the effect of the solute on the interfacial tension. By combining Eqs. 2.6 and 2.7, a correlation of the interfacial tension as a function of the bulk concentration is obtained (Langmuir-Szyszkowski isothermal equation) which is indicated as surface equation of state [48]:

$$\sigma = \sigma_0 - R \cdot T \cdot \Gamma_{i,\infty}^s \cdot \ln \left( 1 + \frac{c_i}{a_L} \right). \quad (2.8)$$

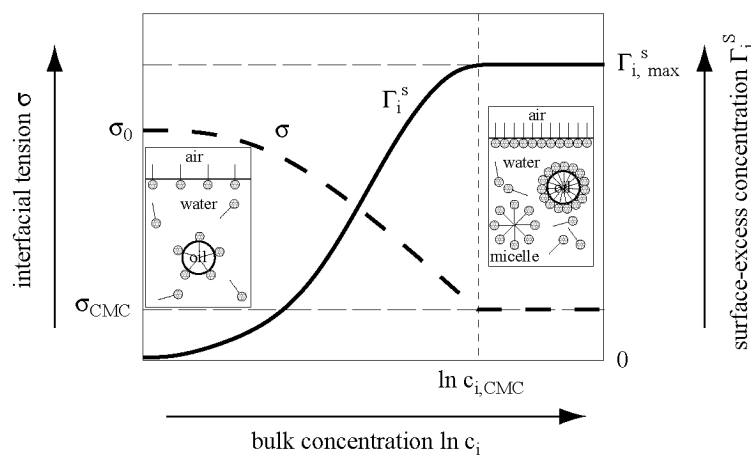


Figure 2.3.: Interfacial tension and surface-excess concentration of species  $i$  as function of bulk surfactant concentration according to Eq. 2.7 and 2.8 [4].



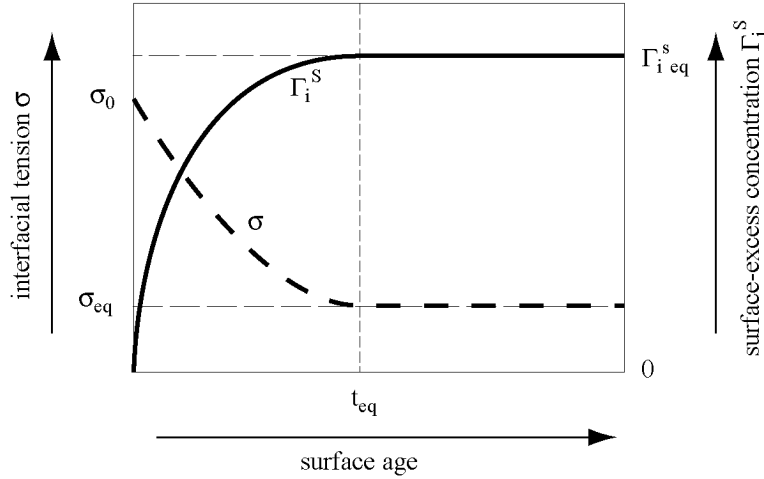


Figure 2.4.: Qualitative illustration of the dynamic surface tension and surface-excess concentration as function of surface age. [4]

The Gibbs adsorption isotherm is plotted qualitatively in Fig. 2.3. From the slopes of the tangents to the curve  $\sigma = \sigma(\ln c_i)$  the equilibrium surfactant concentration at the interface,  $\Gamma_i^s$  at different interfacial tensions can be calculated (see Eq. 2.7).  $\Gamma_i^s$  increases monotonically until the entire interface is covered with surfactant molecules. Corresponding to the increase in surface coverage, the interfacial tension declines with increasing bulk concentration until the critical micelle concentration is reached from where interfacial tension adopts a constant minimum value. At this so-called critical micelle concentration (CMC), the surfactant molecules form micelles in the bulk phase and the desorption flux equals the adsorption flux of surfactant (see Fig. 2.2). In non-equilibrium conditions where the surfactant coverage of the interface has not reached the equilibrium state, the interfacial tension  $\sigma$  may differ significantly from its equilibrium value. In this case, the surface-excess concentration and the interfacial tension are a function of the surface age since the adsorption process is still in progress and the adsorption dynamics play an important role. A non-equilibrium state is generated for example through a change in interfacial area when new bubbles are formed. As illustrated in Fig. 2.4, the equilibrium is again reached after a certain time,  $t_{eq}$  and both the surface-excess concentration and the interfacial tension once again reach a constant value. The interfacial coverage in non-equilibrium is a complex dynamic process. No formula exists for non-equilibrium conditions. A quantitative description is obtained by assuming pseudo-equilibrium conditions. This will not be further discussed here. Detailed reviews on interfacial transport phenomena covering measuring methods, theoretical and experimental investigations are provided by Edwards et al. [49],

Israelachvili [79], Chang and Franses [32], Dukhin et al. [48] and Ravera et al. [141].

### Surfactants

In foamed food products, emulsifiers (low-molecular weight), proteins (high-molecular weight) or a mixture of both are used as surfactants. Detailed information on molecular structure of surface active ingredients is given by Stache and Kosswig [161] and by Stauffer [163]. Synthetic emulsifiers and biopolymers used in the food industry are described by Hasenhuettl [75], Schuster [152] and Krog [95].

Using emulsifiers for foaming, it is important to choose such with high adsorption affinity at the air-water interface. A common way of predicting the solubility from the molecular composition of a surfactant is the use of the HLB-concept (hydrophilic-lipophilic balance). An HLB value  $<6$  indicates a more hydrophobic surfactant, an HLB value  $>8$  a more hydrophilic behavior. The concept was derived for emulsions, it can however be also applied to foams where hydrophobic surfactants should be chosen. Depending on the behavior of the hydrophilic part, surface active substances (emulsifiers) are divided into anionic, cationic, non-ionic and amphoteric molecules [118].

If foams contain both proteins and emulsifiers or other amphiphilic molecules, a competitive adsorption at the interface is observed leading to both synergistic and antagonistic effects [115, 43, 163, 108, 96, 126]. This is currently an important topic in research because many systems involve protein-surfactant interactions [52, 115, 116].

For both low- and high-molecular surfactants, the interfacial stabilization is divided into diffusion and adsorption steps. Since proteins are much larger than surfactants, their diffusion velocity is lower. Low molecular weight surfactants and proteins stabilize interfaces by different mechanisms [180]: surfactants generally stabilize an interface by the Gibbs-Marangoni mechanism that relies on the surfactant having a high degree of lateral mobility involving minimal interactions of surface adsorbed molecules. Conversely, proteins stabilize an interface by forming a strong visco-elastic network in which the protein molecules are essentially immobile and interacting with each other [103]. Proteins are dipolar ions and, thus, amphoteric emulsifiers. Their macromolecular composition with positively and negatively charged groups and hydrophilic and hydrophobic parts allows proteins to have several points of contact between molecule and interface. Compared to low-molecular weight surfactants, the interfacial occupancy by macromolecular proteins is high already at lower concentrations and the critical micelle concentration is consequently reached at lower concentrations. However, the equilibrium interfacial occupancy of proteins is lower. Proteins often change their conformation at the interface making the adsorption process irreversible. Then, the Gibbs isotherm (Eq. 2.7) is not valid. The equilibrium interfacial tension is higher for

proteins than for emulsifiers and proteins build multilayered surface films leading to very stable foams. Proteins can be divided into globular which are rather stiff and flexible ones. Globular proteins build thick interfacial layers which are more resistant to shear. Flexible proteins unfold easily at the interface and build double- to multilayers of relatively low film viscosity. Tab. 2.1 summarizes the interfacial properties of proteins and emulsifiers according to Prins et al. [132]. The diffusion of proteins to the interface is influenced by the degree of denaturation, temperature, pH-value and ionic strength [92, 104, 37]. These parameters will not be further discussed.

Table 2.1.: Interfacial properties of proteins and emulsifiers according to Prins et al. [132].

Parameter	Proteins	Emulsifiers
Interfacial tension [ $\text{mN} \cdot \text{m}^{-1}$ ]	$\approx 50$	$\approx 20\text{-}30$
Interfacial occupancy [ $\text{mol} \cdot \text{m}^{-2}$ ]	low	high
Equilibrium film thickness [nm]	40	4
Adsorption	irreversible	reversible
Conformational change	yes	no

## Wettability and contact angle

The interfacial tension between two liquids or between liquid and gaseous phase can be measured directly, e.g. using the drop volume method [70]. Contrarily, the surface tension of solids can only be determined indirectly via contact angle measurements.

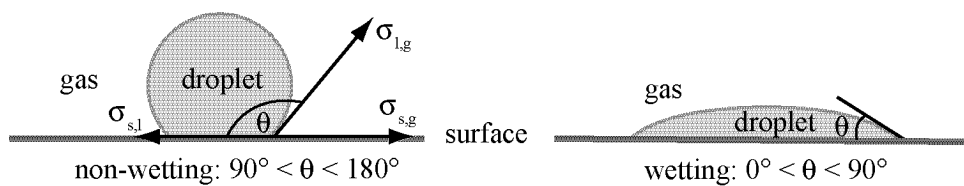


Figure 2.5.: A liquid droplet in equilibrium with a horizontal surface surrounded by gas [190].

The wettability is defined as the contact angle between a droplet in thermal equilibrium on a horizontal surface. Depending on the type of surface and liquid, the droplet may take a variety of shapes as illustrated in Fig. 2.5. The contact angle  $\theta$  is given by the angle between the interface of the droplet and the horizontal

surface. The liquid is wetting when  $0 < \theta < 90^\circ$  and non-wetting when  $90 < \theta < 180^\circ$ .  $\theta = 0^\circ$  corresponds to perfect wetting, the drop spreads and forms a film on the membrane surface. The wetting angle is a thermodynamic variable that depends on the interfacial tension of the surfaces. Let  $\sigma_{l,g}$  denote the interfacial tension at the liquid-gas interface,  $\sigma_{s,l}$  refer to the interfacial tension at the solid-liquid interface and  $\sigma_{s,g}$  indicate the interfacial tension between solid and gaseous phase. In thermodynamic equilibrium, the wetting angle is given by Young's law (see Fig. 2.5, [190]):

$$\sigma_{s,l} = \sigma_{s,g} - \sigma_{l,g} \cos \theta. \quad (2.9)$$

In membrane foaming it is important that bubbles and membrane do not wet since this is advantageous with respect to bubble detachment. If bubble and membrane were wettable, the bubble would instead form a film on the membrane (Fig. 2.6). Since the gas bubble is hydrophobic compared to a water-based continuous phase, it is best to use hydrophilic membranes.

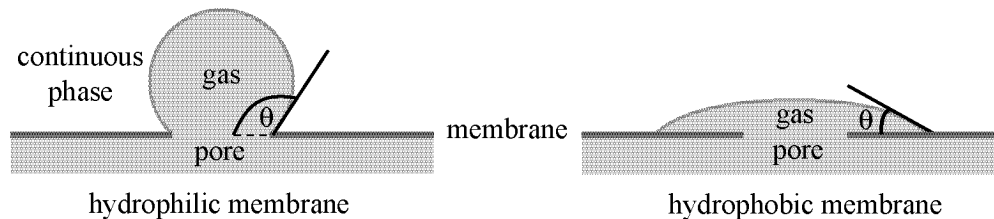


Figure 2.6.: A gas bubble at the pore of a membrane. Wetting angle between bubble and membrane.

## 2.2. Foam generation

Foam generation can be considered as the process where big air bubbles are split into smaller ones by viscous friction forces (shear, elongation) or inertia forces acting on the interface and causing deformation and breakup. Bubble dispersing and its reverse effect, coalescence, are in dynamic equilibrium for constant power and energy input resulting in an equilibrium structure with certain mean bubble size.

An upper limit in achievable gas volume fraction exists. Beyond this limit, so-called blow-by occurs in a continuous whipping process. Blow-by is the inability of a system to disperse all the added gas into the mix. As a result, the foam is no longer homogeneous and the measured gas volume fraction differs from the set one. In a rotor-stator device, blow-by can be explained according to Hanselmann [72]. In a first step of whipping, gas and liquid tend to separate due to centrifugal forces as a consequence of the density difference. A gas cone is built up around the

rotor. Blow-by occurs if gas from such a cone can not be dispersed in the liquid during its passage through the whipping head. Fig. 2.7 shows a picture of blow-by in a high-viscous foam matrix where it manifests as an irregular surface with holes. Blow-by can as well occur in any other continuous foaming process and has to be avoided.



Figure 2.7.: Illustration of blow-by.

In the food industry, foam is mostly produced following two different principles [174]:

- By supersaturating a liquid with gas, either by dissolving the gas under pressure and releasing the pressure, e.g. in beer, or by generating gas in situ, e.g. by fermentation.
- By mechanical means, either injection of gas through narrow openings and/or breaking big bubbles up into smaller ones. This method is used widely in industrial foam production since the amount of gas and the mechanical power/energy input can be controlled.

Whipping apparatus of the second class can be further subdivided into static mixers and dynamic mixers.

- Static mixers consist of a tube or channel with static mixing elements. The gas and liquid phase are dispersed in the flow regime in the vicinity of the mixing elements. The shape of the mixing elements, the overall length of the tube and the volume flow rate influence the mixing and dispersing characteristics. Static mixers are simple to operate and cheap with the disadvantage that the energy input and consequently the dispersing intensity can only be varied by changing the volume flow rate or the geometry of the mixer [187].

- Typically, dynamic mixers consist of a rotor-stator system with whipping blades, which disperse the gas bubbles in a flow field controlled by the circumferential velocity of the rotor and the residence time given by the volume throughput rate.

Another distinction between foaming principles of particular interest in this work is between i) processes where big bubbles are broken up into smaller ones by the shear field, and, ii) processes where the gas is directly introduced into the mix as small bubbles, thus creating a foam. The typical examples for i), rotor-stator devices, and for ii), membrane devices, will be described in further detail.

### 2.2.1. Rotor-stator whipping device (R/S)

Continuous rotor-stator mixers are a common whipping equipment used in industrial applications. They consist of a rotor and a stator each having a series of blades with pins. Stator pins are welded onto the mixing head housing, rotor pins onto the shaft. By spinning the rotor, a complex dispersing flow field between the partially intermeshing rotor and stator pins is generated. Rotor-stator mixers produce foam continuously. A large variety of empirically designed continuous R/S-mixers are available differing in size, pin geometry, gap size, number of pins and/or blades [72]. Depending on circumferential rotor velocity, rotor and stator geometry and viscosity of the two phases/foam systems, laminar or turbulent flow fields are generated in R/S-whipping heads. The bubble size decreases until the equilibrium between shear forces and surface forces is reached if the residence time is long enough. Since in general a residence time and dispersing spectrum exist, the resulting bubble size is not uniform.

### 2.2.2. Static membrane setup

Membrane foaming using static membranes enables the direct incorporation of small gas bubbles into the product. There is no need to break bubbles up in a flow field. The disperse phase is pressed through a membrane into the cross-flowing continuous phase. Bubbles are formed at the pores and wiped off by the flow of the continuous fluid phase. The main advantage of such membrane foaming devices are the small energy input into the product which is important for mechanically sensitive foam products. Most important disadvantages are the coupling of shear force and throughput rate and relatively large resulting bubbles. Fig. 2.8 shows a schematic drawing of bubble and foam generation using a static membrane.

Bals [10] showed that for foams produced with a static membrane containing high gas volume fractions, coalescence leads to bubble sizes significantly larger than pore size up to a factor of 1000. Furthermore, the emulsifier properties are

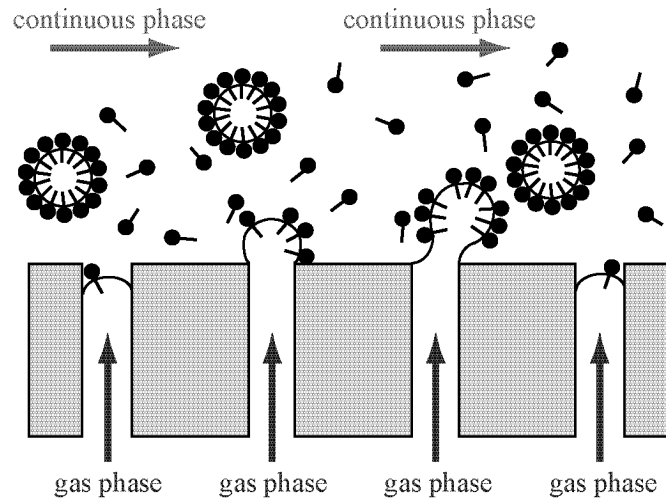


Figure 2.8.: Model of bubble and foam generation when using a static membrane.

of major importance since the energy input is low and a high surface activity is needed to stabilize bubbles via surface forces only [176, 12, 71]. The quantity needs to be above the critical micelle concentration to make sure that at least a monolayer covers the built interface. If proteins are used as the surfactant, a concentration above 5 weight % is needed. Viscosities up to  $0.1 \text{ Pa} \cdot \text{s}$  were found to stabilize the product due to a delay in coalescence and drainage while higher viscosities hindered bubble incorporation. The dominating factors for resulting bubble size were coalescence at the pore and in the subsequent flow, the factor of coalescence depended on the pore size.

### 2.2.3. Dynamically enhanced membrane foaming

Similar to the foaming principle valid for static membranes (see Sec. 2.2.2, gas is pressed through membrane pores and resulting bubbles are detached from the membrane surface by the acting shear stresses. In the new dynamically enhanced membrane foaming device developed during this work, the shear stress no longer depends on the throughput rate of the continuous phase only but can be controlled by the circumferential velocity of the inner cylinder. Circumferential velocities up to  $30 \text{ m/s}$  can be reached. The inner cylinder is either a cylindrical membrane (ROME) or made of compact metal (DESM). In the latter case the membrane is attached to the inner wall of the outer cylinder housing. The ROME type of dynamically enhanced membrane device was also shown to be effective in the field of emulsification (Patent: DE 10 2004 040 735.5) where it led to very small droplets and narrow drop size distributions, i.e. smallest mean droplet size about equivalent to pore size.

Detailed information about the dynamically enhanced membrane foaming device will be given in Sec. 3.3.4.

## 2.3. Bubble deformation and breakup in laminar flow

Foaming processes make use of the breakup of bubbles caused by viscous friction (shear and elongational) or inertia stresses. Such stresses are generated in dispersing flow fields acting in foaming devices. When bubbles are subjected to flow stresses, they deform and break up into smaller bubbles if the stresses are sufficiently high. Investigations concerned with the breakup behavior of single bubbles would allow predictions of bubble dispersing in foams. While a wide range of studies has investigated the correlation of deformation and breakup of single liquid drops to the external flow conditions, only few studies about bubble deformation exist. Bubble breakup is not reported in any publication to date. Detailed review articles on deformation and breakup of droplets are provided by Grace [60], Acrivos [1], Rallison [139] and Stone [164], on deformation of bubbles by Rust and Manga [144] and Canedo et al [27]. Parameters describing deformation and breakup in simple shear and elongational flow will be discussed in this section.

### 2.3.1. Parameters describing bubble deformation and flow stresses

A spherical bubble placed in steady simple shear flow with low Reynolds number deforms with a time-dependent shape and orientation until it reaches a steady deformation or breaks up into smaller bubbles. The steady bubble shape and orientation depend on (i) the ratio of the viscosity of the bubble relative to the surrounding fluid, (ii) the concentration and behavior of surfactant, and (iii) the Capillary number  $Ca$ .  $Ca$  is the ratio of shear stresses generated in the flow that deform the bubble and interfacial tension related stresses represented by the Laplace pressure that tend to keep the bubble spherical.

$$Ca = \frac{\eta_{\text{cont}} \cdot G \cdot x_B}{2 \cdot \sigma} \quad (2.10)$$

In equation 2.10,  $G$  defines the rate of deformation. For quantitative evaluation of flow problems,  $G$  has to be attributed to the flow field.  $G$  may represent any linear combination of shear and elongation flow components. For simple shear, the velocity  $\vec{v}$  is given as



$$\vec{v} = \begin{pmatrix} \frac{\partial v_x}{\partial y} \cdot y \\ 0 \\ 0 \end{pmatrix} = \begin{pmatrix} \dot{\gamma} \cdot y \\ 0 \\ 0 \end{pmatrix}. \quad (2.11)$$

Accordingly, the rate-of-strain tensor results as:

$$\dot{\gamma} = \frac{1}{2} \cdot \begin{pmatrix} 0 & \dot{\gamma} & 0 \\ \dot{\gamma} & 0 & 0 \\ 0 & 0 & 0 \end{pmatrix}. \quad (2.12)$$

As a consequence,  $G$  in Eq. 2.10 is represented by the shear rate  $\dot{\gamma}$  in the case of simple shear flow. Feigl et al. [53] presented modifications of  $G$  for more complex flow fields like uni-axial and planar elongational flows as well as mixed elongational-shear flow.

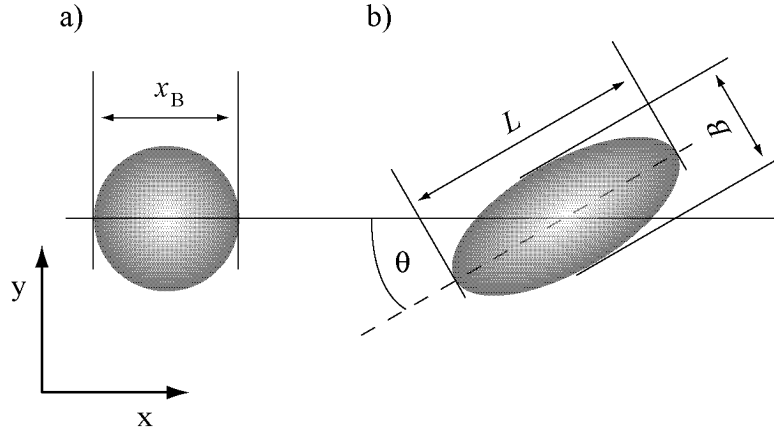


Figure 2.9.: Parameters describing bubble deformation: a) initial, undeformed bubble shape and b) deformed bubble.

At low deformations, the deformed bubble has an ellipsoidal shape. In a two-dimensional approach assuming an axisymmetric bubble shape, its major axis  $L$  and its minor axis  $B$  as well as the rotation angle versus the principal axis of flow  $\theta$  define the bubble shape in flow. Fig. 2.9 shows a schematic drawing of an initial, spherical bubble and a deformed, ellipsoidal bubble. The deformation parameter  $D$  first introduced by Taylor [170] can be used to characterize the degree of deformation for modest shape changes:

$$D = \frac{L - B}{L + B}. \quad (2.13)$$

$D$  is 0 for a sphere and asymptotically approaches unity for higher deformed, long and slender bubbles. For small deformations, the steady-state geometry of a

## 2. Background

---

bubble can be described using Taylor theory [170]:

$$\mathbf{D} = Ca \cdot \frac{19\lambda + 16}{16\lambda + 16}, \quad (2.14)$$

where  $\lambda$  is the ratio of the disperse phase viscosity to the continuous phase viscosity.

For  $Ca \ll 1$  and  $\lambda \ll 1$ , the bubble is nearly spherical with

$$Ca \cong \mathbf{D}, \quad (2.15)$$

see [169, 170, 35]. Experimental data [16, 60, 66, 170, 172, 69, 67] and numerical calculations [138, 129] confirm this relationship.

For highly deformed bubbles, where the shape deviates strongly from an ideal ellipsoid, the dimensionless length  $L/x_B$ , obtained by dividing the longer axis of the deformed bubble  $L$  by the original bubble radius  $x_B$  is an appropriate measure of deformation [16]. At high deformations ( $L \gg x_B$ ), bubbles are elongated with pointed ends. Using slender body theory and assuming bubbles to be circular in cross section, Hinch and Acrivos [77] predict:

$$\frac{L}{x_B} \cong 3.45 \cdot Ca^{0.5} \quad (2.16)$$

for  $Ca \gg 1$ ,  $\lambda \ll 1$  and  $Re \ll 1$ . Canedo et al [27] measured experimentally the deformation of air bubbles suspended in polybutene oil in a concentric cylinder device which approximates simple shear. They found that bubble cross-sections are elliptical and suggested that deformations as a function of  $Ca$  are slightly less than predicted by Eq. 2.16. Their data for  $3 < Ca < 50$  were well described by

$$\frac{L}{x_B} = 3.1 \cdot Ca^{0.43}. \quad (2.17)$$

The basic assumptions of most theoretical calculations that should be closely followed in experimental studies are [27]:

- Steady creeping flow with negligible inertia effects
- Incompressible Newtonian fluids
- No buoyancy effects, negligible net body forces on the bubble
- No wall effects, effectively unbounded suspending flow-field
- No heat or mass transfer, isothermal conditions, constant physical properties

For bubbles, the boundary conditions of "incompressibility" and "no buoyancy" can not be fulfilled.

All above mentioned theories (Eqs. 2.13 to 2.17) have been widely, but not always successfully explored. In early experiments, Taylor [170] found values that were scattered by more than 50 % from his model predictions because his materials were not pure enough and, thus, the viscosity ratio and interfacial tension not constant. Rumscheidt and Mason [143] tested Eq. 2.14 and found a number of systems giving good agreement. However, there were also a number of systems showing significant deviations from the model. More recently, very good agreement was found between the Taylor equation and experimental data [172, 69], even at values of Capillary number considered beyond the range of validity of the Taylor analysis.

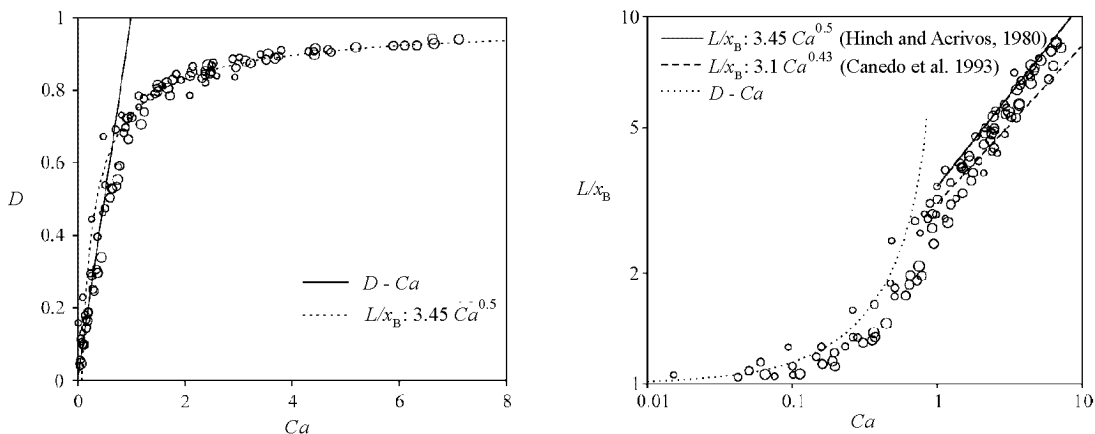


Figure 2.10.: Deformation parameter  $D$  (left side) and dimensionless extension ratio  $L/x_B$  (right side) versus Capillary number  $Ca$  for bubbles in steady simple shear flow with  $\lambda \ll 1$  and  $Re \ll 1$ . Circle size proportional to undeformed bubble ( $0.88 \leq x_B \leq 2.55$  mm). Data and graphs by Rust and Manga [144].

The only fairly recent investigation of bubble behavior under simple shear was published by Rust and Manga [144]. Their experiments comprised shape data for bubbles for  $0.02 < Ca < 7.1$  reaching both spheroidal and slender body model regimes described by Eq. 2.15 and Eq. 2.16, respectively, as well as the transition between small and large deformation limits. Rust and Manga reached bubble deformations  $D$  of 0.94 corresponding to  $L/x_B = 32$  but did not reach bubble breakup neither during shearing nor during relaxation. Their data agreed well with Eq. 2.15 for values of  $\lambda \rightarrow 0$  and  $Re \ll 1$  up to  $Ca \leq 0.5$  and with Eq. 2.16 for  $Ca > 1$  and values of  $\lambda \ll 1$  and  $Re \ll 1$  whereas Eq. 2.17 slightly underestimates the data (see Fig. 2.10).

Associated with the deformation of a bubble under shear, there is an orientation process which makes the deformed bubble reach an angle  $\theta$  with respect to the flow direction. This angle is by definition  $45^\circ$  at rest and decreases with increasing

applied shear-rate as the bubble becomes aligned with the flow direction more and more. This flow-induced orientation depends on the Capillary number and has first been expressed as a linear relationship [28, 29, 137]. From experimental observation, it has however become clear that  $\theta$  does not depend linearly on  $Ca$  when the shear-rate increases. Hence, a non-linear description (transcendental function) must be used. Cox [35] published his theoretical analysis which follows as:

$$\theta = \frac{\pi}{4} - \frac{1}{2} \arctan \left( \frac{19 \cdot \lambda \cdot Ca}{20} \right) \quad (2.18)$$

for bubble orientation under shear flow. In this case, the viscosity ratio between bubble and continuous phase is taken into account. Hinch and Acrivos [77] proposed a model for high Capillary numbers in systems in which the disperse phase has a low viscosity compared to that of the suspending liquid:

$$\theta = \arctan (0.359 \cdot Ca^{-\frac{3}{4}}). \quad (2.19)$$

The phenomenological model of Maffettone and Minale [107] assumes ellipsoidal particle form and describes the orientation as:

$$\theta = \frac{1}{2} \cdot \arctan \left( \frac{f_1}{Ca} \right), \quad (2.20)$$

where  $f_1$  is given by:

$$f_1 = \frac{40(\lambda + 1)}{(2\lambda + 3) \cdot (19\lambda + 16)}. \quad (2.21)$$

Experimental work using Eqs. 2.18 and 2.19 showed reasonably good agreement between theory and experiments for relatively large deformations [27, 144]. However, the Cox equation (Eq. 2.18) fails to predict experimental trends of  $\theta$  for  $\lambda \leq 1$ . The most appropriate range of applicability of the Cox theory is for  $\lambda \gg 1$ , where good agreement has been found with experimental data for any value of  $Ca$  [68].

### 2.3.2. Breakup of single bubbles in 2-dimensional shear and elongational flow

Since no data exist on the breakup of bubbles, the following relationships will instead be discussed for droplets. Stresses generated in a flow field deform a droplet while interfacial tension stresses resist the deformation. A droplet is unable to maintain a steady shape as soon as flow-induced stresses exceed the interfacial tension stress. Consequently, the droplet undergoes a transient, continuous stretching which eventually results in droplet breakup. The burst of a droplet depends not

only on flow type and Capillary number, but on the entire time history of the velocity gradient experienced by the droplet [172, 77]. Transient effects are discussed in Stone et al. [165]. In the following, only steady state investigations are considered. The critical Capillary number

$$Ca_c = \frac{\eta_{\text{cont}} \cdot \dot{\gamma} \cdot x_B}{2 \cdot \sigma}, \quad (2.22)$$

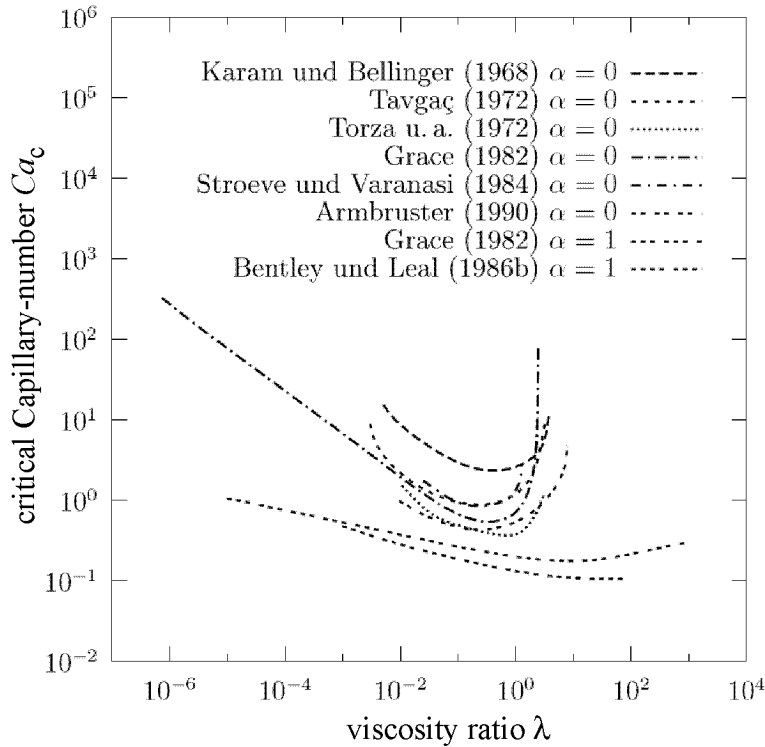


Figure 2.11.: Influence of viscosity ratio  $\lambda$  on critical Capillary number for simple shear ( $\alpha=0$ ) and planar elongation ( $\alpha=1$ ), experimental results of several authors (according to [89]).

is defined as the point where no stable droplet/bubble shape exists because a critical stress leads to breakup. The critical Capillary number depends on the type of flow, i.e. simple shear flow ( $\alpha = 0$ ), mixed shear-elongational flow ( $0 < \alpha < 1$ ) or pure extensional flow ( $\alpha = 1$ ). The viscosity ratio  $\lambda$  of disperse to continuous phase strongly influences the critical Capillary number for simple shear flow and slightly for extensional flow [89].  $Ca$  is, thus, commonly plotted as a function of  $\lambda$  (Fig. 2.11). Critical deformations were investigated for droplets by Rumscheidt and Mason [143], Karam and Bellinger [84], Tavgaç [168], Torza et al. [172], Stroeve and Varanasi [166], Armbruster [6] and Bentley and Leal [16]. The

## 2. Background

---

most extensive results were published by Grace [60] for viscosity ratios between  $10^{-6} \leq \lambda \leq 10^3$  for low viscous droplets in high viscous continuous phases. Fig. 2.11 shows experimental results of several authors. The variations can be explained by the difficulty of such experiments. The curve of Karam and Bellinger [84] is qualitatively correct, it is however shifted due to measuring errors of the interfacial tension [60].

The effect of vorticity of the external flow plays a critical role in determining whether breakup occurs or not. In contrast to pure extensional flow where the vorticity is zero, simple shear flow has equal parts of vorticity and strain rate. In simple shear flow, deformation and breakup are promoted by the straining motion in the external shear and are inhibited by the vorticity in the outer flow. At a viscosity ratio of  $\lambda \approx 1$ , a minimum in critical Capillary number is reached. For  $\lambda > 1$ , the critical Capillary number rises strongly. Taylor [170] showed that breakup in simple shear flow is impossible for  $\lambda \geq \approx 3.6$ . Instead, with further increasing applied shear rate, a slightly deformed droplet remains with an orientation angle of  $\theta \approx 0$ . Higher shear induces a faster circulation of fluid within the drop only. Drops in the low viscosity ratio regime typical for bubbles were shown to require high Capillary numbers for burst and to attain steady slender shapes at very large, under-critical deformations. The lower the viscosity ratio, the greater the sustainable deformation and consequently the higher the critical Capillary number. For such deformations, droplets and bubbles deviate from ellipsoidal shape considerably and develop pointed ends. A special breakup mechanism was observed at such low viscosity ratios for droplets: This so-called tip streaming in simple shear flows is a mode of droplet breakup in which the droplet develops a sigmoidal shape and a stream of tiny droplets is ruptured off the pointed ends/tips of the drop. Tip streaming is observed at under-critical Capillary number for drops [170, 60].

De Bruijn [40] closely investigated tipstreaming by testing suggested causes experimentally, namely the viscosity ratio, the rate of increase of the shear rate and the presence of surfactants. Tip breakup behavior is potentially very important since the shear rates required for this type of breakup have in some circumstances been observed to be two orders of magnitude lower than for the normal type of fracture breakup where a droplet is broken into two or three almost equally sized droplets with a few tiny satellite droplets in between (see Fig. 2.12). Additionally, the resulting particles can be much smaller for tip streaming than for fracture. De Bruijn found that the occurrence of tip streaming depends on the type of liquid and on the deformation history while the viscosity ratio is not important provided it is smaller than unity. Most importantly, de Bruijn found that tip streaming only occurs if interfacial tension gradients can develop, i.e. in the presence of surfactants or impurities in the fluid. The surfactant molecules are swept towards the pointed ends which results in low interfacial tension at the tips and higher tension elsewhere. At high enough surfactant concentrations, the interface gets less mobile and the ends become rigid allowing the shear stresses exerted by the continuous

phase to pull out a stream of droplets. Tip streaming does not occur at extremely low surface active material levels, when the interfacial tension cannot even be lowered locally, nor at high levels where there is so much surface active material present that the interfacial tension is low all over the droplet. Further investigations on the effect of surfactants on drop breakup were performed by Janssen et al. [80, 81] and by Briscoe et al. [24].

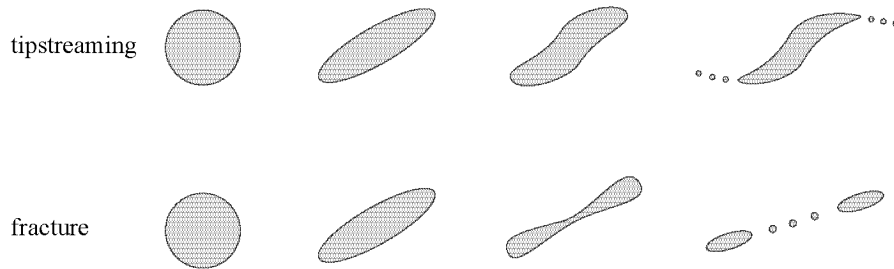


Figure 2.12.: Types of breakup observed in simple shear flow: fracture and tipstreaming [40].

In pure extensional flow, the critical Capillary number decreases with increasing viscosity ratio and remains constant for  $\lambda \geq 3$  (e.g. [16, 53]). Contrarily to simple shear flow, breakup can be achieved for arbitrary values of  $\lambda$  since no vorticity exists in pure extensional flow. When the applied elongational stresses exceed the critical stresses for breakup, the drops become highly extended to a long filament which breaks up due to capillary waves (e.g. [171, 114]).

For mixed flows containing both shear and elongation, the curve describing the critical Capillary number lies in-between the curves for the pure stress components.

As a consequence of all these studies, shear is less effective in drop breakup than elongation.

## 2.4. Bubble formation at pores

The concept of membrane foaming (Sec. 2.2.3 and 2.4.4) is the simultaneous introduction of many small bubbles using a membrane as the dispersing tool. It is essential to understand the formation and detachment of bubbles from pores in order to optimize the process. Both bubble formation and detachment are complex events since bubbles are compressible and transient in size and form.

In this section, the difference between dripping and jetting will be explained. Then bubble formation and detachment into stagnant and flowing continuous phases will be described. In addition, the significant impact of the relative motion of one wall against the other will be discussed to understand the advantages of the dynamically enhanced membrane device compared to a static membrane setup.

Forces acting on the bubbles will be discussed and factors influencing bubble formation and detachment derived.

### 2.4.1. Dripping and jetting

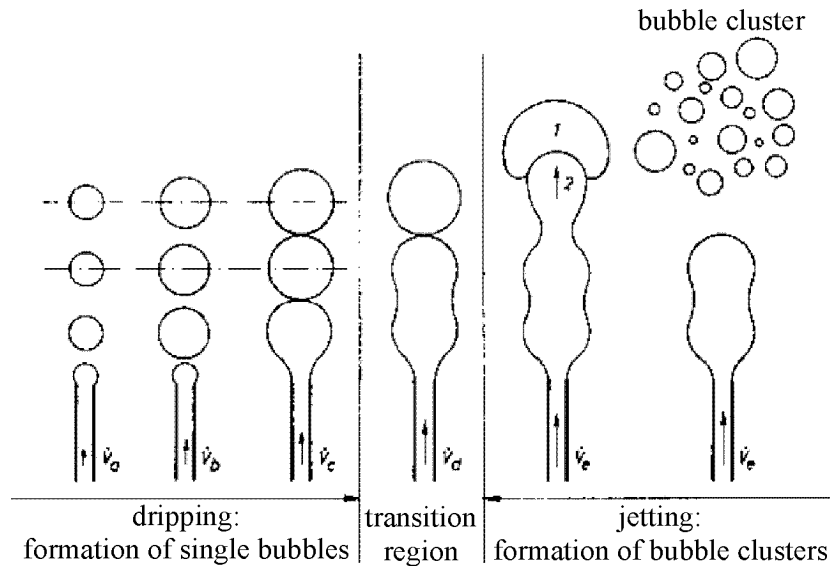


Figure 2.13.: Schematic drawing of bubble formation at capillary tip or pore: dripping and jetting (22).

When talking about bubble formation, a distinction between two mechanisms, i.e. dripping and jetting, is made. Bubble formation in the dripping domain can be described as a periodical formation of single bubbles [22, 135, 97, 140, 38]. Earlier publications [22] state a jetting domain for bubble formation where the air leaves a pore or capillary tip as a jet, hence the name jetting (see Fig. 2.13). Modern measuring techniques showed that no such jet formation happens for bubbles [136] while it does for droplets where liquid drops break up from an extended filament due to capillary waves (see Fig. 2.14). However, with increasing gas throughput rates, a change in bubble formation mechanism was observed: bubbles were observed to be formed as single bubbles or in pairs (see Fig. 2.15, [136]), the latter of which might lead to direct coalescence at the capillary tip or membrane pore.

The transition point between the dripping and jetting domain has been analyzed in detail for droplets while few information is available for bubbles. The dynamics of droplet formation change significantly at the transition point (e.g. [147, 191, 33, 36]). Important parameters affecting the droplet breakup mechanism include the viscosity and density of the disperse phase,  $\eta_{\text{disp}}$  and  $\rho_{\text{disp}}$ , the mean velocity of the



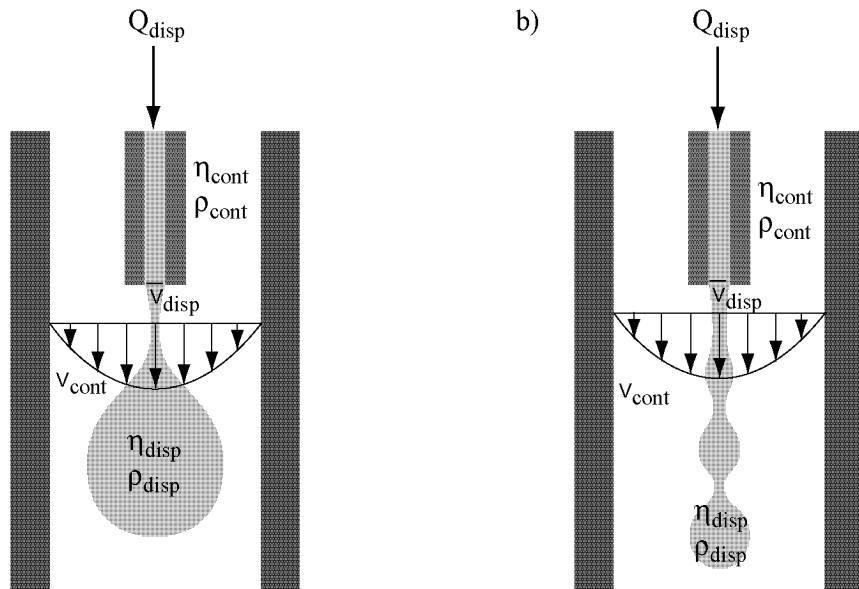


Figure 2.14.: Drop formation mechanism at a capillary tip: a) dripping and b) jetting (according to [36]).

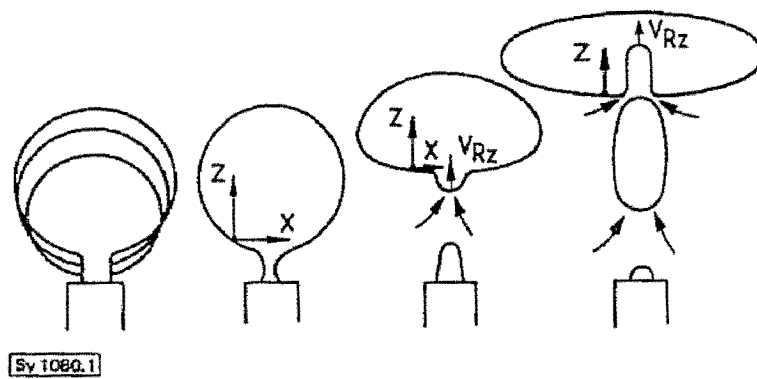


Figure 2.15.: Schematic drawing of bubble formation at capillary tip [136].

disperse phase at the capillary tip  $\bar{v}_{\text{disp}}$  the viscosity and density of the continuous phase,  $\eta_{\text{cont}}$  and  $\rho_{\text{cont}}$ , the velocity of the continuous phase  $v_{\text{cont}}$ , and the capillary diameter  $D_{\text{Ca}}$ .

Since many publications dealing with models on bubble formation and resulting bubble size still distinguish the dripping and jetting domain, the domains will be discussed separately.

## 2.4.2. Bubble formation into stagnant continuous phase

### Dripping: low disperse phase velocity

At low disperse phase flow rates and corresponding low disperse phase velocities, single bubbles are formed and detached from pores as soon as the detaching forces outweigh the retaining forces. This type of bubble formation is called dripping [10], the relevant forces acting in the case of dripping into a stagnant continuous phase are shown in Fig. 2.16 and summarized in Eq. 2.23.

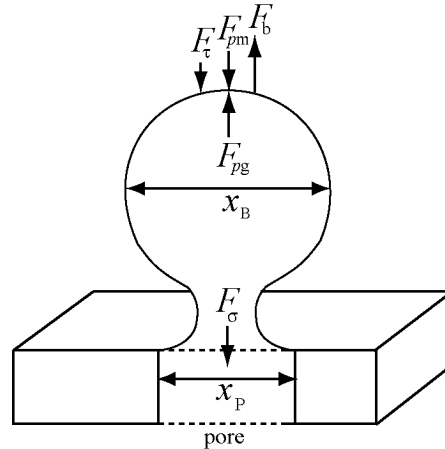


Figure 2.16.: Forces acting on a bubble for dripping at low gas throughputs into stagnant fluid (according to [10]).  $F_b$  is the buoyancy force,  $F_{pg}$  the pressure force of gas,  $F_{pm}$  the pressure force of mix,  $F_\sigma$  the surface tension force,  $F_\tau$  the drag force,  $x_B$  the bubble diameter and  $x_p$  the pore diameter.

$$F_\sigma + F_\tau + F_{pm} + F_b + F_{pg} = 0, \quad (2.23)$$

An important retaining force is the surface tension force,  $F_\sigma$ :

$$F_\sigma = \pi \cdot x_P \cdot \sigma \quad (2.24)$$

By approximation, the pore diameter  $x_P$  and the equilibrium surface tension  $\sigma$  are used to compute the surface tension force. For exact calculation, the pore diameter can only be used in an early phase of bubble formation. In a later phase nearing bubble detachment the narrowest diameter of the bubble neck should be used. This neck diameter is, however, hard to estimate. The time dependent surface tension grows linearly with growing bubble diameter.

One of the detaching forces is the buoyancy force  $F_b$  given by the density difference  $\Delta\rho$  between inner and outer phase:

$$F_b = \Delta\rho \cdot V_B \cdot g, \quad (2.25)$$

where  $V_B$  is the bubble volume and  $g$  the gravity constant.

Following the capillary theory, the resulting bubble size  $x_B$  can then be computed via the equilibrium of these forces for very low gas throughputs [156]:

$$x_B = \sqrt[3]{\frac{6 \cdot x_P \cdot \sigma}{g \cdot \Delta\rho}}. \quad (2.26)$$

It is assumed that the surrounding fluid is not accelerated by the bubble formation and thus only inertia, static pressure and surface tension forces play a role. From the entire balance of forces for bubble detachment into a stagnant continuous phase (Eq. 2.23), the drag force  $F_\tau$  and the pressure forces of mix and gas,  $F_{pm}$  and  $F_{pg}$ , respectively, were neglected in Eq. 2.26.

In Mersmann's model [113], the bubble retaining drag force  $F_\tau$  is additionally considered.  $F_\tau$  results from the resistance of the surrounding fluid against bubble growth and includes a drag coefficient  $c_d$ , the relative velocity of bubble versus fluid  $v_{rel}$  and the bubble cross section  $x_B$ . It is assumed that the drag coefficient does not change.

$$F_\tau = c_d \cdot \frac{v_{rel}^2 \cdot \rho_{cont}}{2} \cdot \frac{x_B^2 \cdot \pi}{4} \quad (2.27)$$

The force balance of this simplified model by Mersmann [113] considering bubble dripping into a stagnant fluid and low gas velocities results as:

$$F_\sigma + F_\tau + F_b = 0 \quad (2.28)$$

Mersmann's model can be modified to include the ratio of Weber ( $We$ ) and Froude ( $Fr$ ) number. This dimensionless notation simplifies the comparison of measured values of different systems. In this case, the We-number ( $We = 2 \cdot Ca$ ) which is the ratio of inertia and surface tension force is defined in such a way that the gas velocity is dependent on the number of pores  $z$ :

$$We = \frac{v_{g,P}^2 \cdot x_P \cdot \rho_g}{\sigma} \quad \text{with} \quad v_{g,P} = \frac{4 \cdot \dot{V}_g}{x_P^2 \cdot \pi \cdot z}, \quad (2.29)$$

where  $v_{g,P}$  is the gas velocity through the pores. High  $We$ -numbers are equivalent to high amounts of stabilizing forces. The  $Fr$ -number is derived from the inertia force generated by the difference in buoyancy and gravitational force:

$$Fr = \frac{v_{g,P}^2}{g \cdot x_P} \quad (2.30)$$

When the  $Fr$ -number is divided by the  $We$ -number, the inertia force cancels if quasi-static conditions are assumed. Eq. 2.31

$$x_B = x_P \cdot 1.817 \left( \frac{Fr}{We} \right)^{\frac{1}{3}} = x_P \cdot 1.26 \left( \frac{3 \cdot \sigma}{\rho_{cont} \cdot g \cdot x_P^2} \right)^{\frac{1}{3}} \quad (2.31)$$

gives good agreement with measured values of Siemes [156] for different systems and nozzles [22].

Mersmann's model was adapted in many ways, e.g. by including the kinetic force of the flowing disperse phase as detaching force [140], iteratively (e.g. [97, 142, 136, 134]), or by depending on the viscosity of the continuous phase [56].

## Transition from dripping to jetting for bubbles

The relationships described above are only valid for low gas flow rates. With increasing gas flow rate, the frequency of bubble formation first increases while the bubble diameter stays the same and remains approximately monodisperse. When the gas flow rate is further increased, the bubbles grow and start touching each other. From some point on, the frequency of bubble formation does not change anymore [156]. Instead, bubbles start to deform each other resulting in a heterodisperse size distribution. A preceding bubble creates a vacuum which sucks out the subsequent bubble. This second bubble is accelerated when the tube linking bubble and pore snaps and the bubble bumps into the first bubble leading to flattened ellipsoidal bubble geometries. The sucking force additionally influences the force balance in this transition region from dripping to jetting. Depending on the acting forces and surface characteristics, colliding bubbles coalesce or are dispersed by flow forces. The resulting bubble size is dependent on three factors [154]: i) dispersion at dispersing tool, ii) system tendency to coalescence and iii) secondary dispersing in continuous phase.

$We > 2$  is defined as the point of transition to jetting in some publications [113, 20, 125]. The boundary between dripping and jetting is shifted to higher Weber-numbers for higher continuous phase viscosities. Experiments showed that the mean bubble diameter decreases and the size distribution widens at the transition

point from dripping to jetting since secondary dispersion in the continuous phase takes place. Some theoretical approaches to calculate the secondary bubble size have been published. However, these theories contain many modulation parameters in addition to system and process parameters (e.g. [93, 134]).

## Jetting

In the lower jetting domain the mean bubble size is smaller than in the dripping domain due to secondary bubble breakup in the continuous phase [22]. At the same time, the width of the size distribution increases. In the higher jetting domain, the mean bubble size again increases due to coalescence [140, 21, 8, 134]. The impact of coalescence is determined by the system's viscosity and surface tension. The coalescence rate is proportional to the collision frequency  $f_{\text{coll}}$  which is determined by the disperse phase fraction  $\phi_V$ , the gas velocity  $v_g$ , the volumetric power input  $P_V$ , the bubble size  $x_B$ , the temperature  $T$ , and the continuous phase viscosity  $\eta_{\text{cont}}$ :

$$f_{\text{coll}} = \frac{\phi_V \cdot v_g \cdot P_V \cdot x_B \cdot T}{\eta_{\text{cont}}}. \quad (2.32)$$

The influence of surface tension on the bubble diameter decreases with increasing gas flow rate and is negligible in the jetting region. Inertia forces dominate the bubble formation. Klug [93] found that for  $We > 6$ , the bubble diameter is independent of the gas flow rate and is only dependent on the flow, the shear field created by neighbor bubbles and the momentum resulting from the rupture of bubble necks connecting bubble and pore.

## Difference between bubble formation at nozzles and porous systems

Contrary to the conditions found for nozzles, the surrounding fluid is limited for porous systems like multipore membranes. The pressure drop is lower for porous systems than for nozzles and the resulting bubble volume linearly dependent on the pressure difference [91]. The plate thickness and the gas filled cavity in front of the membrane are important. Since the complex pore network of a porous plate is difficult to characterize, real porous system are often theoretically treated as multi-nozzle systems.

When using porous plates, interactions between neighboring pores play an important role. If the pore distance is too small, bubbles can coalesce. Flow fields generated by bubble detachment influence detachment of succeeding bubbles. To guarantee defined bubble formation and detachment, the distance between pores should at least equal the bubble size.

### 2.4.3. Bubble formation into flowing continuous phase

In a continuously flowed through membrane, bubbles are not pressed into a stagnant but a flowing continuous phase. The bubble detachment is significantly influenced by the flow forces of the continuous phase. Bikerman [18] found that the resulting bubble size is four to ten times smaller in this case compared to bubbling into a stagnant continuous phase.

Fig. 2.17 shows the forces acting on a bubble in a continuously moved outer phase [9]. Besides the forces acting on a bubble in stagnant fluid (Fig. 2.16), three forces appear if the bubble is pressed into a flowing continuous phase (Fig. 2.17 and Eq. 2.33): (i) the axial drag force  $F_{\tau a}$ , evoked by the flow rate of the continuous liquid phase, (ii) the dynamic pressure force in the axial flow direction  $F_{pa}$  and (iii) a dynamic lifting force  $F_{b,dyn}$ . The direction of  $F_{b,dyn}$  is hard to predict since it strongly depends on the flow conditions near the bubble which are governed by the flow profile in the gap but also by the flow lines passing the bubble.

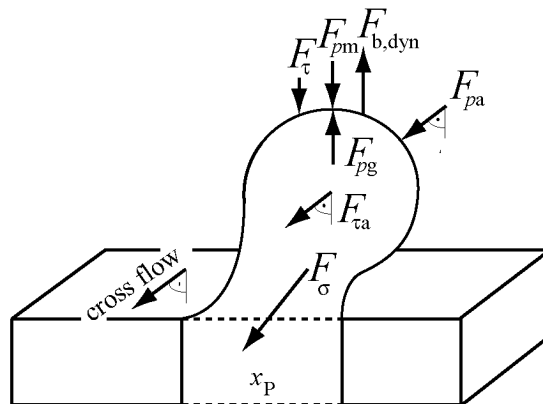


Figure 2.17.: Forces acting on a bubble during its formation and detachment from a pore into a flowing continuous phase.

The resulting balance of forces for bubble detachment in the case of continuous bubble formation into a flowing continuous phase can be stated as:

$$F_{\sigma} + F_{\tau} + F_{pm} + F_{b,dyn} + F_{pg} + F_{pa} + F_{\tau a} = 0 \quad (2.33)$$

The absolute value of the axial drag force now depends on the velocity of the continuous phase and the bubble size. The higher the velocity of the continuous phase, the earlier bubbles are detached.

$$F_{\tau a} = c_d \cdot \frac{v_{cont}^2 \cdot \rho_{cont}}{2} \cdot \frac{x_B^2 \cdot \pi}{4} \quad (2.34)$$

Several coherences were published for the drag coefficient  $c_d$ , e.g. the simplified Stokes-approach published by Brauer [22] valid up to a Reynolds-number of  $10^5$ :

$$c_d = \frac{24}{Re}. \quad (2.35)$$

This equation leads to errors up to 40 %. The Reynolds-number is calculated according to Eqs. 2.40 or 2.41, depending on the device used. Much more exact (maximal error 4 %) is the approximation by Kaskar and Brauer (185):

$$c_d = \frac{24}{Re} + \frac{4}{Re^{0.5}} + 0.4. \quad (2.36)$$

No tangible models are published for the calculation of the resulting bubble size for detachment into a flowing continuous phase. Important influencing parameters are the velocity of the continuous phase, the viscosity of the continuous phase, the wall shear stress and the geometry of the flow channel. The onset of jetting is known to be shifted to higher values when the bubbles are introduced into a flowing medium since the detaching forces are higher [93]. The rupturing of the tube linking bubble and pore can be neglected.

Bals [10] compared several models valid for bubble formation into a stagnant phase to experiments results which were obtained for bubble detachment into a flowing continuous phase. The dominating factors in the experiment were the pore size, surface tension, flow rate of continuous phase, velocity of disperse phase and viscosity of continuous phase. The calculated values were significantly lower than the measured ones, i.e. 2 to 3000 times lower. This is astonishing since the flow forces present in the experiments were not even considered. Bals showed that four models of different complexity [156, 113, 22, 56] resulted in the same value of 68  $\mu\text{m}$  (half the measured bubble size) because the surface tension force was the dominating factor in all four models. Additional terms dealt with the lifting force and the drag force. Three other models [38, 157, 18] led to still smaller bubble sizes since important factors like the pore size and surface tension were not even considered in the equations.

Bals [11] found a relationship between pore size and bubble size in experiments. For small pore sizes, the bubble diameter was shown to increase linearly with the pore diameter. This is in agreement with the results reported for membrane emulsification [88, 82, 127, 7, 155]. For bigger pore sizes, the bubble size was found to increase less than proportionally with increasing pore size. This means that the pore size influences the resulting bubble size less for larger pore sizes. The qualitative influences leading to this result are that: (i) the interfacial tension force increases with increasing pore size but decreases with increasing bubble diameter and (ii) the gas velocity in the pore decreases as the pore size increases.

### 2.4.4. Bubble detachment from pores of a dynamically enhanced membrane into a flowing continuous phase

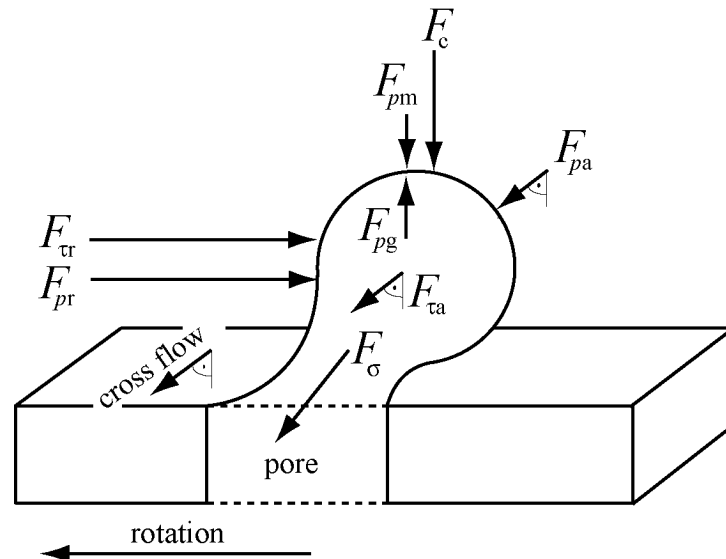


Figure 2.18.: Forces acting on a bubble during its formation and detachment from a pore of the rotating membrane.

Early bubble detachment from the pores is crucial in membrane dispersing processes. Thus, a dynamically enhanced membrane foaming (DEMF) device was developed to be able to define, vary and significantly increase the detaching forces. In this DEMF device, the inner cylinder rotates with circumferential velocities up to 30 m/s. This inner, rotating cylinder can either hold the membrane (rotating membrane type, ROME) or be made of compact metal (no pores) while the membrane is attached to the inner wall of the outer, static cylinder (dynamically enhanced static membrane type, DESM). In both device types, the shear rate is proportional to the velocity difference between inner and outer cylinder, the rotor diameter and reverse proportional to the gap size (Eq. 2.47). If these three parameters are constant and if wall slip is negligible, the acting dispersing forces should be identical for the two set-ups. Fig. 2.18 exemplarily shows the forces acting on the bubbles at a rotating membrane (ROME type). The gas is pressed into a flowing continuous phase. Compared to a non-rotating system, the drag force created by the membrane rotation has to be taken into account and the buoyancy force is replaced by the centrifugal force. Detaching forces are (i) the rotational drag force  $F_{\tau r}$ , (ii) the axial drag force  $F_{\tau a}$  evoked by the flow rate of the continuous



liquid phase, (iii) the pressure force  $F_{pg}$  resulting from the trans-membrane gas pressure difference and leading to bubble growth, (iv) the dynamic pressure force in rotational flow direction  $F_{pr}$  and (v) the dynamic pressure force in the axial flow direction  $F_{pa}$ . Compared to  $F_{\tau r}$ , the influence of  $F_{\tau a}$  on bubble detachment is small to negligible. Both forces depend on bubble size and acting shear stresses. Retaining forces are (vi) the pressure force of the mix  $F_{pm}$ , (vii) the surface tension force  $F_{\sigma}$ , depending on surface tension and pore size (for bubbles attached to the pore by a neck, the pore perimeter is replaced by the smallest perimeter of the tube linking bubble and pore), and (viii) the centrifugal force  $F_c$ , resulting from centrifugal acceleration and density difference of the two phases. Additionally to the forces mentioned above, there is a dynamic buoyancy force  $F_{b,dyn}$ . Its direction is not clear since it strongly depends on the flow conditions near the bubble which are governed by the flow profile in the gap but also by the flow lines passing the bubble.

The resulting balance of forces acting at a rotating membrane is:

$$F_{\sigma} + F_{pm} + F_c + F_{pr} + F_{\tau r} + F_{pg} + F_{pa} + F_{\tau a} = 0 \quad (2.37)$$

The parameters influencing bubble formation and detachment can be deduced from the acting forces. A distinction between process parameters (i.e. circumferential velocity, gas volume fraction, temperature, pressure), construction parameters (i.e. pore size, pore distance, number of pores, membrane diameter, gap size, hydrophilicity of membrane) and product parameters (i.e. viscosity, density, surface tension) can be made. These parameters partly influence each other, too.

## 2.5. Flow characteristics

Gas bubbles in a flow field deform and break up due to viscous friction (shear, elongational) and/or inertia forces exceeding critical limits. In a whipping head of e.g. a rotor-stator device, dispersion and coalescence are in a dynamic equilibrium. The equilibrium does not only depend on material parameters like surface tension and viscosity ratio but correlates with the mechanical power or energy input generated in the whipping flow field. This is why further information on the flow characteristics in a whipping device is needed.

### 2.5.1. Power characteristics

To describe the whipping process, it is necessary to characterize the flow conditions in the mixing head under a given mechanical power input. The flow conditions in a whipping device are characterized by the power characteristics  $Ne = f(Re)$  which can be experimentally determined. The power characteristics depend on geometry

## 2. Background

---

and power input. The power consumption of a mixer depends on geometrical dimensions like gap or pin size, product properties like density and viscosity and process parameters like the rotor speed. The power input  $P$  can be calculated from the measured torque ( $P = 2 \cdot \pi \cdot n \cdot T$  where  $n$  is the rotational speed and  $T$  the torque) or measured via the net electrical power consumption of the motor. The Newton number  $Ne$  is defined as the ratio between mechanical driving force and inertia force and can be expressed as:

$$Ne = \frac{P}{\rho \cdot n^3 \cdot D^5}, \quad (2.38)$$

where  $D$  is the rotor diameter. Hanselmann and Windhab [73] introduced a Newton number adapted to the geometry of a rotor-stator mixer (see Fig. 2.19) taking into account the distance between two pins  $y$ , the free radial distance  $l_{f,r}$ , the number of rotor and stator blade pairs  $e$ , the axial width of the pins  $q$ , and the axial gap between rotor and stator  $s$ :

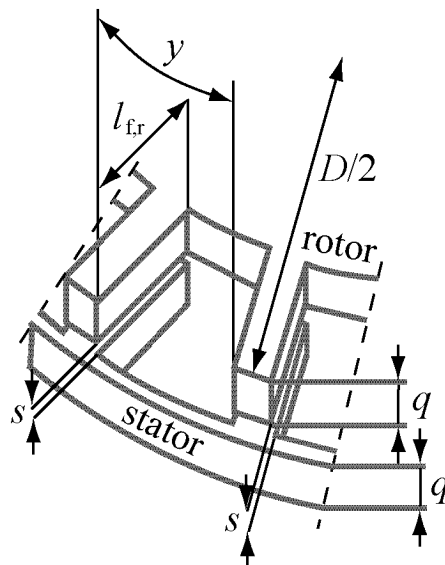


Figure 2.19.: Rotor and stator blades with pins.  $D$  rotor diameter,  $l_{f,r}$  free radial distance,  $q$  axial width of rotor/stator blades,  $e$  number of rotor-stator pairs,  $s$  axial gap between rotor and stator,  $y$  distance between two pins (according to [72]).

$$Ne = \frac{P \cdot y}{\rho \cdot n^3 \cdot D^3 \cdot l_{f,r} \cdot e \cdot q \cdot s}. \quad (2.39)$$

The ratio between inertia force and viscous force is defined as the Reynolds number  $Re$  and describes the flow conditions in a mixer or a pipe:

$$Re = \frac{v_{\text{char}} \cdot l_{\text{char}} \cdot \rho}{\eta}, \quad (2.40)$$

where  $\rho$  denotes the density,  $\eta$  the viscosity,  $v_{\text{char}}$  a characteristic velocity and  $l_{\text{char}}$  a characteristic length.

Eq. 2.40 gives a typical *Re*-number definition for rotating mixing/stirring tools. However, for rotor-stator whipping devices, a gap Reynolds number  $Re_{\text{gap}}$  is suggested, where the gap  $s$  between rotor and stator is taken into account as the characteristic length and the characteristic velocity is the tip speed of the rotor ( $D \cdot n$ ) [73]:

$$Re_{\text{gap}} = \frac{D \cdot n \cdot s \cdot \rho}{\eta(\dot{\gamma})}. \quad (2.41)$$

The relation  $Ne = f(Re)$  describes the specific flow condition in a mixer geometry at a certain power input. Three different flow domains can be distinguished: laminar, transition and turbulent flow domain.

In the laminar flow domain, the Newton number depends linearly on the inverse Reynolds number [123]:

$$Ne = \frac{C_1}{Re}, \quad (2.42)$$

where  $C_1$  is a mixer specific constant. From Eqs. 2.38 and 2.42 it follows that the power input grows proportional to  $n^2$  in the laminar flow domain. It is approximately proportional to the number of rotor-stator blades and number of pins per blade. The power moreover depends on the length and width of the pins and the gap between rotor and stator [182].

In a turbulent flow field, the Newton number is constant:

$$Ne = C_2. \quad (2.43)$$

$C_2$  is another mixer specific constant.

From Eqs. 2.38 and 2.43 the proportionality  $P \sim n^3$  can be deduced. The power dissipated in a turbulent flow field is proportional to the number of rotor-stator units, the number of pins per row and the facial area of a rotor pin. The power is however independent of the gap between rotor and stator due to negligible viscous forces [94].

The transition region between the laminar and turbulent flow domains can be approximated by  $Ne \sim Re^{-\frac{1}{3}}$ . It is a blend of laminar and turbulent flow and, thus, hard to describe analytically.

For various mixer geometries, Kroezen and Wassink [94] found a dependency of foamability on rotational speed and ascribed this to the influence of the rotational speed on the mixing regime which is dependent on the *Re*-number. For laminar

mixing, foamability was found to be moderate, for turbulent good and in the transition region poor.

## 2.5.2. Laminar flow

In a laminar flow field, it can be assumed that only shear stresses contribute to bubble deformation and breakup [72]. The dimensionless Capillary number  $Ca$  denotes the ratio between disrupting shear stress and stabilizing Laplace pressure (see Eq. 2.22). A critical Capillary number  $Ca_c$  can be derived above which bubbles break up. Accordingly, a maximum bubble size can be derived depending on the acting shear force:

$$x_{\max} = \frac{2 \cdot \sigma \cdot Ca_c}{\tau}. \quad (2.44)$$

The shear stress depends on the volumetric mechanical power input  $P_V$  which is a function of rotor speed, geometrical mixer properties and the foam viscosity. The laminar flow region is dominated by viscous forces. The acting viscous shear stress,  $\tau$ , can be calculated from the viscosity function  $\eta(\dot{\gamma})$  of the whipping fluid and the first derivative of the local velocity vector defined as the shear rate  $\dot{\gamma}$ :

$$\tau(\dot{\gamma}) = \eta(\dot{\gamma}) \cdot \dot{\gamma} \quad (2.45)$$

The local maximum shear rate in the most efficient axial dispersing gaps between rotor and stator blades for rotor-stator whipping devices can be approximated as:

$$\dot{\gamma} = \frac{\pi \cdot n \cdot D}{s}. \quad (2.46)$$

For the annular gap between the concentric cylinders of the rotating membrane device, the shear rate is calculated according to DIN 53018 [44] for Newtonian systems:

$$\dot{\gamma}(r) = \frac{1}{r_{\text{B,orbit}}^2} \cdot \frac{2 \cdot R_i^2 \cdot R_o^2}{(R_o^2 - R_i^2)} \cdot \omega, \quad (2.47)$$

where  $R_o$  is the inner radius of the outer cylinder,  $R_i$  the outer radius of the inner cylinder,  $r_{\text{B,orbit}}$  the radius of the bubble orbit, i.e. the length from the center of inner cylinder to the center of the bubble (see Fig. 3.3), and  $\omega$  the angular rate [44]. For narrow gaps, the error is small when Eq. 2.47 is applied to non-Newtonian systems.

The angular velocity can be determined as:

$$\omega = 2 \cdot \pi \cdot n. \quad (2.48)$$

From Eqs. 2.39, 2.41, 2.42, 2.44, 2.45 and 2.46, the maximum bubble size in the laminar flow field considering geometrical, process and recipe parameters can be derived according to Hanselmann and Windhab [73]:

$$x_{\max} = \frac{2 \cdot Ca_c \cdot \sigma \cdot C_1 \cdot n \cdot D \cdot e \cdot l_{f,r} \cdot q \cdot s}{\pi^2 \cdot P \cdot y}. \quad (2.49)$$

### 2.5.3. Turbulent flow

In turbulent flows the deformation and breakup of bubbles depends on the size ratio of the bubbles and the interacting eddies. Depending on the eddy size, regions of macro- and microturbulence can be defined. Microturbulence is most important in dispersing devices since it generates a finely dispersed, homogeneous structure. In microturbulent dispersing flows, the mean velocity difference  $\bar{v}$  acting at the bubble interface will induce the so-called Reynolds shear stress  $\tau_{\text{Re}}$  leading to bubble deformation and breakup.

$$\tau_{\text{Re}} = \rho_{\text{cont}} \cdot \bar{v}^2 \quad (2.50)$$

It can be assumed that the turbulent dispersing flow regime in a whipping apparatus is mainly of so-called inertial convection type, due to the large gas portions which are dosed into the whipping head as large bubbles and due to the low viscosity ratio of disperse to continuous phase  $\eta_{\text{disp}}/\eta_{\text{cont}}$ . Under the assumption that the relevant length scale of the turbulent eddies is equal to the largest bubble diameter and about equal to the Kolmogorov characteristic length of the microturbulence  $K$ , the mean square fluctuation velocity  $\bar{v}$  can be written as:

$$\bar{v}^2 = \psi \cdot \left(\frac{P}{V}\right)^{\frac{2}{3}} \cdot \left(\frac{K}{\rho}\right)^{\frac{2}{3}}, \quad (2.51)$$

where the constant  $\psi$  is  $\approx 2$  according to Batchelor [13]. Hanselmann and Windhab [73] showed that Eq. 2.51 is a good basis for the pre-calculation of maximum bubble sizes for a continuous whipping process including whipping head geometry parameters. Identical to Eq. 2.49 valid for the laminar flow field, the maximum bubble size in the turbulent flow field can be derived considering recipe parameters such as surface tension and critical Capillary number as well as geometry parameters like pin length or gap size and flow condition parameters [73].

$$x_{\max} = \frac{2 \cdot Ca_c \cdot \sigma}{\psi \cdot \rho} \cdot \left(\frac{C_2 \cdot e \cdot l_{f,r} \cdot q \cdot s}{V \cdot y}\right)^{-\frac{2}{3}} \cdot n^{-2} \cdot D^{-\frac{8}{3}}. \quad (2.52)$$

### 2.5.4. Taylor vortex flow

In the narrow annular gap of a rotating membrane device, a special flow field might appear, so-called Taylor vortices. Taylor vortices can occur in the flow field between two coaxial cylinders when the inner cylinder rotates faster than the outer cylinder. A centrifugal instability related to the curved streamlines of the flow results in toroidal Taylor vortices in the annular gap. These vortices manifest themselves as small axisymmetric secondary motions (see Fig. 2.20).

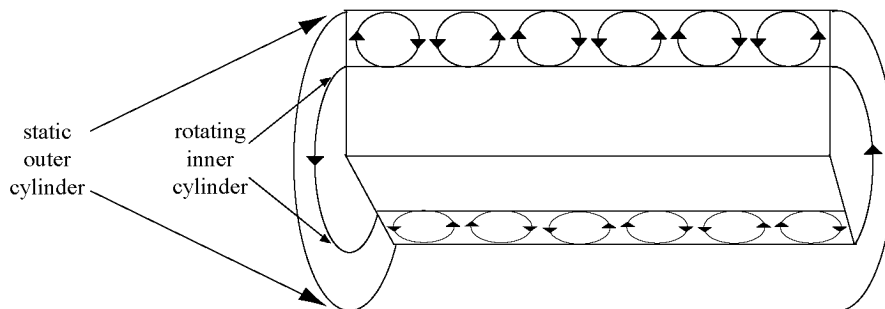


Figure 2.20.: Schematic drawing of Taylor vortices appearing in the gap between a rotating and a static cylinder.

The occurrence of Taylor vortices depends on the rotational speed, the radii of the cylinders and the fluid properties viscosity and density. The flow condition and appearance of Taylor vortices in the gap between the cylinders can be characterized by the dimensionless Taylor number  $Ta$  [23]:

$$Ta = Re_{\text{gap}} \cdot \sqrt{\frac{2 \cdot s}{R_o + R_i}} = \frac{D_i \cdot n \cdot s \cdot \rho}{\eta} \cdot \sqrt{\frac{2 \cdot s}{R_o + R_i}}, \quad (2.53)$$

where  $D_i$  is the diameter of the inner, rotating cylinder,  $n$  the rotor speed,  $s$  the gap between inner and outer cylinder ( $= R_o - R_i$ ),  $\rho$  the density,  $\eta$  the viscosity and  $R_o$  and  $R_i$  the radii of outer and inner cylinder, respectively. This equation does not consider any cross flow perpendicular to the rotation.

For a small gap and infinitely long coaxial cylinders, the instabilities occur at a critical Taylor number  $Ta_c$  of 41.3 [149]:

- $Ta < 41.3$ : flow with laminar layers
- $41.3 \leq Ta < 400$ : laminar flow with Taylor vortices
- $Ta > 400$ : completely developed turbulent flow

Andereck et al. [5] revealed a surprisingly large variety of different flow states in flow-visualization and spectral studies of flow between concentric independently rotating cylinders. Different states were distinguished by their symmetry under

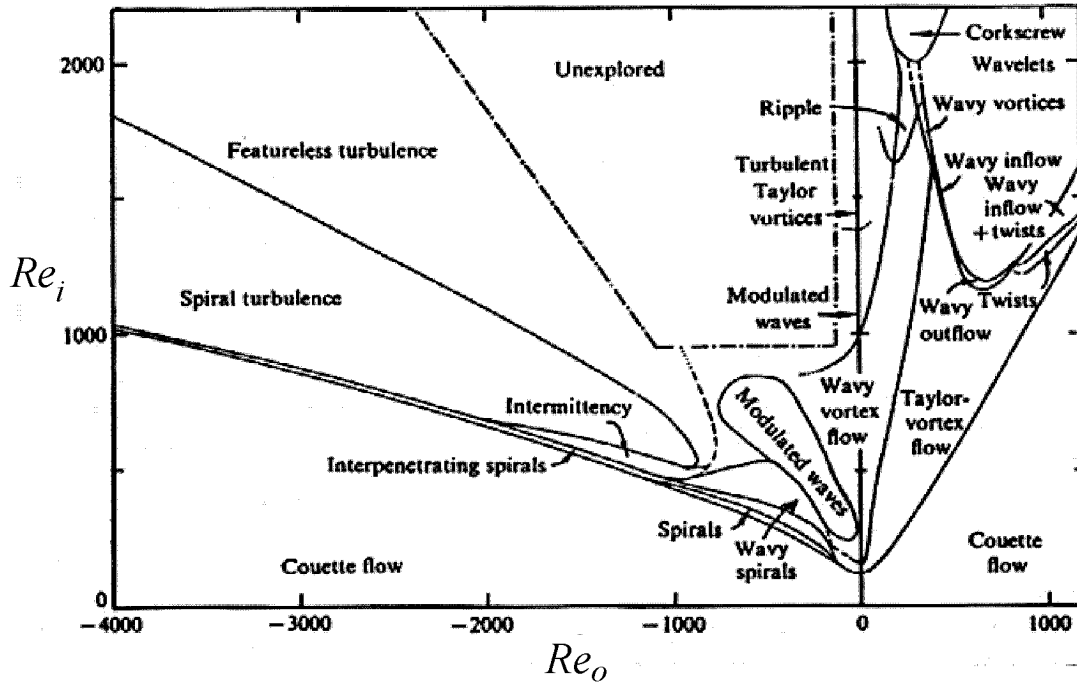


Figure 2.21.: Regimes observed in flow between independently rotating concentric cylinders.  $Re_i$  and  $Re_o$  represent the Reynolds numbers of the inner- and outer-cylinder, respectively. Dashed lines indicate the transition boundaries that are difficult to establish from visual observation alone since there is no abrupt change in the appearance. Dotted lines indicate the expected, but not yet observed, continuation of several boundaries. [5]

rotation and reflection, by their azimuthal and axial wavenumbers, and by the rotation frequencies of the azimuthal travelling waves. Transitions between states were determined as functions of the inner- and outer-cylinder Reynolds numbers,  $Re_i$  and  $Re_o$ , respectively (see Fig. 2.21). Observed states included Taylor vortices, wavy vortices, modulated wavy vortices, vortices with wavy outflow boundaries, vortices with wavy inflow boundaries, vortices with flat boundaries and internal waves (twists), laminar spirals, interpenetrating spirals, waves on interpenetrating spirals, spiral turbulence, a flow with intermittent turbulent spots, turbulent Taylor vortices, a turbulent flow with no large-scale features, and various combinations of these flows. These flow states were all found to be stable to small perturbations, and the transition boundaries between the states were reproducible.

Taylor's linear stability analysis for cylindrical Couette flow [169] can be extended to include an axial flow in the annulus for axisymmetric disturbances in a narrow annular gap [30, 45, 31] or an arbitrarily wide annular gap [76, 46]. The axial

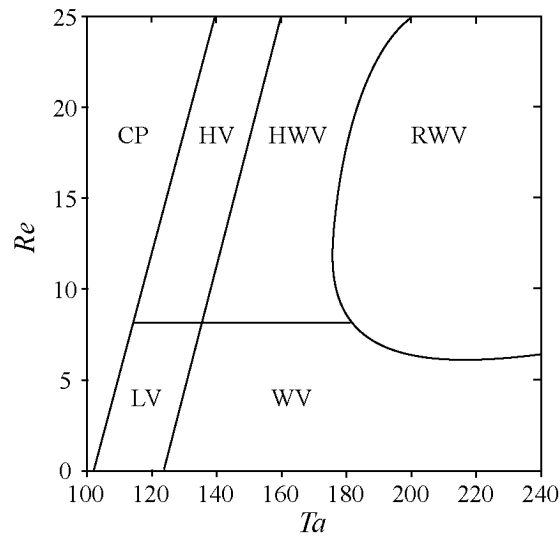


Figure 2.22.:  $Ta$ - $Re$  plane. Curves indicate approximate boundaries between flow regimes. Regimes include nonvortical Couette-Poiseuille (CP) flow, nonwavy laminar vortex (LV) flow, wavy vortex (WV) flow, nonwavy helical vortex (HV) flow, helical wavy vortex (HWV) flow and random wavy vortex (RWV) flow [179].

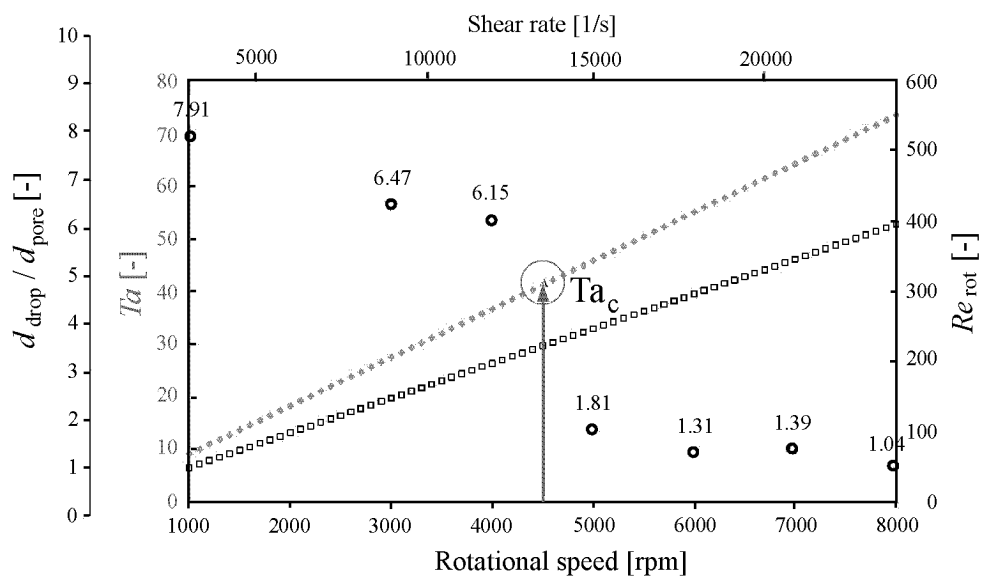


Figure 2.23.: Impact of Taylor vortices on drop detachment from rotating membrane in emulsification [146].



flow stabilizes the cylindrical Couette flow such that transition to Taylor vortex flow occurs at higher Taylor number than with no axial flow [159, 153, 47, 62, 160]. The research described above focuses on the first instability transition from stable Couette-Poiseuille flow to translating toroidal or helical vortex flow [167, 159, 153, 59]. Higher order instability transitions have been mapped out in the Taylor number-Reynolds number plane (see Fig. 2.22, [179]) where a differentiation between nonvortical Couette-Poiseuille flow, nonwavy laminar vortex flow, wavy vortex flow, nonwavy helical vortex flow, helical wavy vortex flow and random wavy vortex flow is made [90, 14, 17, 87, 63, 64, 65, 25, 105]. The ratio of the Taylor number to the axial Reynolds number, representing the ratio of centrifugal to advective accelerations, has been used to characterize the flow [158, 117, 106]. When the ratio is large, the vortices are strong and their effect is readily apparent in the velocity field. When this ratio is small, the dominant axial velocity overwhelms the supercritical vortices resulting in fluid winding around small vortices that are alternatively close to the inner and outer walls.

Murai et al. [122] showed that the structure of Taylor vortices was altered by the presence of bubbles, including an elongation of the vortex arrangement.

In emulsification using a rotating membrane, Taylor vortices were found to lead to significantly smaller resulting droplets. This can be seen from Fig. 2.23 where the ratio of drop to pore size drops as soon as the critical Taylor number is exceeded.

### 2.5.5. Power and energy input

For given geometrical mixer dimensions and given recipe, the volumetric energy input can be influenced by changing the residence time in the shear effective zone via a modification in fluid flow rate or gas volume fraction, or by changing the acting shear stresses via the rotational speed. The volumetric power  $P_V$  and energy input  $E_V$  directly influence the resulting mean bubble size and, thus, the structure and related foam properties. The net volumetric mechanical power input  $P_{V,\text{diss}}$  is

$$P_{V,\text{diss}} = \frac{P_{\text{diss}}}{V}, \quad (2.54)$$

where  $V$  is the free volume of the dispersing head and  $P_{\text{diss}}$  the net power input defined as the measured power during foaming minus the measured idling drive power. Instead of calculating the net volumetric mechanical power input from the measured net power input, it can also be calculated from product viscosity  $\eta$  and shear rate  $\dot{\gamma}$  as:

$$P_{V,\text{diss}} = \eta \cdot \dot{\gamma}^2 \quad (2.55)$$

The volumetric energy input  $E_V$  includes the residence time  $t_V$ :

$$E_V = P_V \cdot t_V = \frac{P}{V} \cdot t_V \quad \text{with} \quad t_V = \frac{V}{\dot{V}_{\text{foam}}}, \quad (2.56)$$

where  $\dot{V}_{\text{foam}}$  is the volume flow of foam. The residence time of a foam  $t_{V,\text{foam}}$  is influenced by the acting static pressure  $p$  since the gas volume is pressure-dependent:

$$t_{V,\text{foam}} = \frac{V}{\frac{\dot{V}_{\text{air}}}{p} + \dot{V}_{\text{mix}}}. \quad (2.57)$$

Bubble sizes are expected to decrease with increasing stresses [(72)]. The probability of bubble break-up also increases with increasing residence time in the shear effective zone, especially in the turbulent flow field. With increasing residence time and/or acting stresses, the volumetric energy input increases as well.

## Dispersing characteristics and energy dissipation rate

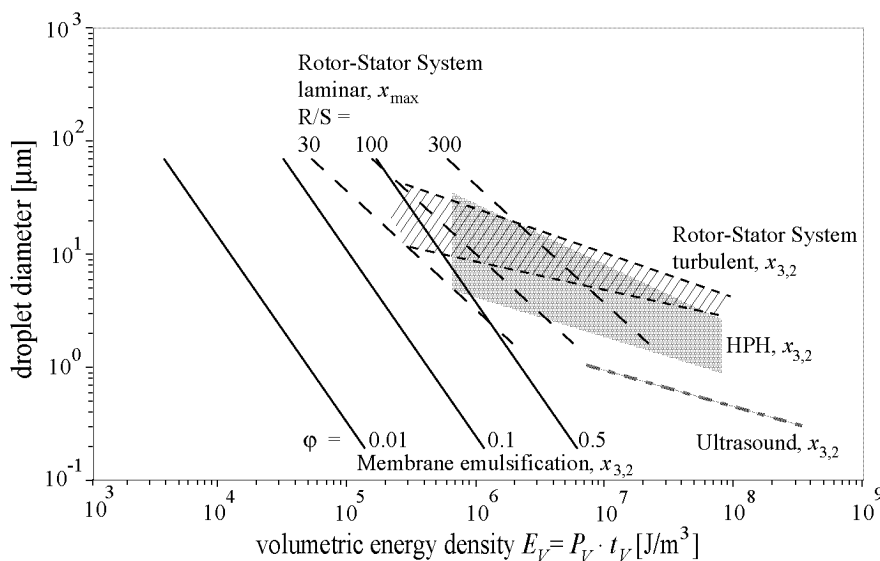


Figure 2.24.: Energy density plot for O/W emulsions produced with different emulsification devices [151].

The bubble size is commonly plotted as a function of the volumetric energy input in dispersing characteristics while it is plotted as a function of the volumetric power input to show the energy dissipation rate. To compare different dispersing methods and/or dispersing parameters with respect to their energetic efficiency for production of small bubbles, the energy density concept  $x_{50,r} = f(E_V)$  can be applied. In contrast to emulsion processing where energy plots are commonly used

to directly compare measured volumetric energy inputs or energy dissipation rates and resulting mean droplet sizes (e.g. [39, 86, 150, 128, 98]), no corresponding publications were found for foams. If the product damage mechanism depends on the acting stresses, the energy dissipation rate (=volumetric power input) should be chosen which focuses on the acting stresses only and disregards time dependency. If the mean residence times are known, one can easily shift the curve  $x_{50,r}=f(E_V)$  to  $x_{50,r}=f(P_V)$ . Fig. 2.24 shows experimental results for different devices used in continuous mechanical emulsification [151]. The results come from work by Armbruster [6], Karbstein [85], Stang [162], Schröder [150] and Behrend [15] for O/W emulsions with disperse and continuous phase viscosities of 60 mPas and 30 mPas, respectively, using fast emulsifiers. The energy density plots for O/W emulsions show a constant decrease in mean bubble size for increasing volumetric energy input in the investigated range. Membrane emulsification using static membranes allow to produce finely dispersed emulsions at low energy densities. The required energy input rises with increasing disperse phase fraction. Likewise, laminar rotor-stator devices require moderate energy inputs, only. It was shown that the decrease in droplet size with increasing energy input is lower for turbulent rotor-stator systems than for laminar ones. However, the turbulent flow field is advantageous for higher viscous emulsions with high disperse fractions since the droplet stabilization was shown to be more efficient [85, 162]. To reach smaller droplet diameters, high pressure homogenizers and ultrasound emulsifying are recommended. The influence of coalescence on the mean droplet size can not be derived from such energy density plots.

## 2.6. Rheology

Rheology is the study of the deformation and flow of materials under well-defined conditions. Factors such as the moving force and the surface of pipes, influence the material flow, whereas pressure and temperature affect the deformation behavior. Rheology uses laboratory measurements to predict and explain some of the flow, deformation and textural changes which take place during processing. This involves steady, changing and unstable flow conditions.

Rheometric flow is normally classified into two types, i.e. shear and elongation. Shear flow can be visualized by placing the material between two parallel plates with gap  $s$  (see Fig. 2.25) which are moving at a constant velocity relative to each other ( $v_1 - v_2$ ). The velocity gradient  $(v_1 - v_2)/s$  is known as the shear rate  $\dot{\gamma}$ . The material will move according to its internal frictional resistance to motion, a parameter called shear viscosity  $\eta_s$ . Particles will rotate in shear flow. In elongational flow (Fig. 2.26), the material is stretched and the particles will not rotate. The measured material parameter is the elongational viscosity  $\eta_e$ .

The simplest measurements are normally one-directional (uniaxial) shear tests,

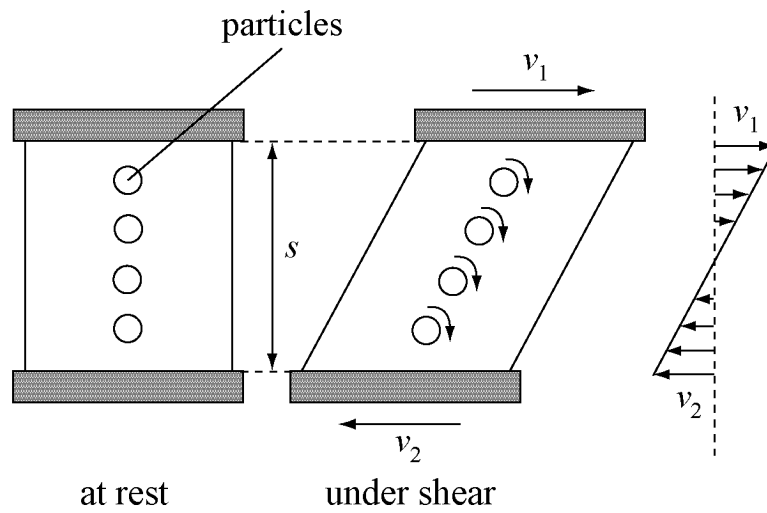


Figure 2.25.: Representation of simple shear flow.

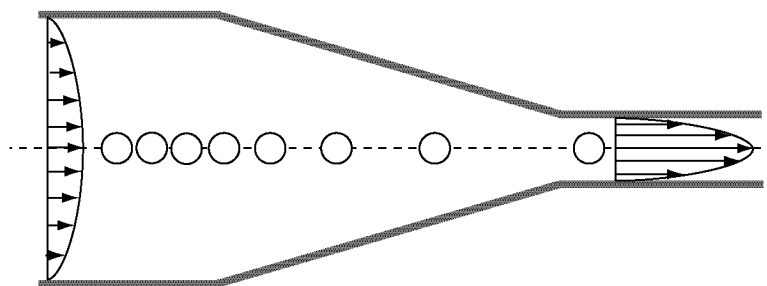


Figure 2.26.: Representation of elongational flow.

although two-dimensional tests are possible, as are one- and two-directional elongational techniques. In food processing, the flow is often very complex, but generally, the uniaxial measurements can satisfactorily estimate or predict actual process conditions.

It is the ratio of shear stress to shear rate ( $\tau/\dot{\gamma}$ ) which enables the rheologist to learn something about the viscous behavior of a liquid. This is known as the "apparent viscosity" which Newton suggested was constant for all shear rates. This is approximately true for some fluids like water. However, most food substances are non-Newtonian in behavior. Figs. 2.27 and 2.28 (right side) show some of the different types of flow behavior which can occur when the apparent viscosity is determined at different shear rates. If the viscosity/shear stress increases with the shear rate, the material is called shear-thickening, the opposite behavior, i.e. decreasing viscosity/shear stress with increasing shear rate is called shear-thinning. Some materials remain virtually solid when a stress is applied until a critical stress, the so-called yield value  $\tau_0$ , is reached.

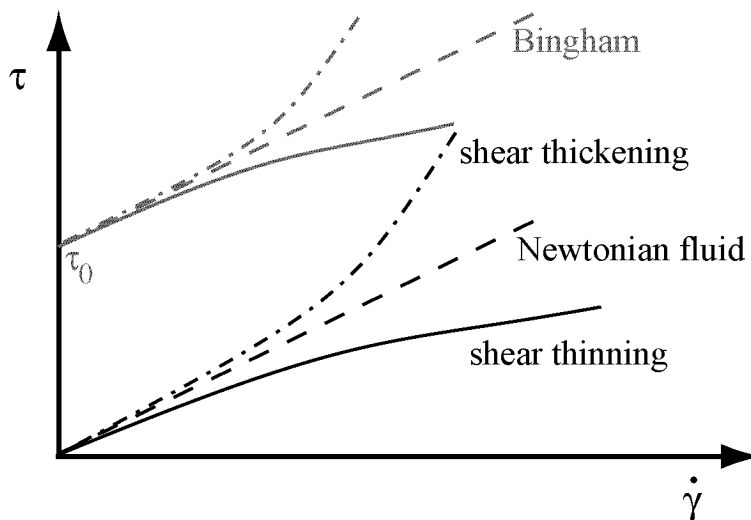


Figure 2.27.: Comparison of Newtonian and non-Newtonian plots [124].

### 2.6.1. Rheological tests

Flow behavior of e.g. foam in the foaming device, in further processing steps and during consumption can be determined in rheological measurements. Foam viscosity depends on the viscosity of the mix as well as on the gas volume fraction and mean bubble size [72]. In principal, foam behaves like a viscoelastic, compressible, non-Newtonian fluid.

Foam rheology can be done off-line using a laboratory rheometer or in-line in the pipes. In this work, rheology was performed off-line. Such measurements yield

significant results only if the foam structure is not changed during sampling and measurement. In the following, typical off-line rheological tests are presented in more detail.

### Shear rate tests

In shear rate tests, the sample is usually measured at a series of defined shear rate steps with given duration. Rate tests probe the Newtonian and non-Newtonian flow behavior of the sample as a function of the increasing shear rate. Fig. 2.28 shows, on the left, the different stress steps. On the right side the linear and non-linear material functions are shown. Since this rate test is an addition of single step experiments, one has to make sure that each single shear rate  $\dot{\gamma}$  or shear stress  $\tau$  lasts long enough to allow the sample to equilibrate [54]. The resulting dependency of viscosity and shear rate is also called flow curve.

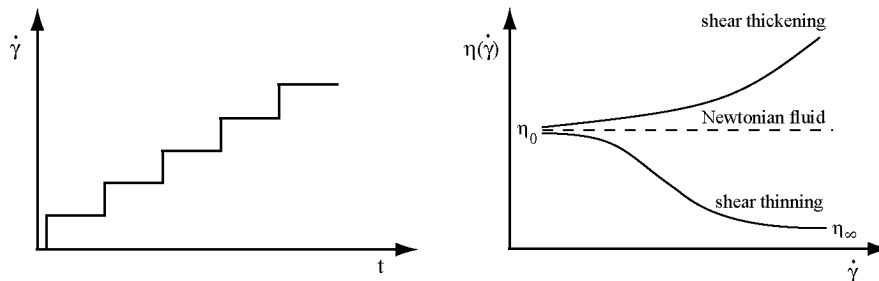


Figure 2.28.: Applied shear rate (left side) and the linear and non-linear behavior of the viscosity (right side).

### Oscillation tests

The measurement of the storage modulus  $G'$  (describing the dynamic elastic properties), the loss modulus  $G''$  (describing the dynamic viscous properties) and the complex viscosity  $\eta^*$  (describing the viscosity in dynamic experiments) is performed in shear oscillation tests. If the deformation amplitude of oscillation is small enough, the measurements are carried out in the linear viscoelastic regime. Oscillation tests are the preferred experiment when the sample should not be damaged in the measurement or for samples with weak structures (e.g. foams). To obtain the linear viscoelastic regime of the probed sample, dynamic stress or strain test are performed (see Fig. 2.29). Keeping the oscillatory frequency constant, the amplitude of the oscillation is increased either by increasing the stress or the strain, i.e. the deformation. As long as the linear viscoelastic regime is present, there will be no change of the viscoelastic properties when they are plotted as a function of

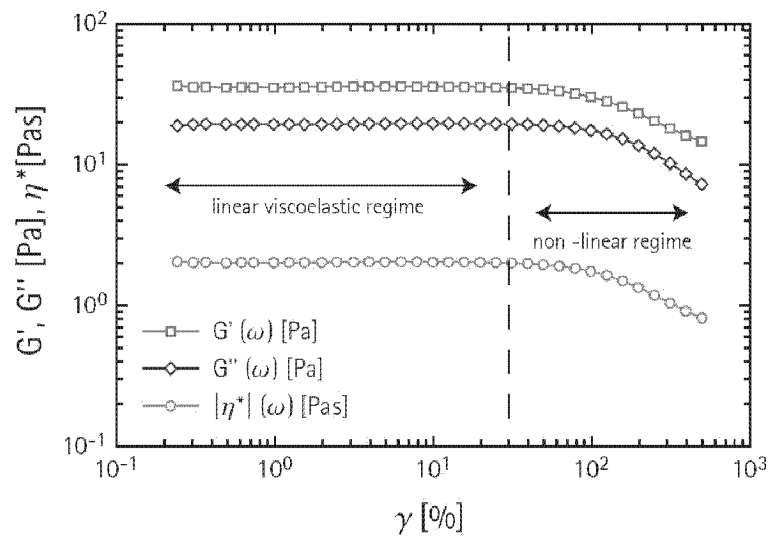


Figure 2.29.: Dynamic properties as function of strain in dynamic strain test [54].

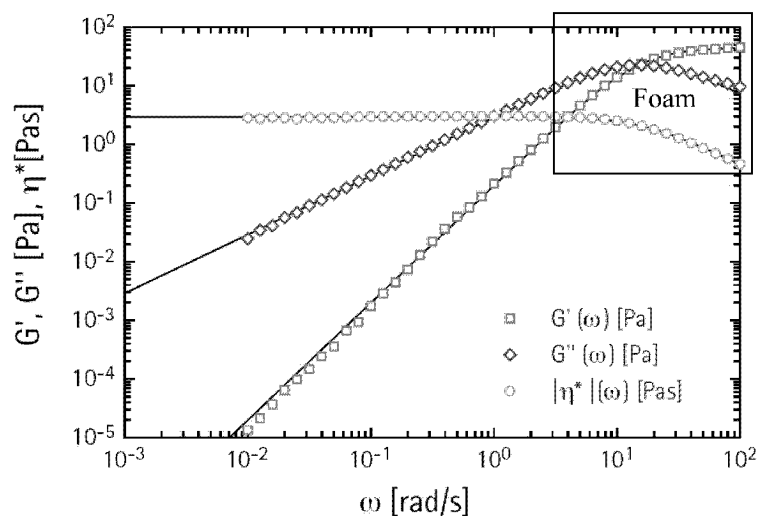


Figure 2.30.: Dynamic properties as a function of frequency in a dynamic frequency test. Typical region for foams marked with box [54].

stress or strain as shown in Fig. 2.29. Once the stress or strain reaches the non-linear regime one observes very complex flow behavior that cannot be described yet. Therefore, it is crucial to perform all other dynamic experiments strictly in the linear viscoelastic plateau [54].

Once the linear viscoelastic regime is known, the dynamic frequency experiment (see Fig. 2.30) can be used to investigate the time-dependent properties of viscous and elastic components of the sample. In this experiment, the oscillatory frequency is performed under a constant stress or strain from low to high frequency, that means, from long to short time periods of deformation. The stress/strain is chosen according to the linear viscoelastic plateau found in the dynamic stress/strain test. A typical frequency sweep experiment is shown in Fig. 2.30 [54]. A box marks the domain common for foam.

## 2.6.2. Empirical modeling of non-Newtonian flow functions

Fitting experimental data to empirical mathematical expressions provides the most economical way of describing any particular physical behavior. In the case of rheology, it also gives the possibility of predicting how a particular liquid will behave in new and more complex situations. Also, in some situations, curve-fitting yields parameters that can be compared to theoretical models that can provide some kind of description of the liquid microstructure. The typical non-linear flow models seek to describe parts of flow curves or entire flow curves of non-Newtonian liquids, as shown in Fig. 2.31. Some of the models that can be used to fit these kinds of flow-curves are described using the following equations. The simplest descriptions of non-Newtonian liquid behavior are the Bingham and "power law" models.

$$\text{Bingham model : } \eta = \frac{\tau_0}{\dot{\gamma}} + \eta_P \quad (2.58)$$

$$\text{Power - law model : } \eta = K \cdot \dot{\gamma}^{n-1} \quad (2.59)$$

$$\text{Herschel - Bulkley model : } \eta = \frac{\tau_0}{\dot{\gamma}} + K \cdot \dot{\gamma}^{n-1} \quad (2.60)$$

$$\text{Cross model : } \eta = \eta_\infty + \frac{\eta_0 - \eta_\infty}{1 + (K \cdot \dot{\gamma})^m} \quad (2.61)$$

$K$ ,  $n$  and  $m$  are fitting parameters,  $\eta_P$  the plastic viscosity. For simple flow curves that do not flatten out at high shear rates (no  $\eta_\infty$ ), although showing the usual behavior at low shear rate, a simplified Cross model is suitable:



$$\text{modified Cross model : } \eta = \frac{\eta_0}{1 + (K \cdot \dot{\gamma})^m} + K \cdot \dot{\gamma}^{n-1}. \quad (2.62)$$

This model simplifies to the Herschel-Bulkley model when  $m$  is unity and  $K \cdot \dot{\gamma}$  is very large.

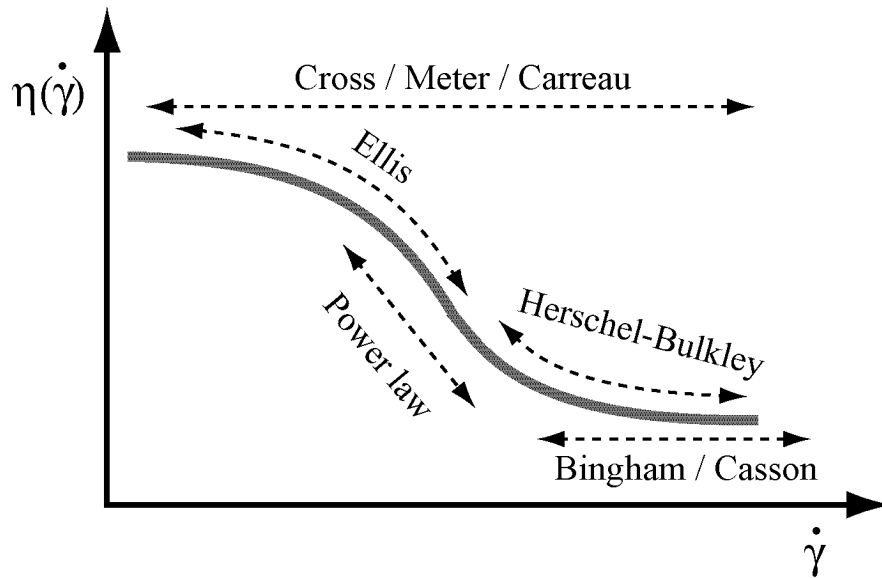


Figure 2.31.: Schematic diagram of the range of the various flow models for viscosity functions [54].

### 2.6.3. Structure - Rheology Relationships

The rheological behavior of fluids is closely related to their inner structure. Macromolecules and disperse particles (solid particles, droplets, gas bubbles) are the major structure components in food systems. For each material there are interacting forces of the specific components (chemical bondings or physical interactions like van der Waals forces, electrostatic forces, fluid-solid interactions) that dominate the structural behavior of the material in the state of rest or under weak deformation/shear conditions. Higher deformations and shear rates increase the "hydrodynamic" forces generated by the viscous and elastic properties of the fluid under the specific flow conditions. It can be assumed that for each shear rate in stationary shear experiments an equilibrium structure exists. The related viscosity is an equilibrium viscosity that leads to the (equilibrium) viscosity function  $\eta(\dot{\gamma})$  which is generally measured [186].

## Equilibrium viscosity function

- $\dot{\gamma} < \dot{\gamma}_1$ : In this shear rate domain the hydrodynamic forces can be neglected. Only the Brownian motion is acting against the structural binding forces.

If the concentration of the disperse phase or of macromolecules in the continuous phase is high their strong interaction generates a yield value. This can be controlled by rotational rheometers which are preferably stress controlled. According to the Newtonian law the shear viscosity for  $\dot{\gamma} \rightarrow 0$  approaches infinity if a yield value  $\tau_0$  exists.

For low disperse and macromolecular concentrations the Brownian motion dominates and isotropic structure is preserved in which the interactions of the components are negligible. As a result, the system behaves like a Newtonian fluid (lower Newtonian viscosity,  $\eta_0$ ).

The deformation dependency (i.e. shear rate dependency) of the viscosity function can be divided into three domains which are fixed by the two "critical" shear rates  $\dot{\gamma}_1$  and  $\dot{\gamma}_2$  as shown in Fig. 2.32.

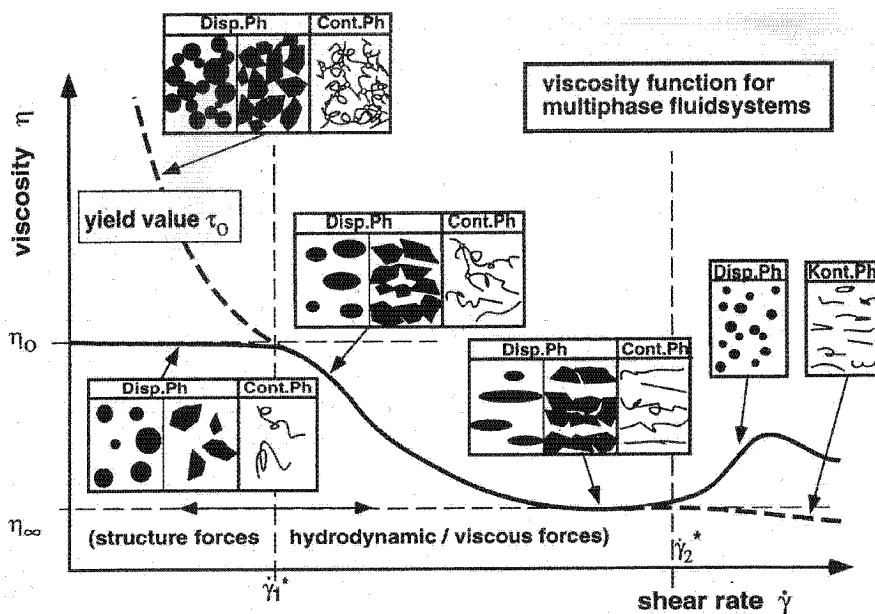


Figure 2.32.: Qualitative structure-rheology relationship in "structured" multiphase fluids like mayonnaise, chocolate or foam [183].

- $\dot{\gamma}_1 \leq \dot{\gamma} \leq \dot{\gamma}_2$ : In this domain the hydrodynamic forces reach the same order of magnitude as the structural forces. This induces the formation of new structures which are different according to the flow shape as well as the

shearing time. If sheared long enough, a specific "equilibrium structure" is reached.

In most cases this equilibrium structure has a reduced "inner" flow resistance and a reduced viscosity at increased shear rate (i.e. shear stress). This behavior is called shear thinning or, in combination with a yield value, also pseudoplastic. The induced structure can be completely or partly reversible if the shear rate is again reduced or altogether stopped. For disperse particle structures, specific changes of the structure can be observed (e.g. via microscopy) in shear thinning. Deformable particles like droplets and bubbles get deformed to an ellipsoidal shape, coarse particles and their agglomerates are oriented. At the upper Newtonian plateau with minimum viscosity  $\eta_\infty$  for  $\dot{\gamma} \rightarrow \dot{\gamma}_\infty$  the maximum "orientation" in flow is reached. If this structure/viscosity is required for the product or for further processing, this state of orientation must be fixed by physical and/or chemical means [188].

- $\dot{\gamma} > \dot{\gamma}_2$ : If the second critical shear rate,  $\dot{\gamma}_2$ , is exceeded, the state of maximum orientation state may be disturbed (e.g. by flow instabilities, sterical particle interactions or changes in the particle structure like bubble breakup). The typical flow behavior of samples containing disperse solid particles is no longer the same as for macromolecular solutions. If macromolecules have reached the maximum orientation and shear rate is further increased, degradation of the phase is possible if the molecules are "weak enough", leading to a further decrease in viscosity. For samples with high particle interactions, the flow resistance, and, consequently, the viscosity will increase again (dilatant).

This classification of three shear rate ranges is experimentally seen for many food systems (e.g. mayonnaise, chocolates, foam).

## 2. *Background*

---

## 3. Materials and Methods

Experimental devices, specific parts thereof and the exact set-ups are listed and described in Sec. 3.1. Exact knowledge of, both, properties of raw material and final product is mandatory for the interpretation of results. The methods section is, thus, divided into (i) the analytical methods to characterize the fluid and foam properties (Sec. 3.2) and (ii) the experimental methods (Sec. 3.3). The latter contains methods for fundamental investigation of bubble formation and breakup and methods used for foam processing. Subsequently, a description of all materials (Sec. 3.4) is given.

### 3.1. Devices

#### 3.1.1. Overview of the used devices

- **TECC (Transparent Enlarged Concentric Cylinder) device**  
Manufacturer: Built in-house  
with *Agitator*  
Type: IKA RE162/P  
Manufacturer: IKA Labortechnik (Germany)
- **Band apparatus**  
Manufacturer: Built in-house
- **CCD-camera**  
Type: DFW-V500  
Manufacturer: Sony Electronics
- **Water quench**  
Type: Bohlin FP50  
Manufacturer: Bohlin Rheologi (Sweden)
- **Coldlight source**  
Type: Intralux dc-1100  
Manufacturer: Volpi AG (Switzerland)

- **Stroboscope**  
Type: Digistrob RDS 30  
Manufacturer: Reglomat AG (Switzerland)
- **Lab-scale ROME (rotating membrane) device**  
Type: Megatron FM 1-56 SO  
Manufacturer: Kinematica AG (Switzerland)
- **Head of lab-scale DESM (dynamically enhanced static membrane) foaming device**  
Manufacturer: built in-house
- **Pilot scale DESM (dynamically enhanced static membrane) foaming device**  
Manufacturer: built in-house
- **Rotor-stator device**  
Type: Megatron FM 8-50/6HR  
Manufacturer: Kinematica AG (Switzerland)  
with *Eccentric worm pump*: type EDS 2.2.
- **Eccentric worm pump**  
Type: NM008BY03512B (rotors and stator sizes: NM005, NM008, NM011)  
Manufacturer: Häny AG (Switzerland)
- **Vacuum pump**  
Type: Vane pump, DUO 1.5 A  
Manufacturer: Arthur Pfeiffer Vakuumtechnik Wetzlar GmbH (Germany)
- **Exsiccator**  
Type: Mobilex 300 mm, 8.2072.47  
Manufacturer: Schott (Germany)
- **Gas mass flow controller**  
Type: Red-y type GSC-B9HA-BB24  
Manufacturer: Vögtlin Instruments AG (Switzerland)
- **Gas mass flow controller**  
Type: Bronkhorst F 201C-FDC-33-V  
Manufacturer: Bronkhorst HI-Tec
- **Gas mass flow controller**  
Type: Bronkhorst F 20 1C-FA-2  
Manufacturer: Bronkhorst HI-Tec

- **Centrifugal pump for cooling circuit**  
Type: GM-2A/115  
Manufacturer: Alfa-Laval
- **Digital power meter**  
Type: Yokogawa WT230  
Manufacturer: Yokogawa
- **Digital power meter**  
Type: Yokogawa 2533  
Manufacturer: Yokogawa
- **High-speed digital camera**  
Type: NAC MEMRECAM fxr6  
Manufacturer: NAC Image Technology
- **Objective**  
Type: AF Micro Nikkor, 105 mm, 1:2.8D  
Manufacturer: Nikon
- **Scale**  
Type: Mettler P1 210  
Manufacturer: Mettler Instrumente AG (Switzerland)
- **Density meter**  
Type: DM 138  
Manufacturer: Anton Paar AG (Austria)
- **Rheometer**  
Type: Physica MCR 300  
Manufacturer: Anton Paar AG (Austria)  
Geometries: Concentric cylinder CC27 and cone-plate CP50-1
- **Inverse light-optical microscope (with CCD-camera)**  
Type: NIKON Diaphot TMD  
Manufacturer: Nikon AG
- **Mixing device**  
Type: Polytron PT 6000  
Manufacturer: Kinematika AG (Switzerland)
- **Mixing device**  
Type: Fryma  
Manufacturer: APV homogenizers (Denmark)

### 3.1.2. Parallel band apparatus

The set-up consisted of a parallel band apparatus (see Fig. 3.1), built in-house, similar to a Taylor band apparatus [170]. The apparatus consists of two metal bands that run around several rolls inside a container of 30 cm in length, 18 cm in width and 6 cm in depth. Metallic ribbons of 3.3 cm width were used, tautened with springs to avoid bending effects. Their motion was computer-controlled independently by two motors. The time sequence of the bubble behavior was recorded with a CCD digital camera (Sony DFW-V500, Japan) placed in azimuthal position. The container was filled with glucose syrups of different viscosities. The disperse phase was air. No emulsifier was added. All experiments were carried out at 18 °C, temperature was controlled via the double-walled base plate of the container cooled via a water-circulating bath. A cold light source plus two halide lamps were placed beneath the container to illuminate the bubbles through a window built into the bottom of the band apparatus. The bubbles were deformed under the action of several shear rates ( $1.8\text{-}17.4\text{ s}^{-1}$ ) set by controlling the relative speed of the bands. A gap width of 9.76 mm between the two ribbons was chosen. The radius of the undeformed bubbles was adjusted in order to avoid edge effects. A schematic drawing of the shear cell is shown in Fig. 3.2.

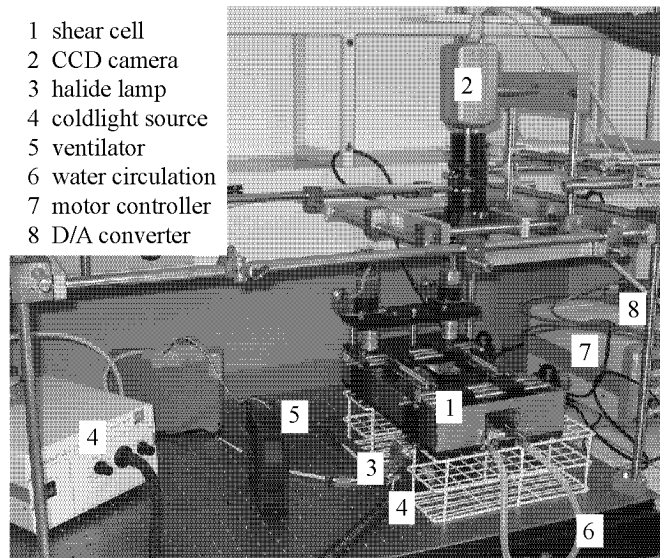


Figure 3.1.: Parallel band apparatus

One of the main difficulties in using a device such as the parallel band apparatus is keeping the bubble in the observation window, because generally it moves while being sheared. As a consequence, high resolution imaging over a long period of time at a defined shear rate is difficult to achieve. Several solutions are possible: (i) Controlling the rotation speed of the motors manually. (ii) Increasing the area



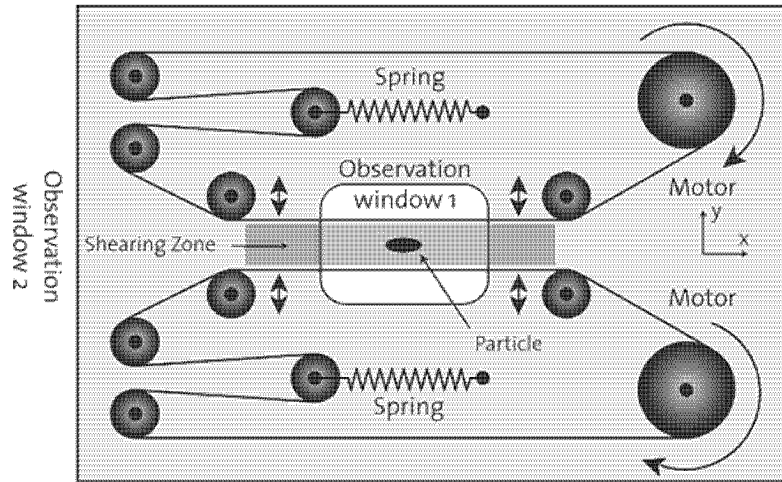


Figure 3.2.: Diagramm of the shear cell (top view) [19].

recorded leading to a smaller image resolution and less accuracy. (iii) Using sliding plate setups (e.g. [189, 67, 66]) where the image capturing device moves along with the bubble, resulting in a limited experimental time (observation time) and limited shear-rate regime. (iv) In this work, a recently developed computer-controlled flow cell based on direct image analysis of the bubble and a PID-controlled motor adjustment [50, 19] was able to continuously adapt the flow parameters in order to keep the observed bubble in the requested position for indefinite times. Steady-state deformation of sheared bubbles could, thus, be observed accurately. The logic of the PID-controller consists of three parts: the proportional control reacts immediately to any displacement of the bubble from the selected position, the integral control suppresses the oscillation introduced by the proportional and the third differential control stabilizes the system. The software detects the position and movement of the bubble in real time and controls the two motors that independently power both ribbons. A bubble tending to escape from the selected position in the observation window is countered by the control software which modifies the output voltage for the two motors. One of the ribbons then moves faster and the other slower, always keeping the relative speed between both bands constant, in order to maintain a constant shear rate. Once the bubble recovers its initial position, the software stabilizes the voltage applied to the motors outputting the same value to them, i.e. both bands are then moved at the same speed. This set-up has been shown to work perfectly in various recent works [111, 110, 112].

### 3.1.3. TECC device

The reason for designing the Transparent Enlarged Concentric Cylinder (TECC) device was the limitation of bubble deformation in the band apparatus where no bubble breakup could be achieved. The advantages of the TECC device compared to the band apparatus are:

- Much higher shear rates possible
- Less fluctuation of the gap width
- Easy cleaning, thus silicone oil can be used instead of glucose syrup
- Higher capillary numbers achievable even though gap width is larger and fixed (higher shear rate, four times lower surface tension of silicone oil)

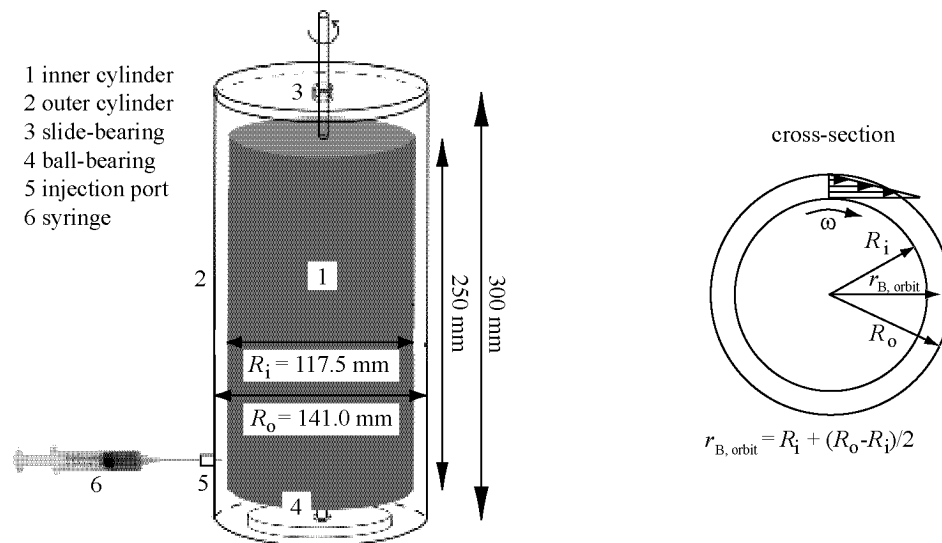


Figure 3.3.: Illustration of the TECC (Transparent Enlarged Concentric Cylinder) device: side view and cross-section.

The TECC device was composed of the following parts (see Fig. 3.3 and Fig. 3.4, numbering corresponds to Fig. 3.4): (1) agitator for low speed with convoluted rubber gaiter for deflection compensation, (2) frequency inverter, (3) inner cylinder: grey Polyvinylchlorid (PVC), diameter 117.5 mm, height 250.0 mm, (4) plexiglass container with inner diameter 141.0 mm and height 300.0 mm, (5) injection port with a silicone-sealing allowing the introduction of gas bubbles into the gap, (6) two CCD cameras and (7) halide lamps. The device was placed on a rubber-coated metal-stand for fixation of the outer container, a metal-stand with rails was used for fixation and movement of the camera, a PC with software Fire-i (Unibrain, version: 3.01.0.60) for image capturing.

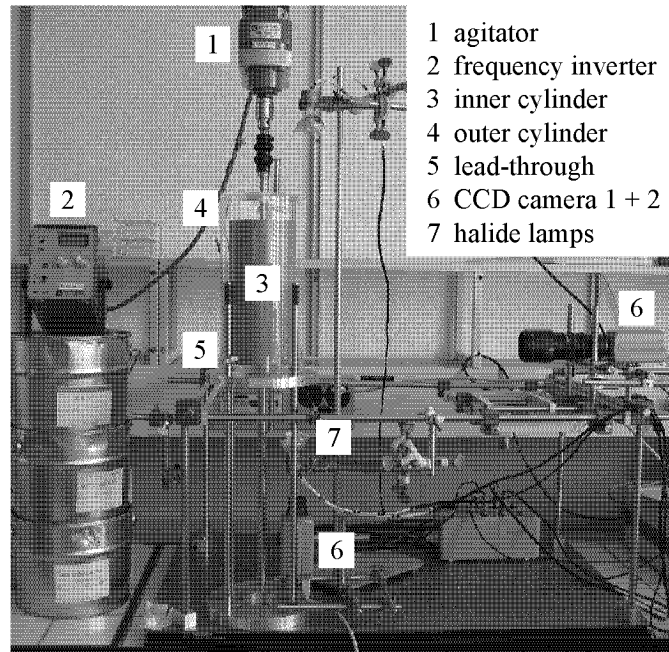


Figure 3.4.: Picture of the TECC (Transparent Enlarged Concentric Cylinder) device.

### 3.1.4. Rotor-stator foaming device

A continuously working rotor-stator mixer (FM 8-50/6HR, Kinematica AG, Switzerland) with two types of rotor-stator geometry (Radax and 12-HR) was used. The Radax geometry was developed at ETH Zurich in the Laboratory of Food Process Engineering [184]. Compared to traditional foaming geometries, the Radax (see Fig. 3.5) offers the advantage that the double-T-shaped pins hinder centrifugal demixing effects [102]. As every single mixing element (stator and rotor blade) can be assembled independently, the configuration and the number of mixing elements can easily be changed. This allows to choose the mixing geometry as a function of the desired shear stresses or energy input to disperse the gas fraction into the liquid. Thus, the mixer can be adapted to the requirements of different products. Other advantages of this pilot scale device are the adjustable gaps between rotor and stator and the small mixing head volume ideal for research and development applications where many systematical trials are needed.

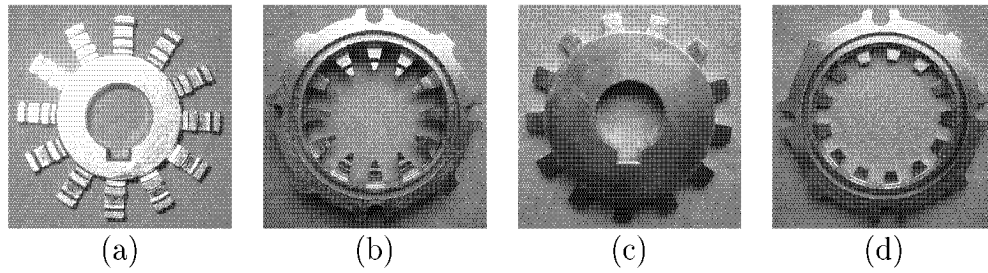


Figure 3.5.: Rotor-stator geometries (a) Radax rotor, (b) Radax stator, (c) 12-HR rotor, (d) 12-HR stator.

#### 3.1.5. Dynamically enhanced membrane foaming (DEMF) devices

In the present work, two foaming set-ups were used (see Fig. 3.6): (1) the rotating membrane (ROME) device (FM 1-56/SO, Kinematica AG, Switzerland) where the inner, rotating part consists of a membrane while the housing is made of compact metal and (2) the dynamically enhanced static membrane (DESM) device (built in-house) where the inner, rotating cylinder is made of compact metal and the membrane is fixed to the housing. In both devices (1 and 2), the bubble detachment is dynamically enhanced by the rotation of the inner cylinder, hence, the thesis title "dynamically enhanced membrane foaming". Set-up (1) was originally constructed since a similar device had been shown to be very effective for emulsification (patent DE 10 2004 040 735.5). However, set-up (2) is much easier construction-wise since no hollow shaft and no complicated seals are necessary. Additionally, the centrifugal forces enhance bubble detachment from the membrane in setup (2). The acting shear rate is proportional to the velocity difference between inner and outer cylinder, the rotor diameter and reverse proportional to the gap size. If these three parameters are constant and if wall slip is negligible, the acting dispersing forces and resulting bubble sizes should ideally be identical for the two setups.

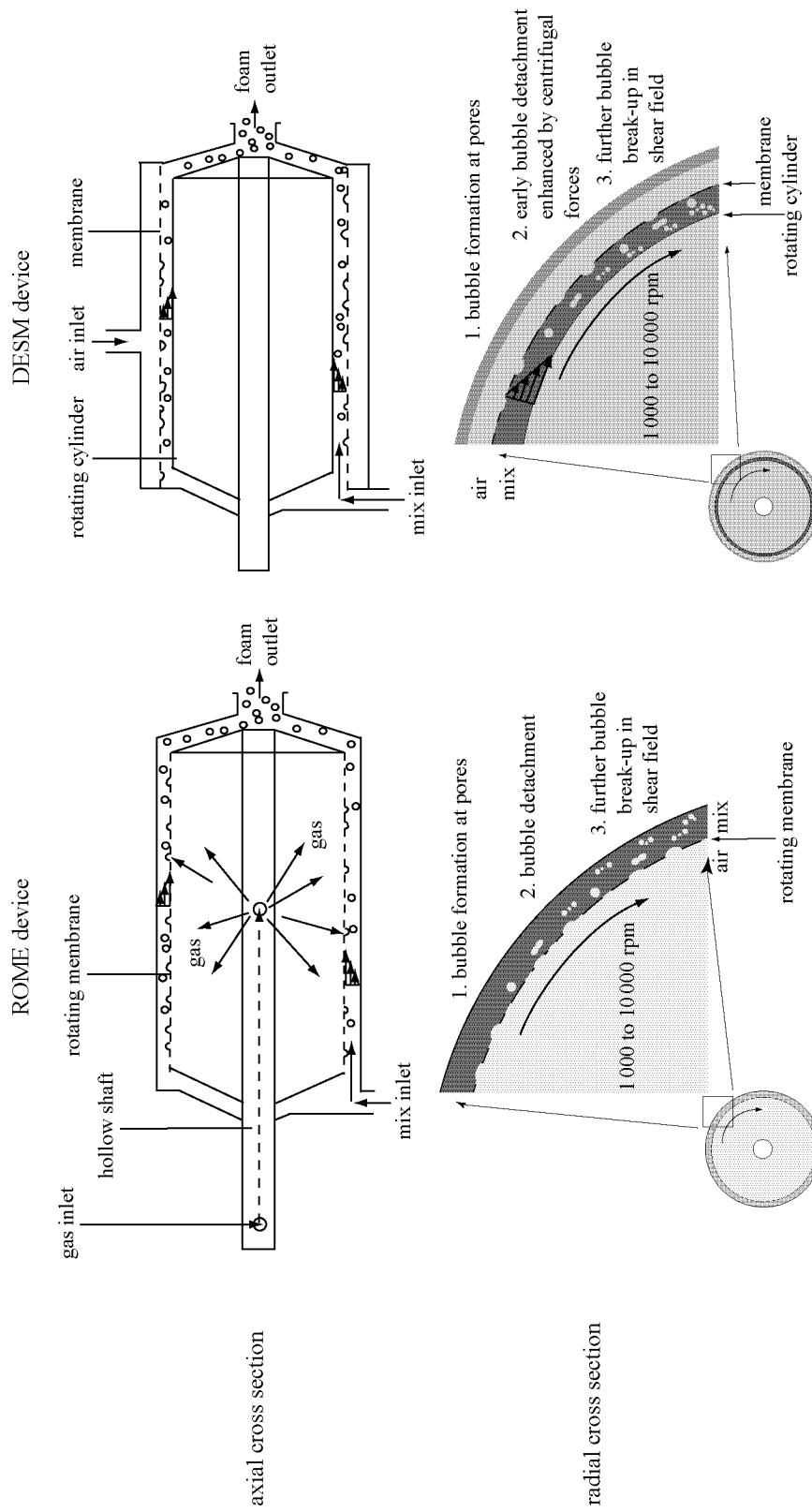


Figure 3.6.: Axial and radial cross-section of ROME (left side) and DESM device (right side).

### 3. Materials and Methods

---

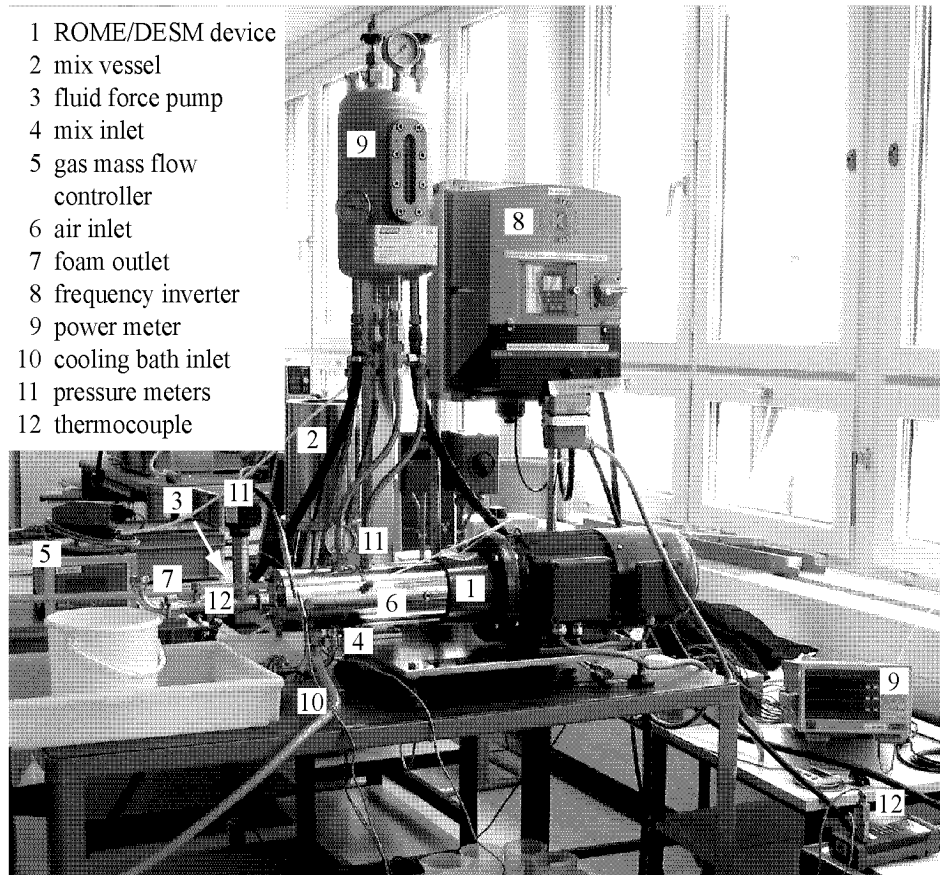


Figure 3.7.: Picture of the dynamically enhanced membrane foaming device (lab-scale) and associated elements used for foaming (exemplarily shown for ROME device).

The dispersing principle of the dynamically enhanced membrane foaming device is described in Sec. 2.2.3 and Sec. 2.4.4. The foaming device basically consisted of a foaming head, a motor and a frequency inverter. Various elements were added to the actual foaming device: (i) an eccentric worm pump to bring continuous phase from a reserve vessel via connecting pipes to the dispersing head, (ii) a power meter detecting the consumed power was connected to the motor of the machine and linked to a computer for recording, (iii) two thermocouples, one measuring the fluid/mix temperature before the dispersing zone (but after the pump), the other measuring the temperature of the fluid/foam after the dispersing zone, (iv) the air supply, warranted by a high pressure air line and dosed by an air mass flow controller and (v) two pressure meters to measure the pressure directly before and after the membrane in order to recognize deleteriously high pressure differences.

The ROME device had a cooling jacket, the DESM did not. Fig. 3.7 illustrates the described assembly of the membrane foaming process (exemplarily shown for ROME device).

### Rotating membrane (ROME)

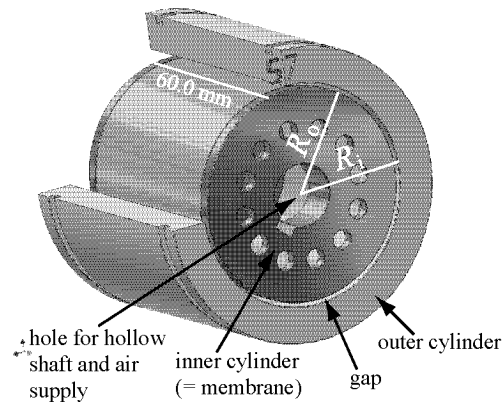


Figure 3.8.: Foaming head of ROME device with rotating inner cylinder ( $R_i$ ), static outer cylinder made of compact metal ( $R_o$ ) and gap in-between.

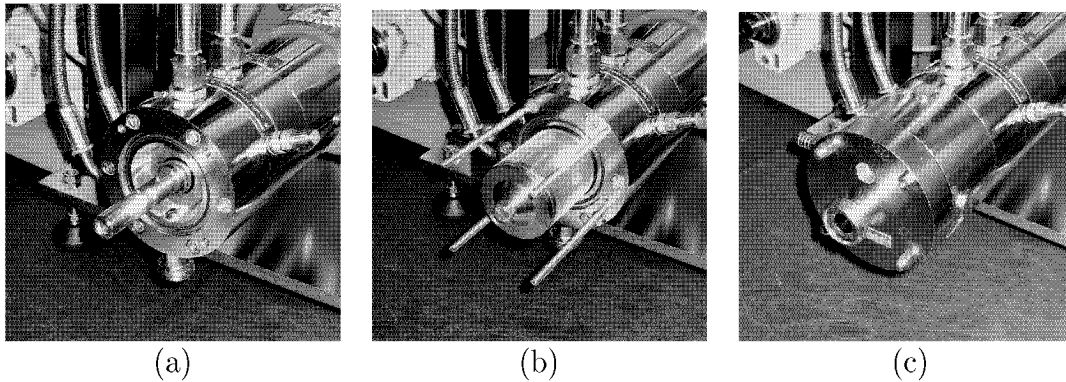


Figure 3.9.: Assembly of the ROME foaming head. (a) hollow shaft, (b) ROME head with membrane and stator screws, (c) completely assembled ROME head.

The foaming head basically consisted of two concentric hollow cylinders, both 60 mm long. The inner cylinder was the membrane. Different types of membranes

were used which are all characterized in Tab. 3.1. The outer cylinder was made of compact metal with varying inner diameter to adjust the gap size. Both phases were supplied to the foaming head separately. Thereby the gaseous phase was led through the hollow shaft to the inside of the membrane and from there forced through the membrane by the pressure of the succeeding air. The continuous phase flowed through the cylindric gap between rotating membrane and outer cylinder. The dispersing head was surrounded by a cooling jacket that could be tempered with ice-water. In Figs. 3.8 and 3.9 the construction of the dispersing head is elucidated for the example of CPDN membranes. Woven open-mesh fabrics (Sefar Nitex), sintered steel membranes and controlled pore distance nano (CPDN) membranes were used in combination with the ROME device (specifications see Sec. 3.1.6).

#### Transparent outer cylinder for rotating membrane

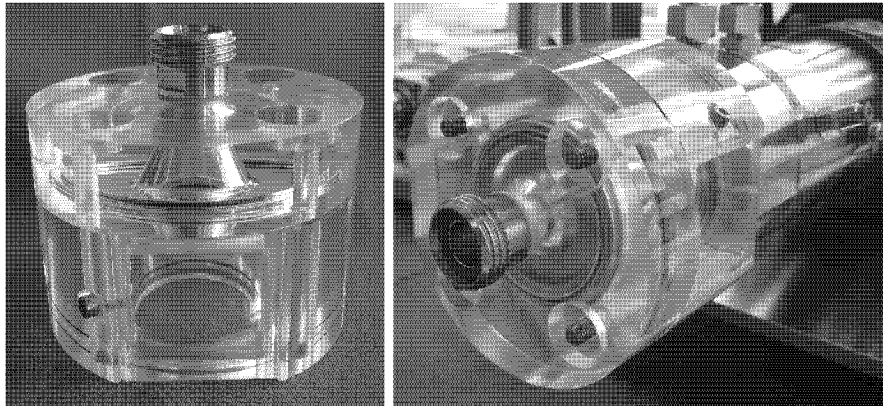


Figure 3.10.: Picture of the transparent outer cylinder by itself (left side) and mounted to the foaming head (right side).

To allow observation of bubble formation, observe bubble geometry (round or flattened) and bubble detachment from the pore of a rotating membrane the outer cylinder and housing of the ROME device were made of transparent plexiglass. Observation was done with a high speed digital camera (NAC MEMRECAM fxr6, NAC Image Technology, frame rates between 10 000 and 120 000) through the white box placed perpendicular to the axis of the rotating membrane. Lighting was done with 9 spots. In principle the operating mode of the membrane device was the same as for the non-transparent device with rotating membrane, however, the continuous phase was circulated in a closed loop. Figs. 3.10, 3.24 and 3.11 illustrate the described assembly of the transparent rotating membrane device.



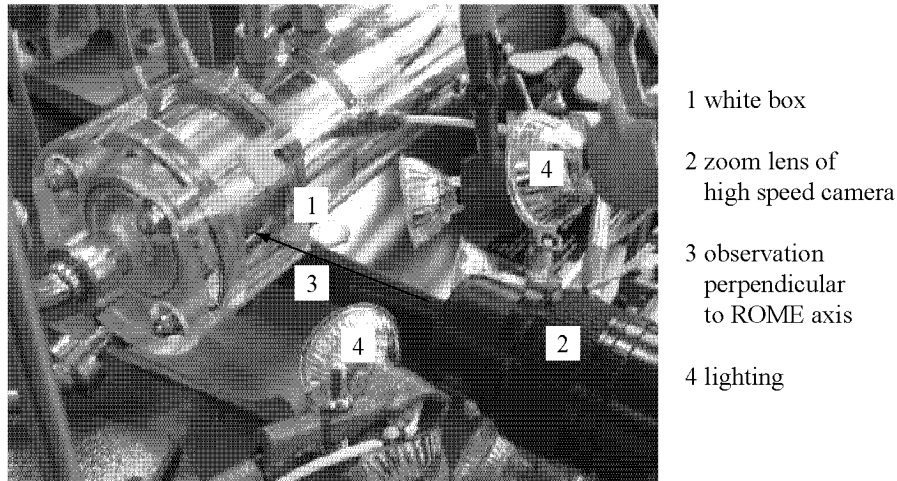


Figure 3.11.: Camera and lighting for the transparent ROME setup.

The foaming head basically consisted of two concentric hollow cylinders. The inner, rotating cylinder was the membrane. The outer cylinder made of Plexiglas with a built-in a whitebox which avoids optical deformation caused by the bend of the outer cylinder. Via a screw top the same fluid used as the continuous phase, i.e. with the same refractive index, could be filled in to avoid the generation of a distorted image.

### Dynamically enhanced static membrane (DESM)

In this construction, the membrane is fixed to the housing while the inner, rotating cylinder is made of compact metal. This set-up is much simpler construction-wise and advantageous process-wise:

- No hollow shaft is needed, the air can be directly pressed into the foaming head, more exactly into the space between membrane and housing.
- Sealing is much simpler.
- The membrane is static/non-rotating.
- Due to the much higher density of the mix compared to air, the centrifugal forces support bubble detachment from the membrane and mixing of the two phases when the air comes from the outside.

Fig. 3.12 shows a CAD-drawing of the foaming head while Fig. 3.13 shows a picture of the housing of the foaming device holding the membrane, both exemplarily

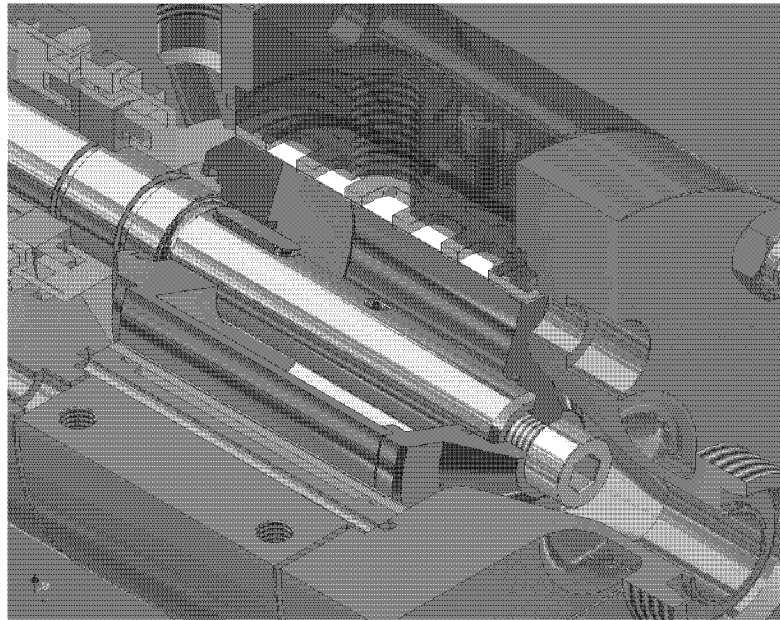


Figure 3.12.: CAD-drawing of the membrane device with membrane mounted to housing and inner, rotating cylinder made of compact metal.



Figure 3.13.: Picture of the housing containing the Sefar Nitex membrane.

for the Sefar Nitex membrane. Woven membranes (Sefar Nitex) and a sintered steel membrane were used in combination with the DESM device (specifications see Sec. 3.1.6).

### Scaled-up DESM device

The DESM device was scaled from lab- to pilot-scale and built in-house. The pilot scale DESM device is depicted in Fig. 3.14, its setup is the same as for the lab-scale DESM device described above. Fig. A.1 in App. A.1 shows the technical drawing of the device head.

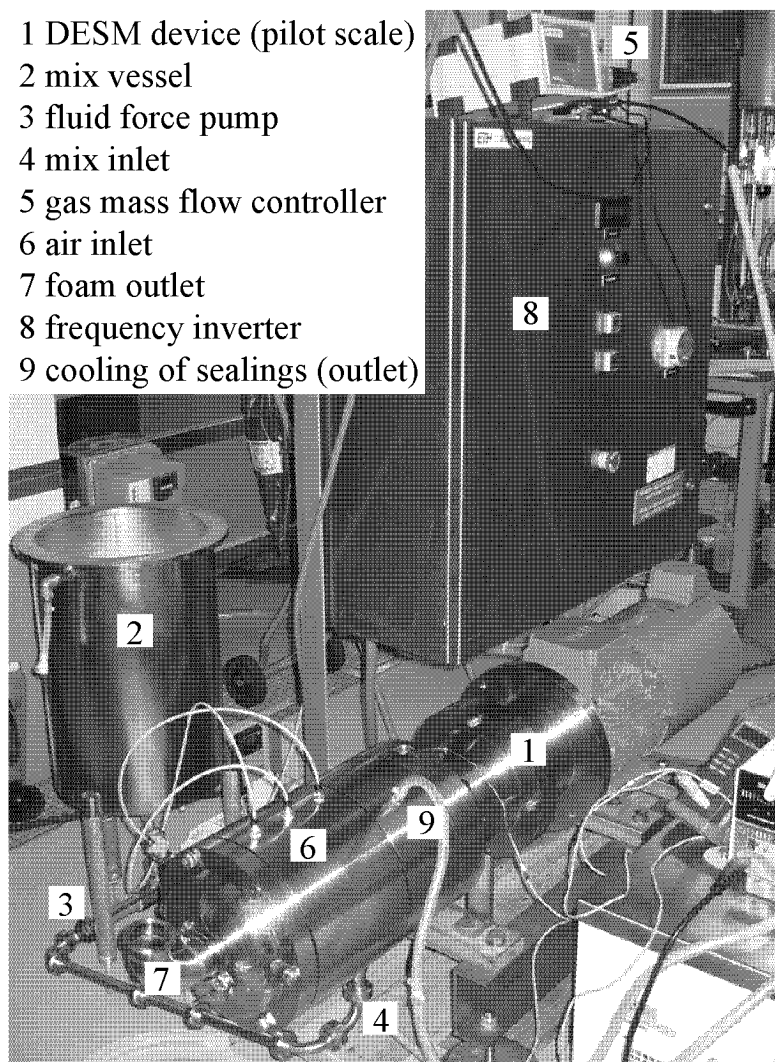


Figure 3.14.: Picture of the pilot-scale DESM device.

### 3.1.6. Membranes

The membranes are most important for the dynamically enhanced membrane foaming process. Within this work, three types of membranes were mainly used. An overview of their specifications is given in Tab. 3.1, the membrane hydrophilicity was not quantified in this work.

Table 3.1.: Membrane specifications. (<sup>1</sup>: CPDN=controlled pore distance nano, German patent, application number 13848399; <sup>2</sup>: derived from known pore size and pore distance; <sup>3</sup>: derived from known pore size and open area, <sup>4</sup>: porosity).

Type	Pore size [ $\mu\text{m}$ ]	Pore size:distance [-]	Open area [%]	Material
CPDN <sup>1</sup> uncoated	5.0	1:11.0	0.55 <sup>2</sup>	Nickel
CPDN <sup>1</sup> coated	1.5	1:39.0	0.05 <sup>2</sup>	Carbon coating
Sefar Nitex 03-6/5	6.0	1:4.6 <sup>3</sup>	5.00	PA 6.6
Sefar Nitex 03-1/1	1.0	1:11.2 <sup>3</sup>	0.80	PA 6.6
SIKA-R 0.5 IS	2.0	unknown	17.00 <sup>4</sup>	1.4306

### Sinter membrane

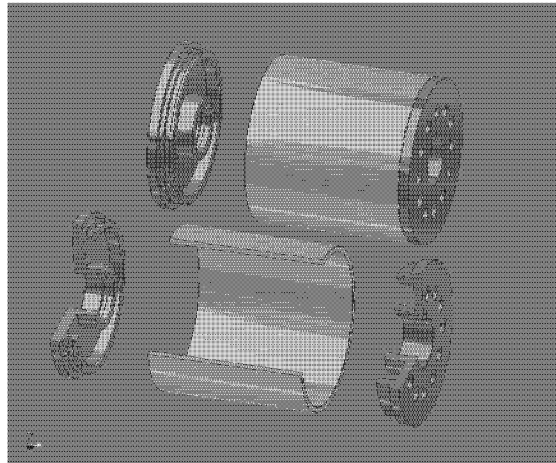


Figure 3.15.: Technical drawing of sinter membrane. The two end pieces allowed easy adaptation of the membrane to the foaming head of the rotating membrane device.

A highly porous stainless sinter membrane (Type: SIKKA R-IS, producer: GKN Sinter metals, D-42477 Radevormwald) with effective mean pore diameter of 2  $\mu\text{m}$  was used. The sinter membrane was lathed to ensure a precise outer diameter. Advantages of this membrane were its shape-stability, i.e. self-supporting structure, which allowed easy adaptation to the device head with two end pieces, and its high permeability. Fig. 3.15 shows sinter membrane and end pieces as used for the ROME device.

### Open mesh fabrics

The precision woven synthetic monofilament fabrics produced by Sefar Inc. (CH-8830 Rüslikon) are highly specialized monofilament fabrics. They are characterized by precisely defined and controlled, consistent and repeatable material properties such as pore size, thickness, tensile strength, dimensional stability and cleanliness. Two polyamide fabrics (SF03-6/5 and SF03-1/1) differing in pore size and open area were used to investigate the influence of pore size on resulting mean bubble size for otherwise identical membranes (see Tab. 3.1). Fig. 3.16 shows a schematic drawing of the woven structure of such membranes. To adapt the flexible fabrics to the foaming head, special constructions had to be made, i.e. it was attached to clamping fixtures for both the ROME and the DESM device. Detailed information on the assembly is given in App. A.2.

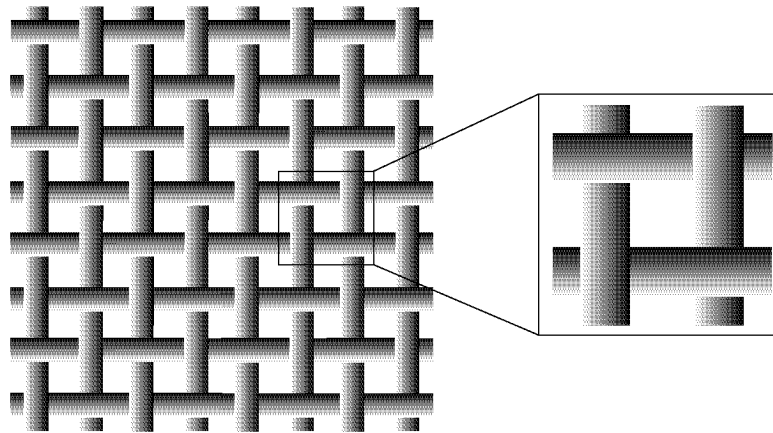


Figure 3.16.: Woven structure of Sefar Nitex membranes.

Fig. 3.17 shows the technical drawing of the clamping fixture exemplarily for the ROME device. The indentations created by the gridlike cage are 0.50 mm deep while the gap between cage and outer cylinder is 0.22 mm thick. The construction for the DESM device is inverted, the dimensions of gap, indentations and windows are identical.

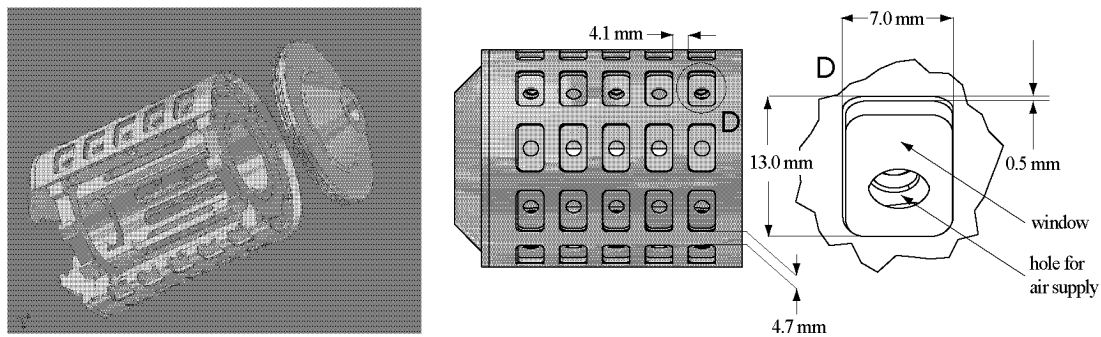


Figure 3.17.: Technical drawing of clamping fixture including dimensions of windows.

## CPDN membranes

Theoretically an ideal membrane has uniform and small pore diameters as well as consistent and large spaces between the pores. Such conditions should allow the generation of foams with identical and small bubbles as well as low coalescence rates at the membrane. In order to meet this demands, a special process has been developed within the PhD thesis of Verena Eisner on rotating membrane emulsification to manufacture so-called CPDN-membranes<sup>1</sup>. As a base for the membranes, nickel sheets are used. Then the locations of the pores are etched and shot through with laser. The pores are arranged in squares of about 1.2 mm side length. Between these squares there are pore-less bands. This CPDN membrane was used without further changes (= "uncoated"). Additionally this membrane coated by a pure carbon layer using the PECVD (plasma enhanced chemical vapor deposition) method was used (= "coated"). The carbon layer led to smaller pore diameters. Both membranes have defined pore diameters and consistent, large distances between the single pores. In Fig. 3.18 SEM pictures of the two membranes can be seen.

To use the membranes in the rotating membrane foaming device, they were fixed to a cylindrical frame. Fig. 3.19 shows the construction of the metallic frame without and with the membrane.

---

<sup>1</sup>CPDN = Controlled Pore Distance Nano. Patent: DE 103 07 568.2-33

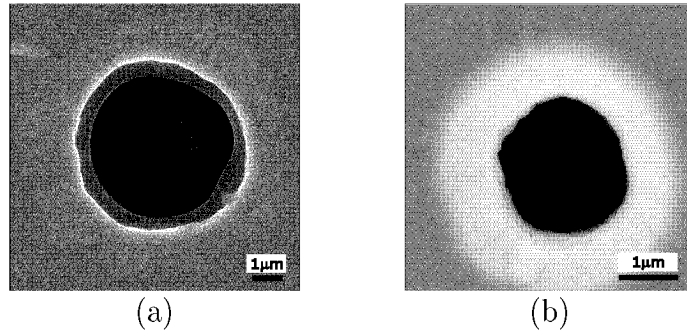


Figure 3.18.: Scanning electron microscope pictures of the membrane pores (courtesy of V. Eisner). (a) uncoated membrane (pore diameter 5.0 μm), (b) coated membrane (pore diameter 1.5 μm). For both membranes the distance from pore center to pore center was 60 μm.

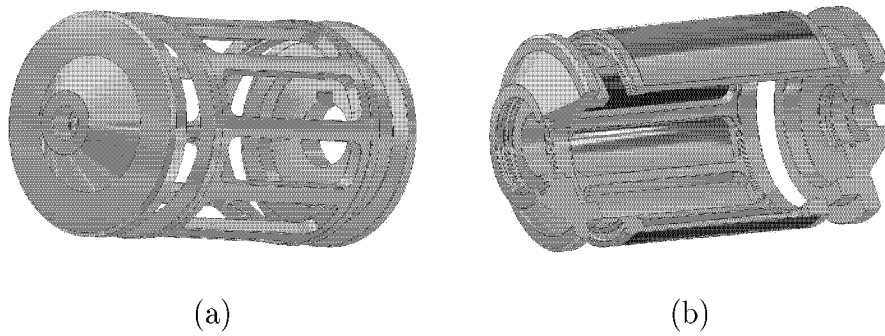


Figure 3.19.: Construction of the cylindrical membrane module: (a) metallic frame on which the membrane was fixed in order to give it a firm cylindrical shape, (b) metallic frame plus membrane.

## 3.2. Analytical characterization of fluid and foam

### 3.2.1. Density measurements

The density of all liquids was measured using the oscillating U-tube method (Anton Paar, DMA-38). The temperature was adjustable by a Peltier element from 15 °C to 40 °C with an accuracy of  $\pm 0.3$  °C. The accuracy of the density measurement is specified as  $\pm 1 \text{ kg} \cdot \text{m}^{-3}$  by the manufacturer.

Foam density was determined gravimetrically by filling a container of known volume with foam and weighing it.

### 3.2.2. Rheological measurements

All rheological investigations were done using a Paar Physica MCR 300 rheometer (Austria) allowing strain-controlled measurements. Applied stresses and resulting strains were evaluated with Orchestrator Software. The rheological properties were measured using the Searle-type concentric cylinder geometry CC27 with rotating inner cylinder (bob radius 13.33 mm, cup radius, 14.46 mm, gap length 40.00 mm, cone angle 120 °) for all experiments except for the ones comparing mix A with foam A where a cone-plate geometry CP50-1 was used (diameter 50 mm, gap: 0.05 mm, angle 1 °). Sample temperature was controlled by a Peltier element with attached water bath.

### Newtonian fluids

To verify the Newtonian flow behavior of the glucose syrups, glucose syrup solutions and silicone oils, rheometrical flow curves were obtained in shear rate tests. The ranges of investigated shear rates and the measuring temperature are given in Tab. 3.2. The measurements were done once for each fluid.

Table 3.2.: Parameters used for flow curve measurements of Newtonian fluids.

Newtonian fluid	Purpose of use	Shear rate range [ $s^{-1}$ ]	Temperature [°C]
Glucose syrup solutions	Power characteristics	$10^{-1} - 10^3$	20
Glucose syrups	Band apparatus	$10^{-1} - 10^3$	18
Silicone oils	TECC device	$10^{-1} - 10^2$	25

Viscosity as a function of temperature was measured in temperature ramps. The chosen temperature ranges and shear rates are given in Tab. 3.3. The measure-



ments were done once for each fluid. The functional relationship between viscosity and temperature was plotted as  $\ln \eta$  versus  $T^{-1}$  since the then resulting curve is close to a straight line and can be linearly approximated.

Table 3.3.: Parameters used for temperature ramps of Newtonian fluids.

Newtonian fluid	Purpose of use	Temperature range [°C]	Shear rate [ $s^{-1}$ ]
Glucose syrup solutions	Power characteristics	20 - 40	100
Glucose syrups	Band apparatus	10 - 40	10
Silicone oils	TECC device	18 - 28	10

## Model mixes and foams

Rheological flow curve measurements were done for model mix A, B, C, D and E and for foam E (gas volume fractions 0.20, 0.33, 0.43, 0.50, 0.56, 0.60). The parameters of the measurements are given in Tab. 3.4. Flow curve measurements of foam E at gas volume fraction 0.56 was done twice with the same, already sheared sample to determine whether the sample undergoes any change during the analysis. Since this was not the case, all other experiments using mix E and foam E at various gas volume fractions were done once, only. Foam E of various gas volume fractions was produced in the dynamically enhanced static membrane device using a Sefar Nitex SF03-6/5 membrane, a gap size of 0.22 mm, a residence time of 0.75 s and a circumferential velocity of  $18.51 \text{ m} \cdot \text{s}^{-1}$ .

Table 3.4.: Parameters used for flow curve measurements of model mixes A to E and foam with different gas volume fractions obtained with mix E.

Sample	Shear rate range [ $s^{-1}$ ]	Temperature [°C]
Mix A	$10^{-1} - 10^3$	18
Mix B	$10^{-3} - 10^3$	18
Mix C	$10^{-3} - 10^3$	18
Mix D	$10^{-1} - 10^3$	18
Mix E	$10^{-2} - 10^3$	18
Foam E (various $\phi_V$ )	$10^{-2} - 10^3$	18

Mix A was compared to foam A containing different gas volume fractions (0.33, 0.50, 0.67, 0.85). The analyzed foams were produced with mix A on the rotor-stator device using the Radax geometry at 8.04 m/s circumferential velocity and 11.0 s

residence time. To determine foam stability during rheological measurements, the same sample of foam A with gas volume fraction 0.70 was used for measurements twice. Since this foam was shown to be shear-sensitive, frequency sweeps were chosen for analysis since the oscillatory measurement is much gentler (chosen parameters listed in Tab. 3.5). A cone-plate geometry CP50-1 was used. Comparable oscillatory measurements using the concentric cylinder geometry CC27 were done for foam E with gas volume fractions 0.33 and 0.56. These foams were produced in the dynamically enhanced static membrane device using a Sefar Nitex SF03-6/5 membrane, a gap size of 0.22 mm, a residence time of 0.75 s and a circumferential velocity of  $18.51 \text{ m} \cdot \text{s}^{-1}$ . For both foam A and E, the linear viscoelastic regimes were first determined in dynamic strain experiments and appropriate deformations for the subsequent frequency sweeps defined.

Table 3.5.: Parameters used for oscillatory measurements of mix A, foam A and foam E containing different gas volume fractions.

Sample	Deformation [%]	Frequency range [ $\text{s}^{-1}$ ]	Temperature [ $^{\circ}\text{C}$ ]
Mix A	0.54	$10^{-1} - 10^2$	18
Foam A	0.54	$10^{-1} - 10^2$	18
Foam E	1.00	$10^{-1} - 10^2$	18

### 3.2.3. Surface tension measurements

Surface tension was measured using the drop volume method for preselected drop formation times [70]. This method is based on measuring the volume of a detaching pendant drop at a vertical capillary tip. The disperse phase volume is increased by slow injection through a capillary. As soon as a critical volume is reached, the drop detaches. The drop formation time (DFT) plays an important role, especially when performing experiments in the presence of surface active compounds where the interfacial tension is a function of the surface age. The drop detachment time depends on the injection velocity, the capillary diameter and well-defined waiting times during the injection. For an appropriate choice of these parameters, steady surface tension measurements are possible for preselected drop formation times (DFT). After drop detachment, a residue of disperse fluid remains attached to the capillary. To determine this fluid volume, an empirical correction according to measurements of Harkins and Brown [74] was used.

### 3.2.4. Determination of gas volume fraction

The gas volume fraction  $\phi_V$  and overrun  $OR$  were calculated according to Eqs. 3.2 and 3.3, respectively.

The gas volume fraction is the amount of gas in the foam:

$$\phi_V = \frac{V_{\text{gas}}}{V_{\text{foam}}}, \quad (3.1)$$

and the overrun given by the amount of gas per mix:

$$OR = \frac{V_{\text{gas}}}{V_{\text{mix}}} \cdot 100\% = \frac{\rho_{\text{fluid}} - \rho_{\text{foam}}}{\rho_{\text{foam}}} \cdot 100\%. \quad (3.2)$$

The overrun can easily be converted to the gas volume fraction:

$$\phi_V = \frac{\frac{OR}{100}}{\frac{OR}{100} + 1}. \quad (3.3)$$

### 3.2.5. Foam microstructure

The foam microstructure was analyzed using inverse light microscopy (transmission mode, magnification 100x, 200x or 400x). Depending on the set parameters and chosen recipe, each microscope picture contained between 50 and 1000 bubbles. For each foam, five to ten micrographs of different samples were recorded to increase the total bubble count. Computational image analysis was used to quantify the bubble size distribution. The pictures were imported into our in-house software BubbleDetect<sup>©</sup> <sup>2</sup> that automatically computes bubble size distribution functions and their parameters via several specific algorithms. A bubble size distribution is characterized either by cumulative sum distribution functions  $Q_r(x_i)$  or incremental density distribution functions  $q_r(x_i)$ . To facilitate comparison of bubble size distributions, specific distribution parameters are taken into account. The mean diameter  $x_{50,r}$  denotes the bubble size where 50 % of the respective amount (e.g. number ( $r=0$ ), surface ( $r=2$ ), volume ( $r=3$ )) relates to smaller bubbles. Cumulative **number** distribution functions  $Q_0(x)$  and their corresponding number density functions  $q_0(x)$  weight all bubble sizes equally while the respective cumulative **volume** distribution functions  $Q_3(x)$  and volume density functions  $q_3(x)$  weight the bubbles proportional to their volume ( $\sim x^3$ ) and, thus, focus on large outliers. Within this thesis, the mean diameters of the cumulative number distribution functions  $x_{50,0}$  were mainly considered. Where coalescence effects played a major role,  $x_{50,3}$  was considered.

In the literature, the Sauter mean diameter is often used as well. It is defined as the equivalent spherical diameter by surface area per unit volume to the full

<sup>2</sup>Copyright 2003 Lab of Food Process Engineering (LMVT), ETH Zurich, Switzerland.

distribution, i.e. the particle diameter that has the same specific surface as that of the full distribution. The Sauter diameter lies in-between the mean diameters of cumulative number and volume distribution function (see examples Tab. 3.6).

Table 3.6.: Comparison of distribution parameters: mean diameters of the cumulative number and volume distribution  $x_{50,0}$  and  $x_{50,3}$ , respectively and Sauter diameter  $x_{3,2}$ .

Example	$x_{50,0}$ [ $\mu\text{m}$ ]	$x_{3,2}$ [ $\mu\text{m}$ ]	$x_{50,3}$ [ $\mu\text{m}$ ]
Foam A	57.695	74.502	79.207
Foam C	47.181	60.792	64.860
Foam E	7.614	11.510	14.429

The evaluation of the bubble size distribution using BubbleDetect<sup>©</sup> proceeds as follows (see also Fig. 3.20). After importing a microscopic picture (Fig. 3.20a) into BubbleDetect<sup>©</sup>, the image is scaled in order to enable the software to convert pixels into micrometers. The corresponding scaling factor is obtained by measuring a defined distance on a micrometer under the microscope. The picture is then thresholded to get a black-and-white picture of the bubble perimeters (Fig. 3.20b). In a next step BubbleDetect<sup>©</sup> automatically searches for the bubble perimeters by a least squares fitting of circles to the bubble perimeters. All detected perimeters are visually marked by showing the fitted circles (Fig. 3.20c). The correct automatic interpretation of incomplete bubble perimeters can be difficult for the program if the picture quality is poor. Thus, incorrectly fitted circles are corrected by using a second algorithm (Fig. 3.20d). To do so, an inadequate circle is manually deleted and the second algorithm is started by a mouse click within the respective bubble. When the best possible matches are reached, the final bubble diameters are added to the bubble size distribution (Fig. 3.20e). All five to ten pictures corresponding to one foam are evaluated the same way and all bubble diameters added to one collective distribution.

### 3.2. Analytical characterization of fluid and foam

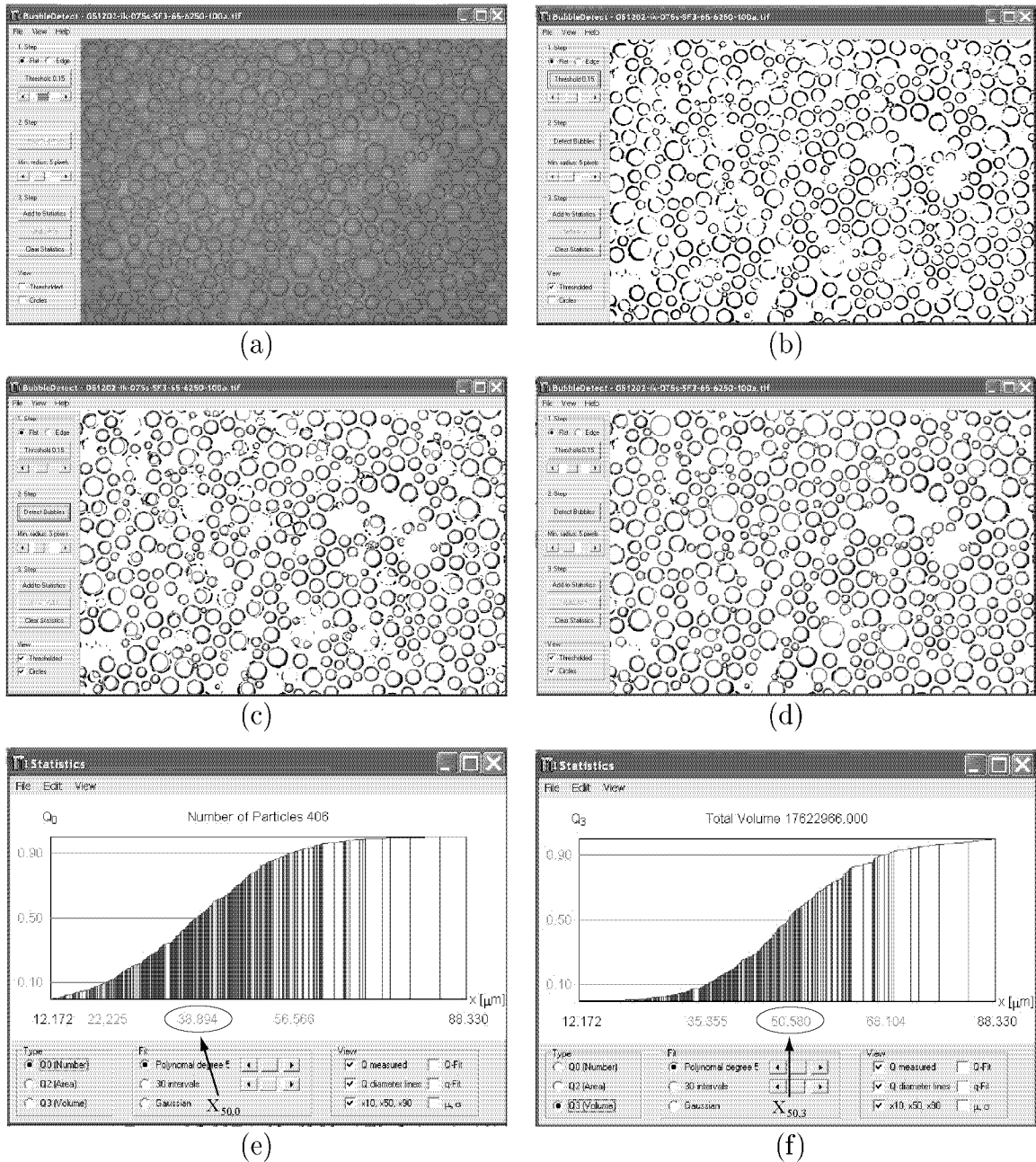


Figure 3.20.: From microscope picture to bubble size distribution: computational image analysis using the software BubbleDetect<sup>©</sup>. (a) Original micrograph. (b) Thresholded black and white picture. (c) Automatically found perimeters marked in light grey. (d) Well analyzed image, incorrectly fitted circles were corrected via a second algorithm. (e) and (f) Cumulative number and volume distribution, respectively, with corresponding distribution parameters.

### 3.3. Processing methods

#### 3.3.1. Mix production

##### Glucose solutions

Differently concentrated solutions of dried glucose syrup were used as Newtonian fluids of different viscosities needed to obtain the power characteristics (see Tab. 3.7).

Table 3.7.: Newtonian fluids used to obtain power characteristics. The concentration refers to the amount of dried glucose syrup in weight percent. Viscosity and density are indicated at 20 °C.

fluid	concentration [weight %]	viscosity [Pa · s]	density [kg · m <sup>-3</sup> ]
tap water	-	0.00102	998.3
glucose syrup solution	12	0.00204	1045.9
glucose syrup solution	30	0.00534	1124.7
glucose syrup solution	40	0.01191	1173.1
glucose syrup solution	58	0.10459	1269.2
glucose syrup solution	69	0.89315	1335.0

Water and dried glucose syrup were stirred manually until glucose powder was dissolved. Fluids were used at room temperature for the experiments. For low concentrations (12 to 40 weight%) the solubility of glucose syrup was good, thus, water of about 22 °C was used and the solution prepared an hour before usage only. For high concentrations (58 and 69 weight%) circa 40 °C warm water was used and the solution prepared one day before usage to allow complete solution of the glucose powder.

The Newtonian behavior of the glucose syrup solutions was verified in rheometrical flow curve measurements and temperature-viscosity relationships obtained in temperature ramps (see Sec. 3.2.2). The temperature-density dependency of all solutions was determined with a density meter (see Sec. 3.2.1).

#### Model mixes A to D

Model Mix A, B, C and D contained Ame-HV and Guar Meyprodor in different concentrations (see Tab. 3.8). Ame-HV and Guar Meyprodor 400 were added to 40 °C warm demineralized water. This mixture was stirred with the Polytron stirring staff (Polytron PT 6000, Kinematica AG, Switzerland) until no clumps were left. The temperature of the mix never exceeded 45 °C to avoid protein denaturation.

The mix was prepared one day before foaming it and was cooled down to 4 °C overnight.

Table 3.8.: Concentrations of Ame-HV and Guar in model mixes A to D.

	Ame-HV [weight %]	Guar Gum [weight %]
model mix A	3.00	1.50
model mix B	5.00	1.00
model mix C	5.00	0.50
model mix D	5.00	0.25

## Model mix E

Model mix E contained 0.60 % emulsifier, 0.25 % stabilizers, 30.00 % sugars and citric acid to adjust pH. The stabilizers and sugars were dissolved in distilled water at 65 °C. Subsequently, the emulsifier was added. The mix was then pasteurized, homogenized and cooled to 5 °C (Fryma, APV Homogenizers, Denmark).

### 3.3.2. Bubble deformation and break-up in simple shear

#### Band apparatus

To investigate high deformation and try to achieve bubble break-up in simple shear, experiments using a parallel band apparatus were performed.

The diameter of the undeformed bubble was determined by evaluating a picture taken with the CCD-camera (DFW-V500, Sony). For this purpose the Java based image processing software imageJ (Version 1.35n, National Institutes of Health, USA) was used. The pixel-millimeter conversion factor was determined via the known band distance.

Newtonian flow behavior of the glucose syrup was verified in rheological flow curve measurements, the temperature dependent viscosities measured and the functional relationship derived. All surface tension measurements were carried out in-house at 18° C using the drop detachment method. The density of the glucose syrup needed for the surface tension measurements was determined with a density meter.

The velocity gradient developed in the parallel band apparatus is linear. The shear-rate was obtained as the ratio between the relative speed at which the bands move and the distance between them.

The major and minor axis of the sheared bubble were determined using the software *imageJ*. First, a black and white threshold was set on every frame of the movie. Afterwards an ellipse was fitted to the deformed bubble and the major and the minor axes of the fitted ellipse measured for every frame. Because the movies were captured with 10 frames per second over several seconds, the time dependent development of the semi-major and semi-minor axes and the corresponding deformation value could be plotted as a function of time. The average  $D$ -value at equilibrium was acquired by averaging the values at constant deformation.

#### TECC device

To place a bubble into the gap, a syringe was inserted into the gap through a lead-through at the bottom of the gap. One CCD-camera (DFW-V500, Sony) looked sideways onto the plexiglass-cylinder and captured movies of bubble size and break-up. The second camera (DFW-V500, Sony) was placed below the TECC to assess the position of the bubble. The software Fire-i was used to operate the cameras. Bubbles were illuminated from top and bottom to create reflections at the bubble surface to increase the contrast between the bubble and the continuous phase. A stroboscope was used to increase reflections at the thin break-up point of the deformed bubble. Because the bubble moved with the sheared continuous phase, a mirror was placed behind the TECC. Thus the moving bubble could be observed during its entire way around the container. The dimensions of the inner cylinder and the outer cylinder were chosen such that the ratio between diameter of inner cylinder and gap width is 10:1.

Pictures of the undeformed bubble plus a ruler were taken to determine the bubble size using *image J*. Because of the bend of the outer Plexiglas cylinder the diameter of the bubble could only be measured vertically. The rotational speed of the inner cylinder was step-wise increased with long waiting periods until break-up occurred. If the actual break-up event was missed because it occurred on the side turned away from the viewer, a small, broken-away bubble following the main bubble proved that breakup had happened.

Rheometrical flow curves were obtained to ensure the Newtonian flow behavior of the silicone oils, their temperature dependent viscosities were measured in temperature ramps. The shear rate ( $\dot{\gamma}$ ) was determined according to DIN 53018 [44] using Eq. 2.47. The values for the surface tension from the manufacturer were assumed to be correct. Such values were approved in former measurements in-house for other silicone oils bought from the same manufacturer.

It is not possible to observe bubble deformation in the current setup because the cylindrical plexiglass wall leads to distortions in rotational direction. These optical distortions could be avoided with the addition of a so-called white-box which consists of a square transparent container placed around the acrylic glass cylinder. Optical distortions can then be eliminated if the space between the two



transparent containers and the gap between the two concentric cylinders is filled with the same fluid. Such a construction can be seen in Fig. 3.21.

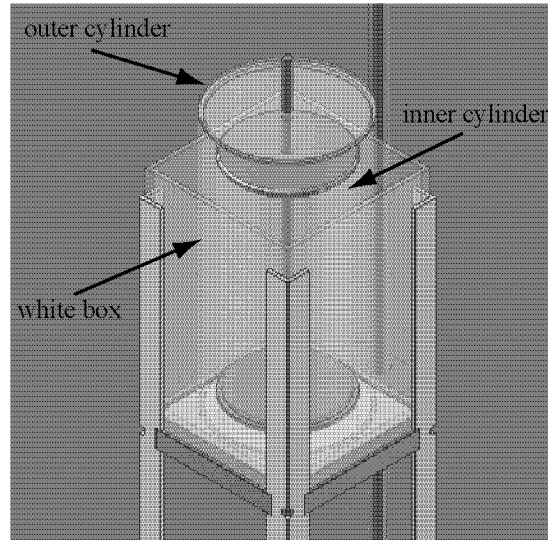


Figure 3.21.: TEC device with white box.

### 3.3.3. Rotor-stator foaming

Foaming experiments were performed varying the gas volume fraction, pressure, volumetric energy input, rotational speed and residence time/product throughput. In Tab. 3.9 the most important parameter combinations analyzed for rotor-stator whipped foams are summarized. Details are given subsequently. Due to the large number of parameter combinations tested, not all experiments could be repeated. Standard deviations are included in the figures whenever results were reproduced.

Table 3.9.: Rotor-stator whipping: analyzed process parameter combinations.

Pressure [bar]	Geometry	Rotational speed [rpm]	Gas volume fraction [-]
0.60	Radax	3 011, 4 048	0.33 to 0.80, plus $\phi_{V,\max}$
0.75	Radax	3 011, 4 048	0.33 to 0.80, plus $\phi_{V,\max}$
atm	Radax, 12-HR	1 978, 3 011, 4 048	0.33 to 0.80, plus $\phi_{V,\max}$
2.00	Radax	3 011, 4 048	0.33 to 0.80, plus $\phi_{V,\max}$
3.00	Radax	3 011, 4 048	0.33 to 0.80, plus $\phi_{V,\max}$
4.00	Radax	3 011, 4 048	0.33 to 0.80, plus $\phi_{V,\max}$

## Standard foaming experiments

In Fig. 3.22 the flow sheet of the standard foaming process is shown as well as foaming at partial vacuum and increased pressure conditions.

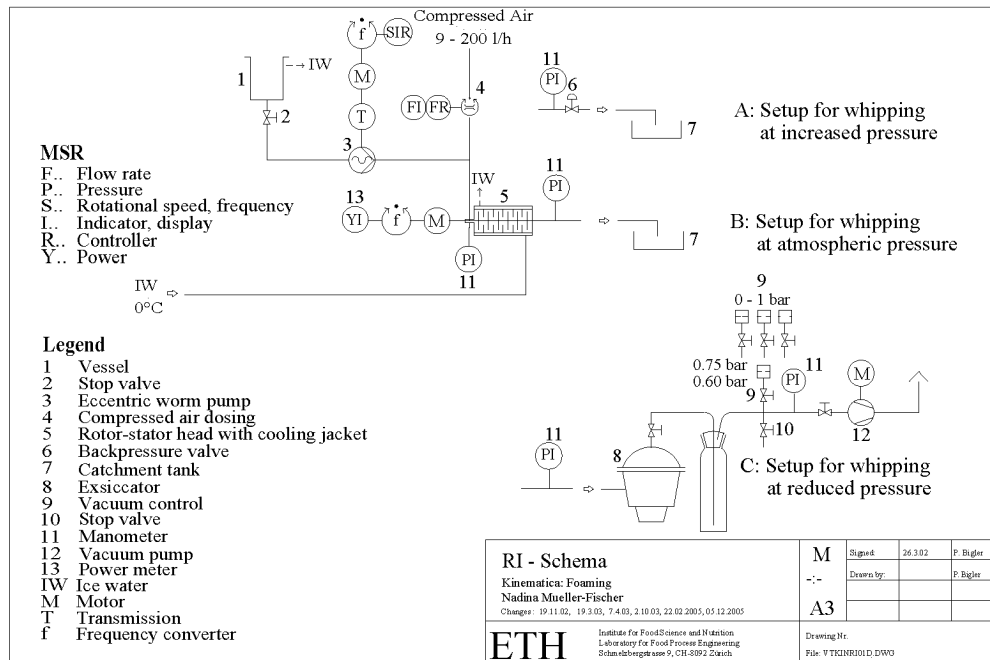


Figure 3.22.: Flow sheet of the pilot plant for experiments conducted at either increased pressure (A), atmospheric pressure (B) or partial vacuum conditions (C).

An eccentric worm pump pumped mix from a vessel through connecting pipes into the rotor-stator head of the Kinematica Megatron. A defined amount of air was injected into the connecting pipes with a gas mass flow controller (either Red-y or Bronkhorst) right before the whipping head. The dispersing head had a cooling jacket, which was cooled with ice-water to minimize a heating up of the mix/foam due to energy dissipation. The foam was gathered in a container from which samples were taken for analysis. Gas volume fraction and bubble size distribution were analyzed within five minutes after foam production.

Most of the pilot batches were duplicated to guarantee the reproducibility of the results. Since the foam temperature strongly influenced foam stability during analysis, the foam outlet temperature was adjusted to  $18 \pm 2^\circ\text{C}$  by adapting both mix inlet temperature and temperature of cooling bath. It was impossible to keep foam temperature in the desired range for rotational speeds higher than 4048 rpm.

### Foaming at reduced pressure

A vane pump (DUO 1.5 A, Arthur Pfeiffer Vakuumentchnik, Germany) was used to set a vacuum of either 0.50 bar absolute or 0.25 bar absolute before starting the experiment to achieve pressures of 0.60 bar and 0.75 bar, respectively, during foaming. This reduction in applied partial vacuum is a consequence of the pressure generated by the product flow. When the chosen partial vacuum was reached, the exsiccator was closed with a valve. Then the standard foaming process began. As soon as the foaming was finished, i.e. when enough foam was gathered, the exsiccator was aerated to atmospheric pressure over a duration of approximately 20 seconds using a valve. Foam samples were then taken from the exsiccator for analysis. Foaming at reduced pressure was thus only possible batch-wise although the rotor-stator device works continuously.

### Foaming at increased pressure

The process itself was similar to the standard foaming process. In addition, a back-pressure valve was installed at the outlet of the rotor-stator head to create product pressures of 2, 3 and 4 bar in the whipping head during the foaming process. Between the dispersing head and this valve a pressure sensor was installed to measure the exact product pressure. The foam expanded as soon as it passed the back pressure valve, because it was then subjected to atmospheric pressure. Foam was gathered in a container from where samples were taken. Foaming at increased pressure was possible in a continuous way.

### Number of rotor-stator pairs

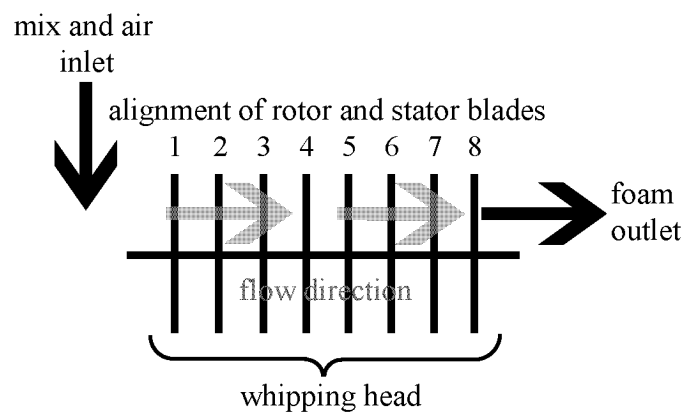


Figure 3.23.: Schematic drawing of the rotor-stator head: alignment of the rotor-stator pairs and flow direction.

The number of rotor-stator pairs added to the whipping head was changed from one to eight using the Radax geometry. The successive increase in rotor-stator pairs mounted to the whipping head was paired with different residence times in the dispersing flow field from e.g. 1.4 s (1 RS-pair) to 11.0 s (8 RS-pairs) for a fluid flow rate of 18.22 l/h and a gas volume fraction of 0.50. This corresponds to an identical residence time per rotor-stator pair of 1.4 s. The rotor-stator pairs were added at the inlet of the head (see Fig. 3.23). The gas volume fraction was increased as far as it was possible without getting blow-by. Rotational velocity was 3011 rpm ( $= 8.04 \text{ m} \cdot \text{s}^{-1}$  circumferential velocity).

### Radax versus 12-HR geometry

To compare the whipping efficiency of the Radax and the 12-HR geometry (see Fig. 3.5), four experimental set-ups were compared:

- 8 pairs of the Radax geometry with a total residence time of 11.0 s (equivalent to 1.4 s per rotor-stator pair)
- 8 pairs of the 12-HR geometry with a total residence time of 11.0 s (equivalent to 1.4 s per rotor-stator pair)
- 12 pairs of the 12-HR geometry with a total residence time of 11.0 s (resulting in a shorter residence time of 0.9 s per rotor-stator pair)
- 12 pairs of the 12-HR geometry with a residence time of 1.4 s per rotor-stator pair (equivalent to a total residence time of 16.8 s)

To use the set-up with 8 rotor-stator pairs of the 12-HR geometry, the remaining length of the whipping head was filled with spacers (rotors and stators without pins). All experiments were done at rotational speeds of 1978 ( $=5.28 \text{ m} \cdot \text{s}^{-1}$  circumferential velocity), 3011 ( $=8.04 \text{ m} \cdot \text{s}^{-1}$ ) and 4048 rpm ( $=10.81 \text{ m} \cdot \text{s}^{-1}$ ). Foams with identical gas volume fractions were produced for all set-ups (0.20, 0.33, 0.50, 0.60, 0.66, 0.75, 0.80,  $\phi_{V,max}$ ). The air and mix flow rate were adapted to vary the gas volume fraction while keeping the residence time constant. By definition, the free volume began with the first rotor and ended with the last stator. It is different for the two geometries and is listed in Tab. 3.10.

### Power measurements

The total real power input in the dispersing machine was measured (Yokogawa 2533, Yokogawa Electronics, Japan). The obtained values were used to calculate the volume specific energy  $E_V$  and power input  $P_V$ . The dispersing power was calculated by subtracting the idling drive power from the total real power. The

Table 3.10.: Specifications and free volume of the Radax and 12-HR geometry.

Geometry	Maximum number of RS-pairs [-]	Free head volume [ml]
Radax	8	112.705
12-HR	12	62.387

idling drive power is the measured real power used at a set rotational speed with empty rotor-stator head.

### 3.3.4. Dynamically enhanced membrane foaming device

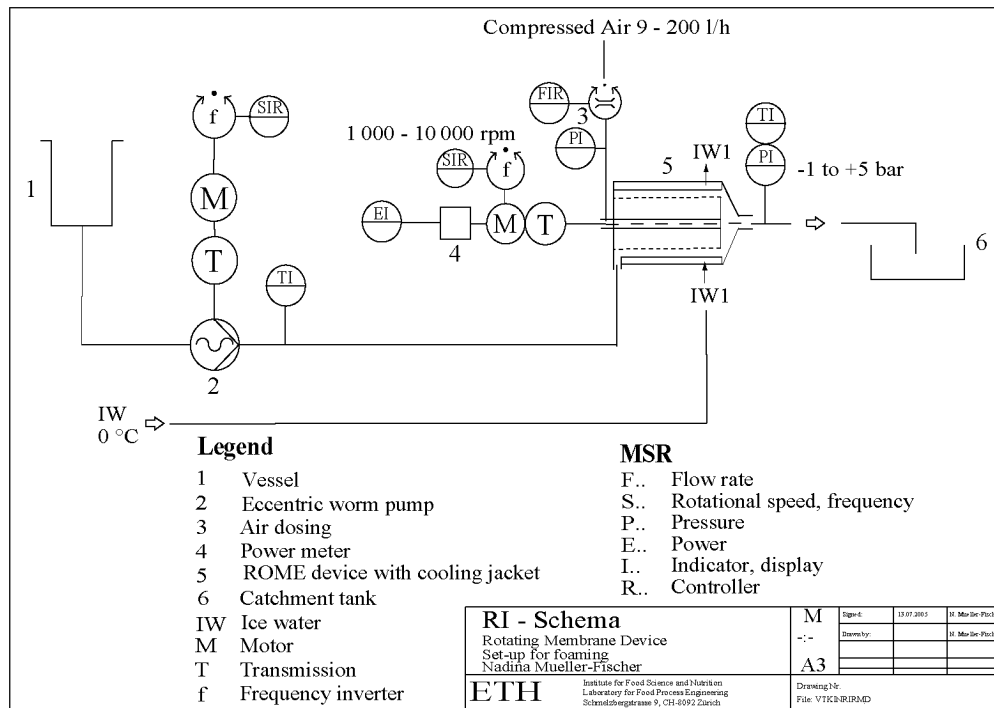


Figure 3.24.: Schematic drawings of the dynamically enhanced membrane foaming device used for the foaming experiments.

The two setups, the rotating membrane foaming device RIME and the dynamically enhanced static membrane foaming device DESM were used for foaming experiments. The experiments were performed varying the gas volume fraction, gap

size, mix recipe, velocity field, pore size, pore distance, membrane type, residence time and membrane area. Due to the large number of tested parameter combinations, it was not possible to repeat every experiment. The standard deviations are included in the figures whenever the results were reproduced.

Fig. 3.24 shows the flow sheet of the standard membrane foaming process. An eccentric worm pump (Nemo NM008BY03512b, Häny AG, Switzerland) brought mix from a vessel through connecting pipes into the head of the dynamically enhanced membrane foaming device. A defined amount of air (red-y GSC-B9HA-BB24, Vögtlin AG, Switzerland) was pressed through a membrane into the narrow annular gap between rotating inner cylinder and static outer cylinder. The resulting foam was gathered in a container. Samples were taken, the gas volume fraction determined and microscope images captured.

## Foaming using the rotating membrane

The systematically varied parameters are listed in Tab. 3.11.

Table 3.11.: Systematically varied parameters for foaming with ROME device.

Membranes and pore sizes:	Sefar Nitex, 6 and 1 $\mu\text{m}$ Sinter membrane, 2 $\mu\text{m}$ CPDN membrane, 5.0 and 1.5 $\mu\text{m}$
Gap width	0.22 mm, 0.50 mm, 0.72 mm, 1.0 mm, 1.5 mm
Circumferential speed	2.9 - 23.5 $\text{m} \cdot \text{s}^{-1}$
Residence times	0.97 s, 0.75 s, 0.50 s
Model mixes	E, C, A
Gas volume fraction	0.20, 0.33, 0.43, 0.50, 0.56, ..., $\phi_{V,max}$

## Foaming with the dynamically enhanced static membrane device

Systematical experiments were performed using the DESM device, the parameters are listed in Tab. 3.12.

Table 3.12.: Parameters used for foaming with DESM device

Membranes and pore sizes:	Sefar Nitex, 6 and 1 $\mu\text{m}$ Sinter membrane, 2 $\mu\text{m}$
Gap width	0.22 mm, 0.50 mm (and 2.0 mm)
Circumferential speed	3.0 - 23.7 $\text{m} \cdot \text{s}^{-1}$
Residence times	0.50 s, 0.75 s (and 2.00, 3.00 s)
Model mixes	E, C
Gas volume fraction	0.20, 0.33, 0.43, 0.50, 0.56, ..., $\phi_{V,max}$

## Experiments used for scale-up calculations of DESM device

Table 3.13.: Parameters for scale-up experiments with small device.

Residence times [s]:	0.75, 0.50, 0.40, 0.30, 0.25, 0.20, 0.15, 0.10
Membrane area [-]	5 units, 3 units, 1 unit

For scale-up calculations of the DESM device, it was necessary to determine the impact of membrane area on the resulting foam microstructure and to test the maximum flow rate/minimum residence time. The experiments were done using the Sefar Nitex membrane with 6  $\mu\text{m}$  pore size, a gap of 0.22 mm and a circumferential velocity of 18.51  $\text{m} \cdot \text{s}^{-1}$ . The clamping fixture for the Sefar membrane had 50 membrane filled windows arranged in five axially rows (see Fig. 3.17). To determine the maximum flow rate/minimum residence time, the residence time was stepwise decreased. Foams of gas volume fraction 0.50 were produced and  $\phi_V$  stepwise increased until blow-by occurred. To analyze the impact of the membrane area, some of the window rows containing the membrane were closed with plastic film. The impact of the 5 maximally possible membrane rows (=5 units) was compared to 3 units (out of 5) and 1 unit (out of five). To ensure comparable shearing per membrane area, membrane filled rows were arranged at the head outlet while the foil covered windows were at the head inlet. Criteria for resulting foam quality compared to optimum foaming parameters were that no blow-by occurred, that drainage did not increase and that bubble sizes were maximally increased by 50 %. It was mandatory that a minimum gas volume fraction of 0.56 was achievable. All

experiments were repeated and the data used for the scale-up calculations. Tab. 3.13 summarizes the experimental set-up.

### Scale-up calculations from lab- to pilot-scale DESM

Scale-up calculations were done using the formulas referred to in Tab. 3.14.

Table 3.14.: References to the formulas used for scale-up calculations.

Total flow rate	see Eq. 2.57
Shear rate	see Eq. 2.47
Foam viscosity	see Fig. 4.46
gap <i>Re</i> -number	see. Eq. 2.41
<i>Ne</i> -number	see Eq. 2.38
<i>C</i> -value	see Eq. 3.6
$v_{\text{sink}}$	see Eq. 2.1
$t_{\text{separation}}$	see Eq. 3.4
$P_{V,\text{diss}}$	see Eq. 2.55
$P_{\text{diss}}$	see Eq. 2.54
$E_{\text{diss}}$	see Eq. 2.56

$$t_{\text{separation}} = \frac{r_{s_i} - r_{r_0}}{v_{\text{sink}}}, \quad (3.4)$$

where  $r_{r_0}$  is the outer diameter of the rotor,  $r_{s_i}$  is the inner diameter of the stator,  $v_{\text{sink}}$  in the centrifugal field is

$$v_{\text{sink}} = \frac{1}{18} \cdot \frac{\Delta\rho \cdot x^2 \cdot C \cdot g}{\eta}, \quad (3.5)$$

and the dimensionless centrifugal acceleration (*C*-value) is defined as

$$C = \frac{r_{r_0} \cdot (2 \cdot \pi \cdot n)^2}{g}. \quad (3.6)$$

### Experiments with pilot-scale DESM device

For direct comparison, the same parameter settings were used for experiments with the pilot-scale DESM device and the lab-scale DESM and ROME device. All experiments were done with mix E, the sinter membrane and a gap width of 0.22 mm. The impact of circumferential velocity, gas volume fraction and residence time on the mean bubble size was investigated, exact parameters are given in Tab. 3.15. The gap sizes of the three devices were not exactly the same due to variations in



raw membrane quality leading to deviations of the membrane diameter (gap sizes: small ROME device 0.230 mm, small DESM device 0.235 mm, large DESM device 0.250 mm).

Table 3.15.: Parameters for experiments with scaled-up device: circumferential velocity  $v_{\text{circ}}$ , residence time  $t_V$  and gas volume fraction  $\phi_V$ . Experiments done with mix E and sinter membrane, gap width: 0.230 mm for lab-scale ROME device, 0.235 mm for lab-scale DESM device and 0.250 mm for pilot-scale DESM device.

$v_{\text{circ}}$ [m · s <sup>-1</sup> ]	$\phi_V$ [-]	$t_V$ [s]
2.961	0.20, 0.43, 0.56	0.75
8.144	0.20, 0.43, 0.56	0.75
13.327	0.20, 0.43, 0.56	0.50, 0.75, 1.00
18.509	0.20, 0.33, 0.43, 0.50, 0.56, ..., $\phi_{V,\text{max}}$	0.50, 0.75, 1.00
23.692	0.20, 0.33, 0.43, 0.55, 0.56, ..., $\phi_{V,\text{max}}$	0.50, 0.75, 1.00

The setup of the large DESM device is depicted in Fig. 3.14.

### Transparent outer cylinder for ROME device and single pore membrane

A single pore membrane was used for these investigations on bubble formation and detachment. It was made of compact brass in which one single pore with a diameter of 100  $\mu\text{m}$  was drilled. To simplify observation, the pore size was chosen much larger than what is common for foaming experiments. The gap size was accordingly increased (4 mm) to avoid wall effects. The gas velocity was chosen in a similar range as used in foaming experiments to get comparable conditions and to determine whether dripping or jetting occurs at such gas velocities. To adapt this, the open area  $A_o$  of the membrane SF03-6/5 was calculated ( $2.25 \cdot 10^{-4} \text{ m}^2$ : 50 windows with an membrane area per window of  $9.0 \cdot 10^{-5} \text{ m}^2$  and open area per membrane area of 5 %). At a typical gas flow rate,  $\dot{V}_{\text{air}}$  of  $151.0 \text{ ml} \cdot \text{min}^{-1}$  (used to obtain gas volume fraction  $\phi_V = 0.56$  at residence time  $t_V = 0.5 \text{ s}$ ), the gas velocity  $v_{\text{air}}$  is  $1.12 \cdot 10^{-2} \text{ m} \cdot \text{s}^{-1}$  ( $v_{\text{air}} = \dot{V}_{\text{air}}/A_o$ ). For the single pore membrane with  $A_o = 7.85 \cdot 10^{-9} \text{ m}^2$ , this corresponds to a gas flow rate of  $5.28 \cdot 10^{-3} \text{ ml} \cdot \text{min}^{-1}$ . First experiments were done with the gas mass flow controller red-y (type GSC-B9HA-BB24) at a gas flow rate of  $30.00 \text{ ml} \cdot \text{min}^{-1}$  (=minimum), further trials were done with a Bronkhorst gas mass flow controller (type: F 201C-FDC-33-V) at a flow rate of  $1.365 \text{ ml} \cdot \text{min}^{-1}$  (=minimum). For the single pore membrane and a gap of 4 mm, only pure water allowed capturing of sharp images and was, thus,

chosen as the continuous phase. The circumferential velocity used for experiments and modelling were chosen identical to those used for foaming experiments as 3.0, 8.1, 13.3 and 18.5  $\text{m} \cdot \text{s}^{-1}$ . It was not possible to generate sharp enough pictures at a circumferential velocity of 23.7  $\text{m} \cdot \text{s}^{-1}$ . The bubble sizes resulting from the use of the single pore membrane were analyzed using the software image J. Scaling was possible via markers on the membrane. Tab. 3.16 lists the parameters of the single-pore system used for experiments, Tab. 3.17 the processing parameters used in the experiments.

Table 3.16.: Parameters used for experiments with single-pore membrane and for model calculations. The continuous phase was water, the disperse phase air, all values are given for a temperature of 18°C.

Surface tension $\sigma$ [ $\text{mN} \cdot \text{m}^{-1}$ ]	72.75
Continuous phase viscosity $\rho_{\text{cont}}$ [ $\text{kg} \cdot \text{m}^{-3}$ ]	998
Disperse phase viscosity $\rho_{\text{disp}}$ [ $\text{kg} \cdot \text{m}^{-3}$ ]	1.20
Rotor radius $R_i$ [m]	0.0245
Gap size $s$ [m]	0.004
Pore size $x_p$ [ $\mu\text{m}$ ]	100

Table 3.17.: Parameters used in experiments performed with ROME device, single pore membrane and transparent outer cylinder. ( $D_i$  rotor diameter,  $D_o$  inner diameter of outer cylinder,  $s$  gap size.)

$D_i$ [m]	$D_o$ [m]	$s$ [m]	Circumferential velocity [ $\text{m} \cdot \text{s}^{-1}$ ]
49.00	57.00	4.00	3.0, 8.1, 13.3, 18.5

### Transparent outer cylinder for ROME device and sinter membrane

Additionally, a sinter membrane with 2  $\mu\text{m}$  mean pore size made of stainless steel was used. The gap size was 1 mm. This membrane was chosen in the transparent set-up because the contrast between bubble and membrane was best and the least light reflections occurred. The aim was to observe bubble detachment from a multi-pore system, to get insight into the foaming process and to investigate bubble break-up and/or coalescence in the gap. For these experiments using the sinter membrane, it was no problem to keep the air velocity identical to foaming experiments using

the red-y gas mass flow controller. For observation of bubble behavior in the gap using the sinter membrane, a solution of 0.6 weight % emulsifier E in water was chosen as the continuous phase. Since bubbles are not at all stabilized in pure water, it could not be used as the continuous phase.

The processing parameters used in experiments are summarized in Tab. 3.18:

Table 3.18.: Parameters used in experiments using the ROME device, sinter membrane and transparent outer cylinder. ( $D_i$  rotor diameter,  $D_o$  inner diameter of outer cylinder,  $s$  gap size.)

$D_i$ [m]	$D_o$ [m]	$s$ [m]	Circumferential velocity [m · s <sup>-1</sup> ]
55.00	57.00	1.00	2.96, 8.14, 13.33

## Power characteristics

To investigate a wide range in Reynolds numbers, Newtonian fluids of different viscosities were used and a wide range in rotational speed tested. Water and differently concentrated solutions of dried glucose syrup in water were used as Newtonian fluids. Their production is described in Sec. 3.3.1. Tab. 3.7 gives an overview of the used fluids. The Newtonian flow behavior of the fluids was checked, its viscosity and density were measured as a function of the temperature (see Sec. 3.3). The flow rate of the fluid was chosen high (5.5 ml · s<sup>-1</sup>) to avoid a heating of the fluid. The experimental set up can be seen in Fig. 3.25. The fluid was poured into a vessel. From there it was pumped through connecting pipes and through the dispersing gap of the dynamically enhanced membrane foaming device. Neither of the concentric cylinders was a membrane, both were made of compact metal and no air was added. The dispersing zone and the seals were not cooled to reduce a deflection of heat energy. The temperature was measured with a thermocouple directly before and after the dispersing zone. The power consumption was measured with a power meter (Yokogawa WT 230, Yokogawa, Japan): one minute after a rotational speed was set, the power was measured for one minute. The minimum and the maximum power were then averaged. All measurements were repeated. The idling drive power was determined the same way, however no fluid was pumped through the gap.

For a rotor diameter of 56.00 mm and a gap width of 0.5 mm, the following parameters were combined systematically:

**Fluid:** tap water / glucose syrup solutions: 12, 30, 40, 58 and 69 weight %

**Rotational speed:** 100, 200, ..., 1 000, 1 500, 2 000, 3 000, ..., 10 000 rpm

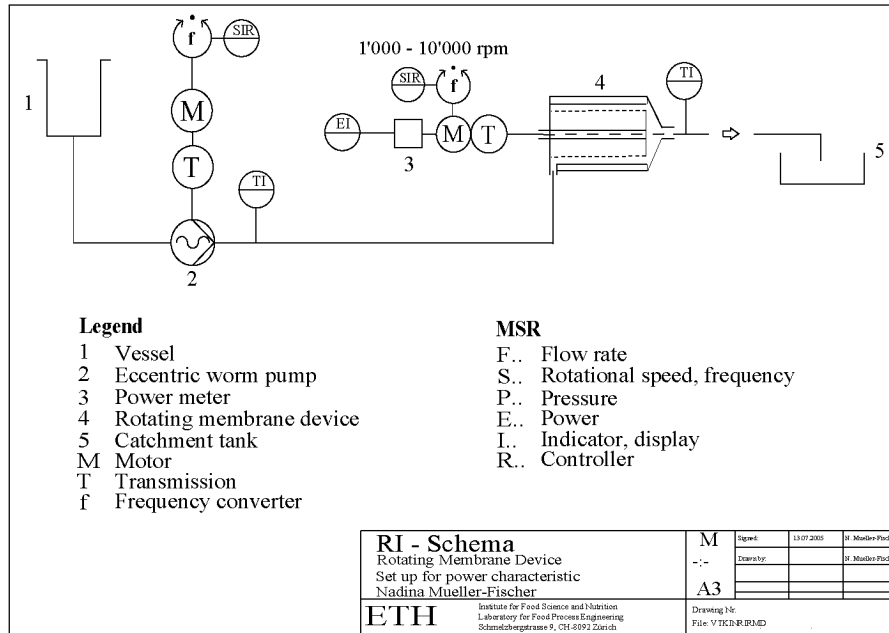


Figure 3.25.: Schematic drawings of the rotating membrane foaming device used to obtain power characteristics.

The Newton- and gap Reynolds number were calculated according to Eq. 2.38 and 2.41 for each rotational speed and fluid. The following values had to be known: rotor diameter ( $D$ ), gap between inner and outer cylinder ( $s$ ), net power input ( $P$ ), rotational speed ( $n$ ), fluid viscosity ( $\eta$ ) and fluid density ( $\rho$ ). Knowing the averaged temperature in the dispersing zone at a certain rotational speed, the actual viscosities and densities could be calculated for each fluid. The net power input was obtained by subtracting the idling drive power from the measured total power consumption. The calculated Newton- and gap Reynolds numbers were plotted in a logarithmic graph. The constants  $C_1$ ,  $C_2$  and the critical Reynolds number  $Re_c$  were determined according to Sec. 2.5.1.

### 3.4. Materials

Several material systems were used within this work ranging from edible model systems for foaming experiments to silicone oils for break-up of single bubbles in simple shear. The relevant material parameters include fluid density  $\rho$ , dynamic fluid viscosity  $\eta$  and surface tension  $\sigma$ . The materials used for single-bubble deformation and break-up are listed in Sec. 3.4.1, the ones used to obtain the power characteristics in Sec. 3.4.2 and the materials used for foaming in Sec. 3.4.3.

### 3.4.1. Materials used for single-bubble deformation and break-up

#### Glucose syrups

Glucose syrup is a liquid starch hydrolysate of mono-, di- and higher saccharides. The degradation of the starch takes either place by acid hydrolysis or enzymatic reactions. The extent of starch degradation is usually given in dextrose equivalents (DE) which is defined as the ratio between cleaved glycosidic bonds and initial number of glycosidic bonds. Pure glucose has a DE of 100 %, pure starch has a DE of about 0 %. The glucose syrup used in this work had a DE between 36 % and 39 %.

All glucose syrups were manufactured by Blattmann Cerestar AG (CH-8820 Wädenswil):

•**C\*Bio-Sweet 11160**: Cleaned and concentrated high-maltose-syrup made of wheat starch via conversion with enzymes.

Sugar-spectrum: dextrose (31.0 % TS), maltose (39.0 % TS), higher molecular fractions (30.0 % TS).

•**BC\*Sweet 01175**: Viscous, transparent syrup made of wheat starch via acidolysis.

Sugar-spectrum: dextrose (14.0-20.0 % TS), maltose (11.5-16.0 % TS), maltotriose (9.5-14.0 % TS), polysaccharides (50.0-65.0 % TS).

•**C\*Bio-Sweet 11144**: Cleaned and concentrated high-maltose-syrup with low dextrose content made of wheat starch via conversion with enzymes.

Sugar-spectrum: dextrose (3.0 % TS), maltose (49.0 % TS), maltotriose (22.0 % TS), higher molecular fractions (26.0 % TS).

Fig. 3.26 shows the Haworth projection formula of the monosaccharide Glucose and the disaccharide Maltose (O- $\alpha$ -D-Glucopyranosyl-(1 $\rightarrow$ 4)- $\beta$ -D-glucopyranose). Maltotriose (O- $\alpha$ -D-Glucopyranosyl-(1 $\rightarrow$ 4)-O- $\alpha$ -D-Glucopyranosyl-(1 $\rightarrow$ 4)-D-Glucopyranose) is not shown but can easily be derived. Tab. 3.19 shows the viscosity, density and surface tension of the used glucose syrups.

#### Silicone fluids

Silicone Fluids are dimethylpolysiloxanes whose unbranched chains are made up of alternate silicon and oxygen atoms, the free valencies of the silicon being saturated by methyl groups. While the carbon chains of organic compounds show little resistance to certain external influences, the stability of inorganic Si-O linkages

### 3. Materials and Methods

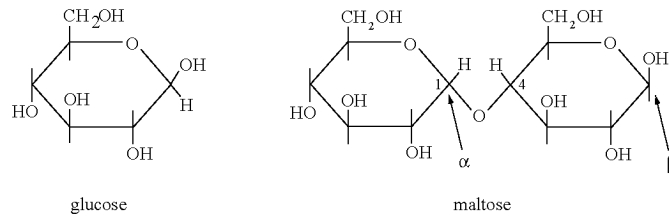


Figure 3.26.: Haworth projection formulas of glucose and maltose.

Table 3.19.: Viscosity, density and surface tension of glucose syrups.

Glucose syrup	Viscosity at 18° C [Pa · s]	Density at 18° C [kg · m <sup>-3</sup> ]	Surface tension at 18° C [mN · m <sup>-1</sup> ]
11160	28.587	1409	80.74
01175	97.282	1412	80.64
11144	141.389	1423	80.69

is, in many ways, like the chemical inertness of silicate mineral. The structure of silicone fluids is shown by the following general formula in Fig. 3.27.

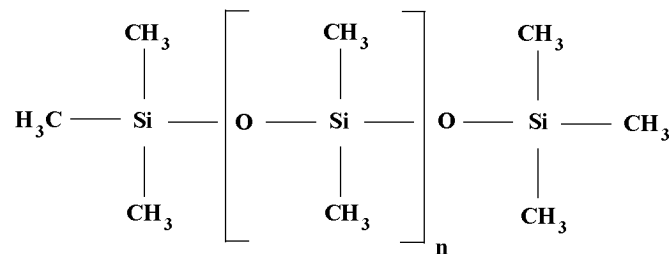


Figure 3.27.: General formula for silicone oil.

All silicone oils were bought from Wacker-Chemie GmbH (D-81737 München):

- Silicone Fluid AK 60 000
- Silicone Fluid AK 100 000
- Silicone Fluid AK 300 000

For the silicone oils, Tab. 3.20 gives the viscosity (as a function of temperature) and the surface tension (surface tension as given by the manufacturer).

Table 3.20.: Viscosity and surface tension of silicone oil (surface tension as given by manufacturer).

Silicone oil	Viscosity $\eta = f(T)$ [Pa · s]	Surface tension at 25 ° C [mN · m <sup>-1</sup> ]
AK 60 000	$\eta = e^{1672.4 \cdot \frac{1}{T[\text{K}]} - 1.538}$	21.5
AK 100 000	$\eta = e^{1641.9 \cdot \frac{1}{T[\text{K}]} - 0.9771}$	21.5
AK 300 000	$\eta = e^{1524.7 \cdot \frac{1}{T[\text{K}]} + 0.5242}$	21.5

### 3.4.2. Materials used to obtain power characteristics

#### Glucose syrup

**Product name:** C\*Dry GL 01934

**Manufacturer:** Blattmann Cerestar AG (CH-8820 Wädenswil)

**Product description by manufacturer:** Dried glucose syrup

In order to get Newtonian fluids of different viscosities, various glucose-water solutions were prepared (see Sec. 3.3.1). Glucose concentration varied between 0 and 69 weight %. The Newtonian behavior was verified in rate sweep tests (not shown), the exact correlation between temperature and viscosity then determined in temperature sweeps (results shown in Fig. 3.28 (left side) and Tab. 3.21) and the density measured with a density meter at different temperatures (results shown in Fig. 3.28 (left side) and Tab. 3.22).

As expected, both viscosity and density were lower at higher temperatures. From the gradient of the curves it can be seen that the temperature dependency of the viscosity was small for water and the 12 weight % glucose syrup solution and became higher with increasing glucose concentration. The values for water were assumed from literature [178]. Analogous to the viscosity, the temperature dependency of the density was stronger at higher glucose syrup concentrations.

### 3.4.3. Materials used for foaming

Air was always used as the disperse phase, while several continuous phases were tested. The two ingredients of mix A to D, AmeHV and Meyprodor™ 400, are further described.

### 3. Materials and Methods

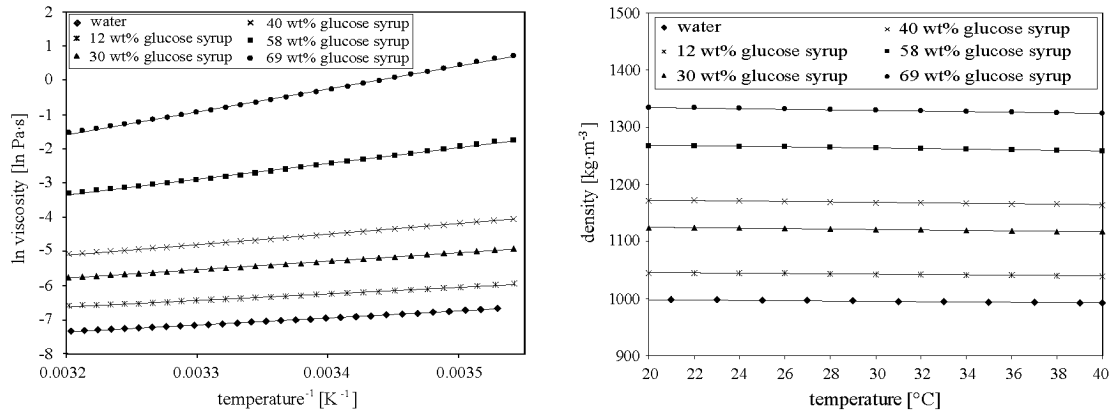


Figure 3.28.: Viscosity and density of water and glucose syrup solutions as a function of the temperature.

Table 3.21.: Viscosity of water and glucose syrup solutions as a function of the temperature.

Liquid	Viscosity $\eta = f(T)$ [Pa · s]
water	$\eta = e^{2036.09 \cdot \frac{1}{T[\text{K}]} - 13.85}$
12 weight % glucose syrup	$\eta = e^{1900.48 \cdot \frac{1}{T[\text{K}]} - 12.68}$
30 weight % glucose syrup	$\eta = e^{2486.22 \cdot \frac{1}{T[\text{K}]} - 13.71}$
40 weight % glucose syrup	$\eta = e^{3052.62 \cdot \frac{1}{T[\text{K}]} - 14.84}$
58 weight % glucose syrup	$\eta = e^{4632.85 \cdot \frac{1}{T[\text{K}]} - 18.13}$
69 weight % glucose syrup	$\eta = e^{6659.92 \cdot \frac{1}{T[\text{K}]} - 22.83}$

Table 3.22.: Density of water and glucose syrup solutions as a function of the temperature.

Liquid	Density $\rho = f(T)$ [kg · m <sup>-3</sup> ]
water	$\rho = -0.00025 \cdot T [^{\circ}\text{C}] + 1.00330$
12 weight % glucose syrup	$\rho = -0.00030 \cdot T [^{\circ}\text{C}] + 1.05196$
30 weight % glucose syrup	$\rho = -0.00038 \cdot T [^{\circ}\text{C}] + 1.13251$
40 weight % glucose syrup	$\rho = -0.00043 \cdot T [^{\circ}\text{C}] + 1.18171$
58 weight % glucose syrup	$\rho = -0.00049 \cdot T [^{\circ}\text{C}] + 1.27882$
69 weight % glucose syrup	$\rho = -0.00053 \cdot T [^{\circ}\text{C}] + 1.34550$



## Total milk protein

**Product name:** AME-HV

**Manufacturer:** Emmi AG (CH-6252 Dagmersellen)

Emmi-Protein AME-HV is a total milk protein (caseins, globulins, albumins) which was solubilized in a special process. It is highly viscous in applications. The protein is produced from fresh skim milk and is carefully spray dried to prevent denaturation.

Milk proteins in soluble and dispersed form are widely valued as food ingredients with excellent surface-active and colloid-stabilizing properties [119]. The two main classes of milk proteins are the caseins (80 %) and the whey proteins (20 %).

## Guar gum

**Product name:** Meyprodor™ 400

**Manufacturer:** Rhodia Food (Meypro, NL-1500 AC Zaandam)

Meyprodor™ 400 is a food and pharmaceutical guar gum, with a neutral taste, a low microbiological count and a well defined medium viscosity.

Guar gum belongs to the family of seed reserve polysaccharides known as galactomannans. It is the ground endosperm of the seeds of *Cyamopsis tetragonoloba*. The chemical structure consists of a long linear chain of  $\beta(1 \rightarrow 4)\text{-D-mannopyranosyl}$  units with single-membered  $\alpha(1 \rightarrow 6)\text{-D-galactopyranosyl}$  units as side branches. The ratio of side branched units to backbone units is 1.55. Guar gum - when sold as commercial food-grade gum - contains small concentrations of proteinaceous material. Its chemical structure is shown in Fig. 3.29. Guar gum is an important thickener and produces the highest viscosity of any natural, commercial gum. Because of its non-ionic nature, the viscosity of guar gum remains unchanged for  $3.5 < \text{pH} < 9.0$ . Guar gum does not produce gels under typical food system conditions. Gelation can however be induced by the addition of sucrose which promotes the interchain binding when highly hydrated.

Fig. 3.30 shows the flow curves of mix A, B, C and D with cross fittings, Tab. 3.23 lists the fitting parameters of the cross model. The viscosities of mix E and foam E are shown in Fig. 4.46 and the density and surface tension of mixes A to E in Tab. 3.24.

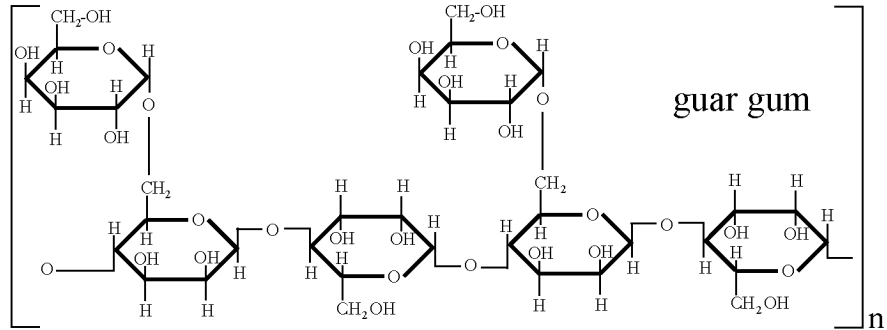


Figure 3.29.: Chemical structure of the basic unit of Guar Gum.

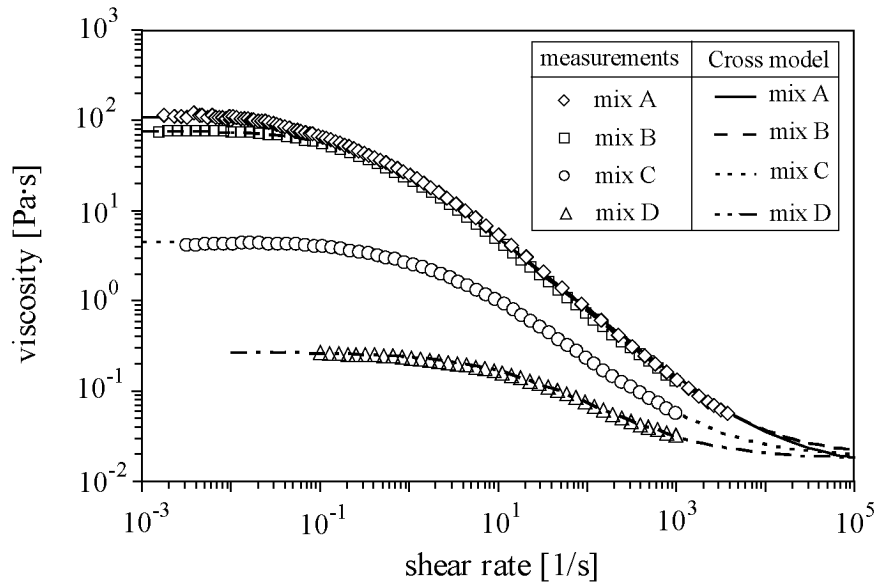


Figure 3.30.: Viscosity of model mixes A, B, C and D: measurements and fitting with cross model. Fitting parameters are listed in Tab. 3.23.

Table 3.23.: Viscosity of mixes A to D as a function of the shear rate fitted with the cross model:  $\eta = \eta_\infty + \frac{\eta_0 - \eta_\infty}{1 + (K \cdot \dot{\gamma})^m}$ .

Model mix	AmeHV/Guar [weight %]	$\eta_0$ [Pa · s]	$\eta_\infty$ [Pa · s]	K [-]	m [-]
A	3.00/1.50	110.00	0.015	4.55	0.80
B	5.00/1.00	77.00	0.020	2.60	0.83
C	5.00/0.50	4.50	0.019	0.57	0.75
D	5.00/0.25	0.27	0.018	0.06	0.70

Table 3.24.: Density and surface tension of mixes A to E.

Model mix	Density [kg · m <sup>-3</sup> ]	Surface tension at 18 ° C [mN · m <sup>-1</sup> ]
A	966 (18 °C)	47.1 (300 s)
B	970 (18 °C)	not measured
C	1024 (18 °C)	49.8 (300 s)
D	1018 (18 °C)	not measured
E	1125 (25 °C)	59.0 (7 s)

### 3. *Materials and Methods*

---

## 4. Results and Discussion

The results were divided into six main parts, of which (i) and (ii) are of fundamental value: single bubble deformation/breakup and static pressure impact on foaming. The knowledge gained in these two sections can be applied to any foaming process. Part (iii) on rotor-stator whipping characterizes the R/S device which serves as the reference foaming process in this work. Results section (iv) focuses on bubble detachment from one single pore of a rotating membrane. The basic knowledge obtained in this section is then applied to the dynamically enhanced membrane foaming in part (v). Last but not least, in section (vi), the two types of dynamically enhanced membrane devices, the rotating membrane ROME and the dynamically enhanced static membrane DESM, are compared to the rotor-stator foaming device characterized in part (iii).

### 4.1. Single bubble deformation and breakup

It is important to gain further knowledge on fundamental mechanisms like bubble formation and breakup to design new foaming processes which allow to tailor-make the structure of the foam product. Deformation and breakup of bubbles was, hence, investigated in simple shear flow. Extrapolation of data by Grace [60] for droplet breakup suggests that the critical Capillary number increases strongly with decreasing viscosity ratio for  $\lambda \leq 1$ . However, only at high viscosities of the continuous fluid phase and correspondingly low viscosity ratios is the velocity of rising bubbles sufficiently low for steady state experiments (see Eq. 2.1), due to the large density difference between gas bubble and continuous fluid phase (see Tab. 4.1). In contrast to experiments with liquid droplets, it is impossible to achieve negligible buoyancy for bubbles. High viscous continuous phases leading to viscosity ratios  $\lambda$  between between  $10^{-6}$  and  $10^{-7}$  were, thus, chosen for all bubble deformation and breakup experiments to slow down the rising velocity of the bubbles. Bubble deformation and breakup are further discussed in sections 4.1.1 and 4.1.2.

Table 4.1.: Rising velocity of bubbles calculated using Stoke’s law (see Eq. 2.1) for  $Re < 0.25$ : exemplary values for glucose syrup of different viscosities at 18 °C as the continuous phase and bubble diameter of 2.0 mm.

Glucose syrup	Viscosity [Pa · s]	Density [kg · m <sup>-3</sup> ]	Rising velocity [mm · s <sup>-1</sup> ]
11160	28.587	1409	0.11
01175	97.282	1412	0.06
11144	141.389	1423	0.02

### 4.1.1. Parallel band apparatus

Fig. 4.1 shows the typical development of bubble deformation in simple shear in the parallel band apparatus. As soon as shearing is started, the spherical bubble undergoes a transient shear deformation. The bubble form changes from spherical via ellipsoidal to sigmoidal with pointed ends. At the same time, the major bubble axis aligns more and more with the flow direction ( $0^\circ < \theta < 45^\circ$ ). Maximum deformation and alignment represent the steady shear state. Upon stopping the shear bands, bubbles relaxed from the sigmoidal shape with pointed ends back to ellipsoids and spheres again. During relaxation, the bubble angle again approaches  $45^\circ$ . The relaxation process is approximately inverse to the deformation process. Different to what is common for droplets [165], no bubble breakup was observed during bubble relaxation.

Steady-state bubble shapes and orientation angles under different deformations in simple shear are shown in Fig. 4.2. The steady state orientation angle approaches  $0^\circ$  for very high deformations while the sigmoidal form and pointed ends get more pronounced.

Data from experiments with 52 bubbles ( $0.86 \text{ mm} \leq x_B \leq 2.75 \text{ mm}$ ) subjected to shear rates between  $3.51$  and  $17.43 \text{ s}^{-1}$  obtained with three glucose syrups (viscosities from  $28.59$  to  $141.34 \text{ Pa} \cdot \text{s}$ ) and resulting in viscosity ratios between  $6.09 \cdot 10^{-7}$  and  $1.23 \cdot 10^{-7}$  was combined to examine relationships between bubble geometry and Capillary number. These results, obtained in the parallel band apparatus, were compared to data from literature and to models. The steady deformations  $D$  of the bubbles as a function of  $Ca$  are plotted in Fig. 4.3. In Fig. 4.4 the part of the results relevant for direct comparison to data from Rust and Manga [144] is shown including modeling data for deformation parameter  $D$  while Fig. 4.5 compares own results to modeling for the deformation parameter  $L/x_B$ .

The deformation parameter  $D$  scales proportionally to  $Ca$  for  $Ca < 1$  (Fig. 4.3) and then asymptotically approaches a value of  $0.89$  for increasing Capillary number. The curve progression in own experiments for bubbles differs from results

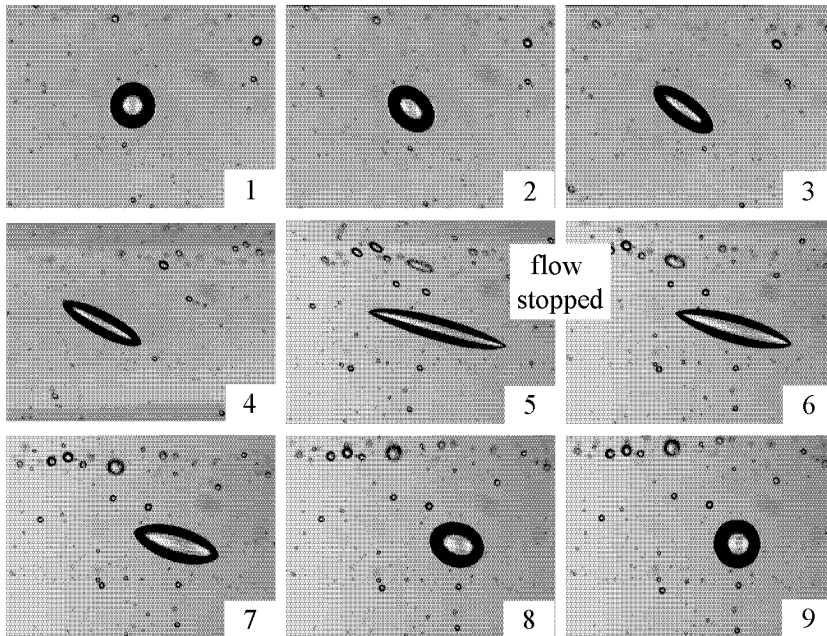


Figure 4.1.: Development of bubble deformation (1-5) and relaxation (5-9) in simple shear flow in the parallel band apparatus.

for droplets found in literature: Experiments by Torza et al. [172] for drops in simple shear flow with  $\lambda \geq 0.8$  or greater showed an increasing slope  $dD/dCa$  with increasing  $Ca$ , representing breakup. An explanation for these differing trends is the significantly lower viscosity ratio in the presented experiments for bubbles. In this case, the Capillary numbers do not get to critical values yet.

Rust and Manga [144] investigated bubble deformation at very low viscosity ratios of  $\lambda = O(10^{-7})$  up to  $Ca=7.1$ . No breakup was achieved. In our experiments a five times higher Capillary number was achieved using the computer-controlled parallel band flow cell. Even at Capillary numbers of 38.9 still no bubble breakup occurred, higher Capillary number could not be achieved. The  $Ca$ -range was limited due to:

- Limitation in upper shear rate: wake and channel formation.
- Limitation in control software: difficulties to keep bubbles in place (observation window) via camera-/computer-controlled adaptation in shear rate for relative band velocities above  $0.17 \text{ m} \cdot \text{s}^{-1}$ .

Results for bubble breakup achieved later in a transparent concentric cylinder device (see Sec. 4.1.2 and Fig. 4.10) indicate that  $Ca_c=38.9$  was just in the

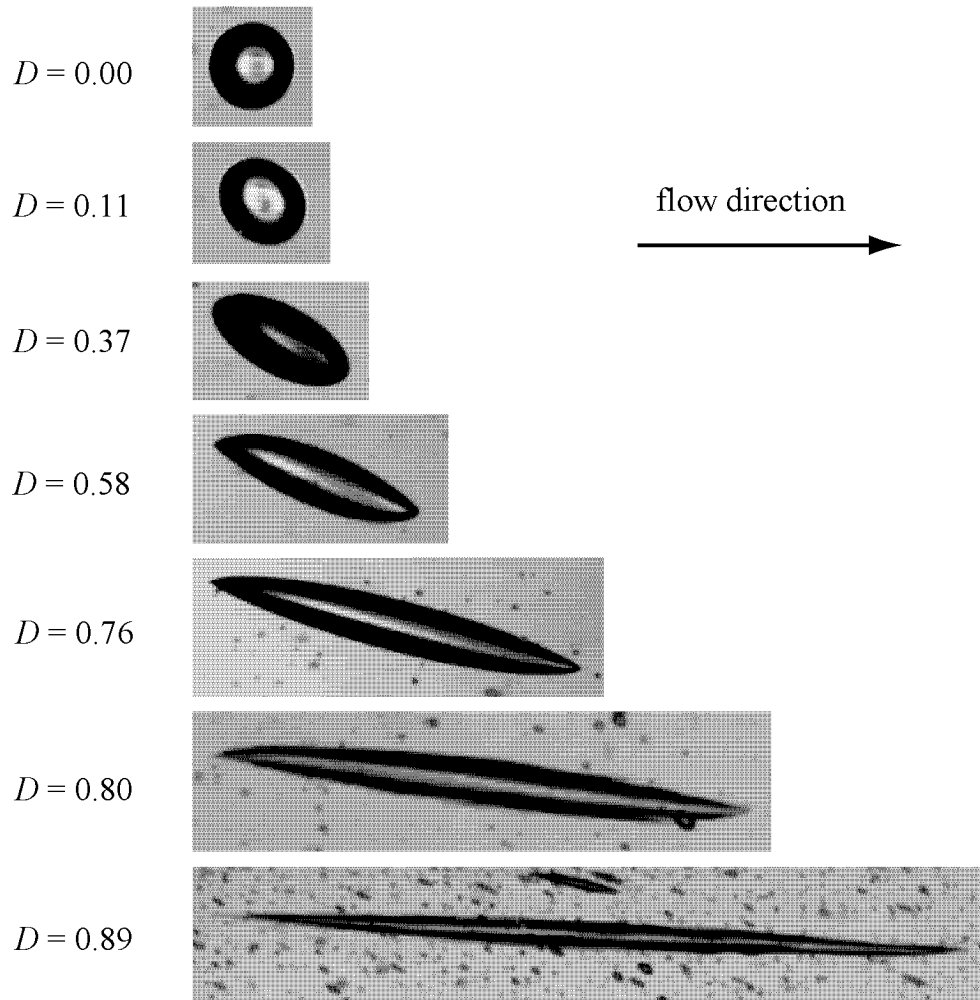


Figure 4.2.: Steady-state bubble shape and orientation at different deformations ( $D = (L - B)/(L + B)$ ) in simple shear. Deformations range from 0.00 (=undeformed bubble) to 0.89.



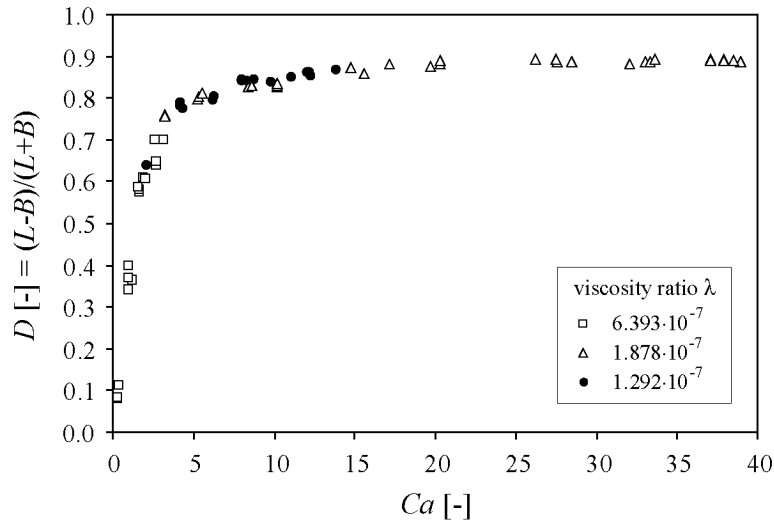


Figure 4.3.: Deformation parameter  $D$  as a function of the Capillary number  $Ca$  for bubbles in simple shear flow obtained with glucose syrup of varying viscosity as the continuous phase leading to different viscosity ratios.

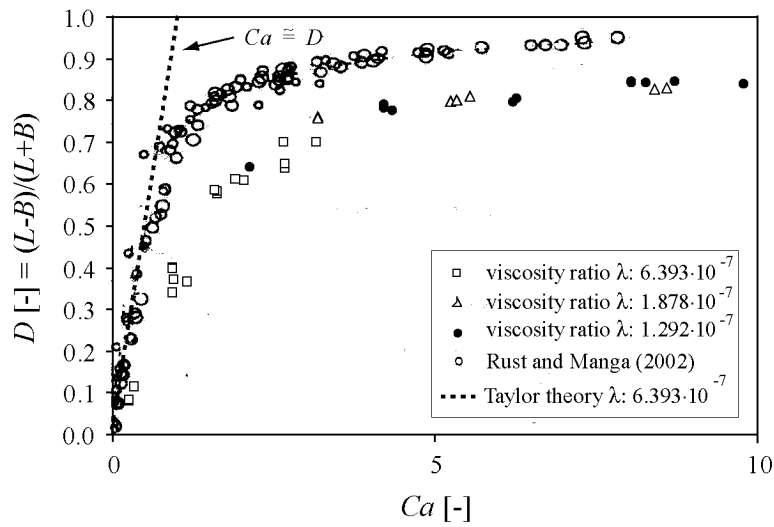


Figure 4.4.: .

[Deformation parameter  $D$  as a function of the Capillary number  $Ca$  for bubbles in simple shear flow. Own experimental results, data from Rust and Manga [144] and fit to Taylor theory (dotted line).

critical domain for breakup. Extrapolation of the data shown in Fig. 4.10 suggests that breakup should have occurred at  $Ca_c=37.8$  for the glucose syrup 11144 in the band apparatus. Naturally, such an extrapolation can only provide an approximate value.

For direct comparison of own experiments to results by Rust and Manga, experiments up to  $Ca = 10$  are plotted in Fig. 4.4. Qualitatively, the  $D=f(Ca)$  functions are alike, but absolute values show clear differences. In contrast to Rust and Manga's findings, the slope of our curve is lower at low Capillary numbers and the curve deviates from Taylor theory ( $Ca \cong D$ ) already for very low  $Ca$  number. In addition, Rust and Manga reached bubble deformations up to values of 0.94 while the highest  $D$ -value in own work was 0.89 even though Capillary number up to 38.9 were reached (see Fig. 4.3) compared to  $Ca=7.1$  in the work of Rust and Manga. However, comparison of own experiments done with several different bubbles at identical Capillary number led to near-identical deformation. Hence, reproducibility is good. The deviation of own results from results by Rust and Manga (Fig. 4.4) and from models must result from some systematic error (see Fig. 4.5). Possible reasons for systematic errors are:

- Wrong determination of viscosity, density, surface tension or temperature.
- Software error resulting in wrong fitting of ellipse to deformed bubble.
- Limitation in image analysis.

Errors 1 and 2 were eliminated by double-checking all results. This leaves explanation three. Fitting of an ellipsoid to highly deformed bubbles might be difficult. The contrast between bubble and continuous phase is not very strong (see bubble at high deformations in Fig. 4.2). At low image resolutions, very thin and pointed ends might not be captured entirely. This leads to an incorrect determination of the major axis and to wrong deformation values.

Fig. 4.5 shows the deformation parameter  $L/x_B$  valid for high deformations as a function of the Capillary number. Own results were compared to theoretical relationships. Both the models by Hinch and Acrivos ([77], Eq. 2.16) and Canedo et al. ([27], Eq. 2.17) clearly overestimate our measured data. However, it is assumed that the resolution of the used CCD camera was limited in capturing the very thin, pointed ends of highly deformed bubbles. This may partially count for the deviations between experimental and model data. On the other hand, the assumption of Hinch and Acrivos that the bubble cross-section is circular is most probably not fulfilled at large bubble deformations. Canedo et al. [27] demonstrated the cross-section to be ellipsoidal. They found similar deviations of model predictions by Hinch and Acrivos from their experiments on bubble deformation in simple shear obtained in a Couette shear gap. In our experiments with the parallel band apparatus, the cross-section was not observed.

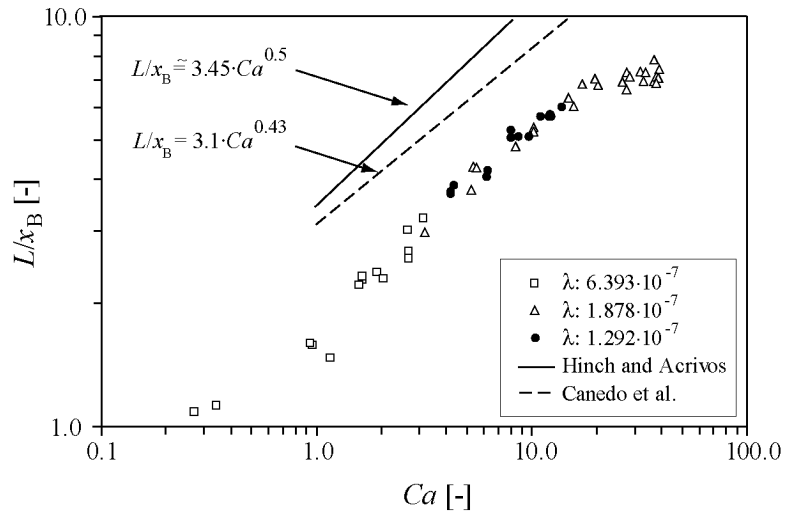


Figure 4.5.: Deformation parameter  $L/x_B$  as a function of the Capillary number  $Ca$  for bubbles in simple shear. Symbols represent measured values, the solid line represents the model prediction by Hinch and Acrivos [77], the dashed line the model for Canedo et al. [27].

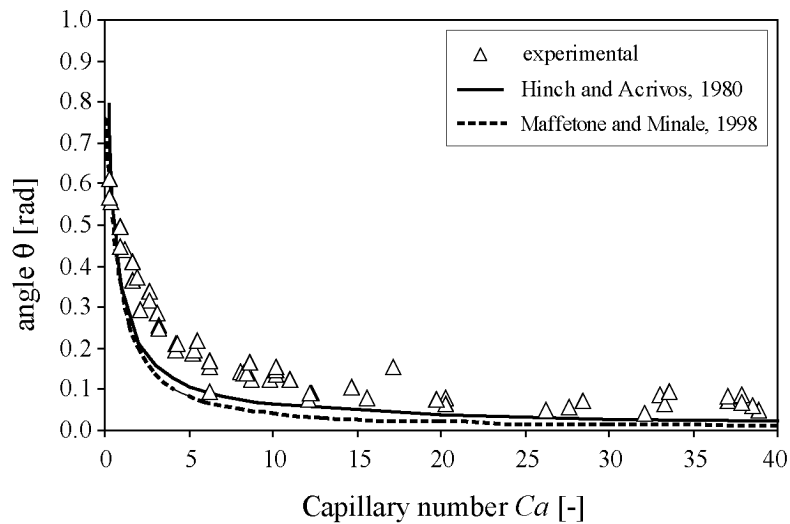


Figure 4.6.: Steady orientation of bubbles in simple shear flow as a function of the Capillary number  $Ca$ . The line is the theoretical relationship by Hinch and Acrivos ([77], Eq. 2.19), the dashed line the model by Maffettone and Minale ([107], Eq. 2.20) the symbols represent our experimentally obtained values.

Fig. 4.6 shows the orientation angle  $\theta$  as a function of the Capillary number  $Ca$ . Own data are again compared to the slender body theory by Hinch and Acrivos ([77], Eq. 2.19) and the phenomenological non-Equilibrium thermodynamics based model of Maffetone and Minale ([107], Eq. 2.20). The trends of the curve progression of experimentally found data and of the two models are again similar. Bubble orientation received from experiments in the parallel band apparatus shows less alignment into flow direction. This tendency was to be expected for the comparison of experimental data to the model by Maffetone and Minale model since it assumes the droplets to be of ellipsoidal, prolate form. Oblate bubbles are excluded by this model.

### 4.1.2. Transparent Enlarged Concentric Cylinder (TECC) device

Simple shear flow can be applied approximately in a narrow gap between coaxially rotating cylinders. The TECC device was built with the aim of achieving bubble breakup. It is a simplified version where only the inner cylinder rotates. This results in the bubbles revolving around the cylinder axis. To determine the critical Capillary numbers for bubble breakup this device was demonstrated to work satisfyingly. To measure bubble deformation, it is advantageous to use counter-rotating cylinders. This enables to locate a circumferential, stationary layer at some radius in the gap where the bubble do not move relative to the observer [60, 27].

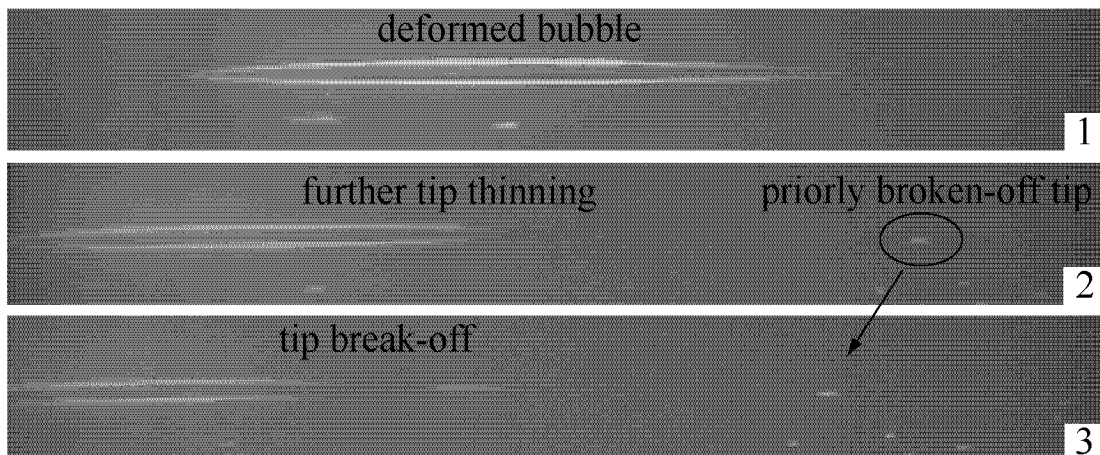


Figure 4.7.: Bubble shapes before and during tip breakup in simple shear obtained in the TECC device. Air bubble in silicone oil AK 100 000, viscosity ratio  $\lambda=1.96 \cdot 10^{-7}$ ,  $Ca_c=33.7$ .

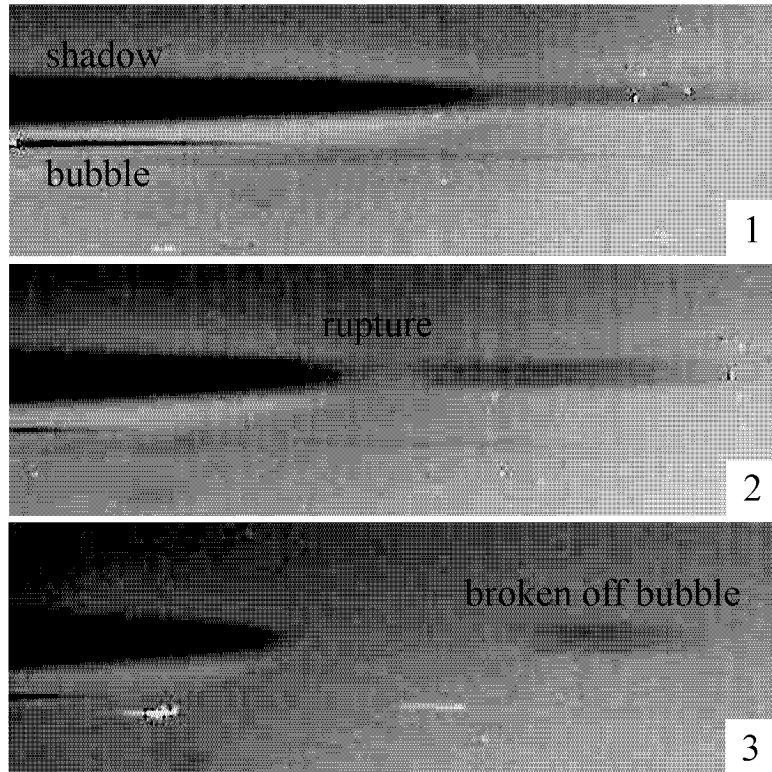


Figure 4.8.: Tip breakup in simple shear obtained in the TECC device. In each picture, the upper object is the shadow of the bubble, the lower one the bubble itself. Breakup can be observed more easily by looking at the shadow due to its 2-D projection nature. Air bubble in silicone oil AK 60 000, viscosity ratio  $\lambda=3.09 \cdot 10^{-7}$ ,  $Ca_c=32.0$ .

It was possible to achieve bubble breakup in the TECC device in three silicone oils of different viscosities. Figs. 4.7 and 4.8 show pictures of the entire bubble and of the bubble tip during breakup in the TECC device, respectively. These pictures are screen shots of a movie captured with a CCD camera. The deformed bubble, depicted in the first picture in Fig. 4.7, is close to ellipsoidally shaped with thin, pointed ends. Its axis nearly aligns with the flow direction. The second picture shows pronounced beginning of tip breakup and points out the limitations in image capturing: it gives the impression of an open bubble tip. This is most probably an "optical illusion" and originates from too low contrast between the very thin, elongated bubble tip and the surrounding fluid. Additionally, an earlier broken-off small bubble can be seen on the right hand side of picture 2. Image 3 shows the actual tip break-off: a small, ellipsoidal bubble has separated from the mother bubble. Since the camera was fixed in place and the bubble revolved around the

cylinder axis, the bubble changes its location from one picture to the next, moving from right to left.

For Fig. 4.8, the tip was particularly focused and the contour of the bubble was sharpened by use of a stroboscope. In each picture, the upper, darker object is the respective shadow. Breakup can more easily be observed by looking at the shadow due to its 2-D projection nature rather than at the bubble itself. The major axis of the deformed bubble orients into the flow direction of the sheared continuous phase (Fig. 4.8 - 1). A thin filament is torn off (Fig. 4.8 - 2) which partially relaxes to an ellipsoid after breakup (Fig. 4.8 - 3).

The observed type of breakup is obviously a tip breakup, not total fracture. Fracture, the other type of breakup, separates a bubble into two or three almost equally sized bubbles with a few tiny satellite drops in between. These two breakup mechanisms were shown to be clearly distinguishable for droplets (e.g. [60, 40]). It was, thus, tried to also achieve fracture of the bubble by further increasing the Capillary number in the TECC device. However, no clear distinction between tip breakup and fracture could be experimentally found for bubbles. Instead a gradual increase in size of the bubbles broken off the tips was found with increasing Capillary number. Hence, it was decided to define bubble breakup as the first separation of a small bubble from the mother bubble at its tips.

De Bruijn [40] closely investigated potential reasons for tip breakup in the case of emulsions, namely the viscosity ratio (i) and the presence of surfactants (ii). He found that tip breakup only occurs for viscosity ratios much smaller than unity and if interfacial tension gradients could develop, resulting in reduced interfacial tension at the tips. Tip breakup did neither occur at extremely low surfactant concentration, nor at high levels where drop coverage by surfactant was guaranteed. In our case, the condition  $\lambda \ll 1$  is fulfilled, but there is no surfactant contained which could cause an interfacial tension gradient. Bubble breakup has not been investigated before, in particular not at such low viscosity ratios. From our findings we conclude that tip breakup occurs preferably for bubbles even if there is no surface tension gradient.

Identical to the findings in the parallel band apparatus, bubble breakup was never observed during bubble relaxation in the TECC device either, neither for subcritical nor critical Capillary numbers. Upon stopping shear flow, bubbles slowly relaxed to their original spherical shapes. Rayleigh instabilities were not observed either.

Figs. 4.9 and 4.10 show the experimentally found relation between viscosity ratio  $\lambda$  and critical Capillary number  $Ca_c$ . Bubble breakup was reached for three different viscosity ratios between  $3.09 \cdot 10^{-7}$  and  $6.67 \cdot 10^{-8}$ , corresponding to critical Capillary numbers between 29.1 and 44.7. The critical  $Ca$ -number was found to be higher at lower viscosity ratios as expected. Comparison of own results with literature data can only be made with publications dealing with droplets since, to the best of our knowledge, no results on bubble breakup have ever been published. Data by Grace [60] in a similar viscosity ratio domain (down to  $10^{-6}$ ) were achieved

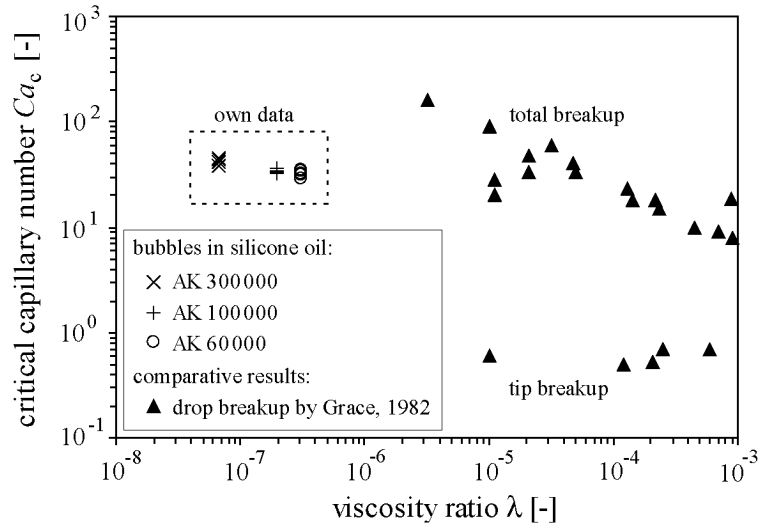


Figure 4.9.: Bubble breakup in simple shear obtained in the TECC device. Own data for bubbles (marked with dashed frame) compared to data from Grace for droplets [60].

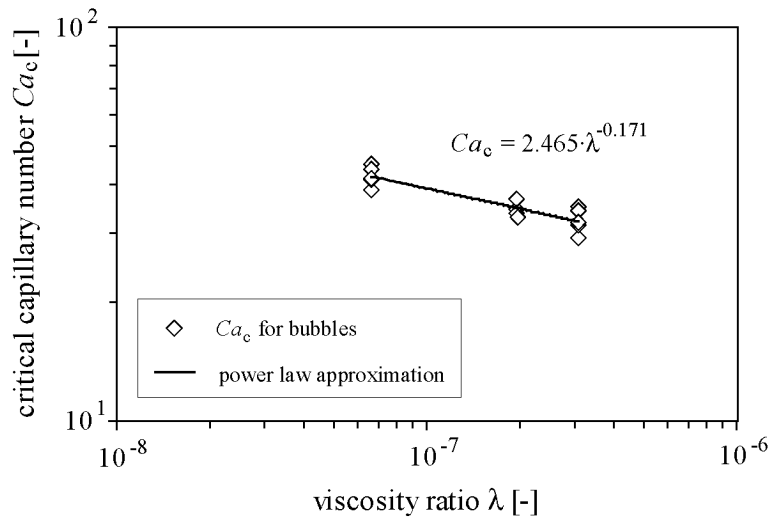


Figure 4.10.: Bubble breakup in simple shear obtained in the TECC device. Own data for bubbles with power law fit for extrapolation.

using low viscous drops in a high viscous surrounding fluid. These data for droplets are depicted in Fig. 4.9, in addition to our bubble data. Grace found two different breakup mechanisms for low viscous droplets: total fracture and tip streaming. No such distinction was found in this work dealing with bubbles. Instead a gradual change from small to larger broken-off bubbles was observed. The critical Capillary numbers found for bubble breakup are lower than an extrapolation of Grace's for droplet fracture would indicate but higher than an extrapolation of Grace's for droplet tip breakup.

It is of further interest to investigate bubble breakup for higher viscosity ratios ( $\lambda = 10^{-6}$  to  $10^{-4}$ ). For now, data in this domain relevant for many real foam systems can only be extrapolated from our data (see Fig. 4.10) as:

$$Ca_c = 2.465 \cdot \lambda^{-0.171} \quad \text{with } \lambda = \frac{\eta_{\text{disp}}}{\eta_{\text{cont}}}. \quad (4.1)$$

This trend is valid in a limited range of viscosity ratio and for single-bubble breakup, only. Inserting  $Ca_c$  according to Eq. 2.22, the equilibrium bubble size can be derived as a function of the disperse and continuous phase viscosity, the surface tension and the shear rate:

$$x_B = 4.930 \cdot \sigma \cdot \dot{\gamma}^{-1} \cdot \eta_{\text{cont}}^{-0.829} \cdot \eta_{\text{disp}}^{-0.171}. \quad (4.2)$$

Vice versa, Eq. 4.2 allows to determine the shear rate needed to obtain a certain bubble size for a given fluid system.

## 4.2. Impact of static pressure on foam microstructure

Compared to dispersion processing in liquid/liquid multiphase systems (emulsions), gas/liquid systems behave very differently. This is due to the large density and viscosity differences between the disperse and continuous phase and due to compressibility of the gas phase. As one expects, gas compression has a strong impact on the gas bubble volume, thus, influencing bubble deformation and breakup also. Generally, a pressure range of 2 to 4 bar absolute is used in industrial foam production to reduce the effective gas volume fraction and, thus, the probability of bubble coalescence. When the foam passes the backpressure valve at the apparatus outlet, the pressure drops to atmospheric conditions and the bubbles expand. This growth in bubble diameter is mostly unfavorable since larger bubbles lead to non-desirable foam properties like reduced stability, increased drainage and Ostwald ripening based disproportionation, and as a result of such structural "coarsening" e.g. to a loss of creaminess [109]. In view of these disadvantageous effects, it was decided to investigate the application of partial vacuum conditions to get an



inverse effect and shrink the bubbles when applying atmospheric pressure at the apparatus outlet. The static pressure was, hence, modified down to partial vacuum conditions of 0.60 bar absolute. This allowed to expand the working pressure range compared to conventional whipping technology and to investigate a "reverse" pressure induced compression behavior and its relevance for applications in foam manufacture. For comparison, foams either whipped at reduced, atmospheric or increased static pressure were analyzed. Since coalescence effects play a major role for these investigations, the mean diameter of the cumulative volume distribution  $x_{50,3}$ , weighing larger bubbles more strongly, was considered in the graphs of this section while the mean diameter of the cumulative number distribution  $x_{50,0}$  was used to analyze all other results.

Contrarily to own work which focuses on the impact of pressure during the whipping process [121, 120], work by Garcia-Moreno et al. [57], Hanselmann [72] and Granger-Guilmin and Barey [61] dealt with the impact of pressure on already formed bubbles and showed that bubble volume changes corresponding to the applied pressure.

### 4.2.1. Ambient pressure

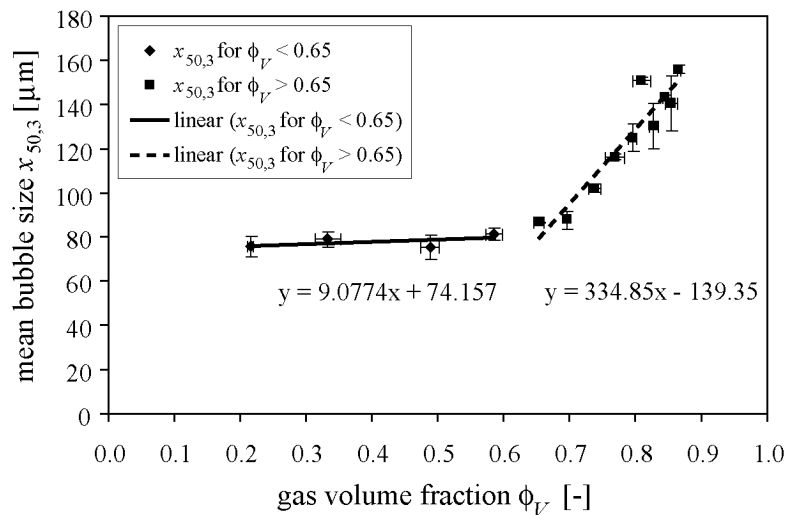


Figure 4.11.: Influence of gas volume fraction on mean bubble size  $x_{50,3}$  for ambient pressure whipped foams. Rotor-stator device, geometry Radax, mix A, residence time 11.0 s (for the entire range of gas volume fractions), circumferential velocity  $8.04 \text{ m} \cdot \text{s}^{-1}$ , resulting shear rate  $8011 \text{ s}^{-1}$ .

In Fig. 4.11 the mean bubble size  $x_{50,3}$  is plotted as a function of the gas volume

fraction for constant residence time (11.0 s). Two different approximately linear curve domains can be distinguished for air volume fractions below or above 0.65. Within the lower air fraction domain, the resulting mean bubble size is about constant with a slight tendency to increase with increasing  $\phi_V$ . For air fractions  $\phi_V \geq 0.65$ , the mean bubble size increases strongly and linearly with increasing air volume fraction. These curve progressions are needed to extract pressure impact from coalescence influences (Sec. 4.2.2). Possible reasons for the different slopes in the curve domains below and above a gas volume fraction of  $\phi_V = 0.65$  will be discussed in Sec. 4.3.2.

### 4.2.2. Whipping at increased pressure or partial vacuum conditions

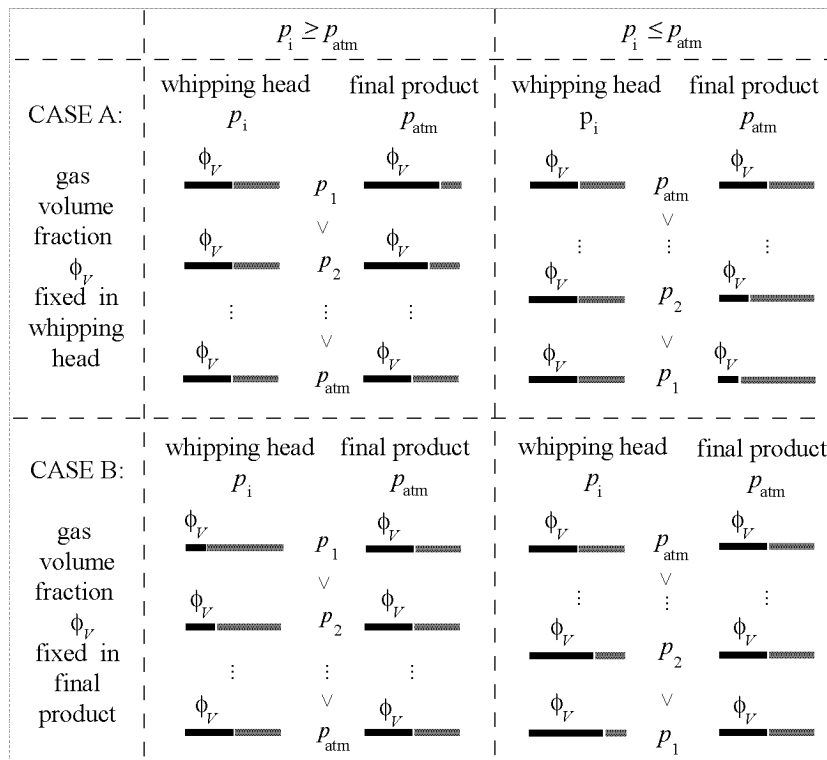


Figure 4.12.: Schematic drawing demonstrating the two cases of pressure impact investigation, namely the pressure impact at fixed gas volume fraction in the whipping head (case A) or in the final product (case B), for whipping pressures above ( $p_i \geq p_{\text{atm}}$ ) and below ( $p_i \leq p_{\text{atm}}$ ) atmospheric conditions.  $\phi_V$  is the gas volume fraction.

Investigations regarding pressure related phenomena need to consider the residence time in the whipping head to eliminate cross-influence. For the results presented here, the mix and air flow rates were adjusted such that the residence time of the two phase system in the whipping head was kept the same at different static pressures. Under these conditions, the impact of static pressure on resulting mean bubble size was extracted [120]. Two cases of pressure impact were investigated separately and are schematically shown in Fig. 4.12. Case A: the air volume fraction was kept constant in the whipping head under different pressures (results shown in Fig. 4.13), and, case B: the gas flow rate was adjusted to generate constant air volume fraction after expansion to atmospheric pressure (results shown in Fig. 4.14). While case A is primarily of scientific interest, case B is of applied importance.

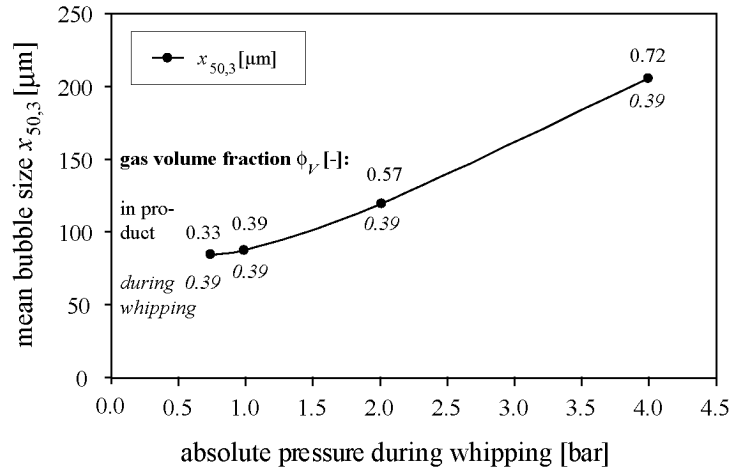


Figure 4.13.: Impact of static pressure applied during whipping on mean bubble sizes in final product at atmospheric pressure.  $\phi_V$  in whipping head 0.39,  $\phi_V$  in final product pressure change dependent. Foams produced in rotor-stator device using Radax geometry, mix A, residence time 22.4 s, circumferential velocity  $8.04 \text{ m} \cdot \text{s}^{-1}$ , corresponding shear rate  $8011 \text{ s}^{-1}$ .

For the function  $x_{50,3} = f(p)$  shown in Fig. 4.13 the air volume fraction in the whipping head was constant at 0.39 under the different pressures applied (case A). As a consequence, the residence time is constant as well (here 22.4 s). As can be seen, the resulting gas volume fraction in the final product is a function of the set pressure. Fig. 4.13 shows clearly that the mean bubble size in the final product is the smaller the lower the pressure in the whipping head. For constant air volume fraction in the dispersing head, an identical maximum bubble size is expected under the pressurized conditions in the whipping head independent of the

acting static pressure since the critical Capillary number is assumed to be pressure independent. Whipping under partial vacuum conditions and subsequent pressure increase to atmospheric conditions led to bubble shrinkage. In contrast, pressure release from higher pressure to atmospheric condition caused bubble expansion. Simultaneously, the gas volume fraction in the aerated product under atmospheric pressure was the higher the higher the pressure acting in the whipping head.

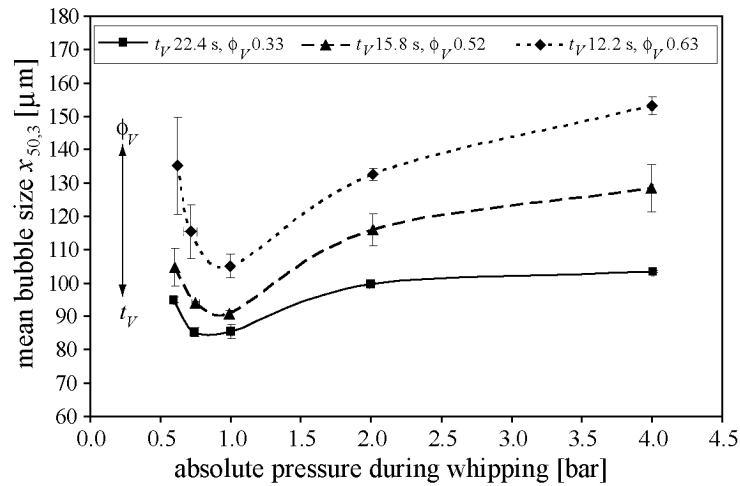


Figure 4.14.: Influence of pressure on mean bubble size for different gas volume fractions. Five corresponding data points connected with line.  $\phi_V$  in final product and  $t_V$  in the whipping head kept constant,  $\phi_V$  in whipping head depending on static pressure during foaming. Foams produced with rotor-stator device, Radax geometry, circumferential velocity  $8.04\text{ m}\cdot\text{s}^{-1}$ , mix A.

Fig. 4.14 represents case B for which the gas flow rate was adjusted to generate foams of constant gas volume fraction after aeration/under atmospheric conditions. This means that different gas volume fractions in the whipping head had to be set according to respectively different set static pressures. Fig. 4.14 clearly shows that foaming at atmospheric pressure led to the smallest mean bubble size.

At pressures below atmospheric pressure acting in the whipping head the air volume fraction in the head is increased compared to the air fraction in the final product at atmospheric conditions. According to Eq. 2.32 the possibility of coalescence is increased for higher gas volume fractions. In addition, worse dispersing results at higher gas volume fractions can be explained with respect to Eqs. 2.50 and 2.51: lower density leads to lower Reynolds stress in the turbulent flow field resulting in larger resulting gas bubbles. It is evident from Fig. 4.14 that the advantage of getting smaller bubbles due to shrinkage after whipping under partial

vacuum conditions (see Fig. 4.13) is more than compensated by the negative effect of increased bubble coalescence at increased gas volume fraction (Fig. 4.11) in the whipping head during the "vacuum whipping" process.

Foams whipped at pressures above atmospheric pressure also led to larger bubble sizes than foams whipped at atmospheric pressure. According to the ideal gas law, the gas volume fraction in the whipping head is smaller at increased static pressure. The results presented in Fig. 4.11 showed that smaller gas volume fractions lead to smaller mean bubble sizes. This effect was attributed to a decrease in coalescence probability and/or a better dispersing effect at lower gas volume fractions. Obviously, the positive influence of lower air volume fraction at increased static pressure is smaller than the negative effect of bubble growth caused by foam lamella elongation and breakage during aeration to atmospheric pressure. These trends, exemplary shown for gas volume fractions of 0.33, 0.52 and 0.63 in Fig. 4.14, were also confirmed for gas volume fractions of 0.44, 0.58 and 0.67.

## 4.3. Rotor-stator whipping

The rotor-stator device was characterized in detail for later comparison to the new dynamically enhanced membrane foaming process. Processing parameters and product quality were mainly analyzed with respect to foam microstructure since the aim of this work was the design of a new foaming process with which smaller bubble sizes and narrower size distributions can be achieved. The process parameters gas volume fraction, circumferential velocity, volumetric energy input, mix recipe, rotor-stator geometry and number of rotor-stator pairs were investigated in detail.

### 4.3.1. Power characteristics

Power characteristics describe the flow field ( $Re$ -number) in the gap between rotors and stators of e.g. a whipping device as a function of the dimensionless specific power input ( $Ne$ -number). In Fig. 4.15, the power characteristics of the rotor-stator whipping device for 2, 4, 6 and 8 rotor-stator pairs of the Radax geometry (see Fig. 3.5) is depicted. The power characteristics were obtained using several Newtonian fluids of different viscosities to allow measuring in a wider range of Reynolds numbers [3]. As expected, a higher number of rotor-stator pairs means a higher power input into the product which should result in smaller bubbles (see Sec. 4.3.2). A distinction of different flow domains can be seen from Fig. 4.15. Based on Eqs. 2.42 and 2.43, a laminar and turbulent region can be defined from the Newton/Reynolds dependencies. For eight rotor-stator pairs, the constants  $C_1$  and  $C_2$  and the critical Reynolds number  $Re_c$  were determined from Fig. 4.15. For the laminar flow field,  $C_1$  was estimated as 204.23, for the turbulent flow field  $C_2$

as 4.76. A critical Reynolds number of about 42.91 was derived which describes the approximated threshold between laminar and turbulent flow domain.

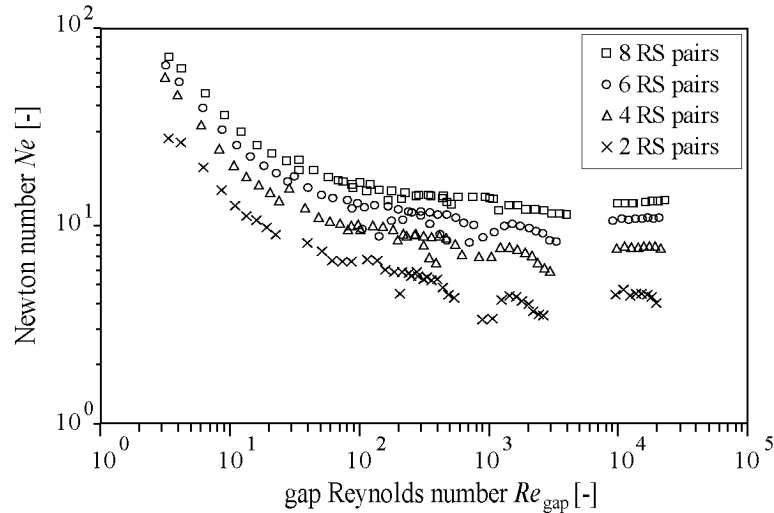


Figure 4.15.: Power characteristics for Kinematica rotor-stator device with 2, 4, 6, and 8 rotor-stator pairs of the Radax geometry [3]. Gap Reynolds number computed including  $\pi$ .

Exemplary dispersing conditions, calculated from the measured net dispersing power at known device dimensions and parameters (3011 rpm, rotor diameter  $5.1 \cdot 10^{-2}$  m, mix A,  $\phi_V$  0.56, net power consumption 223 W) showed that whipping using the rotor-stator device with 8 Radax rotor-stator pairs takes place in the turbulent flow domain. The resulting gap Reynolds number is  $\geq 1000$ , there is some imponderability due to the flat curve progression in the relevant domain, thus a  $Re$ -number range is given.

### 4.3.2. Process parameter impact

In the following, the impact of different process parameters on the mean bubble size will be discussed, namely the gas volume fraction in the dispersing flow field, the circumferential velocity and corresponding shear rate, the volumetric energy input, the gap geometry characteristics and the number of rotor-stator pairs.

#### Gas volume fraction

In Fig. 4.16 the mean bubble size  $x_{50,0}$  is plotted as a function of the gas volume fraction for a constant residence time of 11.0 s and a circumferential velocity of

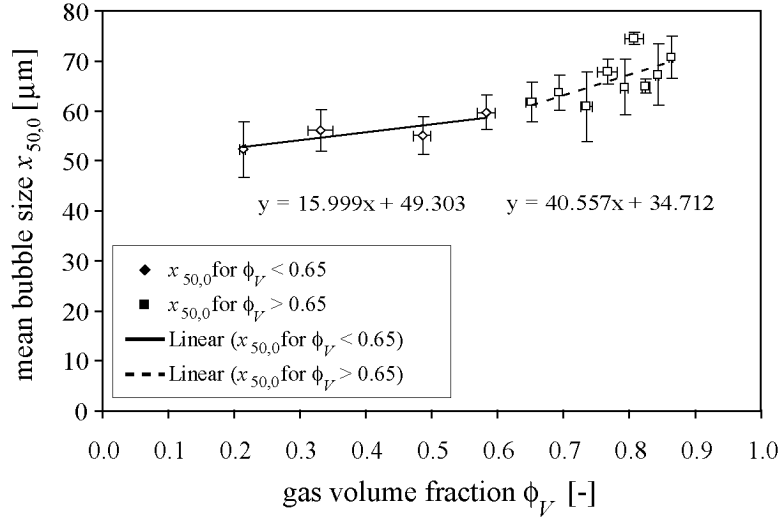


Figure 4.16.: Influence of gas volume fraction on mean bubble size  $x_{50,0}$  for ambient pressure whipped foams. The rotor-stator device with geometry Radax was used, circumferential velocity  $8.04 \text{ m} \cdot \text{s}^{-1}$ , resulting shear rate  $8011 \text{ s}^{-1}$ , residence time  $11.0 \text{ s}$ .

$8.04 \text{ m} \cdot \text{s}^{-1}$ . As in Fig. 4.11, showing the same dependency for  $x_{50,3}$ , two different approximately linear curve domains can be distinguished for air volume fractions below or above 0.65. Within both gas fraction domains, the resulting mean bubble size increases linearly with increasing gas volume fraction (slope 16 in the lower  $\phi_V$ -domain, slope 41 in the higher  $\phi_V$ -domain). The difference between the two domains in gas volume fraction are more distinct for the mean diameter of the cumulative volume distribution  $x_{50,3}$  which weights large bubbles more strongly (see Fig. 4.11). Four possible explanations for the different slopes in the two curve domains for gas volume fractions below and above  $\phi_V = 0.65$  are: i. The density influences the Reynolds shear stress in the turbulent flow region according to Eq. 2.50 and 2.51. Thus, resulting bubble sizes are larger at higher gas volume fractions. ii. The residence time of  $11.0 \text{ s}$  is only sufficient to properly disperse gas up to  $\phi_V = 0.65$  under the fixed circumferential velocity conditions. This can be proved by repeating similar experiments at different residence times. iii. The foam stability decreases continuously for  $\phi_V \geq 0.65$  meaning that coalescence may progress within the time needed for sampling and foam analysis. This can also be checked by analyzing foams of different gas volume fractions directly after production and at some time steps after production. iv. Increase of coalescence in the whipping head due to increased collision frequency of bubbles (see Eq. 2.32 according to (10)).

## Circumferential velocity

Whipping experiments at rotational velocities of 1978, 3011 and 4048 rpm, corresponding to circumferential velocities of 5.28, 8.04 and 10.81  $\text{m} \cdot \text{s}^{-1}$  and to shear rates of 5282, 8040 and 10810  $\text{s}^{-1}$ , were conducted using the Radax geometry and mix A. The energy dissipation increases approximately with the second order of the shear rate, thus, leading to increased foam outlet temperatures. To avoid this, the feeding temperature was adapted to generate foam outlet temperatures of  $18 \pm 2$  °C for all experiments. In addition to  $x_{50,0}$ ,  $x_{50,3}$  is shown in Fig. 4.17 since only the results of the cumulative volume distribution show differences. At low gas volume fractions, higher circumferential velocities lead to smaller mean bubble sizes of the cumulative volume distribution while this tendency is only slight for the cumulative number distribution. With increasing gas volume fraction, the effect is even more diminished. Possible explanations are: i. On the one hand, the faster rotation improves the dispersing efficiency. On the other hand, higher circumferential velocities cause a more frequent contact of bubbles with one another (see e.g. Eq. 2.32 according to [10]). Thus the coalescence rate is more rapidly enhanced with increasing gas volume fractions for 10.81 m/s than for 5.28 or 8.04  $\text{m} \cdot \text{s}^{-1}$ . These two effects counteract and probably compensate at higher gas volume fractions. ii. Even though the foam temperature at the device outlet was  $18 \pm 2$  °C for all experiments, the temperature might be increased locally in some places at circumferential velocities of 10.81  $\text{m} \cdot \text{s}^{-1}$  compared to 8.04  $\text{m} \cdot \text{s}^{-1}$ . iii. The equilibrium between dispersion and coalescence is shifted towards coalescence in the whipping head at increased circumferential speed due to limitation of interfacial structure formation time.

The results also showed that for the higher viscous mix A, a circumferential velocity of 8.04  $\text{m} \cdot \text{s}^{-1}$  is advantageous since heating up was difficult to control at higher circumferential speeds.

## Volumetric energy input

For given geometrical mixer dimensions and given recipe, the volumetric energy input can be influenced by changing the residence time in the shear effective zone via a modification in fluid flow rate and/or gas volume fraction or by changing the acting shear stresses via the rotational speed. The volumetric power  $P_V$  and energy input  $E_V$  directly influence the resulting bubble size and, thus, the structure and related foam properties. Bubble sizes are expected to decrease with increasing stresses [72]. The probability of bubble break-up also increases with increasing residence time in the shear effective zone, especially in the turbulent flow field. With increasing residence time and/or acting stresses, the volumetric energy input increases as well. In Figs. 4.18 and 4.19, the influence of the net volumetric energy input, residence time and gas volume fraction on the resulting mean bubble



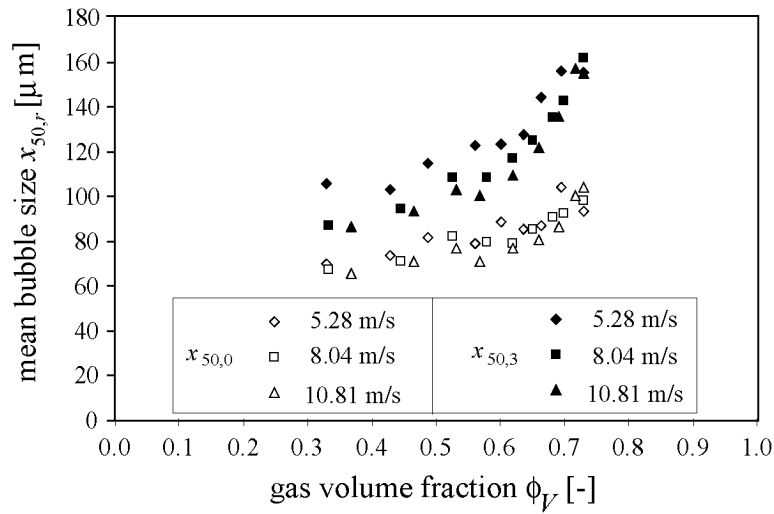


Figure 4.17.: Mean bubble diameters  $x_{50,0}$  and  $x_{50,3}$  as function of circumferential velocity and gas volume fraction. Rotor-stator device, Radax geometry, mix A.

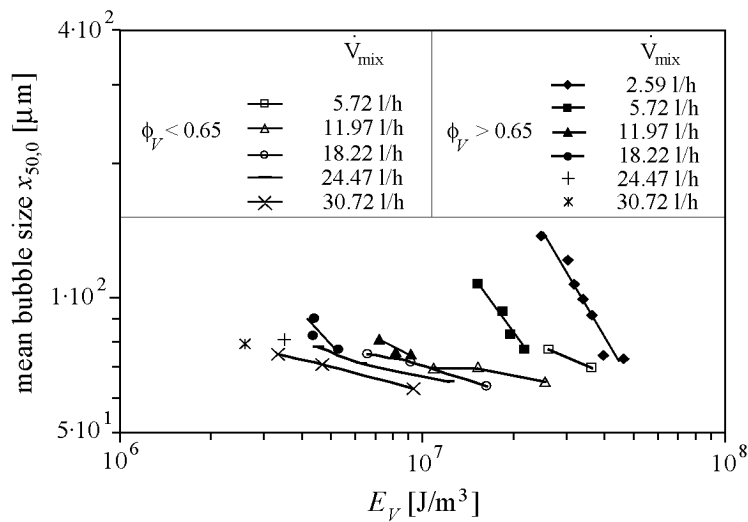


Figure 4.18.: Mean bubble size  $x_{50,0}$  as a function of the volumetric energy input  $E_V$ , residence time (throughput) and gas volume fraction  $\phi_V$  (lines to guide the eye) at a circumferential velocity of  $8.04 \text{ m} \cdot \text{s}^{-1}$ .

size is demonstrated [120] for a constant circumferential velocity of  $8.04 \text{ m} \cdot \text{s}^{-1}$ . The residence time was varied by a factor of  $\sim 12$  by selecting different mix flow rates and adapting the gas flow rate in order to achieve comparable gas volume fractions. Tab. 4.2 shows the comparison of the impact of decreased fluid flow rate on residence time and volumetric energy input. The fact that the coefficients are approximately the same indicates that the increase in volumetric energy input is a direct consequence of the increased residence time.

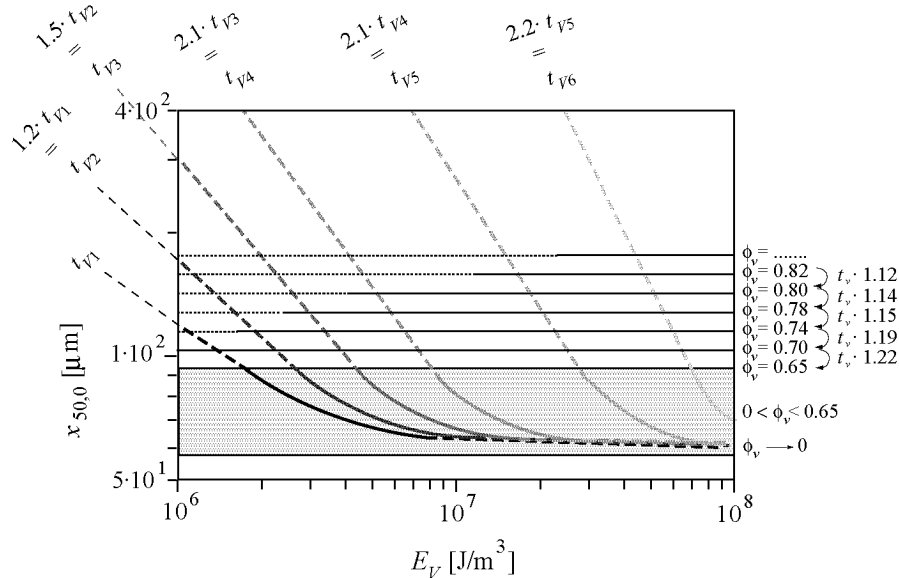


Figure 4.19.: Schematic graph showing the influence of volumetric energy input  $E_V$ , residence time  $t_V$  and gas volume fraction  $\phi_v$  on mean bubble size  $x_{50,0}$ . Data shown in Fig. 4.18 were extrapolated and lines representing equal  $t_V$  and  $\phi_V$  were drawn.

By changing the gas volume fraction, the residence time was also affected, however much less ( $\sim 2$ ). The exact numerical values are listed in Fig. 4.19. To obtain the graph shown in Fig. 4.19, the data points and curves from Fig. 4.18 were schematized and extrapolated. Lines were drawn representing identical gas volume fractions and comparable residence times.

Figs. 4.18 and 4.19 show that when comparing high to low throughput rates and, thus, low to high residence times in the whipping head, the bubble size does not decrease for a specific gas volume fraction even though the volumetric energy input is increased. With increase in gas volume fraction, two different patterns are seen: i. Beyond a gas volume fraction of 0.65, the mean bubble size increases according to a power law equation. ii. for  $0.65 > \phi_V \geq 0$  the mean bubble diameter approaches a minimum value of about 60 micrometers. This means that the main

Table 4.2.: Comparison of effect of decreased fluid flow rate on residence time  $t_V$  (calculated values) and volumetric energy input  $E_V$  (measured values).

Decrease of pump flow rate from ...[l · h <sup>-1</sup> ] to ... [l · h <sup>-1</sup> ]	Calc. coefficient of change in $t_V$ [-]	Meas. coefficient of change in $E_V$ [-]
30.72 to 24.47	1.2	1.4
24.47 to 18.22	1.5	1.5
18.22 to 11.97	2.1	1.7
11.97 to 5.72	2.1	2.4
5.72 to 2.59	2.2	2.1

factor influencing the resulting bubble size at constant acting stresses is the gas volume fraction in the whipping head. The impact of the gas volume fraction on the resulting foam microstructure was discussed in detail in Sec. 4.3.2 for a constant residence time of 11.0 seconds. It can also be seen from Figs. 4.18 and 4.19 that the slope of the different power law curves ( $\phi_V > 0.65$ ) differ from one another. Obviously the residence time has some influence on the impact of increasing gas volume fraction on mean bubble size. Fig. 4.20 shows exemplarily for a constant mix flow rate of  $24.47 \text{ l} \cdot \text{h}^{-1}$  that an increase of the acting flow stresses achieved via a higher rotational speed, leads to a remarkable increase in energy input but only a slight decrease in mean or minimum bubble size. This trend was the same for all tested fluid flow rates ( $18.22 \text{ l} \cdot \text{h}^{-1}$ ,  $24.47 \text{ l} \cdot \text{h}^{-1}$  and  $30.72 \text{ l} \cdot \text{h}^{-1}$ ). Possible reasons for the very small decrease in bubble size with increasing rotational speed have been discussed in Sec. 4.3.2.

## Mix

Three mix recipes were compared for rotor-stator whipping, two containing the same ingredients in different quantities and mixing ratios to vary the viscosity (mix A containing 3.0 % AmeHV and 1.5 % Guar; mix C containing 5.0 % AmeHV and 0.5 % Guar), one containing different ingredients (mix E containing 0.6 % of a fast emulsifier). The results are shown in Fig. 4.21 where the mean bubble size is depicted as a function of the gas volume fraction for the three different continuous phases. Differing to the data representation in Fig. 4.16, no distinction between the slopes in a lower and upper gas volume fraction range was made here for mix A since it is not visible in this compacted graph.

The mean bubble sizes increase linearly with increasing gas volume fraction for all three mixes. However, the slope is four- to three-fold steeper for mix A and C (slope 27 and 22, respectively) than for mix E (slope 7). Mix E also led to much smaller mean bubble sizes than mix A and C (one fourth to one fifth). The slopes

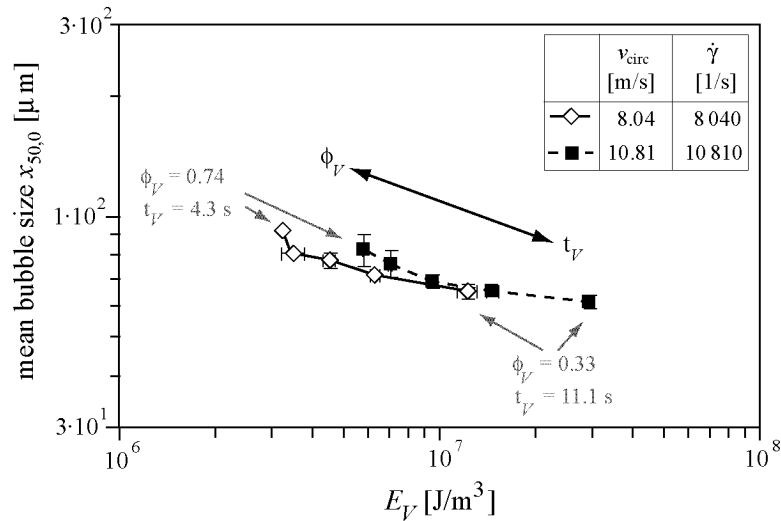


Figure 4.20.: Influence of circumferential velocity/shear stresses on energy density and bubble size for gas volume fractions 0.33, 0.52, 0.63, 0.70 and 0.74 (from right to left) and corresponding residence times from 11.1 s, 7.9 s, 6.1 s, 5.0 s, 4.3 s (again from right to left). Rotor-stator device, Radax geometry, mix A, mix flow rate  $24.47 \text{ l} \cdot \text{h}^{-1}$ .

and absolute mean bubble sizes may be an indicator for the efficiency of interfacial coverage and stabilization. Clearly, mix E is the most favorable of the three mixes if small bubble sizes are desired. Mix C results in smaller mean bubble sizes than mix A. This is most probably a consequence of the higher protein content leading to more efficient interfacial stabilization. The lower viscosity of mix C can not be the reason since viscosity has no impact on dispersion efficiency under turbulent flow conditions.

However both, mix A and C allow to reach much higher gas volume fractions ( $\sim 0.9$ ) than mix E ( $\sim 0.7$ ). It is possible that the lower emulsifier content of mix E (0.6 weight %) compared to 3 and 5 weight % of protein in mix A and C, respectively, is only able to sufficiently cover bubble interfaces up to gas volume fractions of 0.7. Since the smaller bubble sizes of foam E lead to a strongly increased surface/volume ratio, the interfacial properties of mix E can however be judged to be even more efficient compared to the protein system used in mix A and C.

Rheological analysis of foam A and E showed that foam A is partly destroyed in gentle oscillatory tests at a deformation which is in the linear viscoelastic regime (0.54 %), while foam E is not changed under much less gentle flow curve measurement conditions up to shear rates of  $1000 \text{ s}^{-1}$  (see Figs. 4.22 and 4.45). This was confirmed by measuring the same foam samples twice. It is suspected that part of the bubbles of foam A ruptured during the measurement leading to lower

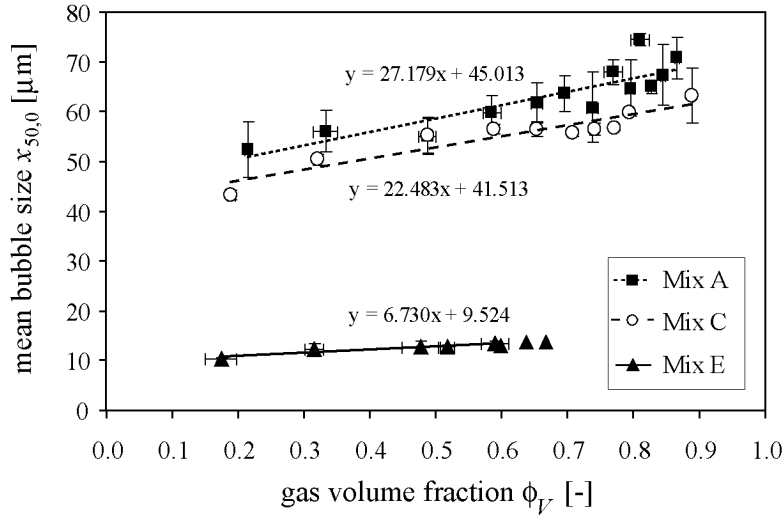


Figure 4.21.: Mean bubble size as function of gas volume fraction for different continuous fluid phases. Mix A (3.0 % AmeHV and 1.5 % Guar), mix C (5.0 % AmeHV and 0.5 % Guar), mix E (0.6 % of a fast emulsifier and stabilizers). Rotor-stator device, Radax geometry, mix A and C:  $t_V$  11.0 s,  $v_{\text{circ}}$  8.04 m · s<sup>-1</sup>, mix E:  $t_V$  14.0 s,  $v_{\text{circ}}$  10.81 m · s<sup>-1</sup>.

viscosities in a second trial with the already once sheared foam. This fact could be observed by eye (less and bigger bubbles after measurement) but could unfortunately not be measured via a gas volume fraction determination since the foam was totally destroyed as soon as the cone was moved apart from the plate and since the amount of foam was anyway too small for such a measurement.

Fig. 4.23 shows frequency sweeps of mix A and foam A in a wide range in gas volume fraction between 0.33 and 0.85. Foam A was produced on the rotor-stator device at a circumferential velocity of 8.04 m · s<sup>-1</sup> and a residence time of 11.0 s. The storage  $G'$  and loss moduli  $G''$  and the complex viscosity  $\eta^*$  are shown as a function of the frequency. The absolute values can only partly be trusted since it was shown (see Fig. 4.22) that foams obtained with model system A are partly destroyed in such rheological investigations as described before. The trend in viscosity change is however trustworthy (see Fig. 4.23). It shows a distinct increase in  $G'$ ,  $G''$  and complex viscosity with increasing gas volume fraction.

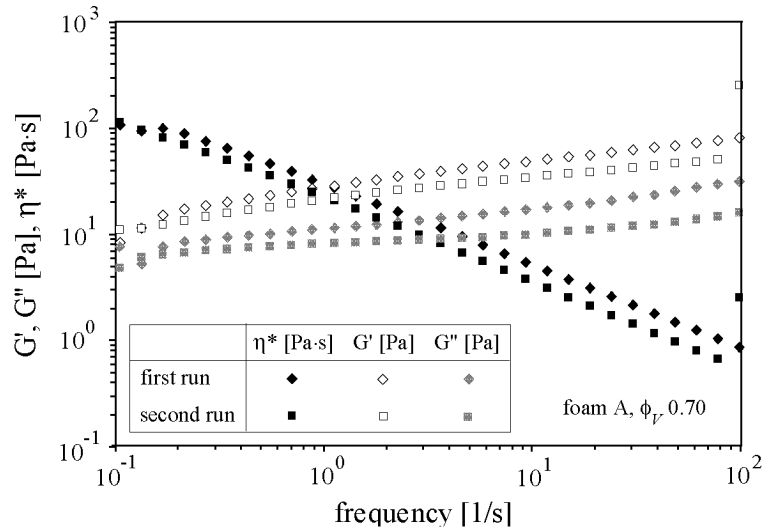


Figure 4.22.: Storage modulus  $G'$ , loss modulus  $G''$  and complex viscosity  $\eta^*$  of foam A ( $\phi_V = 0.70$ ) in first and second trial as function of the frequency at deformation  $\gamma$  of 0.54 % (deformation corresponding to the linear viscoelastic regime) at 18 °C.

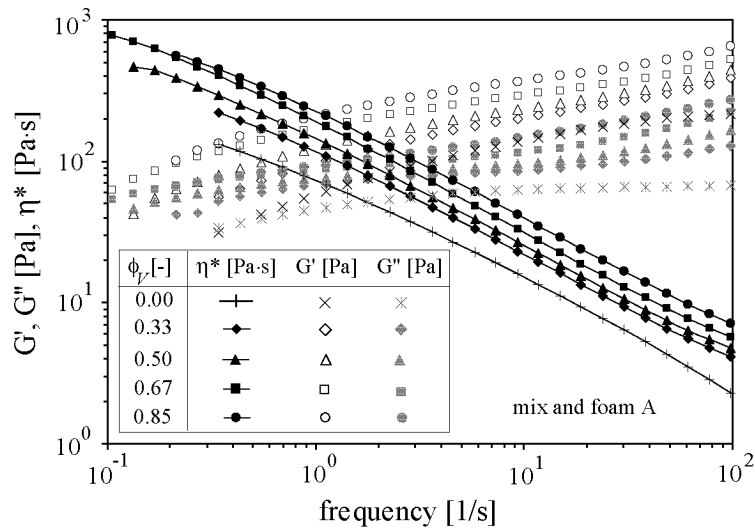


Figure 4.23.: Storage modulus  $G'$ , loss modulus  $G''$  and complex viscosity  $\eta^*$  as function of frequency of mix and foam A for a gas volume fractions between 0.33 and 0.85. The deformation  $\gamma$  of 0.54 % corresponds to the linear viscoelastic regime determined in dynamic strain test.

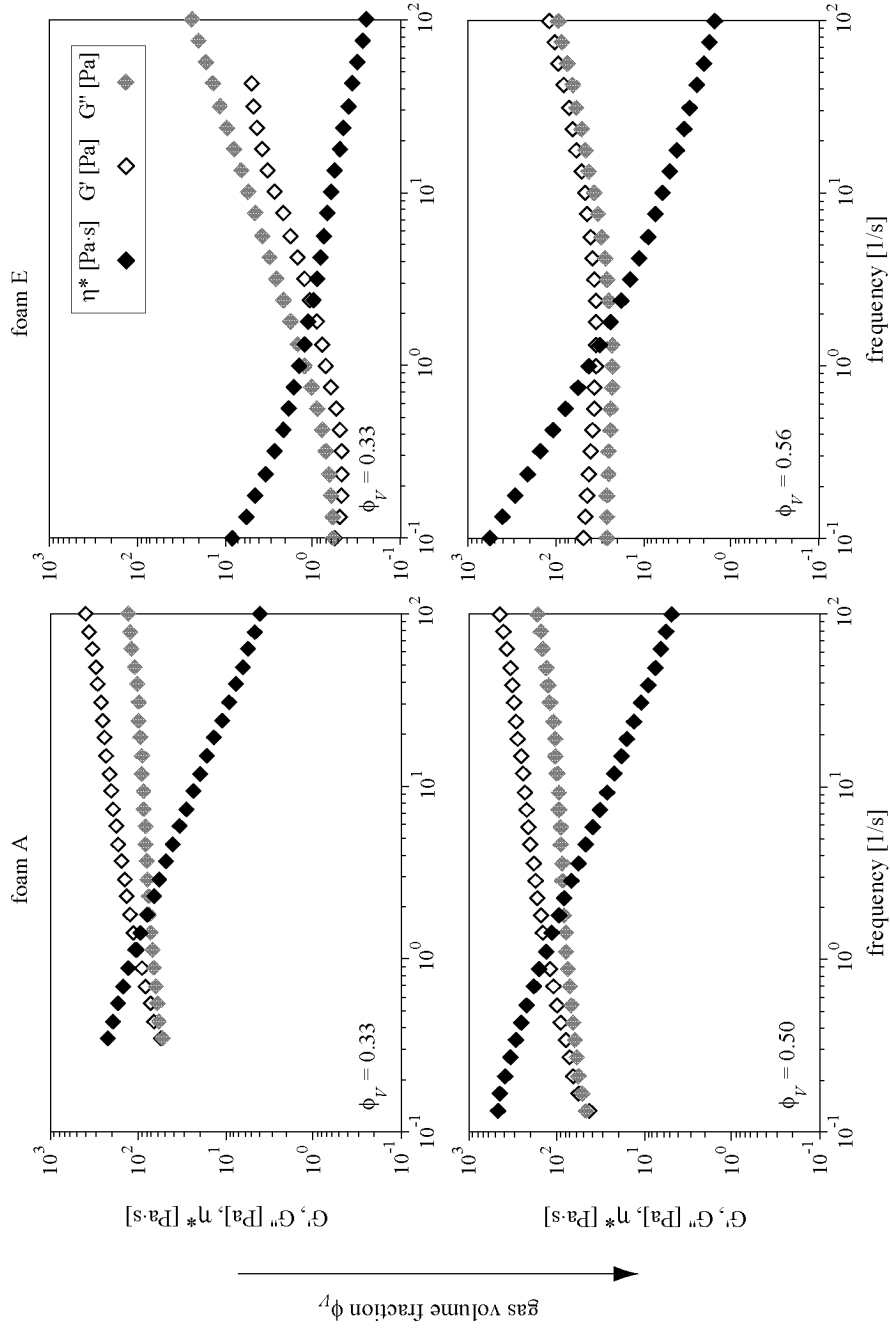


Figure 4.24.: Storage modulus  $G'$ , loss modulus  $G''$  and complex viscosity  $\eta^*$  as a function of the frequency ("frequency sweeps") of foam A and E, each at two different gas volume fractions. The deformation  $\gamma$  was 0.54 % for mix A and 1.00 % for mix E. Deformations chosen according to linear viscoelastic regime found in dynamic rate tests. Foam A produced on rotor-stator device (geometry Radax,  $v_{circ}$  8.04  $m \cdot s^{-1}$ ), foam E produced with DESM device (membrane SF 03-6/5, gap size 0.22 mm,  $v_{circ}$  18.51  $m \cdot s^{-1}$ ).

Furthermore, frequency sweeps of both foam A and E were compared (Fig. 4.24) for two exemplarily chosen gas volume fractions. Foam A was again produced on the rotor-stator device at a circumferential velocity of  $8.04 \text{ m} \cdot \text{s}^{-1}$  and a residence time of 11.0 s while foam E was produced using the dynamically enhanced membrane foaming device with membrane SF03-6/5 at a circumferential velocity of  $18.51 \text{ m} \cdot \text{s}^{-1}$ , a gap size of 0.22 mm and a residence time of 0.75 s. An increase in complex viscosity with increasing gas volume fraction was found for both foam A and E, however much more distinct for foam E. The frequency sweeps of foam A (Fig. 4.24, left side) show typical viscoelastic behavior. The system is largely independent of the gas volume fraction. Contrarily, foam E (Fig. 4.24, right side) shows viscous behavior at a gas volume fraction of 0.33 while it shows viscoelastic behavior at  $\phi_V$  0.56. The fluid is not yet immobilized in the lamella at  $\phi_V$  0.33, the system is still capable of flowing. At a gas volume fraction of 0.56, the mobility of the matrix phase is more constricted to the lamellae, thus, the elastic behavior of the lamellae dominates the rheological behavior.

### Rotor-stator geometry

The two geometries Radax and 12-HR were compared at circumferential velocities of 5.28, 8.04 and  $10.81 \text{ m} \cdot \text{s}^{-1}$  over a wide range of gas volume fractions (Fig. 4.25) using mix A. For the Radax geometry, one fixed set-up was used, i.e. the total possible 8 rotor-stator pairs and a total residence time of 11.0 s corresponding to a residence time of 1.4 s per rotor-stator pair. For the 12-HR geometry, either 8 or 12 rotor-stator pairs were used. For 8 pairs of the 12-HR geometry, the same total residence time of 11.0 s was used resulting in the same residence time per rotor-stator pair as well. For 12 rotor-stator pairs of the 12-HR geometry, either the total residence time (11.0 s) or the residence time per rotor-stator pair (1.4 s) could be kept identical to the residence time chosen for the Radax geometry. Details on the geometries and the process parameters is given in Sec. 3.3.3.

Fig. 4.25 shows that no consistent and significant difference in resulting mean bubble size could be found between the two geometries Radax and 12-HR. For all geometries, number of rotor-stator pairs and residence times, the bubble sizes are smallest at low gas volume fraction. Comparing circumferential speeds of 5.28 and  $10.81 \text{ m} \cdot \text{s}^{-1}$ , higher velocities tend to result in slightly smaller bubble size in the entire investigated gas volume fraction domain. The curves obtained at  $8.04 \text{ m} \cdot \text{s}^{-1}$  do not properly fit into this scheme, the mean bubble sizes are not between the mean bubble sizes obtained at lower or higher rotational speed. The most probable reason is that those results were obtained at a much higher room temperature of around  $30^\circ \text{ C}$  ( $\Delta T = 10^\circ \text{ C}$ ) than the experiments at 5.28 and  $10.81 \text{ m} \cdot \text{s}^{-1}$ . This might have resulted in accelerated destabilization mechanisms (Ostwald ripening and coalescence) between foam production and analysis. The impact of such destabilization mechanisms is more pronounced at higher gas volume



fractions. Another possible explanation can be derived from the counteracting impacts of increased Reynolds stress (i) and increased centrifugal forces (ii) with increasing rotational velocity. (i) enhances dispersing, (ii) enhances centrifugal demixing and, thus, may lead to reduced dispersing efficiency. At a circumferential velocity of  $\sim \text{m} \cdot \text{s}^{-1}$  the combination of (i) and (ii) may cause maximum bubble size.

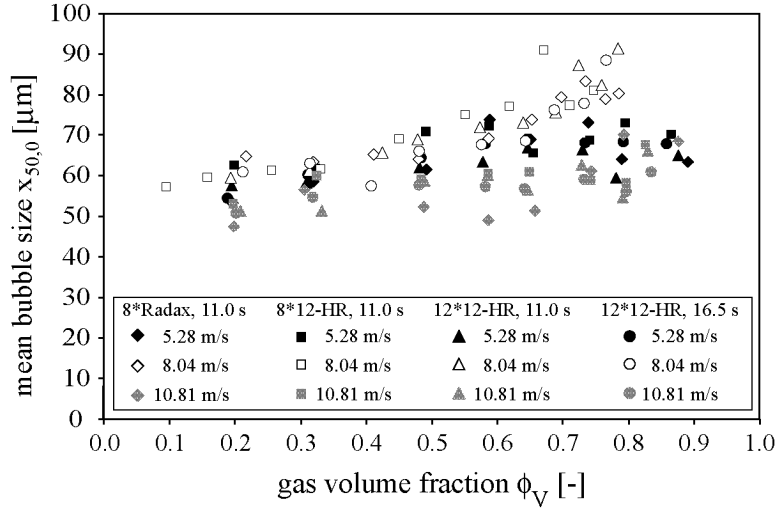


Figure 4.25.: Impact of rotor-stator geometry on resulting bubble size at 5.28, 8.04 and  $10.81 \text{ m} \cdot \text{s}^{-1}$  circumferential velocity. Geometries compared were: 8 pairs of the Radax geometry at total residence time 11.0 s (8\*Radax, 11.0 s), 8 pairs of 12-HR geometry at residence time 11.0 s (8\*12-HR, 11.0 s), 12 pairs of 12-HR geometry at residence time 11.0 s (12\*12-HR, 11.0 s) and 12 pairs of 12-HR geometry at residence time 16.5 s (12\*12-HR, 16.5 s).

Tab. 4.3 shows the highest possible gas volume fractions achievable without blow-by for the four different geometrical set-ups and three circumferential velocities investigated for mix A. Higher rotational velocities might enhance centrifugal separation mechanisms in the whipping head. Highest gas volume fractions without blow-by could be reached with the Radax geometry at all tested circumferential velocities, most significantly at  $10.81 \text{ m} \cdot \text{s}^{-1}$ . This is probably due to the Radax' double-T-shaped geometry which hinders centrifugal de-mixing effects.

## Number of rotor-stator pairs

The number of rotor-stator pairs mounted to the whipping head was successively increased from one to eight. The residence time was accordingly increased from e.g.

#### 4. Results and Discussion

Table 4.3.: Maximally achievable gas volume fractions for the four different geometrical set-ups, the three chosen circumferential velocities  $v_{\text{circ}}$  and mix A.

$v_{\text{circ}}$	8*Radax, 11.0 s	8*12-HR, 11.0 s	12*12-HR, 11.0 s	12*12-HR, 16.5 s
$5.28 \text{ m} \cdot \text{s}^{-1}$	0.89	0.85	0.88	0.85
$8.04 \text{ m} \cdot \text{s}^{-1}$	0.88	0.85	0.86	0.85
$10.81 \text{ m} \cdot \text{s}^{-1}$	0.88	0.83	0.82	0.83

1.4 to 11.2 s for a fluid flow rate of  $18.22 \text{ l} \cdot \text{h}^{-1}$  and a gas volume fraction of 0.50. The rotor-stator pairs were mounted onto the shaft (see Fig. 3.23). At a constant circumferential velocity of  $8.04 \text{ m} \cdot \text{s}^{-1}$ , corresponding to a representative shear rate of  $8011 \text{ s}^{-1}$ , the gas volume fraction was increased as far as it was possible before occurrence of blow-by. For clarity reasons, only the resulting bubble sizes for 2, 4, and 8 rotor-stator pairs are shown in Fig. 4.26.

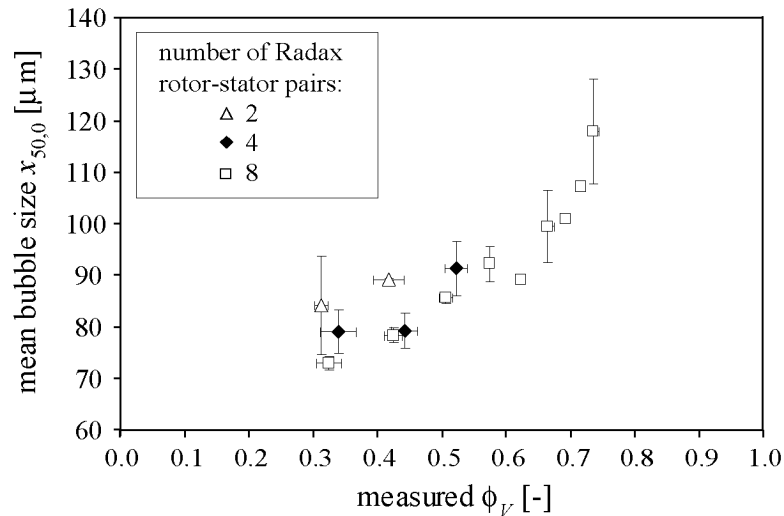


Figure 4.26.: Mean bubble size  $x_{50,0}$  as a function of the number of Radax rotor-stator pairs for  $v_{\text{circ}} 8.04 \text{ m} \cdot \text{s}^{-1}$  and mix A. Exemplarily shown are 2, 4, and 8 pairs.

The tendency is that resulting mean bubble sizes were smaller when more rotor-stator pairs were mounted to the shaft. Additionally, higher gas volume fractions were reached with more rotor-stator pairs. Obviously, a prolonged passage through the dispersing gaps between rotors and stators prevents blow-by effects more effectively. Fig. 4.15 shows that at given  $Re$ -number the power input rises when increas-

ing the number of rotor-stator pairs. This is another explanation for the smaller resulting  $x_{50,0}$  at higher number of rotor-stator pairs used. The reproducibility of the foam microstructure got better with an increasing number of rotor-stator pairs and correspondingly increased residence time.

### 4.3.3. Dispersing characteristics

To compare different dispersing methods and/or dispersing parameters with respect to their energetic efficiency for production of small bubbles/droplets, the energy density concept  $x_{50,0}=f(E_v)$  can be applied. In contrast to emulsion processing where energy plots are commonly used to directly compare measured volumetric energy inputs or energy dissipation rates to resulting mean bubble size (e.g. [39, 86, 150, 128, 98]), no such publications were found for foams. In Fig. 4.27 all results obtained for model mix A and the turbulent rotor-stator device (various gas volume fractions, circumferential velocities  $8.04$  and  $10.81 \text{ m} \cdot \text{s}^{-1}$ , absolute pressures between  $0.6$  and  $4.0 \text{ bar}$ ) are summarized in an energy density plot. Complementary information on comparable emulsification processes was obtained from literature [151] and added to the graph.

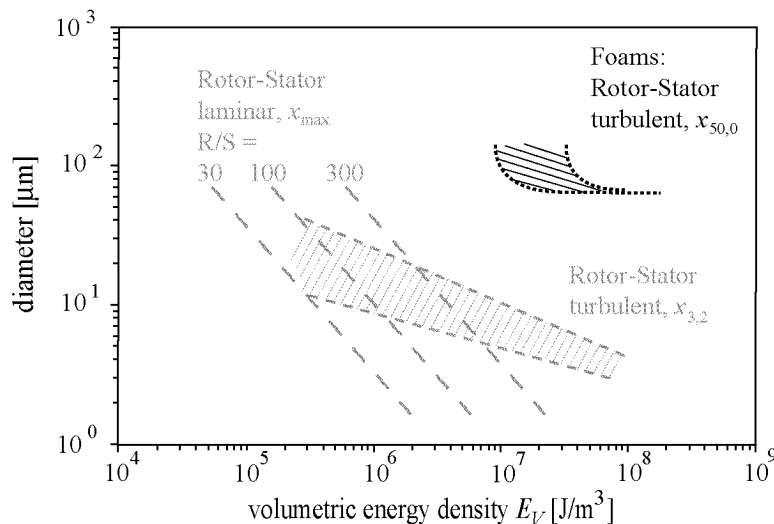


Figure 4.27.: Energy density plot: own data for foam produced with model recipe A in the turbulent rotor-stator device (displayed in black) were compared to data for emulsions published by Schubert [151] (displayed in grey).

The absolute values of both particle size and volumetric energy input can not directly be compared with each other since the properties of the dispersions are

not alike. Own foaming experiments with mix E containing a fast emulsifier led to five times smaller mean bubble sizes compared to the results shown in this chart which were obtained with mix A. Model mix A was not optimized with respect to foam microstructure since only the relative change in bubble size for varying processing parameters was of interest. The difference in volumetric energy input needed for rotor-stator foaming and emulsification can be explained with the critical Capillary number. Compared to emulsions, the critical Capillary number is known to be much higher for the very small viscosity ratios typical for foams (one to two orders of magnitude, depending on the type of flow). Consequently, the stresses leading to bubble/drop break-up are higher for foams than for emulsions. The shift in volumetric energy input (factor 30 to 50, see Fig. 4.27) is in the same order of magnitude as the difference in critical Capillary number. The trends of the curves are of special interest for the comparison. For model foam A whipped in the turbulent rotor-stator device, a plateau in minimum mean bubble diameter of about 60  $\mu\text{m}$  was found. Possible explanations for this limitation in bubble size are that (i) the equilibrium between dispersion and coalescence is shifted towards coalescence at higher circumferential velocities, (ii) a higher residence time leads to local temperature increase or (iii) the emulsifier/protein is damaged at higher circumferential velocity and/or residence time. In contrast, energy density plots for emulsions found in literature show a constant decrease in mean bubble size for increasing volumetric energy input in the investigated range.

### 4.4. Bubble detachment from single pore membrane

To understand and optimize the dynamically enhanced membrane foaming process, insight into the foaming head was obtained using a transparent housing. The results helped to understand the bubble detachment mechanism from the pores of the dynamically enhanced membrane and solved some of the remaining questions.

For this purpose, a plexiglass jacket and a single pore membrane with pore diameter 100  $\mu\text{m}$  were built. A large gap size was chosen to avoid wall effects and bubble detachment at different circumferential velocities was observed with a high speed camera. This setup works for the rotating membrane (ROME) type of device where bubbles are detached from the outer surface of the cylindrical membrane. For the reverse construction (DESM device), there is no access for visualization of the bubble detachment from the inner surface of the cylindrical membrane. The following issues were evaluated:

- Breakup mechanism: Does the air build a film at the membrane surface as a consequence of resulting centrifugal forces due to the density difference

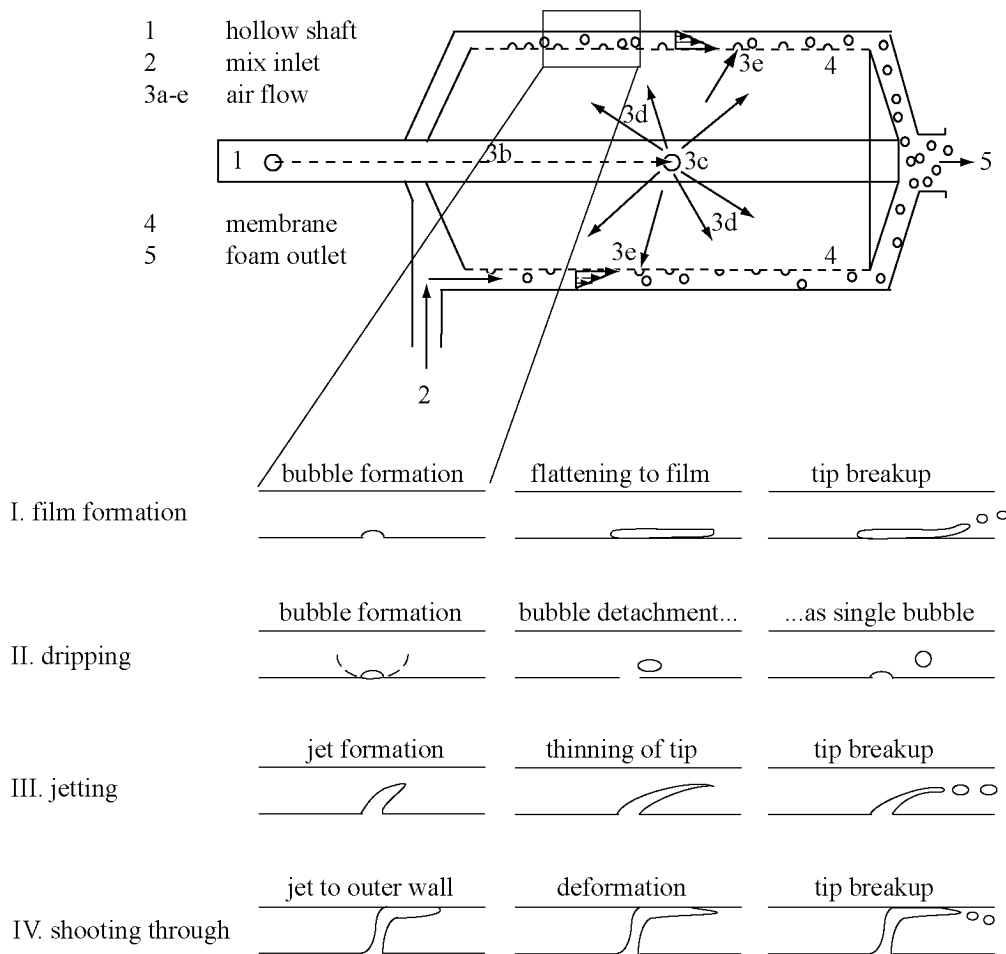


Figure 4.28.: Possible types of bubble formation at rotating membrane and in shear field between concentric cylinders: film formation with subsequent tip breakup (I), dripping of single bubbles (II), jet formation and subsequent tip breakup (III), shooting to outer wall with subsequent tip breakup (IV).

between the disperse and continuous phase from which filaments are ripped off and broken up into small bubbles by the shear stresses acting in the gap (Fig. 4.28, case I)? Does the air drip into the gap leading to the most desirable detachment of single bubbles (Fig. 4.28, case II)? Does the air jet into the gap leading to Rayleigh wave based filament breakup (Fig. 4.28, case III)? Or does the air shoot right through the gap reaching the opposite wall (Fig. 4.28, case IV)?

The last mechanism can most probably be excluded since the centrifugal forces counteract such behavior in the ROME device. Jetting is possible. However, differing from emulsions, the results obtained on single bubble breakup in Sec. 4.1 never showed filament breakup. Rayleigh wave breakup seems to be an exclusive feature of liquid droplets. Gas filaments either relaxed to a spherical bubble or tip breakup occurred.

- Bubble shape: is the bubble after detachment round or is it flattened towards the wall due to the acting centrifugal forces?
- Behavior in the gap: is there any re-coalescence and/or secondary dispersion in the gap?

### 4.4.1. Visualization of bubble detachment

Investigating bubble detachment from a membrane, a distinction between dripping and jetting domain is made. The transition from dripping to jetting is, among other influencing factors (e.g. surfactants) mainly determined by the gas velocity through the pore (see Sec. 2.4.1). It is, thus, important to adapt the gas velocity used for single pore experiments as far as possible to the ones used in real foaming experiments. It was not possible to achieve identical gas velocities due to technical limitations. Constant gas flow rates could only be achieved when using a gas mass flow controller that can manage to compensate for pressure fluctuations. However, at very low gas flow rates the pressure drop within the membrane after detachment of a bubble can not be fully compensated instantaneously. Instead, sufficient pressure for further bubble production is only reached again after long waiting times at such low gas flow rates. This behavior had to be avoided as far as possible because the resulting pressure drop leads to a wide variation in detached bubble size. Two gas flow rates, i.e.  $30.00 \text{ ml} \cdot \text{min}^{-1}$  and  $1.37 \text{ ml} \cdot \text{min}^{-1}$  were tested resulting in gas velocities of  $63.69$  and  $2.90 \text{ m} \cdot \text{s}^{-1}$ , respectively. The pore velocity of the gas in typical foaming experiments is in the range of  $10^{-2} \text{ m} \cdot \text{s}^{-1}$  ( $1.2 \cdot 10^{-2} \text{ m} \cdot \text{s}^{-1}$  at gas volume fraction 0.56, residence time 0.50 s and Sefar Nitex SF03-6/5 membrane (see Tab. 3.1).

Figs. 4.29 and 4.30 show pictures of bubble detachment at a gas velocity of  $63.69 \text{ m} \cdot \text{s}^{-1}$  and two different circumferential velocities, i.e.  $1.00$  and  $4.16 \text{ m} \cdot \text{s}^{-1}$ . Fig.

4.31 and Fig. 4.32 show pictures of bubble detachment using a gas velocity of  $2.90 \text{ m} \cdot \text{s}^{-1}$  at circumferential velocities of  $2.97$  and  $8.14 \text{ m} \cdot \text{s}^{-1}$ .

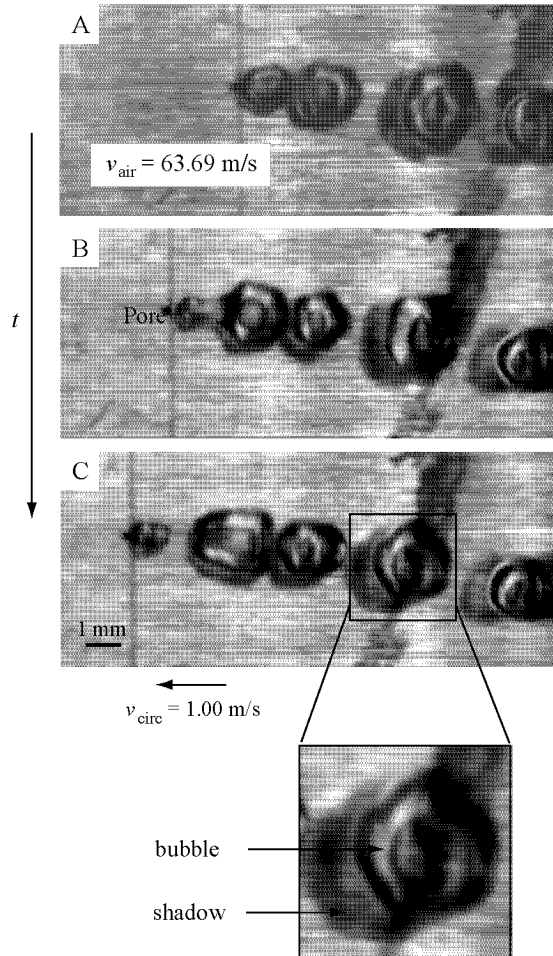


Figure 4.29.: Bubble detachment for single pore experiments for air velocity  $63.69 \text{ m} \cdot \text{s}^{-1}$  and circumferential velocity  $1.00 \text{ m} \cdot \text{s}^{-1}$ . Pore size was  $100 \mu\text{m}$ , gap size  $4.0 \text{ mm}$ , water the continuous phase, camera frame rate  $10\,000 \text{ s}^{-1}$ . Image sequence A to C corresponds to time period of  $3.2 \cdot 10^{-3} \text{ s}$ .

For a gas velocity of  $63.69 \text{ m} \cdot \text{s}^{-1}$ , bubbles were not always detached individually at low circumferential velocities (Fig. 4.29). Some of the bubbles were interconnected when leaving the pore and coalesced immediately (see Fig. 4.29). The resulting bubbles were near-spherical, rather large and with a wobbly contour. This is a consequence of the large interface and the gas compressibility. At high circumferential velocities (Fig. 4.30), it is evident that experiments at gas velocity

#### 4. Results and Discussion

$63.69 \text{ m} \cdot \text{s}^{-1}$  correspond to the jetting domain. Often, bubbles are not detached separately but build a chain of connected bubbles. Sometimes the gas even leaves the pore as a jet. This is in contradiction to results by Räßiger and Vogelpohl [136] who found that bubbles are detached as single bubbles or in pairs even in the jetting domain. It is possible that such jets only occur at high circumferential velocities of the membrane as used here.

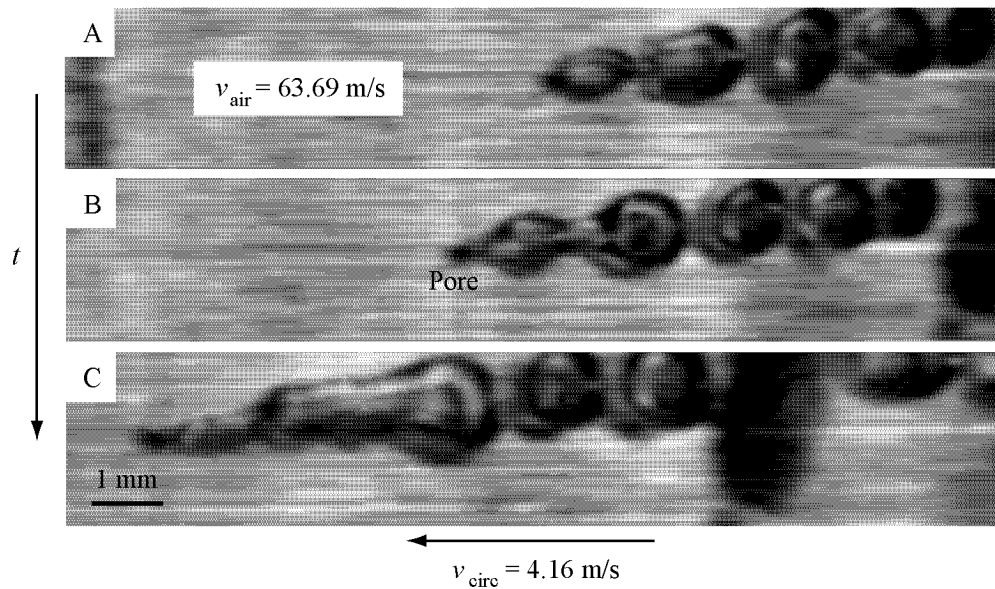


Figure 4.30.: Bubble detachment in single pore experiments at air velocity  $63.69 \text{ m} \cdot \text{s}^{-1}$  and circumferential velocity  $4.16 \text{ m} \cdot \text{s}^{-1}$ . Pore size was  $100 \mu\text{m}$ , gap size  $4.0 \text{ mm}$ , water the continuous phase, camera frame rate  $20\,000 \text{ s}^{-1}$ . Image sequence A to C corresponds to time period of  $1.4 \cdot 10^{-3} \text{ s}$ .

At low gas flow rates, bubbles are detached as single bubbles independent of the circumferential velocity. The chosen gas velocity of  $2.90 \text{ m} \cdot \text{s}^{-1}$  clearly corresponds to the dripping regime. Looking at the bubble sizes in Figs. 4.31 and 4.32, a significant decrease in mean diameter of the detached bubbles can be seen with increasing circumferential velocity. Even though the gas volume flow rate per pore area is still 244 times higher than during an average foaming experiment, the results are judged to be comparable since both the single pore under the conditions given before and multipore experiments took place in the dripping regime.

The shadows of the bubbles visible on the membrane (Figs. 4.29 to 4.32, best visible in Fig. 4.29) supports the freely moving bubble without wall adhesion. Due to the large density difference between mix and air, it had been suspected that centrifugal forces would move the mix outwards and the gas inwards, thus,



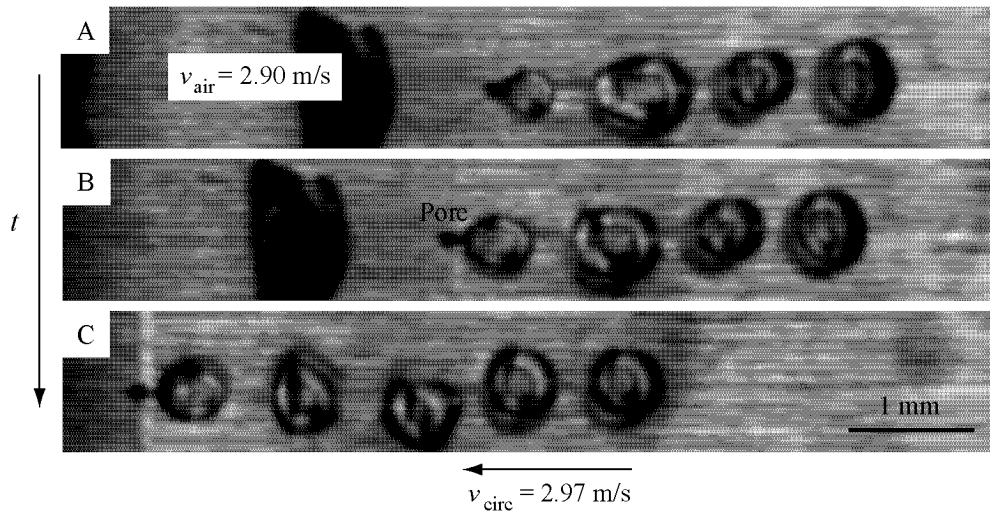


Figure 4.31.: Bubble detachment in single pore experiments at air velocity  $2.90 \text{ m} \cdot \text{s}^{-1}$  and circumferential velocity  $2.97 \text{ m} \cdot \text{s}^{-1}$ . Pore size  $100 \text{ }\mu\text{m}$ , gap size  $4.0 \text{ mm}$ , water as continuous phase, camera frame rate  $30\,000 \text{ s}^{-1}$ . Image sequence A to C corresponds to time period of  $1.0 \cdot 10^{-3} \text{ s}$ .

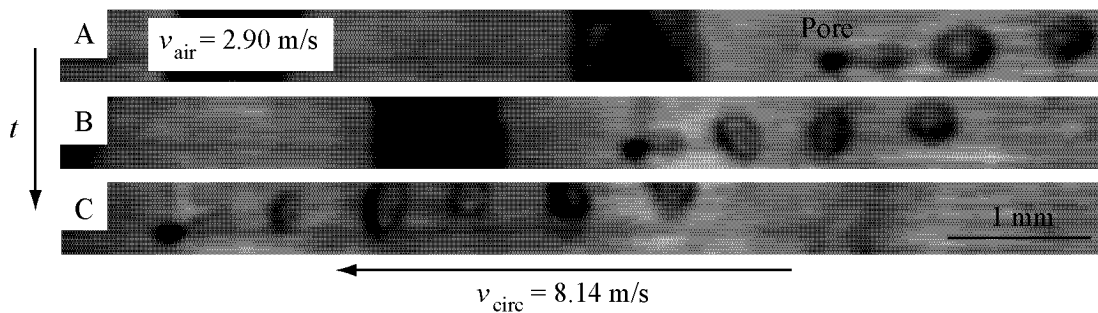


Figure 4.32.: Bubble detachment in single pore experiments at air velocity  $2.90 \text{ m} \cdot \text{s}^{-1}$  and circumferential velocity  $8.14 \text{ m} \cdot \text{s}^{-1}$ . Pore size  $100 \text{ }\mu\text{m}$ , gap size  $4.0 \text{ mm}$ , water the continuous phase, camera frame rate  $70\,000 \text{ s}^{-1}$ . Image sequence A to C corresponds to time period of  $5.6 \cdot 10^{-4} \text{ s}$ .

separating the two phases. Since the air is pressed through the membrane from the inside, the air could have accumulated at the membrane surface and built a film around the membrane. Contrarily to this scenario, bubbles float between membrane and outer cylinder even though the bubbles are very large compared to the size achieved in real foaming experiments. It could be observed by eye that the bubbles never touched the outer cylinder either. It can be concluded that bubbles are with high probability detached from the membrane as single bubbles during foaming and that there is neither a film formation around the membrane nor jetting for gas pore velocities  $\leq 2.90 \text{ m} \cdot \text{s}^{-1}$ . Since the gas pore velocity is even 244 times lower in real foaming experiments compared to the single pore experiments, hence, it is ensured that bubbles are detached individually in the standard foaming experiments. The question whether there is any re-coalescence or further bubble dispersing in the gap can however not be definitively answered from these visualization results. To get more certainty, detailed insight into the gap is needed when a multi-pore membrane is used. Foaming results using both the rotating membrane (ROME) and the dynamically enhanced static membrane (DESM) suggest that there may exist a dynamic equilibrium between dispersion and coalescence in the gap. This is based on the findings that it did not play a role whether the air is injected from inside (ROME) or outside (DESM) nor did the pore size influence the resulting mean bubble size for the range in pore size investigated (1 - 6  $\mu\text{m}$ ). These issues will be further discussed in Sec. 4.5.

#### 4.4.2. Model describing bubble detachment

A model was derived with which the mean size of the detached bubbles can be computed as a function of the shear rate. The model was based on the forces acting on a bubble at a continuously flowed through pore of a rotating membrane (see Sec. 2.4.4). Compared to Eq. 2.37, the forces in axial direction, i.e. the axial drag force  $F_{\tau a}$  and the axial pressure force  $F_{pa}$ , were neglected since the flow in axial direction (mean velocity  $0.1 \text{ m} \cdot \text{s}^{-1}$ , see Tab. 4.7) is negligible compared to the velocity in rotational direction (mean velocity  $2.9 - 28.6 \text{ m} \cdot \text{s}^{-1}$ ;  $18.5 \text{ m} \cdot \text{s}^{-1}$  at optimal foaming conditions, see Tab. 4.7). The pressure force in rotational flow direction  $F_{pr}$  was also neglected since the sum of static and dynamic pressure is assumed to be the same on both sides (upstream and downstream) of the bubble. Fig. 4.33 shows the remaining acting forces, divided into detaching forces (pressure force of gas  $F_{p,tm}$  and rotational drag force  $F_{\tau r}$ ) and retaining forces (surface force  $F_{\sigma}$  and centrifugal force  $F_c$ ). To facilitate the model description, all forces were connected in the bubble center (see Fig. 4.33).

The forces  $F_{p,tm}$  and  $F_c$  act in radial (y-) direction while  $F_{\tau r}$  acts in rotational (x-) direction. The surface tension force is inclined to the horizontal axis by an angle of  $\alpha$  and is, thus, divided into one part acting in x- and one acting in y-

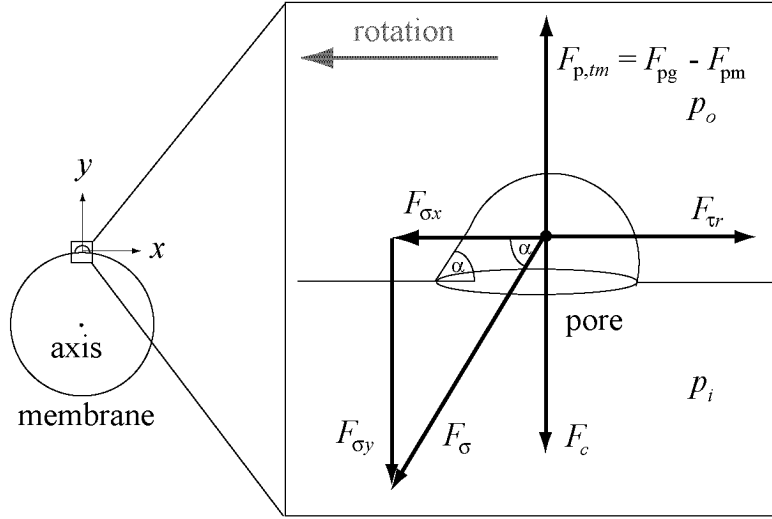


Figure 4.33.: Most important forces acting on bubble at pore.  $F_{p,tm}$  is the transmembrane pressure force (difference between the pressure force of gas  $F_{pg}$  and mix  $F_{pm}$ ),  $F_{\tau r}$  the rotational drag force,  $F_c$  the centrifugal force,  $F_{\sigma,x}$  and  $F_{\sigma,y}$  are the surface tension force in rotational (x-) and radial (y-) direction, respectively.

direction. The resulting equations valid for the rotational  $F_{ix}$  and radial direction  $F_{iy}$  contain the two unknowns, bubble size  $x_B$  and angle  $\alpha$ :

$$F_{ix} : F_{\tau r} + F_{\sigma,x} = 0 \quad (4.3)$$

$$F_{iy} : F_{p,tm} + F_{\sigma,y} + F_c = 0 \quad (4.4)$$

The solution of this model leading to a polynomial of degree 8 is further discussed in Sec. 4.4.4. The model will be named model XY from here on.

A gas mass flow controller was used in all foaming experiments as well as in the single pore experiments. This device adapts the pressure such that an adequate transmembrane pressure difference results controlling the gas flow rate required. The resulting force in radial direction is, thus, small. This is why in a second, further simplified model (model X) only the forces in rotational/x- direction (rotational drag force and surface tension force) were taken into account. The angle  $\alpha$  (see Fig. 4.33) then is  $180^\circ$  meaning that bubbles are detached in rotational direction. This result agrees well with observations obtained and described in Sec. 4.4.1. To calculate the resulting, detached bubble diameter as a function of the circumferential velocity/shear rate, Eq. 4.3 has to be solved (see Eq. 4.8). Detachment takes place as soon as the rotational drag forces gets larger than the the

surface tension force.

For simplicity reasons, the bubble was assumed to be spherical in both model X and model XY. Since the used single-pore membrane is made of metal and is, thus, hydrophilic while the gas bubble is hydrophobic when compared to the surrounding water-based continuous phase, a spherical bubble shape can be expected. In addition, the bubble was assumed to be placed entirely outside the membrane. Thus, the diameter of the entire sphere was taken into account instead of subtracting a small part inside the pore. This simplification is justifiable when looking at the visualization shown in Figs. 4.29 to 4.32 and has also been used in Mersmann's model describing bubble detachment from pores into a stagnant outer fluid [113]. The inner and outer wall of the gap can be assumed to be flat because the gap size is much smaller than the rotor diameter (gap : rotor  $\approx$  1 : 14) and because the area of interest is point-like.

### 4.4.3. Results of experiments and model X

Fig. 4.34 depicts the remaining acting forces determining bubble detachment in model X. The corresponding force balance is given in Eq. 4.3. The visualization experiments described in Sec. 4.4.1 were evaluated, the absolute values of the bubbles which were detached from the single pore membrane determined and the experimental results compared to the results of modeling.

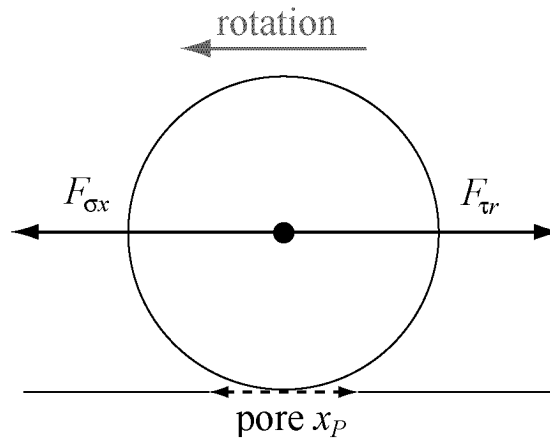


Figure 4.34.: Acting forces of model X. Simplifications: bubble placed entirely outside the membrane, forces in rotational (x-) direction taken into account only.

The surface tension force can be calculated as:

$$F_{\sigma,x} = \sigma \cdot p_P \cdot \cos \alpha, \quad (4.5)$$

where  $\sigma$  is the surface tension and  $p_P$  is the pore perimeter ( $p_P = \pi \cdot x_P$ ). The angle  $\alpha$  in this simplified model is  $180^\circ$  and, thus,  $\cos \alpha = 1$ . The rotational drag force is defined as (185):

$$F_{\tau r} = c_d(Re_{\text{gap}}) \cdot \frac{v_{\text{rel}}^2 \cdot \rho_{\text{cont}}}{2} \cdot A_B, \quad (4.6)$$

where  $c_d$  is the drag coefficient calculated as a function of the gap Reynolds number  $Re_{\text{gap}}$ ,  $\rho_{\text{cont}}$  the continuous phase density,  $A_B$  the cross-sectional area of the bubble perpendicular to the flow ( $A_B = \pi/4 \cdot x_B^2$ ) and  $v_{\text{rel}}$  the velocity of the bubble relative to the medium. The drag coefficient was calculated following the approximation of Kaskar and Brauer (see Eq. 2.36, [185]) which leads to an error of maximally 4 % and is valid for spheres in a flowing liquid phase. The relative velocity  $v_{\text{rel}}$  between bubble and surrounding continuous phase depends on the location in the gap. It is highest at the wall of the outer cylinder, zero on the membrane surface because the bubble moves along with the membrane as long as it is linked to the pore. The relative velocity approximately relevant for the entire bubble cross section, thus, depends on the bubble size. The center of the bubble was chosen for the calculation of the representative relative velocity:

$$v_{\text{rel}} = \dot{\gamma} \cdot \frac{x_B}{2} = \frac{2 \cdot \pi \cdot n \cdot R_i}{s} \cdot \frac{x_B}{2}, \quad (4.7)$$

where  $\dot{\gamma}$  is the shear rate,  $n$  the rotational speed,  $R_i$  the rotor radius and  $s$  the gap size. To compute  $\dot{\gamma}$ , Eq. 2.46 was used and a linear shear profile assumed.

Detachment from the pore results as soon as the surface tension force acting in rotational direction is exceeded by the rotational drag force. Combining Eqs. 4.5, 4.6 and 4.7, the bubble size  $x_B$  consequently results as:

$$x_B = \sqrt[4]{\frac{8 \cdot \sigma \cdot x_P \cdot s^2}{c_d(Re_{\text{gap}}) \cdot \rho_{\text{cont}} \cdot (\pi \cdot n \cdot R_i)^2}} = \sqrt[4]{\frac{32 \cdot \sigma \cdot x_P}{c_d(Re_{\text{gap}}) \cdot \rho_{\text{cont}} \cdot \dot{\gamma}^2}}. \quad (4.8)$$

This means that - for a given mix recipe - the resulting bubble size is smaller for smaller pore size and higher shear rate.

Fig. 4.35 compares the visualization results on bubble detachment achieved by using the single pore membrane with water as the continuous phase to the results obtained from model X (see Eq. 4.8). The fluid characteristics used for the calculations are summarized in Tab. 3.16, the experimental setup including device dimensions is described in detail in Sec. 3.3.4.

Comparing measured and modeled data (see Fig. 4.35) it is obvious that bubble sizes obtained from modeling are too large at low shear rates, but are in good agreement with measured bubble diameters at high shear rates. Both modeling and experimental results show that a minimum bubble size is approached for increasing shear rate. This finding confirms the impact of shear rate on mean bubble

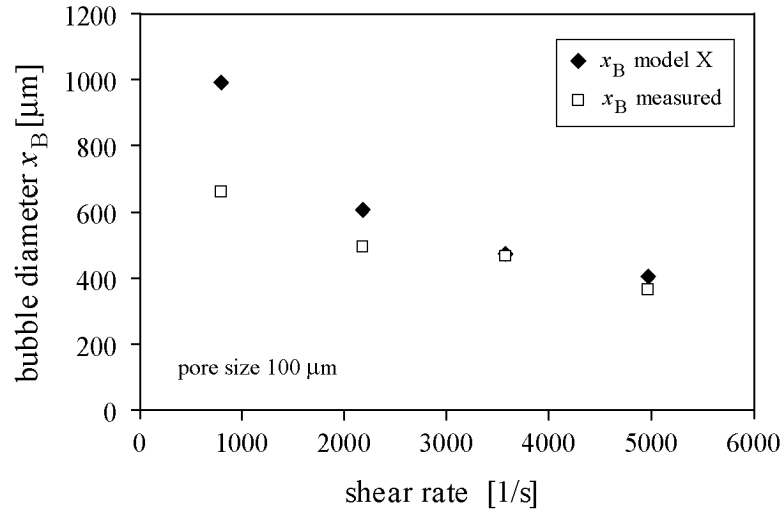


Figure 4.35.: Single pore membrane: comparison between bubble sizes resulting from modeling (model X) and visualization experiments.

size found in foaming trials (see Sec. 4.5.6). Since the model described in Eq. 4.8 is a simplified model disregarding several minor forces, the fitting for higher circumferential velocities is really satisfying. The deviation of measured and calculated bubble sizes at shear rates below  $2000 \text{ s}^{-1}$  are probably due to neglected acting axial forces. These were neglected in the model since they are very low compared to the rotational flow forces under typical foaming conditions. They are however not completely negligible at low circumferential velocities/shear rates like used in the single pore experiments. For the exemplary shear rate of  $794 \text{ 1/s}$  referred to in Fig. 4.35, the circumferential velocity is only 30 times higher than the axial flow velocity while it is 180 times higher under typical foaming conditions. It can also be derived from Fig. 4.35 that the resulting bubble diameter is always larger than the pore size. It will be interesting to experimentally test whether a decreased surface tension (e.g. by usage of mix E instead of water) would cut the size of the detached bubbles down to the pore size. For the modeling, decreased surface tension does not lead to significantly smaller bubble sizes. It was tried to observe bubble detachment from the single pore membrane using a 0.6 weight % solution of emulsifier E in water. However, the resulting turbid system made it impossible to capture sufficiently sharp movies. It might be possible for narrower gap size, but then the pore size should be chosen much smaller as well to avoid wall interaction of the bubbles. This would certainly result in smaller bubble sizes, thus, higher image resolution would be necessary as well. Another remaining question is whether the experimentally obtained bubble sizes would have been smaller if a lower gas flow rate and thus lower gas velocity through the pore were possible. However,

Bals [10] found for multi-pore membranes that bubble sizes did not increase significantly with increasing gas flow rate. It would be interesting and advisable for future work to check if and how the viscosity influences bubble detachment by repeating the single-pore experiments with continuous fluid phases of different viscosity. An impact of continuous phase viscosity on bubble detachment is expected since the results using multipore membranes (e.g. Fig. 4.62) showed smaller mean bubble sizes in the higher gas volume fraction range at corresponding higher foam viscosity.

Table 4.4.: Parameters used for model calculations applied to real foaming system where a multi-pore sintermembrane and mix E were used. All values given at 18 °C. For density and viscosity, average values between mix and foam used in model calculations.

Surface tension $\sigma$ [mN · m <sup>-1</sup> ]	59.00
Mix density $\rho_{\text{cont}}$ [kg · m <sup>-3</sup> ]	1125
Foam density $\rho_{\text{foam}}$ [kg · m <sup>-3</sup> ]	495
Gas volume fraction of foam $\phi_V$ [-]	0.56
Mix viscosity $\eta_{\text{cont}}$ [Pa · s]	$\eta = 0.07 \cdot \dot{\gamma}^{-0.15}$
Foam viscosity $\eta_{\text{foam}}$ [Pa · s]	$\eta = 0.99 \cdot \dot{\gamma}^{-0.26}$
Rotor radius $R_i$ [m]	$25.50 \cdot 10^{-3}$
Gap size $s$ [m]	$0.235 \cdot 10^{-3}$
Mean pore size $x_P$ [µm]	2.0

Table 4.5.: Multi pore membrane (sinter membrane): comparison between experimental results (mean bubble sizes of foam E with gas volume fraction 0.56 obtained with the sinter membrane) and model X using Eq. 4.8.

Circumferential velocity [m · s <sup>-1</sup> ]	Shear rate [s <sup>-1</sup> ]	$x_{50,0; \text{experimental}}$ [µm]	$x_{\text{model X}}$ [µm]	factor [-]
3.0	12 716	39.764	42.055	1.1
8.2	34 964	15.153	32.457	2.1
13.4	57 224	11.019	28.155	2.6
18.6	79 460	10.476	25.429	2.4
23.8	101 720	8.351	23.460	2.8

The model was also applied to the typical pore size, gap size and continuous phase used in foaming experiments (sinter membrane, DESM device). Since the model addresses a single pore system while the experiments were done using multi-pore systems, this gave an estimate of the impact of bubble interaction and shearing

in the narrow annular gap on mean size (see Tab. 4.5). The used sinter membrane, continuous phase and foam had the dimensions and characteristics listed in Tab. 4.4. From Fig. 4.5 it is evident that the model overestimates the resulting bubble sizes at all shear rates except the lowest one. The model fails to predict the change in mean bubble size with increasing shear rate: the deviation between model and experimental results increases with increasing shear rate. Assuming the model to give correct results when applied to bubble detachment from the single pore membrane, this result means that further bubble dispersion takes place in the narrow annular gap between rotating membrane and static outer cylinder and that the impact of gap dispersion on the mean bubble size grows with increasing shear rate. This conclusion could explain why e.g. the pore size did not have an impact on the resulting mean bubble size in experiments obtained with the dynamically enhanced membrane foaming device (see Sec. 4.5).

#### 4.4.4. Results of refined model XY

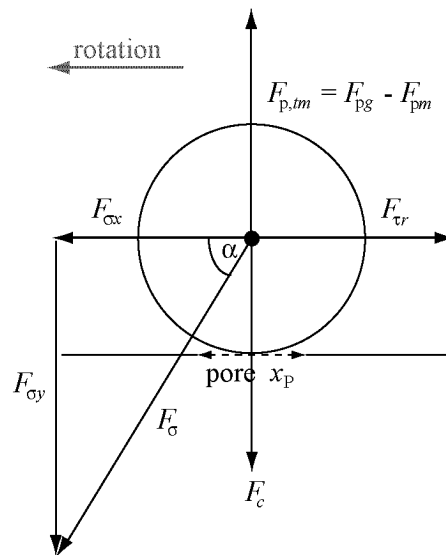


Figure 4.36.: Forces acting on bubble in model XY. Simplifications: bubble placed entirely outside membrane.

The simplified model X is only valid for gas bubbles in the ROME device for which the centrifugal force acts as a retaining force and is directed towards the rotation axis. This is true for all foams. However, for emulsions where droplets may have higher density than the continuous phase, the centrifugal force will be directed opposite and will act as a detaching force. Then, the absolute value and



angle of the resulting askew force have to be computed. Doing this, the vector sum of the forces shown in Fig. 4.36 has to be solved:

$$(F_{p,\text{tm}} + F_c)^2 + F_{\tau\text{r}}^2 = F_{\sigma}^2, \quad (4.9)$$

where

$$F_{\tau\text{r}} = \frac{\pi^3}{8} \cdot \frac{c_d \cdot \rho_{\text{cont}} \cdot r^2 \cdot n^2}{s^2} \cdot x_{\text{B}}^4 = f_{\tau\text{r}} \cdot x_{\text{B}}^4. \quad (4.10)$$

The centrifugal force,  $F_c$  and the pressure force acting in the gas phase,  $F_{p\text{g}}$  are defined as (185):

$$F_c = V_{\text{B}} \cdot \Delta\rho \cdot R_i \cdot \omega^2 = \frac{2}{3} \cdot \pi^3 \cdot r \cdot n^2 \cdot \Delta\rho \cdot x_{\text{B}}^3 = f_c \cdot x_{\text{B}}^3, \quad (4.11)$$

$$F_{p,\text{tm}} = \Delta p_{\text{transmembrane}} \cdot A_{\text{P}} = \Delta p_{\text{transmembrane}} \cdot \frac{x_{\text{P}}^2}{4} \cdot \pi, \quad (4.12)$$

where  $V_{\text{B}}$  is the bubble volume,  $R_i$  is the rotor radius,  $\omega$  the angular velocity,  $n$  the rotational speed,  $\Delta\rho$  the density difference between disperse and continuous phase and  $\Delta p_{\text{transmembrane}}$  the transmembrane pressure difference. The transmembrane pressure difference was measured in all experiments, the mean pressure differences (at respective circumferential velocity) used in model XY were  $0.20 \cdot 10^5$  bar (at  $v_{\text{circ}} 3.0 \text{ m} \cdot \text{s}^{-1}$ ),  $0.25 \cdot 10^5$  bar ( $v_{\text{circ}} 8.1 \text{ m} \cdot \text{s}^{-1}$ ),  $0.39 \cdot 10^5$  bar ( $v_{\text{circ}} 13.3 \text{ m} \cdot \text{s}^{-1}$ ),  $0.40 \cdot 10^5$  bar ( $v_{\text{circ}} 18.5 \text{ m} \cdot \text{s}^{-1}$ ).

Inserting Eq. 2.24 and Eqs. 4.10 to 4.12 into Eq. 4.9 leads to a polynomial of degree 8 which can be solved with Newton's method (130).

$$f_{\tau\text{r}}^2 \cdot x_{\text{B}}^8 + f_c^2 \cdot x_{\text{B}}^6 + 2 \cdot f_c \cdot F_{p,\text{tm}} \cdot x_{\text{B}}^3 + F_{p,\text{tm}}^2 - F_{\sigma}^2 = 0. \quad (4.13)$$

This model approach XY including, both, rotationally and radially acting forces, was applied to the system used in the single pore visualization experiments (Fig. 4.35). Tab. 4.6 compares the experimentally obtained bubble diameters to both the simplified model X (Eq. 4.8) and the more refined model XY (Eq. 4.13).

The two models led to comparable results. This proves that the simplification from model XY to model X can be justified. Obviously, the rotational drag force is the main force leading to bubble detachment from the pore of a rotating membrane.

#### 4.4.5. Sinter membrane

The possible occurrence of bubble breakup and/or coalescence was observed through the transparent housing. Using the sinter membrane, a gap width of 1.00 mm, a circumferential velocity of  $1.87 \text{ m} \cdot \text{s}^{-1}$ , a solution of 0.60 weight % emulsifier E in water and a gas velocity typically used in foaming experiments, a high-speed

Table 4.6.: Comparison of measured bubble sizes to results of both the simplified model X (Eq. 4.8) and the refined model XY (Eq. 4.13).

Circ. velocity [m · s <sup>-1</sup> ]	Shear rate [s <sup>-1</sup> ]	$x_{\text{experimental}}$ [μm]	$x_{\text{modelX}}$ [μm]	$x_{\text{modelXY}}$ [μm]
3.0	794	659	973	958
8.1	2177	495	597	533
13.3	3564	464	470	439
18.5	4951	363	400	357

movie was captured. The contrast of the original movie (see Fig. 4.37, left side) was enhanced to get more distinct bubble contours (Fig. 4.37, right side).

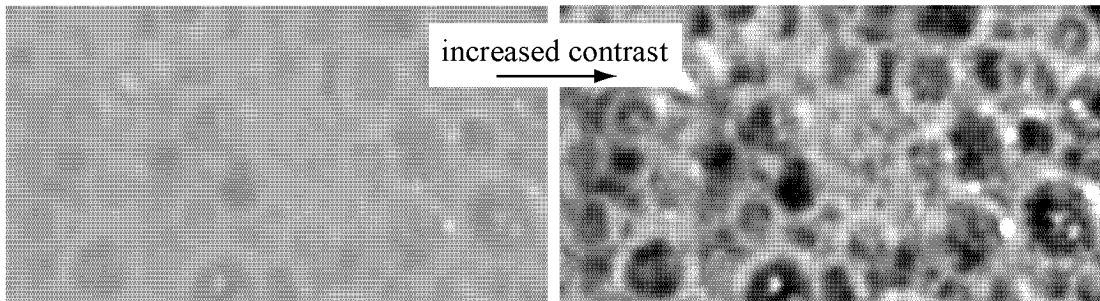


Figure 4.37.: Bubbles produced with sinter membrane at circumferential velocity  $1.87 \text{ m} \cdot \text{s}^{-1}$  in ROME using a 0.60 weight % solution of emulsifier E in water at gap size 1.0 mm, captured with CCD camera at frame rate  $20\,000 \text{ s}^{-1}$ . Original image (left side) and image where contrast was enhanced (right side).

In Fig. 4.38, two pictures are shown, captured in quick succession. It is possible to follow the path of certain bubbles (marked with circles). This might enable to observe bubble detachment and possibly coalescence and dispersing in the gap in future experiments. At the relatively large gap size and low rotational velocity used here, resulting shear rates are however low and there is no significant bubble deformation or dispersion visible. A smaller gap would certainly contribute to improve picture quality, approach realistic shear rates and most probably also show up bubble deformation and dispersion in the gap. By changing rotational velocity and, thus, shear rate, such results might in a further work be compared to the modeling results obtained with the single pore membrane (see Sec. 4.4.2) and the model adapted to multipore systems.

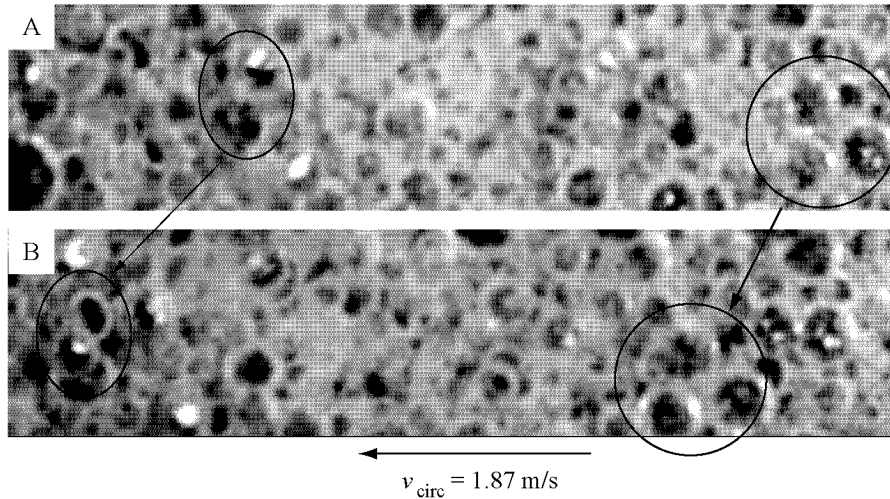


Figure 4.38.: Bubbles produced with sinter membrane at circumferential velocity  $1.87 \text{ m} \cdot \text{s}^{-1}$  in ROME using a 0.60 weight % solution of emulsifier E in water at gap size 1.0 mm, captured with CCD camera at frame rate  $20\,000 \text{ s}^{-1}$ . Two pictures are shown which were captured in quick succession. The path and change of some bubbles (marked with circles) can be observed.

#### 4.4.6. Taylor vortices

Using the sinter membrane with a diameter of 55.0 mm, a gap width of 1.0 mm and water as the continuous phase, the occurrence of Taylor vortices was observed. For this setup, circumferential velocities of  $0.2 \text{ m} \cdot \text{s}^{-1}$  corresponding to a rotational speed of 76 rpm were high enough to obtain Taylor vortices (see Eq. 2.53). Hence, Taylor vortices can be observed from the minimum to the maximum rotational speed of the applied device. A picture of such Taylor vortices is depicted in Fig. 4.39. However, no Taylor vortices can be achieved in typical foaming experiments (see Sec. 4.5). At a gap size of 0.22 mm and the - compared to water - higher viscosity of the mix/foam, rotational velocities of 20 800 rpm are needed to reach the critical Taylor number  $Ta_c$  of 41.3 whereas the device is limited to 10 000 rpm. To investigate the effect of Taylor vortices on the mean bubble size a gap size of 1.5 mm was used. The results are discussed in Sec. 4.5.4.

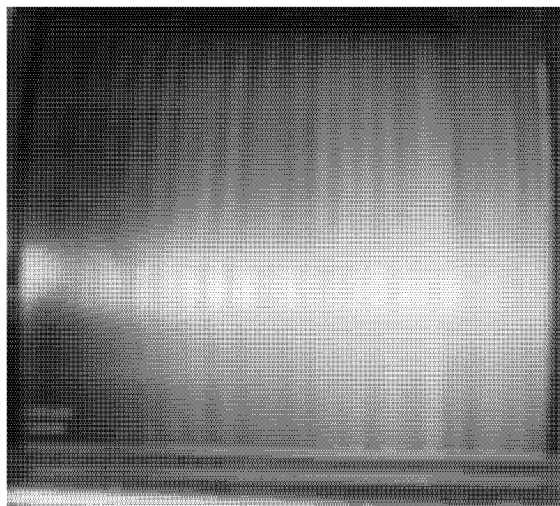


Figure 4.39.: Taylor vortices observed through the transparent housing of the ROME device.

## 4.5. Dynamically enhanced membrane foaming

Two types of dynamically enhanced membrane foaming device were tested in this work: the rotating membrane device (ROME) and the dynamically enhanced static membrane (DESM), both described in Sec. 3.3.4. In the ROME device, the inner cylinder holds the membrane. In the DESM device, the inner cylinder is compact (no pores), the membrane is attached to the inner housing wall (=outer cylinder). For both devices, a similarly defined shear field can be created in the narrow annular gap by rotating the inner cylinder. The shear forces detach the bubbles from the membrane in an early formation stage. Additionally, the shear field may further break bubbles up on their passage through the narrow annular gap depending on the system and processing parameters used. First, the foam microstructure obtained with the two types of device, ROME and DESM, was compared. Then, the devices were characterized with respect to their power and dispersing characteristics. Furthermore, detailed investigations were performed varying the processing parameters gap size (i), mix recipe (ii), velocity field (iii), pore size (iv), pore distance (v), membrane type (vi), residence time (vii) and membrane area (viii). Subsequently, scale-up calculations from lab- to pilot-scale were done, a respective pilot-scale device built, and received experimental results again compared to respective data for the two lab-scale devices (ROME, DESM) using identical membranes, gap sizes and shear rates in order to reevaluate/reconfirm the scaling laws derived.

## 4.5.1. Power characteristics

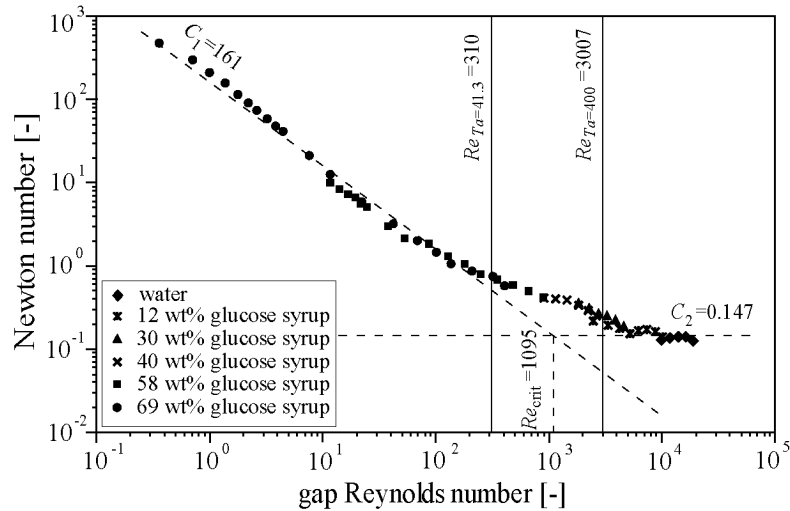


Figure 4.40.: Power characteristics for dynamically enhanced membrane foaming device (gap size 0.50 mm) obtained with water and glucose solutions of different viscosities. The constants  $C_1$  and  $C_2$ , the critical gap  $Re$ -number,  $Re_c$  and the gap  $Re$ -numbers at Taylor-numbers of 41.3 and 400 are depicted. Gap Reynolds number was computed including  $\pi$ .

The power characteristics (Fig. 4.40) were obtained using a gap width of 0.50 mm. Chart 4.40 shows that the laminar flow region is predominant for the dynamically enhanced membrane devices. The slope of minus one, corresponding to laminar flow, extends up to a gap  $Re$ -number of approximately 250. The transition region between laminar and fully developed turbulent flow domain is located between  $Re_{\text{gap}}$  250 and 10 000. To obtain a turbulent flow field, gap  $Re$ -numbers of 10 000 and higher need to be achieved. This was only possible with water. For all tested foam systems, viscosity was clearly higher than for water (e.g factor 52 for foam E with  $\phi_V$  0.56 at shear rate  $84\,468\text{ s}^{-1}$ ). It can be deduced that foaming within ROME/DESM devices is performed under laminar flow conditions. Exemplary dispersing conditions, calculated from the measured net dispersing power at known device dimensions and preferred processing parameters (6 250 rpm, 0.50 mm gap, mix C,  $\phi_V$  0.50, net power consumption 230 W) confirmed that whipping in the investigated ROME/DESM apparatus takes place in the laminar flow domain. The exact resulting gap Reynolds number for these distinct conditions was 41. The finally preferred use of gap size 0.22 mm instead of 0.50 mm further shifts to lower  $Re$ -numbers and, thus, even more into the laminar flow domain. The characteristic constants of the power characteristics  $C_1$  and  $C_2$  characterizing laminar and

turbulent flow conditions, respectively, and the critical Reynolds number  $Re_c$  denoting the transition "point" between laminar and turbulent flow, were explicitly determined and are depicted in Fig. 4.40. Additionally, the flow conditions in the gap with regard to Taylor vortex flow patterns was analyzed. The critical Taylor number  $Ta_c$  of 41.3 characterizes the onset of Taylor vortices. Taylor numbers of  $\sim 400$  indicate fully developed turbulent flow [149]. For these two characteristic Taylor-numbers, the corresponding gap  $Re$ -numbers were computed and are also depicted in Fig. 4.40. This shows that the transition region in the rotating membrane device is affected by the occurrence of Taylor vortices. For emulsions (see Fig. 2.23 [146]), the appearance of such Taylor vortices was shown to lead to smaller mean droplet sizes down to the range of the mean pore size.

### 4.5.2. Dispersing characteristics

In Fig. 4.41 all results obtained for model mix C in the ROME device under laminar dispersing flow conditions (various gas volume fractions, circumferential velocities of  $2.93 - 23.46 \text{ m} \cdot \text{s}^{-1}$ ) are summarized in an energy density plot. Complementary information for comparable emulsification processes was obtained from literature [151] and inserted into Fig. 4.41. As discussed in Sec. 4.3.3, the different properties of foams and emulsions (density, viscosity ratio, compressibility) and the type of system (e.g. emulsifier) play a major role with respect to the dispersing efficiency of the applied device. This is why the absolute values of bubble and droplet sizes can not be directly compared. The difference in volumetric energy input between membrane emulsification and dynamically enhanced membrane foaming can be explained with the magnitude of the critical Capillary number (see Sec. 4.3.3). The trends of the curves shown in Fig. 4.41 are of interest for comparison. For model system C, foamed in the laminar ROME device, a plateau in minimum mean bubble diameter of about  $35 \mu\text{m}$  was found. In addition to the early detachment of bubbles from the membrane, further dispersion takes place in the gap. It is thus possible, that the minimum mean bubble size of  $35 \mu\text{m}$  is given by the device and mix characteristics, i.e. equilibrium of dispersion and coalescence in the gap, depending on the acting shear forces, for the chosen protein-based recipe. In contrast, the energy density plots for emulsions show a constant decrease in mean bubble size with increasing volumetric energy input in the investigated range. The data points given for the ROME device, valid for the two gas volume fractions 0.09 and 0.52 and the curves for gas volume fractions 0.01, 0.10 and 0.50 given for membrane emulsification, highlight the different trends nicely.

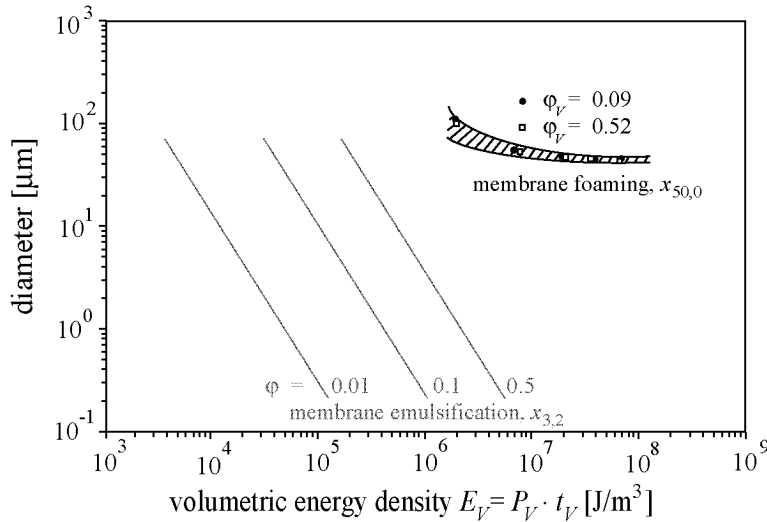


Figure 4.41.: Energy density plot: own data for foams produced with model recipe C in the laminar ROME device within this work (displayed in black) compared to data for emulsions published by Schubert [151] (displayed in grey).

### 4.5.3. ROME versus DESM

With respect to construction, the DESM device is more simple than the ROME device, offering distinct advantages: 1. the air enters the foaming head from the outside and does not have to be injected via a hollow rotating shaft into the inner cylinder. Hence, complicated seals can be avoided. 2. The rotating part consists of a compact metal cylinder instead of a membrane while the membrane is fixed to the housing. Bubble detachment from the membrane is dependent on the forces acting on the bubble which are related to the shear field between rotating and static concentric cylinders. The shear rate is proportional to the velocity difference between inner and outer cylinder, the rotor diameter and reverse proportional to the gap size (Eq. 2.47). If these three parameters are constant and if wall slip is negligible, the acting dispersing forces and resulting bubble sizes should ideally be identical for the two set-ups where either the membrane is rotating or the membrane is fixed but an inner cylinder rotates. To confirm this assumption, the ROME/DESM foaming devices were systematically compared with respect to foamability and foam microstructure. Fig. 4.42 shows the resulting mean bubble size  $x_{50,0}$  as a function of the gas volume fraction. The two devices were compared for mix C at a mean residence time of 0.50 s and for mix E at a mean residence time of 0.75 s. The circumferential velocity was  $18.51 \text{ m} \cdot \text{s}^{-1}$  for all experiments corresponding to a shear rate of 84 468, the gap width was fixed to 0.22 mm.

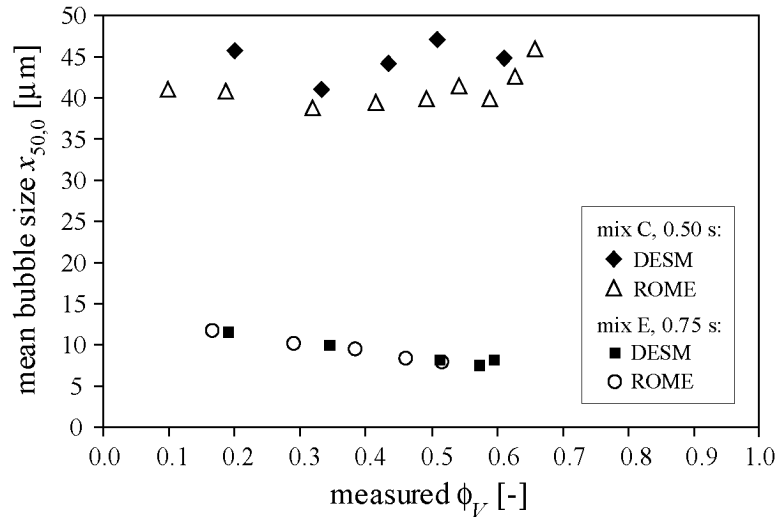


Figure 4.42.: Comparison of the two types of membrane foaming device, ROME and DESM, for mix C at 0.50 s and for mix E at 0.75 s mean residence time. Circumferential velocity  $18.51 \text{ m} \cdot \text{s}^{-1}$  for all experiments (shear rate  $84\,468 \text{ s}^{-1}$ ), gap size 0.22 mm, membrane SF 03-6/5.

No significant difference between the two devices was found for mix E. Both mean bubble size and maximally achievable set gas volume fraction were nearly identical. However, set and measured gas volume fraction always deviated for the ROME device (average deviation -10.7 %), while it was identical to slightly higher for the DESM device (average deviation +2.8 %). It was suspected that the density difference between continuous and disperse phase combined with the ROME air supply from inside to outside may lead to air pockets at the membrane surface. This however never manifested as blow-by in the evaluated trials. No valid explanation for the slight deviation of set and measured gas volume fractions was found. When the air was pressed from the outer cylinder surface into the continuous phase (DESM device), the centrifugal forces enhanced the homogeneous dispersion of mix and air in the gap. This seemed to improve foam homogeneity. At a rotational speed of 6479 rpm, a rotor diameter of 54.56 mm and a gap size of 0.22 mm, the separation time in the gap (calculated for a single bubble of mean diameter of  $10 \mu\text{m}$  according to Eqs. 3.4 to 3.6), is still much shorter than the residence time for mix E (0.0001 s compared to 0.75 s). This means that centrifugal separation of mix and air could in principle also take place within the DESM device.

For mix C, the DESM device leads to slightly larger mean bubble sizes than the ROME device, the curve progression is however very similar (Fig. 4.42). The DESM device had no cooling jacket and consequently foam outlet temperatures were about  $10 \text{ }^\circ\text{C}$  higher than for the ROME device. Experiments with mix C and



E showed that mix C is temperature sensitive with regard to foam destabilization mechanisms while mix E is not influenced by temperature as long as it does not exceed 45 °C. This explains why no difference between the two types of dynamically enhanced membrane device was found for mix E while some shift in mean bubble size was found for mix C.

Since the results obtained with the two types of dynamically enhanced foaming device, ROME and DESM, were found to be very much alike, the impact of process parameters (see Sec. 4.5.4 to 4.5.13) was not analyzed for both devices for all experimental variations carried out.

#### 4.5.4. Gap size

The impact of gap size was evaluated and found to be important with respect to foam homogeneity and mean bubble size. Gap sizes of 1.50, 1.00, 0.72, 0.50 and 0.22 mm were tested for the ROME device and mix C, gap sizes of 0.50 and 0.22 mm for mix E. It was shown that within the tested range in gap size, the maximum gap size allowing the production of optimally homogeneous foam is 0.50 mm for fluid system C while it is 0.22 mm for the less viscous fluid system E.

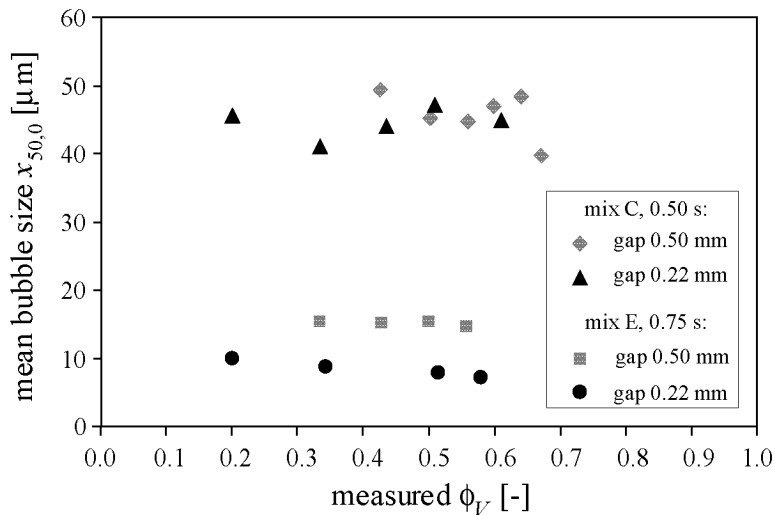


Figure 4.43.: Impact of gap size on resulting mean bubble size for the DESM device. The circumferential velocity was  $18.51 \text{ m} \cdot \text{s}^{-1}$  for all experiments, the membrane Sefar Nitex 03-6/5 was used, mixes C and E were tested.

The gap sizes 0.50 and 0.22 mm were also tested for the DESM device (see Fig. 4.43). The impact of gap size on mean bubble size was not strong for mix C whereas a reduction in gap size from 0.50 mm to 0.22 mm cut the mean bubble

sizes roughly in half for mix E. This reduction in  $x_{50,0}$  found for mix E was to be expected since the shear rate was 2.3 times higher at gap size 0.22 mm compared to 0.50 mm at identical circumferential velocity ( $84\,468\text{ s}^{-1}$  compared to  $37\,351\text{ s}^{-1}$ ). Why the microstructure of mix C did not change with the same decrease in gap size could be a consequence of locally increased temperature leading to impaired functional properties of the protein. For mix E, optimally homogeneous foams were achieved at gap size 0.22 mm while gap size 0.50 mm led to a slight separation of the foam into higher and lower dense areas. The zigzagging curve received for mix C at gap size 0.50 mm also indicates the reduced reproducibility at this larger gap size compared to a gap size of 0.22 mm.

Additionally, the impact of Taylor vortices on the mean bubble size was tested for both the ROME and DESM devices with mixes C and E using either the sinter membrane or the Sefar Nitex membrane and gap widths of 1.5 and 2.0 mm. The critical Taylor number was determined using Eq. 2.53 based on the following procedure and assumptions:

- Shear rate for concentric cylinders was calculated according to Eq. 2.47.
- Viscosity functions of mix and foam were extrapolated to shear rates acting in the gap (see Fig. 4.46). The mean value between mix and foam was used since at the inlet there is pure mix while at the outlet there is the fully developed foam.
- An average value between mix and foam density was used to represent the foam product over the entire membrane length.
- Foam was considered a continuum and Eq. 2.53 used to compute the Taylor number.

Taylor vortices were found not suitable for reducing foam bubble sizes since it was not possible to generate foams without massive blow-by at gap 1.5 or 2.0 mm. It is suspected that demixing effects superimposed the desired flow effects due the large density difference between continuous and disperse phase. A flow perpendicular to the rotation is known to shift  $Ta_c$  to higher values [159, 153, 47, 62, 160]. However, Taylor numbers up to  $7 \cdot Ta_c$  were tested here. Also, emulsification results in a similar setup using an axial flow (see Fig. 2.23) showed no shift in critical Taylor number.

### 4.5.5. Mix

The impact of the fluid system on the mean bubble size is demonstrated in Fig. 4.44 for different gas volume fractions. The two fluid systems compared were model system C containing protein (surfactant) and guar gum (thickeners) and

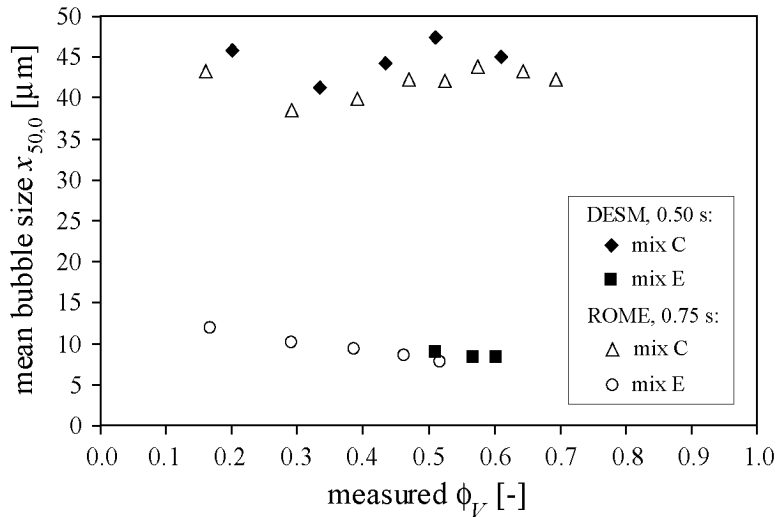


Figure 4.44.: Influence of continuous fluid phase (mix C versus mix E) on resulting mean bubble size. ROME or DESM, circumferential velocity  $18.51 \text{ m} \cdot \text{s}^{-1}$ , gap size  $0.22 \text{ mm}$ , membrane Sefar Nitex 03-6/5.

model system E containing a specific fast surfactant and thickeners. In the case of model system C, the mean bubble size decreases up to gas volume fractions of about 0.3 and tends to increase for higher gas volume fractions. The latter effect is probably caused by bubble coalescence at the membrane due to the smaller pore distance of the Sefar Nitex membrane compared to CPDN membranes (see Sec. 4.5.7) and due to the slow bubble interface coverage by the protein. For model system E, the mean bubble size decreases up to  $\phi_V$  of 0.60 which is the maximum achievable gas volume fraction without blow-by. System E leads to clearly smaller mean bubble sizes (about factor 4). However, higher gas volume fractions were obtained with system C. The reason is that system C contains a significantly higher amount of surfactant (factor 8.3) and additionally, less interface is generated per volume gas due to larger mean bubble sizes. All these observations indicate the advantage of improved interfacial activity (interfacial tension reduction and interface stabilization) of the surfactant used in model mix E compared to the protein used in model system C.

The decrease in mean bubble size with increasing gas volume fraction for foam E is significant (Fig. 4.44, slope better visible in less compacted graph shown in Fig. 4.63) and was suspected to be a consequence of the foam viscosity. Foam viscosity was, thus, measured as a function of the shear rate for mix E and foam E of varying gas volume fraction. The  $\eta(\dot{\gamma})$  curves were approximated using the power law. The flow curves are shifted to higher values of viscosity with increasing gas volume fraction  $\phi_V$ . A higher foam viscosity in the dynamically enhanced

foaming device leads to detachment of smaller bubbles from the membrane and/or probably to enhanced dispersion in the narrow annular gap since the shear stress is linearly dependent on the viscosity in the laminar flow domain (Eq. 2.45). Hence, this dependency of viscosity on gas volume fraction explains the smaller resulting mean bubble size at higher gas volume fraction.

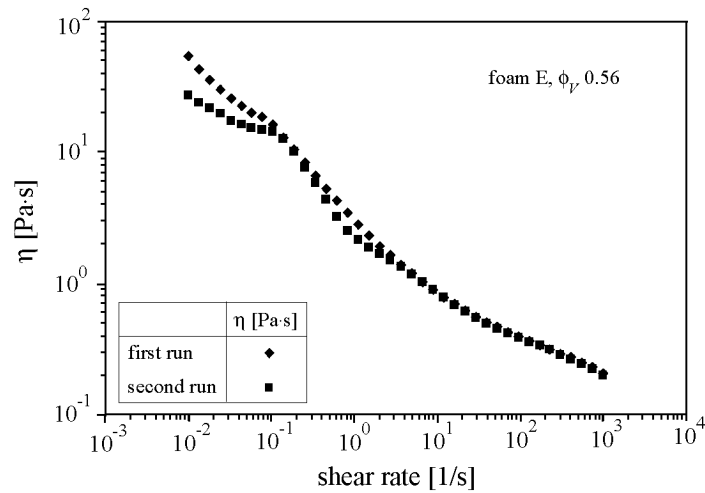


Figure 4.45.: Viscosity as function of shear rate for foam E ( $\phi_V = 0.56$ ). Two runs with identical foam.

When plotting mean bubble size of the foams used for the viscosity measurements versus measured viscosity at production shear rate of  $84\,468\text{ s}^{-1}$  (see Fig. 4.47), the relationship between viscosity and mean bubble size can be approximated as:

$$x_{50,0} = 2.933 \cdot \eta_{\text{foam}}^{-0.358} \quad (4.14)$$

This experimentally found relationship between foam viscosity and resulting mean bubble size may be used to tailor make foam microstructure in a further step by adjusting the continuous phase viscosity such that the smallest achieved mean bubble sizes of  $\sim 8\ \mu\text{m}$  (for mix E achieved at  $\phi_V=0.56$ ) could already be reached at lower gas volume fractions. Assuming that the trend of decreasing  $x_{50,0}$  with increasing  $\phi_V$  persists, even smaller mean bubble size could then be achieved at  $\phi_V=0.56$ .

In addition, the data shown in Fig. 4.47 can be used to evaluate whether bubbles are detached from the pores of the dynamically enhanced membrane foaming device in their final size or are further dispersed in the narrow annular gap flow to the outlet. To test this, two models were applied: (i) model X describing bubble detachment from the membrane derived in Sec. 4.4.2 and (ii) the model  $Ca_c$  derived in Sec. 4.1.2 dealing with breakup of bubbles in simple shear.

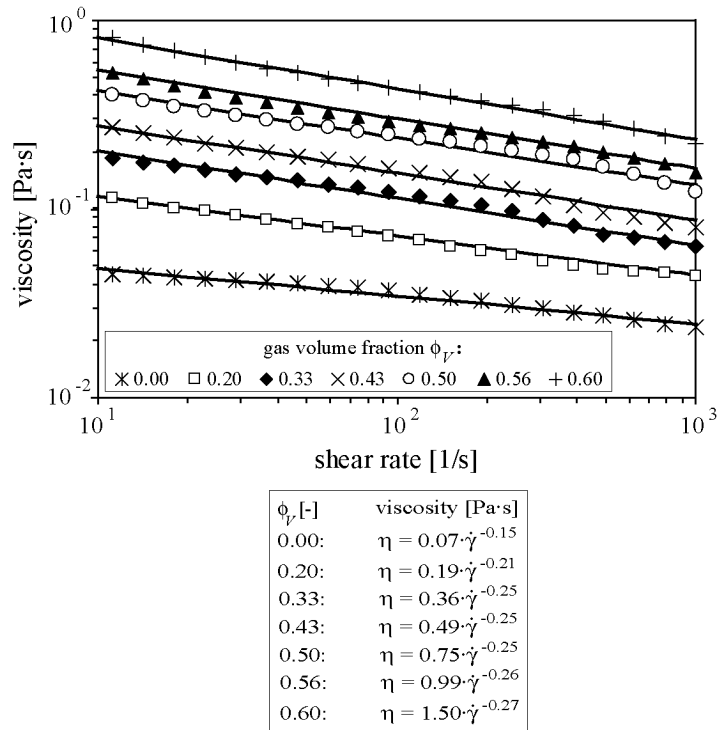


Figure 4.46.: Viscosity  $\eta$  of mix E and foam E with different gas volume fractions as a function of the shear rate  $\dot{\gamma}$ .

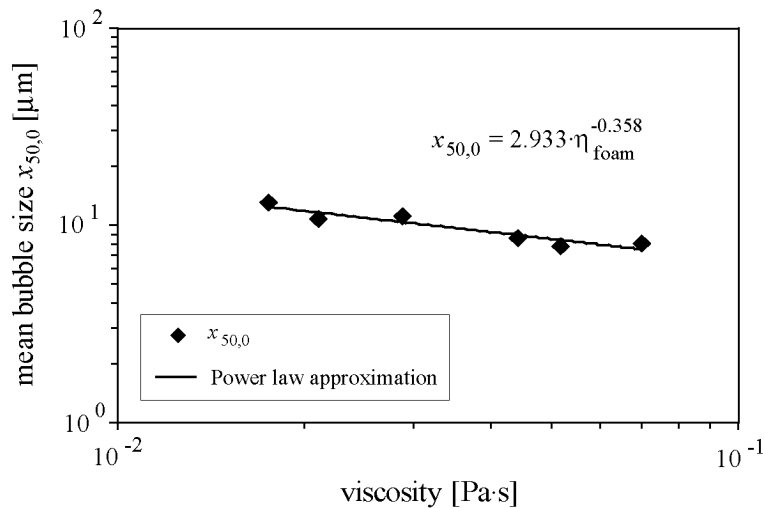


Figure 4.47.: Dependency of mean bubble size  $x_{50,0}$  on foam viscosity. Viscosity extrapolated to  $84\,468 \text{ s}^{-1}$ .

In a first step, model X (Eq. 4.3) for bubble detachment is adapted to the system. Model X computes the mean bubble size detached from a pore as a function of the foam viscosity. Using the Stokes approach to compute the drag coefficient (Eq. 2.35) and  $v_{\text{rel}}$  as defined in Eq. 4.7, the dependency of the size of the detached bubble on the foam viscosity follows as:

$$x_{\text{model X}} = \sqrt[4]{\frac{4 \cdot \sigma \cdot x_P \cdot s^2}{3 \cdot \pi \cdot \eta_{\text{foam}} \cdot \dot{\gamma}}} \quad (4.15)$$

yielding the relationship:

$$x_{\text{model X}} \sim \eta_{\text{foam}}^{-0.25} \quad (4.16)$$

In a second step, model  $Ca_c$  describing possible secondary dispersion in the narrow annular gap is applied to the system. It is based on the calculation of the functional dependency of the critical Capillary number on the viscosity ratio  $\eta_{\text{cont}}/\eta_{\text{disp}}$  discussed in Sec. 4.1.2. Assuming the foam to act as a continuum surrounding each bubble, the relation between mean bubble size and foam viscosity (Eq. 4.2) can be derived as:

$$x_{\text{model } Ca_c} \sim \eta_{\text{foam}}^{-0.829} \quad (4.17)$$

The experimentally found relation between mean bubble size  $x_{50,0}$  and foam viscosity (Fig. 4.47, Eq. 4.14) consequently lies between the relations found for bubble detachment (Eq. 4.16) and for secondary dispersion in the narrow annular gap (Eq. 4.17), but clearly closer to the first. This suggests that the dominating bubble formation process determining the resulting mean bubble size in the dynamically enhanced membrane foaming device is the detachment of small bubbles from the membrane. There is some additional, but less pronounced dispersing effect in the gap.

For the flow curves depicted in Fig. 4.46, a master curve  $\eta(\phi_V, \dot{\gamma})$  was derived for the shift factors  $a_\eta(\phi_V)$  at shear rate  $10^2 \text{ s}^{-1}$ . The master curve shown in Fig. 4.48 led to the approximation

$$a_\eta = 0.117 \cdot e^{4.322 \cdot \phi_V}, \quad (4.18)$$

where the value  $a_\eta = 1$  corresponds to the gas volume fraction 0.50. Eq. 4.18 can be used to predetermine the foam viscosity at any gas volume fraction for the measured system. Additionally, it may in future experiments suffice to measure foam viscosity for  $\phi_V = 0.50$ , only, if the mix recipe is the same. The viscosity of foams with different gas volume fractions can then be derived as a function of the shear rate via the equation:

$$\eta(\phi_V, \dot{\gamma}) = \eta(\phi_V = 0.5, \dot{\gamma}) \cdot a_\eta(\phi_V) \quad (4.19)$$

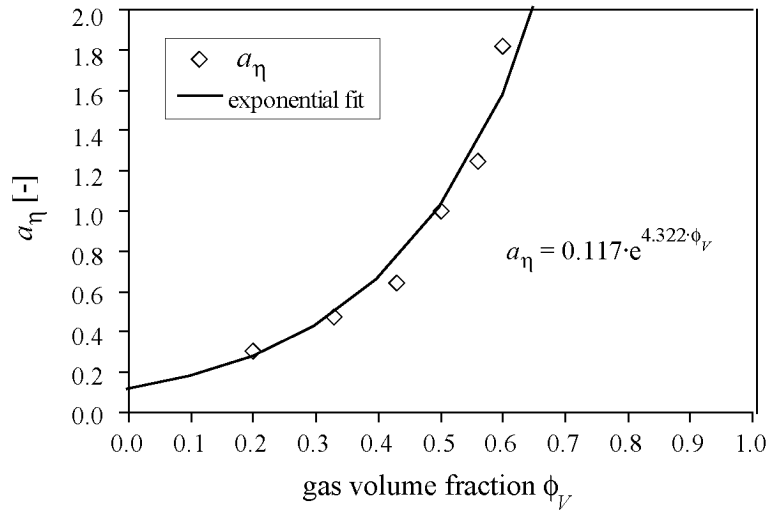


Figure 4.48.: Master curve for flow curves shown in Fig. 4.46 derived at shear rate  $10^2 \text{ s}^{-1}$ .

Up to here, mix C and E were compared which contain totally different ingredients. This resulted in distinct deviations with respect to the resulting foam microstructure. Now, mix B, C and D will be compared which all contained the same two ingredients but differed in their guar content and, thus, zero shear viscosity. Model mix B, C and D contained 5.00 weight % protein and 1.00, 0.50 and 0.25 weight % guar, respectively. The resulting mix viscosities are summarized in Tab. 3.23. Foams were produced with the ROME device, the uncoated CPDN membrane, a gap size of 0.50 mm and a circumferential velocity of  $18.33 \text{ m} \cdot \text{s}^{-1}$  (Fig. 4.49). No consistent and considerable difference between the results obtained with the three model mixes were found. Identical experiments at circumferential velocities of 2.93, 8.06, 13.19 and  $23.46 \text{ m} \cdot \text{s}^{-1}$  led to qualitatively identical result, however, the absolute values of the mean bubble diameters were shifted. Theoretically, a viscosity increase can have positive or negative impact on the mean bubble size: a decrease in coalescence and drainage in the final product and an increase in acting shear stresses on the positive side, hindering of the milk proteins to reach and stabilize the interfaces efficiently on the other side. Here, the negative consequences obviously cancelled the positive ones out. In addition, the difference in viscosity of the three compared, strongly shear-thinning mixes was found to be low at high shear rates like used in the foaming experiments.

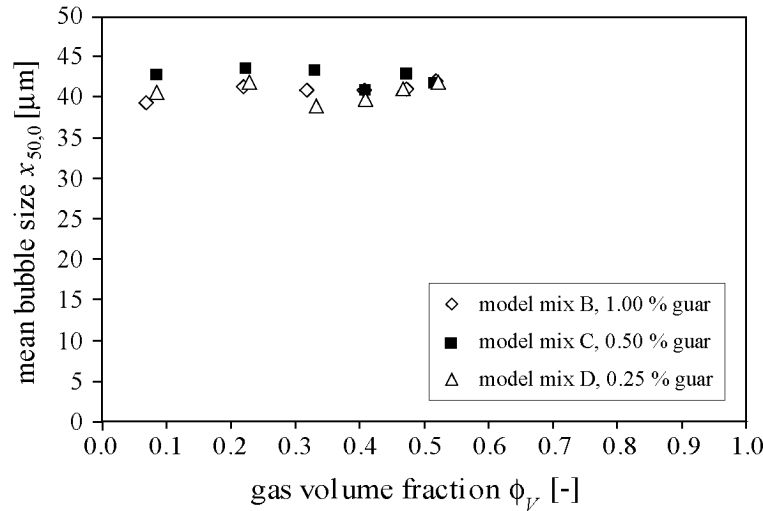


Figure 4.49.: Influence of mix viscosity on mean bubble size. ROME device, uncoated CPDN membrane, gap size 0.50 mm, circumferential velocity  $18.33 \text{ m} \cdot \text{s}^{-1}$ , model mixes B, C and D with 1.00, 0.50 and 0.25 weight % guar content, respectively.

#### 4.5.6. Velocity field

Fig. 4.50 shows the impact of the circumferential velocity and corresponding shear rate on the mean bubble size for the two gas volume fractions 0.43 and 0.56. Mix E was foamed using the DESM device, the sinter membrane, a gap size of 0.22 mm and a residence time of 0.75 s. The mean bubble sizes decrease with increasing circumferential velocity and asymptotically approach a minimum in mean bubble size of about  $8 \mu\text{m}$ . This means that smaller bubbles are detached from the membrane at higher circumferential velocities (i) and/or are further dispersed after detachment in the narrow annular gap flow (ii). Experiments using a single pore membrane and a high speed camera for bubble detachment visualization (see Sec. 4.4) proved (i), while (ii) was shown to be less important in Sec. 4.5.5.

The impact of the shear rate on the mean bubble size was as well systematically investigated for the ROME device, a gap size of 0.50 mm and mix C by varying the circumferential velocity (see Fig. 4.51). The same trends were found as shown in Fig. 4.50 for mix E, the mean bubble sizes were however significantly larger since the gap size of 0.50 mm leads to lower shear rates than 0.22 mm gap and since mix C was shown to result in larger bubbles than mix E.



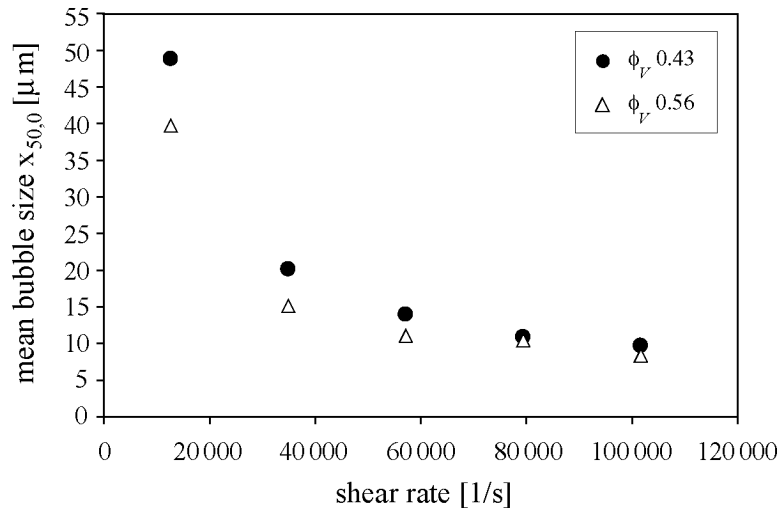


Figure 4.50.: Impact of shear rate on mean bubble size. DESM device, mix E, sinter membrane, gap size 0.22 mm, residence time 0.75 s.

#### 4.5.7. Pore size and pore distance

Fig. 4.51 shows mean bubble sizes as a function of the gas volume fraction for the ROME device and two CPDN membranes differing in pore size by a factor of 3.33 at circumferential velocities ranging from 2.93 to 23.46  $\text{m} \cdot \text{s}^{-1}$ . Trends and absolute values are very similar for both pore sizes: higher circumferential velocity reduces bubble size as expected. For low gas volume fractions, the mean bubble size shrinks with increasing  $\phi_V$ . The slope  $dx_{50,0}/d\phi_V$  is more pronounced for lower circumferential velocities. Above a certain threshold in gas volume fraction, the bubble size is about constant with slight growth tendency. The change from negative to zero or slightly positive slope is observed at low gas volume fraction and high circumferential velocity. The reason for bubble size reduction with increasing gas volume fraction (limit depends on circumferential velocity) is related to the corresponding increase in foam viscosity as described in detail in Sec. 4.5.5. The existence of a dynamic equilibrium between bubble breakup and recoalescence in the gap is supported by: i. The limited bubble size of about 35  $\mu\text{m}$  approached asymptotically with increase in circumferential velocity, and ii. The resulting mean bubble size being significantly larger than the pore size (factor 10 to 33).

Fig. 4.52 depicts the impact of pore size on the mean bubble size at different gas volume fractions for membranes with less defined pore form, size and distance than the CPDN membranes. Two membranes of the same type but differing mean pore size were used and compared for model mixes C and E: SF 03-6/5 with a mean pore size of 6  $\mu\text{m}$  and SF 03-1/1 with a mean pore size of 1  $\mu\text{m}$ . All experiments

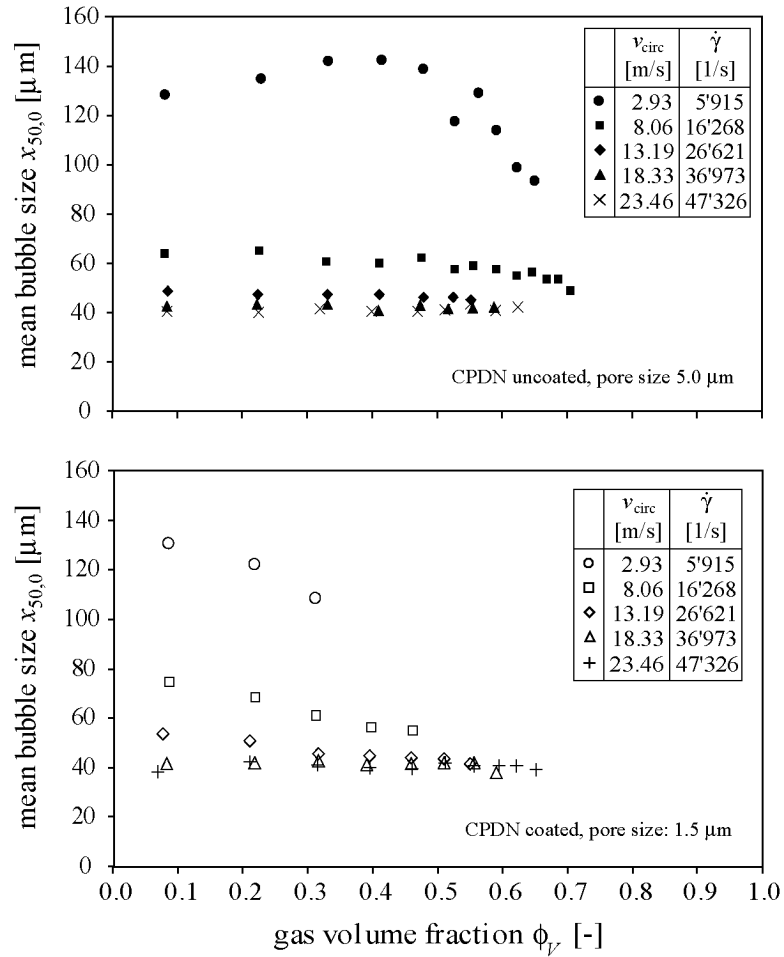


Figure 4.51.: Influence of pore size and circumferential velocity/shear rate on mean bubble size. Uncoated CPDN membrane (upper graph): pore diameter 5.0  $\mu\text{m}$ , coated CPDN membrane (lower graph): pore diameter 1.5  $\mu\text{m}$ . Residence time 0.97 s, gap size 0.5 mm, mix C.

were conducted using a gap size of 0.22 mm, a circumferential velocity of  $18.51 \text{ m} \cdot \text{s}^{-1}$  and a residence time of 0.75 s. The bubble size is in the size range of the pore size for mix E and the membrane SF 03-6/5. However, since the resulting bubble sizes are the same for the membrane SF 03-1/1 and, thus, five times larger than the pore size, it can be deduced that the resulting bubble size is independent of the pore size. For mix C, the pore size plays no role either. The difference in mean bubble size between the two mixes has been discussed before (see Sec. 4.5.5). Two reasons for the independency of bubble on pore size are suggested: i) the pore velocity of the gas which increases at constant residence time of the foam but smaller pore size and smaller open area of the membrane (e.g. 5 % open area for SF 03-6/5, 1 % open area for SF 03-1/1), impacts bubble detachment, and ii) dispersion and/or coalescence in the gap after detachment. i) can be eliminated because residence time was shown to have no impact on the mean bubble size (see Sec. 4.5.9) even though the air velocity is then changed as well. Bals [10] showed a slight change in bubble size with air velocity. Possibility (ii) is supported by the combination of results on single bubble breakup in simple shear (Sec. 4.1.2), on bubble detachment from a rotating single-pore membrane (Sec. 4.4) and on the impact of foam viscosity on the resulting mean bubble size (Sec. 4.5.5) which all together showed that bubble formation in the DEMF device is primarily dependent on the detachment of small bubbles from the membrane with an additional, however less important, effect of bubble breakup in the narrow annular gap.

#### 4.5.8. Type of membrane

The impact of the type of membrane on the mean bubble size should be analyzed for an identical gap size and pore distance. These conditions could not be fully satisfied. The sinter membrane was compared to the uncoated CPDN membrane for mix C at a gap size of 0.50 mm. Fig. 4.53 demonstrates that the two compared membranes had no significantly different impact on the mean bubble size. The sinter membrane tends to lead to slightly smaller mean bubble sizes.

For model mix E and a gap size of 0.22 mm, the sinter membrane and the Sefar Nitex membrane SF 03-6/5 were compared. The clamping fixture of the latter caused cavities of 0.50 mm depth. It is of interest for future experiments and follow-up constructions to prove whether these microcavities have a positive or negative impact on the foaming result with respect to product microstructure. The comparison of these two membrane modules (Fig. 4.54) shows clear differences in mean bubble size which are shifted to significantly smaller values for the SF03-6/5 membrane. This suggests a positive impact of the cage construction used to fix the Sefar Nitex membrane to a cylinder. The microcavities formed by the membrane fixing grid are suspected to create microturbulences (see schematic drawing in Fig. 4.55 and technical drawing in Fig. 3.17). The results suggest that such

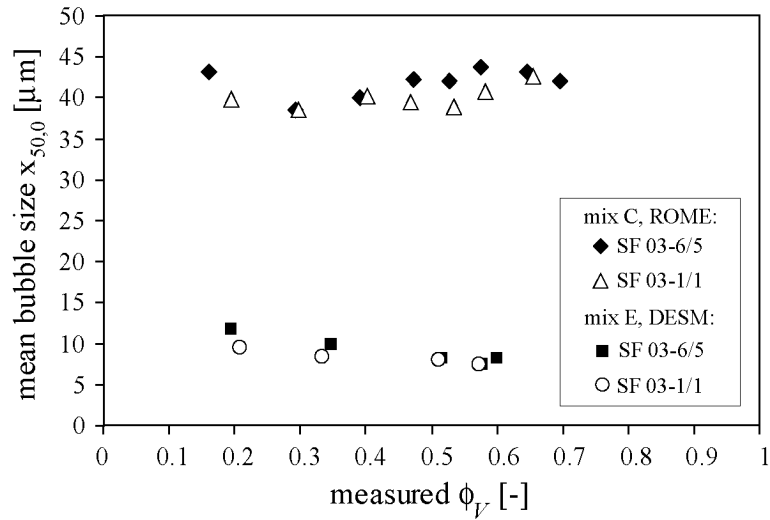


Figure 4.52.: Impact of pore size on bubble size for ROME device using mix C and for DESM device using mix E. Two membranes (see Tab. 3.1) of the same type and differing pore size: SF 03-6/5, pore size 6  $\mu\text{m}$ ; SF 03-1/1 pore size 1  $\mu\text{m}$ . Gap size 0.22 mm, circumferential velocity 18.51  $\text{m} \cdot \text{s}^{-1}$ , residence time 0.75 s.

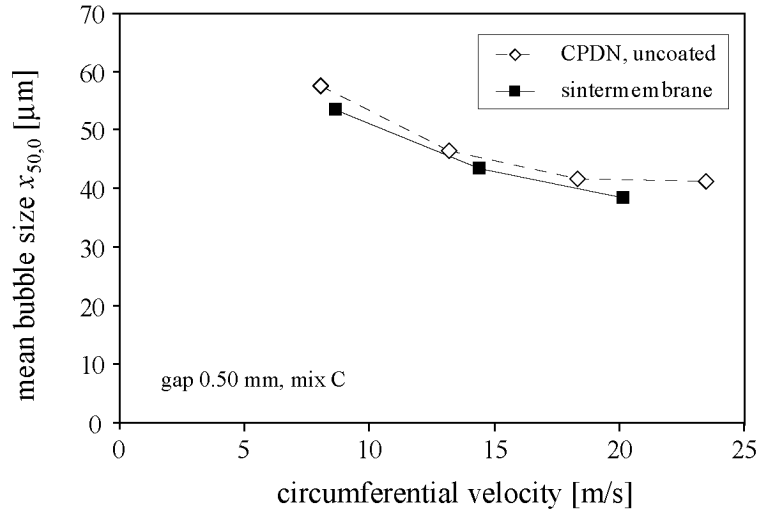


Figure 4.53.: Impact of type of membrane (sinter membrane versus uncoated CPDN membrane) on bubble size for the ROME device at different circumferential velocities. Mix C, gap size 0.50 mm, residence time 1.0 s, gas volume fraction 0.50 for the sinter membrane and 0.52 for uncoated CPDN membrane.

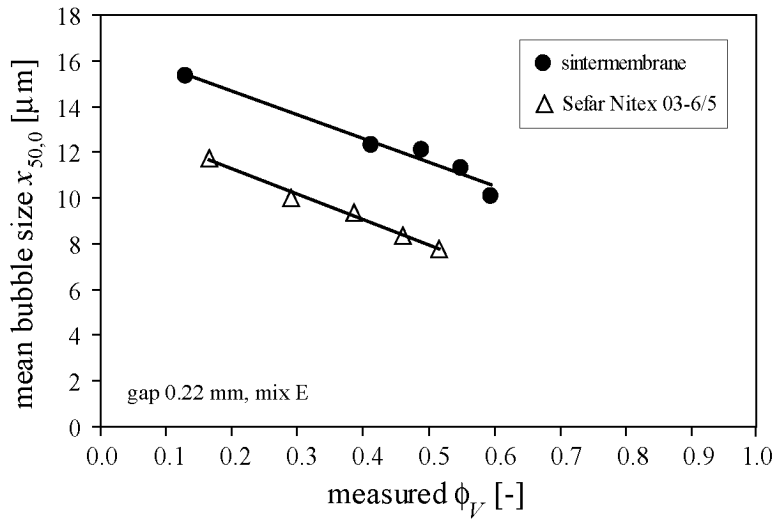


Figure 4.54.: Impact of membrane type and membrane module construction (sinter membrane versus Sefar Nitex membrane) on mean bubble size at various gas volume fractions. ROME device, mix E, gap size of 0.22 mm, circumferential velocity  $18.51 \text{ m} \cdot \text{s}^{-1}$ , residence time 0.75 s.

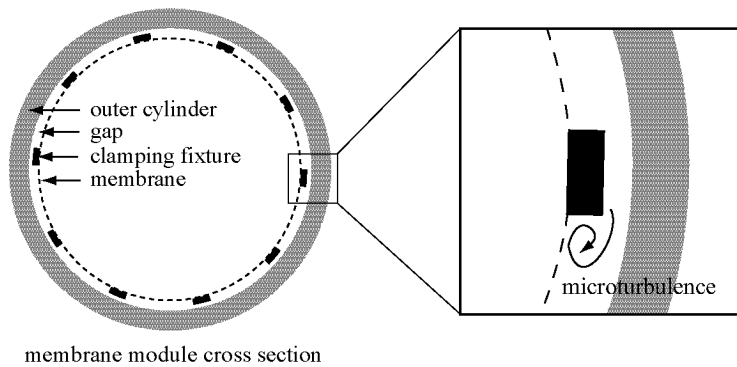


Figure 4.55.: Clamping fixture for Sefar Nitex membrane and microturbulences caused by the microcavities.

microturbulences cause an either improved detachment of the bubbles from the membrane or an improved dispersion of the bubbles in the narrow annular gap.

First selective measurements of mix and foam temperatures at  $18.51 \text{ m} \cdot \text{s}^{-1}$  circumferential velocity and a gap size of 0.22 mm showed that the temperature difference  $\Delta T$  between in- and outlet is  $\sim 7^\circ \text{ C}$  higher when the clamping fixture for Sefar Nitex membranes is used. This could be an indicator for the existence of microturbulences since the relationship "power  $P$  is proportional to the mass specific heat quantity  $Q_m$  which is again proportional to  $\Delta T$ " is assumed to be valid. Microturbulences should cause an increase of  $\Delta T$  with  $n^3$  due to the proportionality  $P \sim n^3$  in turbulent flow fields explained in Sec. 2.5.1. Meanwhile  $\Delta T$  should be proportional to  $n^2$  in the laminar flow field since  $P \sim n^2$ . To prove the occurrence of microturbulences, systematic temperature measurements at different circumferential velocities have to be carried out using mix E which is not susceptible to changes in foam microstructure up to  $T = 45^\circ \text{ C}$ .

### 4.5.9. Residence time

The minimal residence time and maximum foam volume flow rate, respectively, were determined using the DESM device, the Sefar Nitex SF 03-6/5 membrane, a circumferential velocity of  $18.51 \text{ m} \cdot \text{s}^{-1}$ , a gap size of 0.22 mm and model mix E. The results are shown in Fig. 4.56. The residence time was stepwise decreased and gas volume fractions from 0.50 up to the highest possible one were tested.

Evaluation criteria for still satisfactory results were:

- Gas volume fractions up to at least 0.56 without blow-by obtainable.
- Mean bubble size in the range of mean bubble diameter  $\pm 50\%$  at the optimum residence time of 0.75 s.
- Reproducible results.

Independent of the residence time, the mean bubble size decreases with increasing gas volume fraction. The maximum achievable gas volume fraction decreases with decreasing residence time, it was however always possible to produce foams up to gas volume fraction 0.56. The data could only be reproduced down to 0.4 s residence time, lower residence times worked one day but not the next and should consequently not be taken for granted. The maximum foam flow rate in the DESM device with a gap volume of  $2.272 \cdot 10^{-3} \text{ l}$  is, thus,  $20.45 \text{ l} \cdot \text{h}^{-1}$ , corresponding to a residence time of 0.40 s in the gap. Compared to a rotor-stator device, the residence time is less important by far in the dynamically enhanced membrane foaming device and can be as low as 0.40 s since the bubble formation is not dominated by bubble breakup but is instead dependent on the detachment of small bubbles from the membrane.

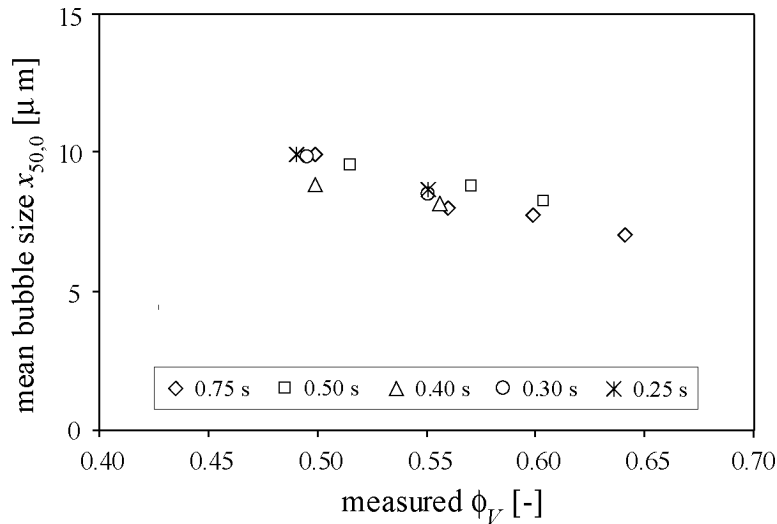


Figure 4.56.: Impact of residence time on mean bubble size. DESM device, mix E, gap width 0.22 mm, circumferential velocity  $18.51 \text{ m} \cdot \text{s}^{-1}$ .

#### 4.5.10. Membrane area

The relationship between membrane area and foaming result, i.e. maximum gas volume fraction and mean bubble size, was determined using the membrane Sefar Nitex SF 03-6/5 since the clamping fixture allowed the desired adaptation of membrane area. The clamping fixture for woven fabrics has fifty membrane windows arranged in 5 axial rows of 10 windows (one window row = one unit). To determine the impact of the membrane area, the foaming results obtained with the total five units was compared to three and one units. The unused window rows were stringed with a plastic film and were placed at the head inlet to avoid a, relative to the membrane area, prolonged shearing of the bubbles in the narrow annular gap. Fig. 4.57 shows the received impact of membrane area (5 units versus 3) on mean bubble size and maximum gas volume fraction for the DESM device, the membrane SF 03-6/5, circumferential velocity  $18.51 \text{ m} \cdot \text{s}^{-1}$ , gap size 0.22 mm and mix E. Gas volume fractions between 0.50 and the highest value possible without blow-by were tested. It was not possible to produce foam with one unit only, blow-by could not be avoided at any parameter setting. Comparing three and five units, no significant impact of membrane area on mean bubble size, maximum gas volume fraction or minimum residence time was found. Three units allowed shorter residence time than five units on one experimental day, this result could however not be reproduced. Already formed bubbles are obviously not influenced by increased coalescence or dispersion during a longer passage through the narrow annular gap of the foaming head. This agrees well with the results discussed in Sec. 4.5.5 which

suggest that bubble detachment is the primarily important bubble formation step in the DEMF device while bubble dispersion in the narrow annular gap is of minor impact.

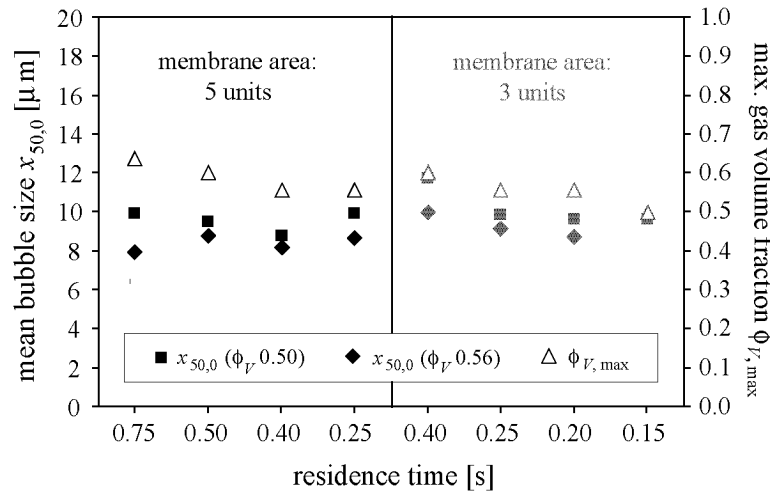


Figure 4.57.: Impact of membrane area on mean bubble size for different residence times. DESM device, mix E, gap width 0.22 mm, circumferential velocity  $18.51 \text{ m} \cdot \text{s}^{-1}$ .

#### 4.5.11. Scale-up calculations from lab- to pilot-scale DESM

For scale-up calculations, both fluid-dynamics and the structuring-dynamics similarities had to be considered. The fluid dynamics conditions are determined by the shear rate and the shear stress. The shear rate was adapted to  $\sim 84\,468 \text{ s}^{-1}$  for lab- and pilot-scale device via the rotational speed since the gap size was kept identical at 0.22 mm. The shear stress was not explicitly taken into account because it is directly correlated to the shear rate (Eq. 2.45). For structuring-dynamics similarity, the shear rate, shear stress and residence time are crucial. Although the results shown in Sec. 4.5.9 showed no impact of the residence time on the resulting mean bubble size in the investigated range when using the clamping fixture with the SF 03-6/5 membrane, it was decided to keep the residence time for lab-scale and pilot-scale device identical at 0.75 s. It was further decided to use the sinter membrane for the pilot-scale device even though it was shown in Sec. 4.5.8 that the clamping fixture leads to smaller mean bubble sizes due to microturbulences caused by the indentations. The reasons for this decision were that the sinter membrane is (i)



robust, (ii) CIP-cleanable, (iii) self-supporting and (iv) commercially available in its final cylindrical form.

The length to diameter ratio of lab- and pilot-scale device was chosen similar instead of keeping the length constant. This decision was based on (i) results shown in Sec. 4.5.10 which showed that a prolonged passage through the narrow annular gap did not affect the resulting foam microstructure and on (ii) the fact that larger device dimensions are of advantage with respect to product flow rate. Details of all used equations for scaling calculations are shown in Sec. 3.3.4. Tab. 4.7 gives an overview of the results of the scale-up calculations for both the lab-scale and pilot-scale device.

Table 4.7.: Results of scale-up calculations of DESM device from lab- to pilot-scale.

	Unit	Lab-scale device	Pilot-scale device
Length	[mm]	60	195
Rotor radius	[mm]	27.28	97.78
Stator radius	[mm]	27.50	98.00
Gap size	[mm]	0.22	0.22
Head volume	[l]	$2.272 \cdot 10^{-3}$	$26.386 \cdot 10^{-3}$
Gas volume fraction	[-]	0.56	0.56
Residence time	[s]	<i>0.75</i>	<i>0.75</i>
Total flow rate	[l · h <sup>-1</sup> ]	10.90	126.70
Optimum rotational speed	[rpm]	6479	1813
Shear rate	[s <sup>-1</sup> ]	<i>84 468</i>	<i>84 477</i>
Foam viscosity	[Pa · s]	0.052	0.052
Mix density	[kg · m <sup>-3</sup> ]	1125.0	1125.0
Air density	[kg · m <sup>-3</sup> ]	1.2	1.2
Foam density	[kg · m <sup>-3</sup> ]	495.0	495.0
Mean bubble size	[µm]	10	10
<i>Re</i>	[-]	88.361	88.628
<i>Ne</i>	[-]	1.828	1.824
<i>C</i> -value	[-]	1 290 435	360 088
<i>v</i> <sub>sink</sub>	[m · s <sup>-1</sup> ]	1.525	0.425
Separation time	[s]	0.0001	0.0005
<i>P</i> <sub>V,diss</sub>	[kW · m <sup>-3</sup> ]	369 895	369 968
<i>P</i> <sub>diss</sub>	[kW]	0.840	9.762
<i>E</i> <sub>diss</sub>	[kJ]	0.630	7.319

It is possible to reach the desired values in shear rate and residence time in the up-scaled device and at the same time keep the optimum gap size of 0.22 mm and

ratio of head length to diameter. Due to the lower circumferential velocity needed to reach the desired shear rate in the pilot-scale device, the  $C$ -value is lower. This is advantageous because centrifugal de-mixing effects will, thus, be reduced.

### 4.5.12. Results obtained with pilot-scale DESM device

Fig. 4.58 shows the resulting mean bubble sizes obtained with the scaled-up DESM device (pilot scale). The relation between gas volume fraction and resulting foam microstructure is depicted for two residence times and two shear rates.

The results (Fig. 4.58) show that the mean bubble size decreases with increasing gas volume fraction for all investigated settings. Blow-by free foam production was possible within a gas volume fraction range of (i) 0.5 and (ii) 0.7: (i) For  $\phi_V$  smaller than 0.5, the relatively low foam viscosity enhances a separation of mix and air since the bubble mobility is high. (ii) At gas volume fractions above 0.7, the lamellae are very thin and rupture happens more easily, enhancing foam destruction in the gap. Gas volume fractions between 0.5 and 0.7 seem to be ideal with respect to foam viscosity and lamellae thickness, thus resulting in homogeneous, stable, blow-by free foams.

The residence time influences the microstructure in so far that the slope of the curves is steeper at longer residence time, the mean bubble size decreases more strongly with increasing gas volume fraction for 1.00 s residence time compared to 0.75 s residence time. This means that a residence time of 1.00 s allows to reach a further optimized dispersion quality when using the sinter membrane, possibly due to an enhanced dispersion in the narrow annular gap. Additionally, slightly higher gas volume fractions can be obtained without blow-by at 1.00 s residence time compared to 0.75 s residence time. It can not be said whether this improved dispersion quality at 1.00 s residence time differs for pilot- and lab-scaled device since this residence time was never tested for the lab-scale device at gap size 0.22 mm. A residence time of 0.50 s was tested for the pilot-scale DESM device as well, the results are not shown since it was only possible to get blow-by free foams at shear rate  $94868 \text{ s}^{-1}$  for the residence time 0.50 s and since the window of achievable gas volume fraction was considerably narrower ( $0.60 < \phi_V < 0.67$ ). An increased shear rate ( $94868 \text{ s}^{-1}$  compared to  $74124 \text{ s}^{-1}$ ) leads to a curve shift to smaller mean bubble sizes (Fig. 4.58). This means that the higher shear rate leads to earlier detachment from the membrane and/or better dispersion in the narrow annular gap. Additionally, the mean size decreases faster with increasing gas volume fraction at higher shear rate. This trend can be expected since the shear stress equals the product of viscosity and shear rate in laminar flow conditions (see Eq. 2.45). The combination of higher viscosity at higher gas volume fraction and higher shear rates is obviously best with respect to the resulting mean bubble sizes.

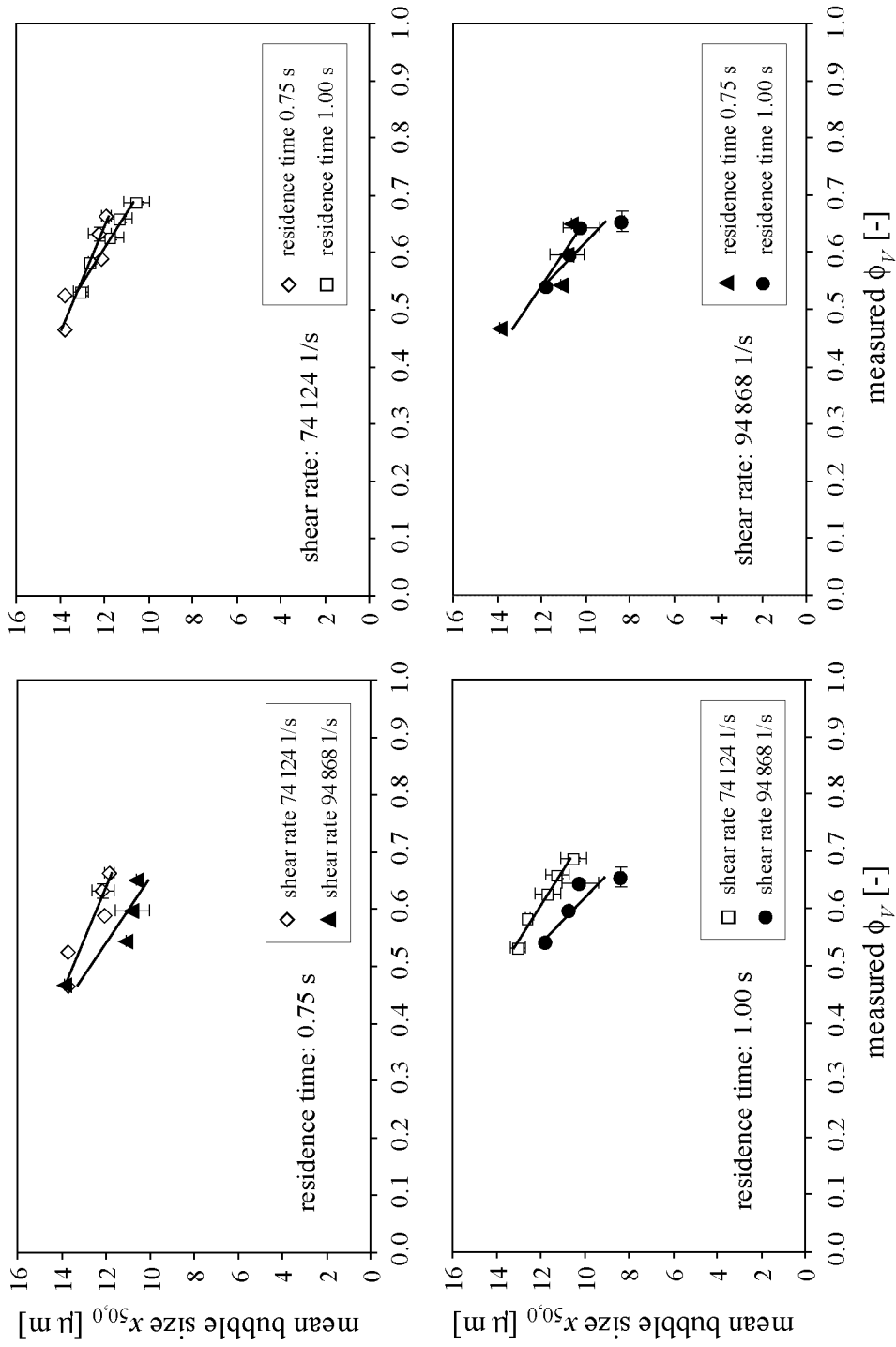


Figure 4.58.: Impact of shear rate and residence time on mean bubble size of foams obtained with pilot-scale DESM device. Sinter membrane, gap 0.25 mm, mix E.

### 4.5.13. Comparison of lab- and pilot-scale device

The lab-scale ROME, lab-scale DESM and pilot-scale DESM device were compared at different gas volume fractions with respect to resulting foam microstructure in Fig. 4.59. All foams were produced using the sinter membrane, mix E and a residence time of 0.75 s. The gap size of the pilot-scale DESM device was slightly larger (0.250 mm instead of 0.230 (lab-scale ROME) or 0.235 mm (lab-scale DESM)) due to differences in raw membrane quality. Hence, the circumferential velocity of  $18.51 \text{ m} \cdot \text{s}^{-1}$  led to shear rates of  $74\,124 \text{ s}^{-1}$  only for the pilot-scale DESM device while for both the lab-scale ROME and the lab-scale DESM device, the shear rate was  $\sim 80\,000 \text{ s}^{-1}$ . Thus, a higher circumferential velocity of  $23.69 \text{ m} \cdot \text{s}^{-1}$  was tested for the pilot-scale DESM device as well, leading to a shear rate of  $94\,868 \text{ s}^{-1}$ .

The curves for the lab-scale ROME, the lab-scale DESM and the pilot-scale DESM device are close together with some differences in slope. No consistent trend can be found for the deviation in bubble size and curve slope between the different device types. While a shear rate of  $74\,124 \text{ s}^{-1}$  led to larger mean bubble sizes for the pilot-scale DESM device, a shear rate of  $94\,868 \text{ s}^{-1}$  led to values very similar to the lab-scale device. This was to be expected since the shear rate does have a significant impact on the mean bubble size. A clear distinction between ROME and DESM device can be made with respect to the achievable gas volume fraction. No gas volume fractions below 0.4 and 0.5, respectively, could be achieved with the lab- and pilot-scale DESM device, while this was possible when using the ROME device. No explanation was found for this difference.

The three devices were furthermore compared in Fig. 4.60 with respect to the impact of shear rate on resulting foam microstructure. The impact of the shear rate on the resulting mean bubble sizes in the dynamically enhanced membrane foaming process was discussed in detail in Sec. 4.5.6 for the lab-scale DESM device and the sinter membrane. It was shown that resulting mean bubble sizes are smaller at higher shear rates due to an earlier bubble detachment from the membrane and/or an additional bubble dispersion in the narrow annular gap. Values obtained for the lab-scale ROME and the pilot-scale DESM device were additionally included in Fig. 4.60. The results show that the dependency of mean bubble size on the shear rate is similar for both the lab-scale ROME device, the lab-scale DESM device and the pilot-scale DESM device.

The comparison between lab- and pilot-scale DESM device verifies that appropriate scale-up criteria were chosen.

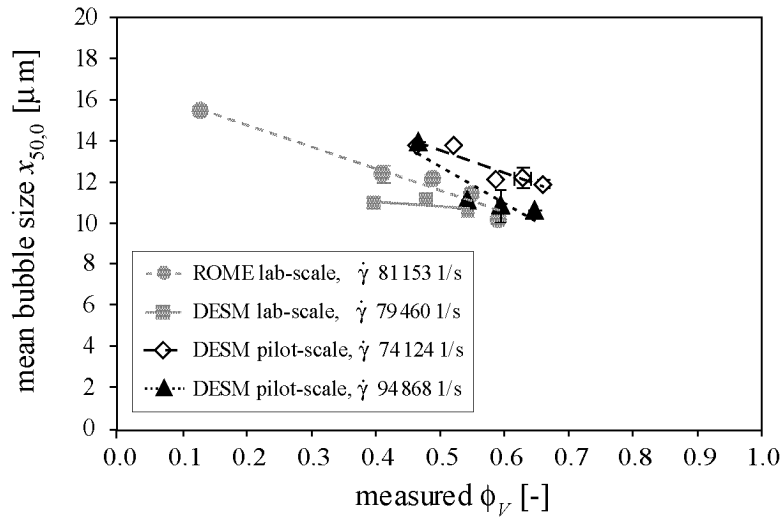


Figure 4.59.: Mean bubble sizes as function of gas volume fraction for lab-scale ROME, lab-scale DESM and pilot-scale DESM device. Sinter membrane, mix E, residence time 0.75 s. Small ROME: gap size 0.230 mm, shear rate  $81\,153\text{ s}^{-1}$ , small DESM: gap size 0.235 mm, shear rate  $79\,460\text{ s}^{-1}$ , large DESM device: gap size 0.250 mm, shear rates  $74\,124$  and  $94\,868\text{ s}^{-1}$ .

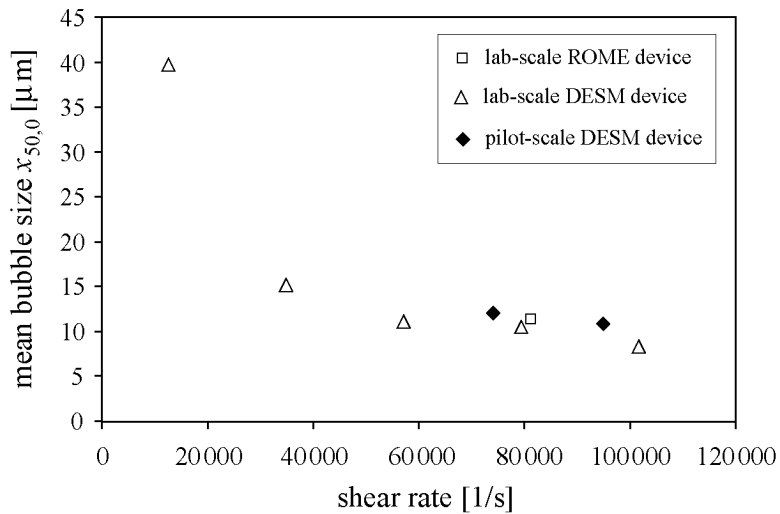


Figure 4.60.: Impact of shear rate on mean bubble size for lab-scale ROME and DESM and pilot-scale DESM device. Sinter membrane,  $t_V$  0.75 s, gas volume fraction 0.56, mix E.

## 4.6. Comparison of R/S, ROME and DESM device

In the following, the most important results for the rotor-stator device (R/S) and the two types of dynamically enhanced membrane foaming device (ROME and DESM) are summarized for direct comparison.

### 4.6.1. Power characteristics

The power characteristics shown in Fig. 4.61 show that the laminar flow domain is predominant for the dynamically enhanced membrane foaming device (DEMF) while the turbulent flow region dominates for the rotor-stator device. The critical *Re*-number representing the transition between laminar and turbulent flow is 1095 for the DEMF device while it is 43 for the R/S device. The laminar flow region is advantageous with respect to power consumption and mechanical gentleness while the turbulent flow region is known to be most effective for bubble break-up if the process depends on dispersion efficiency. However, since the bubble formation mechanism in the DEMF device is dominated by the detachment of small bubbles from the pores of the membrane instead of bubble breakup as in the R/S device, it is even an advantage with respect to the resulting microstructure to foam in the laminar flow domain. The reason for the different onset of the turbulent flow domain is the aeration head geometry: the surface of the membrane is flat, no obstacles disturb the well defined laminar flow. Contrarily, the dispersing zone of the rotor-stator device is built of intermeshing pins. Typical dispersing conditions ( $Re_{\text{typ}}$ ) for the two devices show that foaming takes place in the laminar flow domain for the DEMF device and in the turbulent flow domain for the R/S device (for calculation see Sections 4.3.1 and 4.5.1).

### 4.6.2. Impact of gas volume fraction on mean bubble size

Fig. 4.62 shows the mean bubble size as a function of the gas volume fraction for mix C and the ROME and R/S device at nearly identical circumferential velocities of  $8.06$  and  $8.04 \text{ m} \cdot \text{s}^{-1}$ , respectively. Since the gap size of the ROME device was half as large for the ROME device ( $0.5 \text{ mm}$  compared to  $1.0 \text{ mm}$ ) and the rotor diameters similar ( $0.056 \text{ m}$  compared to  $0.051 \text{ m}$ ), the corresponding shear rate is about twice as large ( $16\,268 \text{ s}^{-1}$  for ROME (Eq. 2.47),  $8\,040 \text{ s}^{-1}$  for R/S (Eq. 2.46). Optimum foaming conditions were chosen for each fluid system in the comparison of foams produced with mix E and either the R/S, ROME and DESM device in Fig. 4.63.

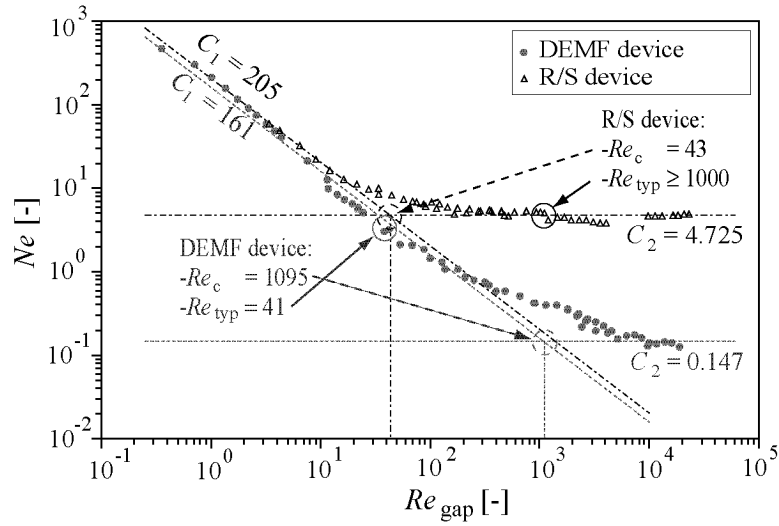


Figure 4.61.: Power characteristics of DEMF and R/S device. Constants  $C_1$  and  $C_2$  were estimated,  $Re_c$  derived. Typical aeration conditions are marked,  $Re_{gap}$  was computed including  $\pi$ .

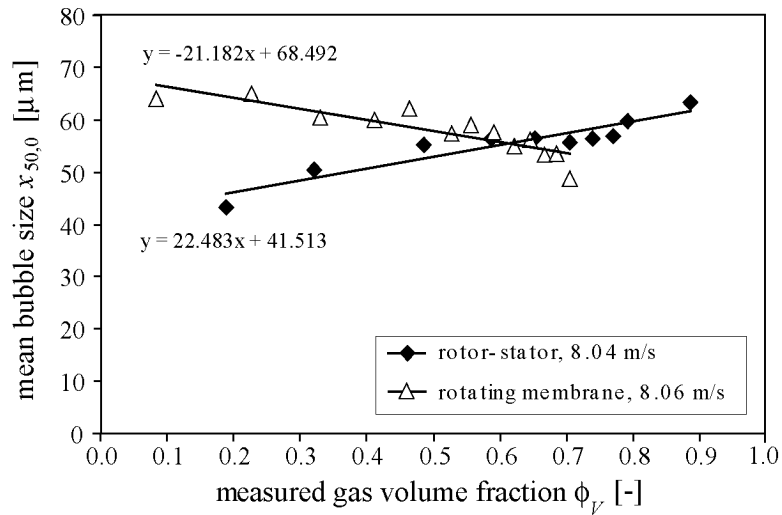


Figure 4.62.: Comparison between foams produced with ROME (gap size 0.5 mm, residence time 0.97 s) and R/S device (gap size 1.0 mm, residence time 10.86 s). Model system C, circumferential velocity, 8.06 and 8.04  $\text{m} \cdot \text{s}^{-1}$ , respectively.

Both Figs. 4.62 and 4.63 highlight the clearly different curve trends of the rotor-stator device on one side and the two types of dynamically enhanced membrane foaming device (ROME and DESM) on the other side. For the R/S device, the mean bubble size increases with increasing gas volume fraction while it decreases with  $\phi_V$  for the ROME and the DESM device. For the turbulent flow field present in the rotor-stator device, viscosity does not play a role with regard to the foaming result. However, density influences the Reynolds shear stress in the turbulent flow field according to Eqs. 2.50 and 2.51. Since the foam density decreases with increasing gas volume fraction  $\phi_V$ , the increase in bubble size with increasing  $\phi_V$  could be expected for the rotor-stator device. In the laminar flow domain acting in the gap of the dynamically enhanced membrane foaming device, the opposite tendency, i.e. smaller bubbles with increased gas volume fractions, is expected: the increased viscosity at increased gas volume fraction (shown in Fig. 4.46) leads to correspondingly increased shear stresses and consequently to earlier detachment of the bubbles from the membrane and to a possibly enhanced dispersion in the narrow annular gap.

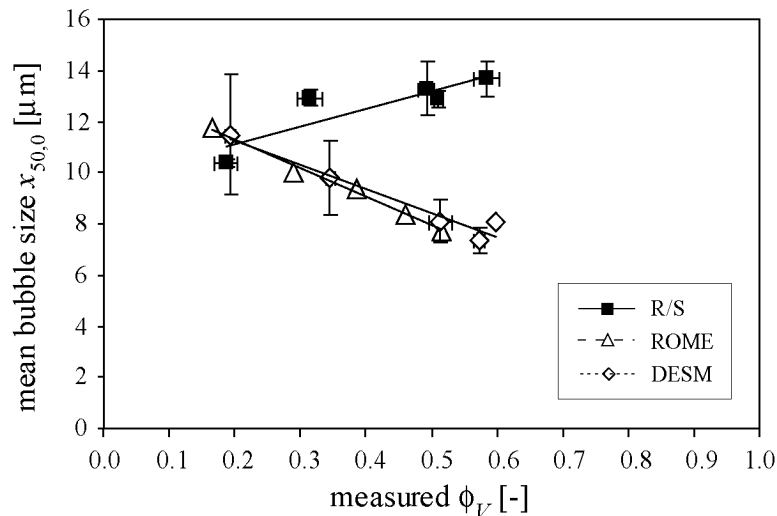


Figure 4.63.: Impact of gas volume fraction on mean bubble size for foams produced with ROME (gap size 0.22 mm, residence time 0.75 s), DESM (gap size 0.22 mm, residence time 0.75 s) and R/S device (gap size 1.0 mm, residence time 14.00 s) with mix E at optimized circumferential velocities for each device (ROME and DESM:  $18.51 \text{ m} \cdot \text{s}^{-1}$ , R/S:  $10.81 \text{ m} \cdot \text{s}^{-1}$ )

The distribution width  $x_{90,0}/x_{10,0}$  is smaller for the membrane devices compared to the R/S device (see Fig. 4.64). This effect is more pronounced at higher gas volume fractions. Since bubble dispersion between rotor and stator is the predominant



bubble formation mechanism in the rotor-stator device, but of little importance in the dynamically enhanced membrane foaming device, this difference in distribution width was to be expected.

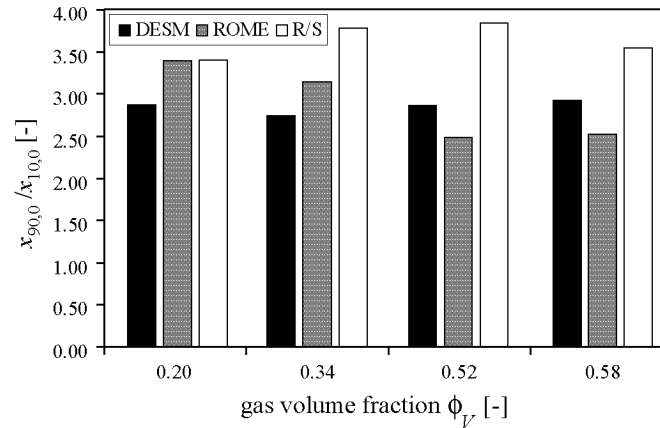


Figure 4.64.: Distribution widths of foams produced with ROME (gap size 0.22 mm, residence time 0.75 s), DESM (gap size 0.22 mm, residence time 0.75 s) and R/S device (gap size 1.0 mm, residence time 14.00 s) with mix E, circumferential velocities optimized for each device (ROME and DESM:  $18.51 \text{ m} \cdot \text{s}^{-1}$ , R/S:  $10.81 \text{ m} \cdot \text{s}^{-1}$ )

### 4.6.3. Dispersing characteristics

Depending on circumferential velocity and gap size, the real shear rates in the laminar DEMF device flow are roughly one- to ten-fold the values of the apparent/representative shear rates in the turbulent R/S flow. However, such different shear rates should in principle not be compared. The attribute "gentle" is used for the membrane device since bubbles are already formed at the membrane surface and detached by the acting shear stresses close to their final size if the bubble interface gets stabilized fast enough by surfactants. Supposably, only few breakup events occur in the gap. In the R/S device, large gas portions/bubbles have to be cut down to the final equilibrium mean bubble size by a series of break-up steps. As a consequence, layers of adsorbed surfactants are repeatedly torn apart. This leads to increased mechanical treatment, in particular of surfactant molecules, and may cause a loss of microstructuring efficiency of such molecules.

Fig. 4.65 shows the mean bubble size as a function of the volumetric energy input (dispersing characteristics or energy density plot) and volumetric power input (energy dissipation rate) for the two devices. The measurements were obtained

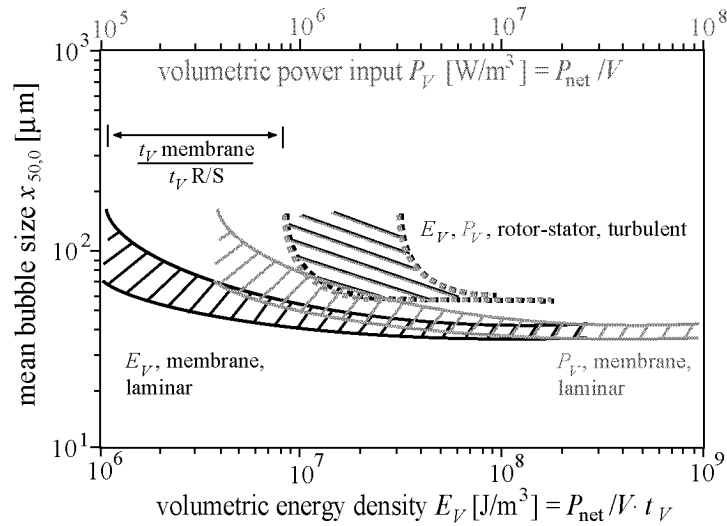


Figure 4.65.: Dispersing characteristics ( $x_{50,0} = f(E_V)$ ) and energy dissipation rates ( $x_{50,0} = f(P_V)$ ) of the DEMF and R/S device.

at various gas volume fractions and circumferential velocities using mix A (R/S device) and C (DEMF device). The volumetric energy input couples power input and mean residence time. The energy dissipation rate (=volumetric power input) focuses on the acting stresses only and disregards time dependency. If the mean residence times are known, one can easily shift the curve  $x_{50,0}=f(E_V)$  to  $x_{50,0}=f(P_V)$ . Since the residence time of the two devices are very different (about factor 10 longer in the R/S device), the energy density plot allows for good differentiation with respect to the specific dispersing apparatus characteristics. If the product damage mechanism however depends on the acting stresses (mainly viscous friction based in the laminar membrane device, inertia force based in the R/S device), the power dissipation rate allows for better differentiation. The plot depicting the mean bubble size as a function of the energy dissipation rate shows that the power input required to reduce the mean bubble diameter seems to be approximately independent from the device used. An exemplary bubble diameter of 60  $\mu\text{m}$  is reached at approximately identical volumetric power input but about ten times lower volumetric energy input for the membrane device than for the rotor-stator device. The energy and power density plot show minima in mean bubble size  $x_{50,0}$  for both devices: approximately 35  $\mu\text{m}$  for the DEMF device and 60  $\mu\text{m}$  for the R/S device. The minimum is lower for the membrane device since the effect of centrifugal de-mixing is less pronounced in its laminar flow field compared to the turbulent flow field acting in the R/S device. Additionally, mix C was shown to lead to about 10 % smaller mean bubble size than mix A (see Fig. 4.21).

## 5. Conclusions and Outlook

The new dynamically enhanced membrane gas dispersion/whipping processes for foam production are described and compared to results obtained with a commonly used rotor-stator device. It is shown that the foam microstructure can be significantly improved, i.e. smaller mean bubble sizes and narrower size distributions can be achieved. In the following, the main findings are summarized and possibilities for further optimization given. The chapter is divided into five sections: single bubble deformation and breakup (i), impact of static pressure on foam microstructure (ii), bubble detachment from the pore of a rotating membrane (iii), dynamically enhanced membrane foaming (iv) and scale-up of DESM device (v).

### 5.1. Single bubble deformation and breakup

Experiments in a parallel band apparatus and a transparent concentric cylinder construction allowed the observation of bubble deformation and breakup, respectively. It was shown in parallel band experiments that bubbles can be deformed strongly without achieving breakup, that breakup does not happen during relaxation and that the deformed bubbles have very thin, pointed ends. It was possible to achieve bubble breakup in experiments using the transparent concentric cylinder construction at critical Capillary numbers  $Ca_c$  in the range of 29 to 45. The corresponding viscosity ratios were between  $3.1 \cdot 10^{-7}$  and  $6.7 \cdot 10^{-8}$ , respectively. Such high critical Capillary numbers explain why very small bubbles can only be achieved at high shear rates. Bubble breakup was found to be different from drop breakup in two distinct ways: i. Even though a surfactant free system was used, tip breakup occurred. ii. No clear distinction between tip breakup and total breakup was found for bubbles. Instead the size of the detached tip grew with increasing shear rate. From the fact that tip breakup occurs instead of total breakup, it can also be derived that the residence time has a governing impact on bubble size if the foaming process is dispersion-controlled: it takes time to split up one bubble into several smaller ones via tip breakup. If the residence time is not long enough, wide size distributions will result.

It is certainly of interest to go one step further in such investigations by introducing surfactants into the system. This is expected to either accelerate the tip

breakup process dramatically or may directly lead to total bubble fracture.

With respect to foam production, it is advantageous to use foaming processes like the rotating membrane (ROME) or dynamically enhanced static membrane (DESM) devices where small bubbles are introduced into the system by flow enhanced detachment from a membrane surface. Compared to this, many breakup steps are necessary for the same result in conventional rotor-stator foaming where the air is introduced as big bubbles to be dispersed stepwise.

## 5.2. Impact of static pressure on foam microstructure

The pressure applied to the whipping head during foaming has shown a strong impact on the resulting foam microstructure. Static pressures acting in the rotor-stator whipping head during foaming between 0.6 bar absolute and 4.0 bar absolute were used. It was demonstrated that bubble size changes with pressure according to the ideal gas law. Coalescence effects counteracted the impact of pressure. For rotor-stator whipping, foaming at atmospheric pressure led to the smallest bubble sizes in the final product compared to foaming under increased pressure or partial vacuum conditions.

It is up to date common in industrial foam production to incorporate the gas at increased pressure since the gas volume is accordingly smaller in the whipping head and blow-by can be prevented more easily. The results of this work however show that it is preferable to foam at atmospheric pressure when using a rotor-stator whipping device. Foam recipes and foaming devices should be developed such that the desired gas volume fraction can be achieved at atmospheric pressure.

If the combination of dynamically enhanced membrane foaming device and recipe allowed to reach e.g. double of the gas volume fraction desired in the final product, the application of partial vacuum conditions (e.g. 0.50 bar absolute) would theoretically lead to even smaller bubbles because the resulting mean bubble size was found to be smaller at larger gas volume fractions in the DESM device.

## 5.3. Bubble detachment from single pore of rotating membrane

In order to obtain insight into the dynamically enhanced membrane foaming process, a transparent jacket was built which allowed to observe bubble detachment from the pore of a single-pore membrane. At higher shear rates achieved through faster rotation of the membrane, bubbles were detached in an earlier stage of formation,

thus, leading to smaller resulting bubbles. A balance of forces based model considering the most important forces acting in the rotating membrane device was derived and showed good agreement with experiments using a single-pore membrane. It was further demonstrated that bubbles do not adhere to the membrane but float freely and have an approximately spherical shape until detachment. The same model computations however resulted in an overestimation of the mean bubble diameter up to a factor of 2.8 when compared to foaming experiments using multi-pore membranes and in an underestimation of the decrease in mean bubble size with increasing shear rate.

Future experiments on bubble detachment should be done using continuous phases of different viscosity to verify its impact on the size of the detached bubbles. The model suggests that a higher viscosity of the continuous phase leads to the detachment of smaller bubbles. Similar conclusions were drawn from foaming experiments where the mean bubble size is lower at higher gas volume fraction due to corresponding higher foam viscosity. In addition, membranes of different hydrophilicity should be tested to determine the impact of wettability and corresponding contact angle on bubble detachment from a pore of the rotating membrane.

## 5.4. Dynamically enhanced membrane foaming

Contrary to rotor-stator whipping, the dynamically enhanced membrane foaming processes leads to a decrease in mean bubble size with increasing gas volume fraction resulting in about half the mean bubble size at a gas volume fraction of 0.56. Rheological tests showed that foams containing higher gas volume fractions are higher viscous. The increased viscosity leads to higher shear stresses in the gap and, as a consequence, to earlier detachment of bubbles from the membrane and possibly improved dispersion in the narrow annular gap. The volumetric energy input  $E_V$  is about one order of magnitude lower for the dynamically enhanced membrane device. The two types of dynamically enhanced membrane foaming device, i.e. the rotating membrane device (ROME) and the dynamically enhanced static membrane device (DESM), showed strong impacts of circumferential velocity and gap size on the resulting mean bubble size. The type of the membrane was of importance in that the clamping fixture used for woven fabrics had cavities (0.5 mm) which were shown to result in foams containing smaller bubbles, most probably due to microturbulences. Contrarily, within the investigated ranges, both the residence time and pore size did not influence the resulting mean bubble sizes significantly. Foaming results are nearly identical for the two types of dynamically enhanced membrane foaming devices, i.e. ROME and DESM. However, the dynamically en-

hanced static membrane DESM is simpler in design. The combination of results on single bubble breakup in simple shear, of visualization of bubble detachment from the single pore of a rotating membrane and of foam viscosity measurements showed that the dominating bubble formation process is the detachment of small bubbles from the membrane in an early detachment state (i). There is some additional, subordinated dispersing effect in the gap (ii). (i) and (ii) explain why a narrow gap size and high shear rates are advantageous with respect to refined foam microstructure. Furthermore, (i) agrees well with the results that the foam microstructure does not depend on residence time or membrane area while (ii) explains why no impact of pore size on the mean bubble size was observed.

It will be interesting to adapt the continuous phase viscosity used to obtain different gas volume fractions such that the resulting foam viscosity is the same for all gas volume fractions. If the results support the theory that a higher continuous phase viscosity leads to smaller mean bubble sizes, it would be possible to control and tailor make the resulting foam microstructure via the mix viscosity.

### 5.5. Scale-up of DESM device

The scaling of the DESM device was successfully carried out within the framework of the project reported here. The application of lab scale ROME and DESM as well as scaled-up pilot DESM devices resulted in approximately similar mean bubble sizes, dependencies on gas volume fraction and shear rate.

For future large scale devices, it is advisable to stay with a narrow gap (<0.25 mm) since its governing impact on resulting mean bubble size and foam homogeneity was clearly shown for the small DESM device. Further optimization with respect to the type of membrane is suggested: the structured surface of the clamping fixture for woven fabrics has been shown to lead to significantly smaller bubble sizes than the smooth sinter membrane. The indentations are suspected to cause microturbulences, leading to an earlier bubble detachment and/or improved dispersing efficiency in the narrow annular gap. However, the production of such a cage construction is cost-intensive and not ideal for industrial usage due to reasons of both delicacy and microbiology. Another as yet untested possibility to create microturbulence might be the corrugating of the sinter membrane itself.

# Bibliography

- [1] ACRIVOS, A. The breakup of small drops and bubbles in shear flows. *Ann. N.Y. Acad. Sci.* 404 (1983), 1.
- [2] AKERS, R. *Foams*. Academic Press, London, 1976.
- [3] ALEX, T. Charakterisierung einer neuartigen Schaumaufschlagmaschine. Masters thesis, Laboratory of Food Process Engineering, ETH Zürich, 1998.
- [4] ANBARCI, A., AND ARMBRUSTER, H. Bestimmung der Grenzflächenbesetzungskinetik. *Tenside Surf. Deterg.* 24 (1987), 111.
- [5] ANDERECK, C., LIU, S., AND SWINNEY, H. Flow regimes in a circular couette system with independently rotating cylinders. *J. Fluid Mech.* 164 (1986), 155.
- [6] ARMBRUSTER, H. *Untersuchungen zum kontinuierlichen Emulgierprozess in Kolloidmühlen unter Berücksichtigung spezifischer Emulgatoreigenschaften und der Strömungsverhältnisse im Dispergierspalt*. PhD thesis, Universität Friedericiana Karlsruhe (TH), 1990.
- [7] ASANO, Y., AND SOTOYAMA, K. Viscosity change in oil/water food emulsions prepared using a membrane emulsification system. *Food Chem.* 66 (1997), 327.
- [8] BACH, H. *Einfluss der Konstruktions-, Betriebs- und Stoffgrößen auf die Fluidodynamik und damit Funktion von Blasensäulen*. PhD thesis, TU München, 1977.
- [9] BALS, A. Grundlagen der Blasenbildung an Einzelporen und Lochplatten. *Chem. Ing. Tech.* 74 (2002), 337.
- [10] BALS, A. *Verfahrenstechnik und Substratfaktoren beim Aufschäumen mit Membranen*. PhD thesis, Fortschritt-Berichte VDI, Reihe 14, Nummer 105, 2002.
- [11] BALS, A., AND KULOZIC, U. The influence of pore size, the foaming temperature and the viscosity of the continuous phase on the properties of foams produced by membrane foaming. *J. Membrane Sci.* 220 (2003), 5.

- [12] BANIEL, A., FAINS, A., AND POPINEAU, Y. Foaming properties of egg albumin with a bubbling apparatus compared with whipping. *J. Food Sci.* 62 (1997), 377.
- [13] BATCHELOR, G. Pressure fluctuations in isotropic turbulence. *Proc. Cambridge Phil. Soc.* 47 (1951), 359.
- [14] BECKER, K., AND KAYE, J. Measurements of diabatic flow in an annulus with an inner rotating cylinder. *J. Heat Transfer* 84 (1962), 97.
- [15] BEHREND, O. *Mechanisches Emulgieren mit Ultraschall*. PhD thesis, Universität Karlsruhe, 2001.
- [16] BENTLEY, B., AND LEAL, L. An experimental investigation of drop deformation and breakup in steady, two-dimensional linear flows. *J. Fluid Mech.* 167 (1986), 241.
- [17] BERANEK, K., STREDA, I., AND SESTAK, J. On the flow of viscous liquids through annular clearances with the rotating inner cylinder. *Acta Tech. CSAV* 24 (1979), 665.
- [18] BIKERMAN, J. *Foams*. Springer Verlag, Berlin, 1973.
- [19] BIRKHOFFER, B., EISCHEN, J.-C., MEGIAS-ALGUACIL, D., FISCHER, P., AND WINDHAB, E. Computer-controlled flow cell for the study of particle and drop dynamics in shear flow fields. *Ind. Eng. Chem. Res.* 44 (2005), 6999.
- [20] BLASS, E. Bildung und Koaleszenz von Blasen und Tropfen. *Chem.-Ing. Tech.* 60 (1988), 935.
- [21] BOWONDER, B., AND KUMAR, R. Studies in bubble formation - IV: bubble formation at porous disc. *Chem. Eng. Sci.* 25 (1970), 25.
- [22] BRAUER, H. *Grundlagen der Einphasen- und Mehrphasenströmungen*. Verlag Sauerländer, Aarau, Frankfurt am Main, 1971.
- [23] BREITSCHUH, B. *Continuous dry fractionation of milk-fat - application of high shear fields in crystallization and solid-liquid separation*. PhD thesis, ETH Zürich, 1998.
- [24] BRISCOE, B., LAWRENCE, C., AND MIETUS, W. A review of immiscible fluid mixing. *Adv. Colloid Interface Sci.* 81 (1999), 1.
- [25] BÜHLER, K., AND POLIFKE, N. Dynamical behavior of Taylor vortices with superimposed axial flow. *Nonlinear evolution of spatio-temporal structures in dissipative continuous systems, Series B: Physics* 225 (1990), 21.



- 
- [26] CAMPBELL, G., AND MOUGEOT, E. Creation and characterization of aerated food products. *Trends Food Sci. Technol.* 10 (1999), 283.
- [27] CANEDO, E., FAVELUKIS, M., TADMOR, Z., AND TALMON, Y. An experimental study of bubble deformation in viscous liquids in simple shear flow. *AIChE J.* 39 (1993), 553.
- [28] CERF, R. Recherches theoretiques sur l'effet Maxwell des solutions de macromolecules deformables, 2. applications de la theorie de la sphere elastique aux solutions de macromolecules en chianes. *J. Chimie Physique et de physico-chimie biologique* 48 (1951), 85.
- [29] CHAFFEY, C.E., B. H. A second-order theory for shear deformation of drops. *J. Colloid Interface Sci.* 24 (1967), 258.
- [30] CHANDRASEKHAR, S. The hydrodynamic stability of viscid flow between coaxial cylinders. *Proc. Natl. Acad. Sci. USA* 46 (1960), 141.
- [31] CHANDRASEKHAR, S. The stability of spiral flow between rotating cylinders. *Proc. R. Soc. London, Ser. A* 265 (1962), 188.
- [32] CHANG, C., AND FRANCES, E. Modified Langmuir-Hinshelwood kinetics for dynamic adsoption of surfactants at the air-water interface. *Coll. Surf.* 69 (1992), 189.
- [33] CLANET, C., AND LASHERAS, J. Transition from dripping to jetting. *J. Fluid Mech.* 383 (1999), 307.
- [34] COONEY, C. *A study of foam formation by whey proteins*. PhD Thesis, University of Minnesota, 1974.
- [35] COX, R. The deformation of a drop in a general time-dependent fluid flow. *J. Fluid Mech.* 37 (1969), 601.
- [36] CRAMER, C. *Continuous drop formation at a capillary tip and drop deformation in a flow channel*. PhD thesis, ETH Zürich, 2004.
- [37] DAMODARAN, S. *Structure-function relationship of food proteins*. In: Protein functionality in food systems, Marcel Dekker, New York, 1994.
- [38] DAVIDSON, J., AND SCHÜLER, B. Bubble formation at an orifice in a viscous liquid. *Trans. Inst. Chem. Eng.* 38 (1960), 144.
- [39] DAVIES, J. Drop sizes of emulsions related to turbulent energy dissipation rates. *Chem. Eng. Sci.* 40 (1985), 839.

- [40] DE BRUIJN, R. Tipstreaming of drops in simple shear flows. *Chem. Eng. Sci.* 48 (1993), 277.
- [41] DICKINSON, E. *Food Emulsions and Foams*. The Royal Society of Chemistry, London, 1987.
- [42] DICKINSON, E., AND PATINO RODRIGUEZ, J. *Food Emulsions and Foams. Interfaces, Interactions, Stability*. Royal Soc. Chem., Cambridge, 1999.
- [43] DICKINSON, E., AND WOSKETT, M. *Competitive adsorption between proteins and small-molecule surfactants in food emulsions*. Food Colloids, ed. Bee, R.D., Richmond, P., Mingins, J., 1988.
- [44] DIN53018. *DIN 53018 Teil 1: Viskosimetrie: Messung der dynamischen Viskositäten und Fließkurven mit Rotationsviskosimetern mit Standardgeometrie: Normausführung*. DIN Deutsches Institut für Normung, Beuth Verlag GmbH, Berlin, 1976.
- [45] DIPRIMA, R. The stability of a viscous fluid between rotating cylinders with an axial flow. *J. Fluid Mech.* 9 (1960), 621.
- [46] DIPRIMA, R., AND PRIDOR, A. The stability of a viscous flow between rotating concentric cylinders with an axial flow. *Proc. R. Soc. London, Ser. A* 366 (1979), 555.
- [47] DONNELLY, R., AND FULTZ, D. *Proc. Natl. Acad. Sci. USA*.
- [48] DUKHIN, S., KRETSCHMAR, G., AND MILLER, R. *Dynamics of adsorption at liquid interfaces*. Elsevier, Amsterdam, 1995.
- [49] EDWARDS, D.A.; BRENNER, H. W. D. *Interfacial transport processes and rheology*. Butterworth-Heinemann, Boston, 1991.
- [50] EISCHEN, J. *Orientierungsverhalten von faserförmigen Partikeln in Scherströmungen*. PhD thesis, ETH Zürich, 1999.
- [51] EXEROWA, D., AND KRUGLYAKOV, P. *Foam and Foam Films: Theory, Experiment, Application*. Elsevier, Amsterdam, 1998.
- [52] FAINERMANN, V., ZHOLAB, S., LESER, M., MICHEL, M., AND MILLER, R. Competitive adsorption from mixed nonionic surfactant/protein solutions. *J. Colloid Interface Sci.* 274 (2004), 496.
- [53] FEIGL, K., KAUFMANN, S., FISCHER, P., AND WINDHAB, E. A numerical procedure for calculating droplet deformation in dispersing flows and experimental verification. *Chem. Eng. Sci.* 58 (2003), 2351.

- 
- [54] FISCHER, P., AND WINDHAB, E. Food rheology. *Lecture documents, ETH Zurich* (2003).
- [55] FRUMKIN, A. Die Kapillarkurve der höheren Fettsäuren und die Zustandsgleichung der Obeflächenschicht. *Z. Phys. Chemie* 116 (1925), 466.
- [56] GADDIS, E., AND VOGELPOHL, A. Bubble formation in quiescent liquids under constant flow conditions. *Chem. Eng. Sci.* 41 (1986), 97.
- [57] GARCÍA-MORENO, F., BABCSAN, N., AND BANHART, J. X-ray radioscopy of liquid metal foams: influence of heating profile, atmosphere and pressure. *Coll. Surf. A: Physicochem. and Eng. Asp.* 263 (2005), 290.
- [58] GIBBS, J. *The collected works of J. Williard Gibbs, Vol. 1*. Yale University Press, New Haven, 1957.
- [59] GIORDANO, R., PRAZERES, D., AND COONEY, C. Analysis of a Taylor-Poiseuille vortex flow reactor. I: Flow patterns and mass transfer characteristics. *Chem. Eng. Sci.* 53 (1998), 3635.
- [60] GRACE, H. Dispersion phenomena in high viscosity immiscible fluid systems and application of static mixers as dispersing devices in such systems. *Chem. Eng. Commun.* 14 (1982), 225.
- [61] GRANGER-GUILMIN, C., AND BAREY, P. Impact of formulation on ice cream air phase structure and stability. *Proc. 4th Int. Symp. on Food Rheol. Struct., ISFRS 4* (2005), 149.
- [62] GRAVAS, N., AND MARTIN, B. Instability of viscous axial flow in annuli having a rotating inner cylinder. *J. Fluid Mech.* 86 (1978), 385.
- [63] GU, Z., AND FAHIDY, T. Visualization of flow patterns in axial flow between horizontal coaxial rotating cylinders. *Can. J. Chem. Eng.*, 14.
- [64] GU, Z., AND FAHIDY, T. Characteristics of Taylor vortex structure in combined axial and rotating flow. *Can. J. Chem. Eng.* 63 (1985), 710.
- [65] GU, Z., AND FAHIDY, T. The effect of geometric parameters on the structure of combined axial and Taylor-vortex flow. *Can. J. Chem. Eng.* 64 (1986), 185.
- [66] GUIDO, S., AND GRECO, F. Drop shape under slow steady shear flow and during relaxation, experimental results and comparison with theory. *Rheol. Acta* 40 (2001), 176.

- [67] GUIDO, S., GRECO, F., AND VILLONE, M. Experimental determination of drop shape in slow steady shear flow. *J. Colloid Interface Sci.* 219 (1999), 298.
- [68] GUIDO, S., SIMEONE, M., AND ALFANI, A. Interfacial tension of aqueous mixtures of Na-caseinate and Na-alginate by drop deformation in shear flow. *Carbohydrate polymers* 48 (2002), 143.
- [69] GUIDO, S., AND VILLONE, M. Three-dimensional shape of a drop under simple shear flow. *J. Rheol.* 42 (1998), 395.
- [70] GUNDE, R., DAWES, M., HARTLAND, S., AND KOCH, M. Surface tension of wastewater samples measured by the drop volume method. *Environ. Sci. Technol.* 26 (1992), 1036.
- [71] HALLING, P. Protein-stabilized foams and emulsions. *CRC - Critical Review in Food Sci. Nutr.* 155 (1981), 155.
- [72] HANSELMANN, W. *Influences of continuous whipping process parameters on foam structure and stability*. PhD Thesis ETH No. 11865, 1996.
- [73] HANSELMANN, W., AND WINDHAB, E. Flow characteristics and modeling of foam generation in a continuous rotor/stator mixer. *J. Food Eng.* 38 (1999), 393.
- [74] HARKINS, W., AND BROWN, F. The determination of surface tension (free surface energy), and the weight of falling drops: the surface tension of water and benzene by the capillary height method. *J. Amer. Chem. Soc.* 41 (1919), 499.
- [75] HASENHUETTL, G. Design and selection of emulsifiers in the food industry. *Food emulsions and foams: theory and practice Symposium Series 277* (1990), 86.
- [76] HASOON, M., AND MARTIN, B. The stability of viscous axial flow in an annulus with a rotating inner cylinder. *Proc. R. Soc. London, Ser. A* 352 (1977), 351.
- [77] HINCH, E., AND ACRIVOS, A. Long slender drops in a simple shear flow. *J. Fluid Mech.* 98 (1980), 305.
- [78] HUI, Y. *Bailey's industrial oil and fat products, Ed. 5, Vol. 3, Edible oil and fat products: products and application technology*. John Wiley and Sons, New York, 1996.

- 
- [79] ISRAELACHVILI, J. *Intermolecular and surface forces*. Academic Press Inc., London, 1991.
- [80] JANSSEN, J., BOON, A., AND AGTEROF, W. Influence of dynamic interfacial properties on droplet breakup in simple shear flow. *AIChE J.* 40 (1994), 1929.
- [81] JANSSEN, J., BOON, A., AND AGTEROF, W. Influence of dynamic interfacial properties on droplet breakup in plane hyperbolic flow. *AIChE J.* 43 (1997), 1436.
- [82] JOSCELYNE, G., AND TRÄGARDH, G. Food emulsions using membrane emulsification: conditions for producing small droplets. *J. Food Eng.* 39 (1999), 59.
- [83] JOSHI, K. *Foam inhibition using aqueous antifoam dispersions of organic particles or drops*. PhD thesis, ETH Zurich, 2006.
- [84] KARAM, H., AND BELLINGER, J. Deformation and breakup of liquid droplets in a simple shear field. *Ind. Eng. Chem. Fundam.* 4 (1968), 576.
- [85] KARBSTEIN, H. *Untersuchungen zum Herstellen und Stabilisieren von Öl-in-Wasser Emulsionen*. PhD thesis, Universität Karlsruhe, 1994.
- [86] KARBSTEIN, H., AND SCHUBERT, H. Developments in the continuous mechanical production of oil-in-water macro-emulsions. *Chem. Eng. Proc.* 34 (1995), 205.
- [87] KATAOKA, K., DOI, H., AND KOMAI, T. Heat/mass transfer in Taylor vortex flow with constant axial flow rates. *Int. J. Heat Mass Transfer* 20 (1977), 57.
- [88] KATOH, R., ASANO, Y., FURUYA, A., SOTOYAMA, K., TOMITA, M., AND OKONOGLI, S. Methods for preparation of w/o food emulsions using the membrane immersed with oils and fats. *Nippon Shokuhin Kagaku Kogaku Kaishi* 44 (1997), 238.
- [89] KAUFMANN, S. *Experimentelle und numerische Untersuchungen von Tropfendispergiervorgängen in komplexen laminaren Strömungsfeldern*. PhD thesis, ETH Zürich, 2002.
- [90] KAYE, J., AND ELGAR, E. Modes of adiabatic and diabatic fluid flow in an annulus with an inner rotating cylinder. *Transactions of ASME* 80 (1958), 753.

- [91] KEMNADE, J. *Blasenbildung und Phasengrenzfläche beim Dispergieren von Gasen in Flüssigkeiten an einzelnen Gaszulauföffnungen*. PhD thesis, Universität Karlsruhe, 1977.
- [92] KINSELLA, J., AND WHITEHEAD, D. Proteins in whey: chemical, physical and functional properties. *Adv. Food Nutrition Res.* 33 (1989), 343.
- [93] KLUG, P. *Der Blasenbildungsvorgang bei der Gasverteilung an Lochplatten*. PhD thesis, TU Clausthal, 1983.
- [94] KROEZEN, A., AND WASSINK, G. Foam generation in a rotor-stator mixer. *Chem. Eng. Proc.* 24 (1988), 145.
- [95] KROG, N. *Food emulsifiers*. in: Lipid technologies and applications. Marcel Dekker, New York, Basel, Hongkong, 1997.
- [96] KROG, N., AND BARFOD, N. *Interfacial properties of emulsifier/protein films related to food emulsions*. in: Food emulsions and foams, theory and practice, Am. Inst. Chem. Eng., Symp. Ser. 277, 86, 1990.
- [97] KUMAR, R., AND KULLOOR, R. Blasenbildung in nichtviskosen Flüssigkeiten unter konstanten Fließbedingungen. *Chem.-Ing. Tech.* 19 (1967), 657.
- [98] LAMBRICH, U., AND SCHUBERT, H. Emulsification using microporous systems. *J. Membrane Sci.* 257 (2005), 76.
- [99] LANGMUIR, I. the adsorption of gases on plane surfaces of glass, mica and platinum. *J. Am. Chem. Soc.* 40 (1918), 1361.
- [100] LAPLACE, P. *Mechanique celeste*. 1806.
- [101] LEJA, J. *Surface Chemistry of Froth Flotation*. Plenum Press, 1982.
- [102] LEPLAT, S. *Practical training report Laboratory for Food Process Engineering, Institute for Food Science and Nutrition, ETH Zurich* (1998).
- [103] LESER, M., AND MICHEL, M. Aerated milk protein emulsions - new microstructural aspects. *Curr. Opinion Coll. Interf. Sci.* 4 (1999), 239.
- [104] L.G., P., WHITEHEAD, D., AND KINSELLA, J. *Structure function properties of food proteins*. Academic Press, San Diego, 1994.
- [105] LUEPTOW, R., AND DOCTER, A.; MIN, K. Stability of axial flow in an annulus with a rotating inner cylinder. *Phys. Fluids A* 63 (1985), 2446.
- [106] LUEPTOW, R., AND HAJILOO, A. Flow in a rotating membrane plasma separator. *Am. Soc. Artif. Int. Organs J.* 41 (1995), 182.

- 
- [107] MAFFETONE, P., AND MINALE, M. Equation of change for ellipsoidal drops in viscous flow. *J. Non-Newton. Fluid Mech.* 78 (1998), 227.
- [108] MARIN, I., AND RELKIN, P. Foaming properties of  $\beta$ -lactoglobulin: impact of preheating and addition of isoamyl acetate. *Int. J. Food Sci. Technol.* 34 (1999), 517.
- [109] MCCLEMENTS, D. *Food emulsions, principles, practice and techniques*. CRC Press, New York, 1999.
- [110] MEGIAS-ALGUACIL, D., FEIGL, K., DRESSLER, M., FISCHER, P., AND WINDHAB, E. Droplet deformation under simple shear investigated by experiment, numerical simulation and modeling. *J. Non-Newton. Fluid Mech.* 126 (2005), 153.
- [111] MEGIAS-ALGUACIL, D., FISCHER, P., AND WINDHAB, E. Experimental determination of interfacial tension by different dynamical methods under simple shear flow conditions with a novel computer-controlled parallel band apparatus. *J. Colloid Interface Sci.* 274 (2004), 631.
- [112] MEGIAS-ALGUACIL, D., FISCHER, P., AND WINDHAB, E. Determination of the interfacial tension of low density difference liquid-liquid systems containing surfactants by droplet deformation methods. *Chem. Eng. Sci.* 61 (2006), 1386.
- [113] MERSMANN, A. Druckverlust und Schaumhöhen von gasdurchströmten Flüssigkeitsschichten auf Siebböden. *VDI-Forschungsheft, VDI-Verlag, Düsseldorf* 491 (1962).
- [114] MIKAMI, T., AND MASON, S. The capillary break-up of a binary liquid column inside a tube. *Can. J. Chem. Eng.* 53 (1975), 372.
- [115] MILLER, R., FAINERMAN, V., LESER, M., AND MICHEL, M. Kinetics of adsorption of proteins and surfactants. *Curr. Opinion Coll. Interf. Sci.* 9 (2004), 350.
- [116] MILLER, R., LESER, M., MICHEL, M., AND FAINERMAN, V. Surface dilatational rheology of mixed beta-lactoglobuline/surfactant layers at the air/water interface. *J. Phys. Chem. B* 109 (2005), 13327.
- [117] MIN, K., AND LUEPTOW, R. Circular couette flow with pressure-driven axial flow and a porous inner cylinder. *Exp. Fluids* 17 (1994), 190.
- [118] MOLLENHAUER, H. *Emulgatoren*. Behr's Verlag, Hamburg, 1983.

- [119] MULDER, H., AND WALSTRA, P. *The milk fat globule*. Pudoc, Wageningen, 1974.
- [120] MÜLLER-FISCHER, N., SUPPIGER, D., AND WINDHAB, E. Impact of static pressure and volumetric energy input on the microstructure of food foam whipped in a rotor-stator device. *J. Food Eng.* 80 (2007), 306.
- [121] MÜLLER-FISCHER, N., AND WINDHAB, E. Influence of process parameters on microstructure of food foam whipped in a rotor-stator device within a wide static pressure range. *Coll. Surf. A: Physicochem. and Eng. Asp.* 263 (2005), 353.
- [122] MURAI, Y., OIWA, H., AND TAKEDA, Y. Bubble behavior in a vertical Taylor-Couette flow. *J. Physics: Conf. Series* 14 (2005), 143.
- [123] NAGATA, S. *Mixing principles and applications*. Wiley, London, 1975.
- [124] NELSON, R. in: *Industrial chocolate manufacture and use, 2nd edition, 167-173*. Ed. Beckett, S.T., 1994.
- [125] NEUBAUER, G. *Beitrag zur Auslegung von Lochböden für Flüssigkeitsbegabung in Blasensäulen unter Hochdruck*. PhD thesis, TU München, 1977.
- [126] PELAN, B., WATTS, K., CAMPBELL, I., AND LIPS, A. *Food colloids: proteins, lipids and polysaccharides*. Royal Soc. Chem., Cambridge, 1997, ch. On the stability of aerated milk protein emulsions in the presence of small-molecule surfactants.
- [127] PENG, S., AND WILLIAMS, A. Controlled production of emulsions using a crossflow membrane. *Part. Part. Syst. Charact.* 15 (1998), 21.
- [128] PHONGIKAROON, S., CALABRESE, R., AND CARPENTER, K. Elucidation of polyurethane dispersions in a batch rotor-stator mixer. *JCT research* 1 (2004), 329.
- [129] POZRIKIDIS, C. On the transient motion of ordered suspensions of liquid drops. *J. Fluid Mech.* 246 (1993), 301.
- [130] PRESS, W., TEUKOLSKY, S., VETTERLING, W., AND FLANNERY, B. *Numerical Recipes in C++, the art of scientific computing*. Cambridge University Press, 2002.
- [131] PRINS, A. Food emulsions and foams. *Proc. Int. Symp. Food Chem. Royal Soc. Chem., Leeds* (1987), 30.



- 
- [132] PRINS, A., BOS, M., BOERBOOM, R., AND VAN KAALSBECK, H. *Proteins at liquid interfaces*. Elsevier, Amsterdam, ch. Relation between surface rheology and foaming behavior of aqueous protein solutions.
- [133] PUGH, R. Foaming, foam films, antifoaming and defoaming. *Adv. Colloid Interface Sci.* 64 (1996), 67.
- [134] RÄBIGER, N. Blasenbildung an Düsen sowie Blasenbewegung in ruhenden und strömenden Newtonschen und nicht-Newtonschen Flüssigkeiten. *VDI-Forschungsheft, VDI-Verlag, Düsseldorf 625* (1984).
- [135] RÄBIGER, N., AND VOGELPOHL, A. Blasenbildung in ruhenden und bewegten Newtonschen Flüssigkeiten. *Chem.-Ing. Tech.* 53 (1981), 976.
- [136] RÄBIGER, N., AND VOGELPOHL, A. Berechnung der Blasengröße im Bereich des Blasen- und Strahlgases bei ruhender und bewegter Newtonscher Flüssigkeit. *Chem.-Ing. Tech.* 54 (11) (1982), 1082.
- [137] RALLISON, J. Note on the time-dependent deformation of a viscous drop which is almost spherical. *J. Fluid Mech.* 98 (1980), 625.
- [138] RALLISON, J. A numerical study of the deformation and burst of a viscous drop in general shear flows. *J. Fluid Mech.* 109 (1981), 465.
- [139] RALLISON, J. The deformation of small viscous drops and bubbles in shear flows. *Ann. Rev. Fluid Mech.* 16 (1984), 45.
- [140] RAMAKRISHNA, S., KUMAR, R., AND KUOOR, N. Studies in bubble formation - i: bubble formation under constant flow conditions. *Chem. Eng. Sci.* 24 (1969), 731.
- [141] RAVERA, F., FERRARI, M., AND LIGGIERI, L. Adsorption and partitioning of surfactants in liquid-liquid systems. *Adv. Colloid Interface Sci.* 88 (2000), 129.
- [142] RUFF, K. Bildung von Gasblasen an Düsen bei konstantem Volumendurchsatz. *Chem.-Ing. Tech.* 44 (42) (1972), 1360.
- [143] RUMSCHEIDT, F., AND MASON, S. Particle motions in sheared suspensions. xii. deformation and burst of fluid drops in shear and hyperbolic flow. *J. Colloid Sci.* 16 (1961), 238.
- [144] RUST, A., AND MANGA, M. Bubble shapes and orientation in low Re simple shear flow. *J. Colloid Interface Sci.* 249 (2002), 476.

- [145] SADOC, J., AND RIVIER, N. *Foams and Emulsions*. Kluwer Academic Publisher, Dordrecht, 1999.
- [146] SCHADLER, V., AND WINDHAB, E. Continuous membrane emulsification by using a membrane with controlled pore distance. *Desalination* 189 (2006), 130.
- [147] SCHEELE, G., AND MEISTER, B. Drop formation at low viscosities in liquid-liquid systems. *AIChE J.* 14 (1968), 9.
- [148] SCHELUDKO, A. *Adv. Colloid Interface Sci.* 1 (1971), 391.
- [149] SCHLICHTING, H. *Grenzschichttheorie*. G. Braun-Verlag, Karlsruhe, 1982.
- [150] SCHRÖDER, V. *Öl-in-Wasser-Emulsionen mit mikroporösen Membranen*. PhD thesis, Universität Karlsruhe, 1999.
- [151] SCHUBERT, H. Production and short-term stability of emulsions. *Proceedings of NFRI-BRAIN workshop, ISPUC-III, Japan* (2000), 625.
- [152] SCHUSTER, G. *Emulgatoren für Lebensmittel*. Springer-Verlag, Berlin, Heidelberg, New York, 1985.
- [153] SCHWARZ, K., SPRINGETT, B., AND DONNELLY, R. Modes of instability in spiral flow between rotating cylinders. *J. Fluid Mech.* 20 (1964), 281.
- [154] SCHWARZER, J. *Untersuchungen im Strahlgasbereich in Newtonschen Flüssigkeiten*. PhD thesis, TU Clausthal, 1989.
- [155] SHIOMORI, K., HYASHI, T., BABA, Y., KAWANO, Y., AND HANO, T. Hydrolysis rates of olive oil by lipase in a monodispersed o/w emulsion system using membrane emulsification. *J. Ferment. Bioeng.* 80 (1995), 552.
- [156] SIEMES, W. Gasblasen in Flüssigkeiten. Teil I: Entstehung von Gasblasen an nach oben gerichteten kreisförmigen Düsen. *Chem.-Ing. Tech.* 26 (1954), 479.
- [157] SIEMES, W., AND GÜNTHER, K. Gasdispergierung in Flüssigkeiten durch Düsen bei hohen Durchsätzen. *Chem.-Ing. Tech.* 28 (1956), 389.
- [158] SIMMERS, D., AND CONEY, J. The experimental determination of velocity distribution in annular flow. *Int. J. Heat Fluid Flow* 1 (1979), 177.
- [159] SNYDER, H. Experiments on the stability of spiral flow at low axial Reynolds numbers. *Proc. R. Soc. London, Ser. A* 265 (1962), 198.

- 
- [160] SOROUR, M., AND CONEY, J. Characteristics of spiral vortex flow at high Taylor numbers. *J. Mech. Eng. Sci.* 21 (1979), 65.
- [161] STACHE, H., AND KOSSWIG, W. *Tensidhandbuch*. Carl Hanser Verlag, München, 1990.
- [162] STANG, M. *Zerkleinern und Stabilisieren von Tropfen beim mechanischen Emulgieren*. PhD thesis, Universität Karlsruhe, 1998.
- [163] STAUFFER, E. *Emulsifiers, 1-3*. Eagan Press, St. Paul, 1999.
- [164] STONE, H. Dynamics of drop deformation and breakup in viscous fluids. *Ann. Rev. Fluid Mech.* 26 (1994), 65.
- [165] STONE, H., BENTLEY, B., AND LEAL, L. An experimental study of transient effects in the breakup of viscous drops. *J. Fluid Mech.* 173 (1986), 131.
- [166] STROEVE, P., AND VARANASI, P. An experimental study on double emulsion drop breakup in uniform shear flow. *J. Colloid Interface Sci.* 2 (1984), 360.
- [167] TAKEUCHI, D., AND JANKOWSKI, D. A numerical and experimental investigation of the stability of spiral poiseuille flow. *J. Fluid Mech.* 102 (1981), 101.
- [168] TAVGAC, T. *Drop deformation and breakup in simple shear fields*. PhD thesis, University of Houston, 1972.
- [169] TAYLOR, G. The viscosity of a fluid containing small drops of another fluid. *Proc. R. Soc. London, Ser. A* 138 (1932), 41.
- [170] TAYLOR, G. The formation of emulsions in definable fields of flow. *Proc. R. Soc. London, Ser. A* 146 (1934), 501.
- [171] TOMOTIKA, S. On the stability of a cylindrical thread of a viscous liquid surrounded by another viscous fluid. *Proc. Royal Soc. London, Ser. A* 150 (1935), 322.
- [172] TORZA, S., COX, R., AND MASON, S. Particle motions in sheared suspensions: XXVII. transient and steady deformation and burst of liquid drops. *J. Colloid Interface Sci.* 38 (1972), 395.
- [173] WALSTRA, P. Food emulsions and foams. *Proc. Int. Symp. Food Chem., Royal Society of Chemistry, Leeds* (1987), 242.

- [174] WALSTRA, P. *Principle of Foam Formation and Stability*, in: *Foams: Physics, Chemistry and Structure*, pp 1-15. Springer Verlag, 1989.
- [175] WAN, P. Food emulsions and foams: theory and practice. *Am. Inst. Chem. Eng., Symp. Ser. 277* (1990), 86.
- [176] WANISKA, R., AND KINSELLA, J. Foaming of protein solutions: comparison of a column aeration apparatus using ovalbumin. *J. Food Sci.* 44 (1979), 1398.
- [177] WEAIRE, D., AND HUTZLER, S. *The physics of foams*. Clarendon Press, Oxford, 1999.
- [178] WEAST, R. *Handbook of Chemistry and Physics*. CRC Press, 1974.
- [179] WERELEY, S., AND LUEPTOW, R. Velocity field for Taylor-Couette flow with an axial flow. *Phys. Fluids* 11 (1999), 3637.
- [180] WILDE, P., NINO, M., CLARK, D., AND PATINO, J. Molecular diffusion and drainage of thin liquid films stabilized by bovine serum albumine tween 20 mixtures in aqueous solutions of ethanol and sucrose. *Langmuir* 13 (1997), 7151.
- [181] WILSON, A. *Foams: Physics, Chemistry and Structure*. Springer Verlag, London, 1990.
- [182] WINDHAB, E. Zur Technologie geschäumter Stoffsysteme im Lebensmittelbereich. *Lebensmitteltechnik* 3 (1991), 95.
- [183] WINDHAB, E. *Physico-chemical aspects of food processing*. Blackie Academic and Professional, London, 1995, ch. 5: Rheology in Food Processing.
- [184] WINDHAB, E. *Registered design (Gebrauchsmuster), Number 297 09 060.7*. Germany, Filed: 31.7.1997, 1997.
- [185] WINDHAB, E. *Verfahrenstechnik II, ETH Zurich*. Lecture notes, 2001.
- [186] WINDHAB, E., AND WOLF, B. Proc. food ingredients europe 93, paris. p. 267.
- [187] WITSCHI, F. *Influence of Microstructure on the drying kinetics of foamed amorphous model food concentrates*. PhD thesis, ETH Zurich, No. 13336, 1999.
- [188] WOLF, B. *Untersuchungen zum Formverhalten mikroskopisch kleiner Fluidtropfen in stationären und instationären Scherströmungen*. PhD thesis, ETH Zurich, 1995.

- [189] WOLF, B., AND WINDHAB, E. Interfacial rheology of deformable droplets in viscometric flows. *Applied Rheol.* 5 (1995), 182.
- [190] YOUNG, T. An essay on the cohesion of fluids. *Phil. Trans. Roy. Soc., London* 5 (1805), 65.
- [191] ZHANG, D.F.; STONE, H. Drop formation in viscous flows at a vertical capillary tube. *Phys. Fluids* 9 (1997), 2234.

*Bibliography*

---

# Appendix





## A. Illustrations of devices and membranes

### A.1. Technical drawing of pilot-scale DESM device

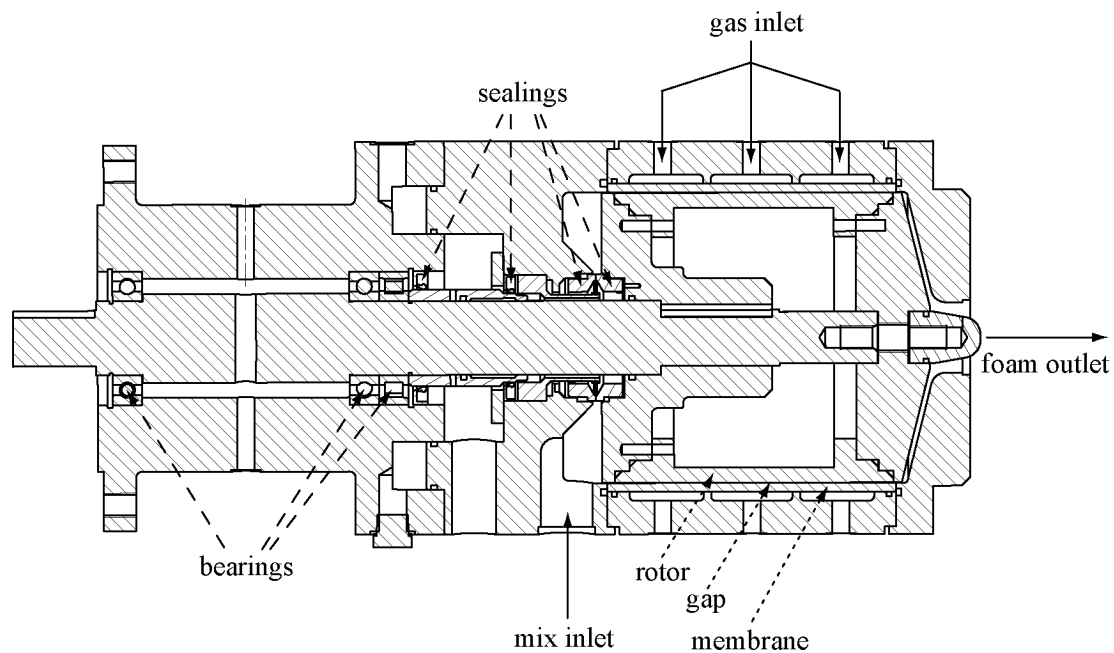


Figure A.1.: Technical drawing of large DESM device.

## **A.2. Fitting of open mesh fabrics to clamping fixture**

### **A.2.1. Open mesh fabrics and rotating membrane**

To assemble the rotating membrane, a fitting piece of open mesh fabric is put inside the outer cylinder and clamped with the aid of 10 inner elements and two tension rings. Fig. A.2 shows the fixation of the membrane to the clamping fixture: 1) End piece and tension ring, 2) outer cylinder with 50 windows, 3) insertion of membrane, 4-6) exact placing and centering of 10 inner elements, 7-8) clamping with second tension ring, 9) end piece.

### **A.2.2. Open mesh fabrics and DESM device**

The fixation of an open mesh fabric to the head of the DESM device is shown in Fig. A.3: 1) inner cylinder of cage (again 50 windows), 2) membrane, 3-5) addition of the two halves of outer cylinder of cage, 6-8) fixation of cage construction to housing.

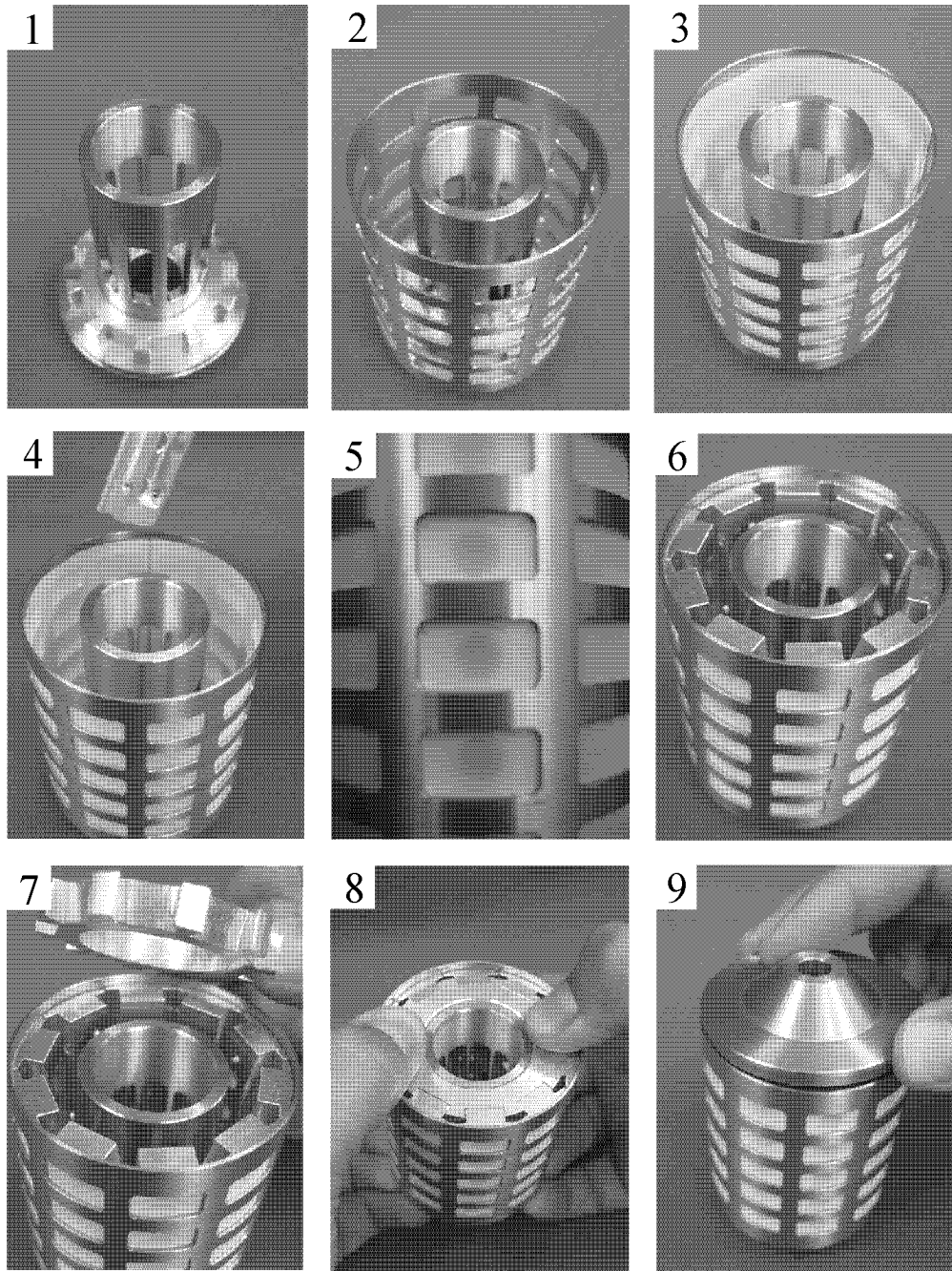


Figure A.2.: Assembling of open mesh fabric to clamping fixture for ROME device.

*A. Illustrations of devices and membranes*

---

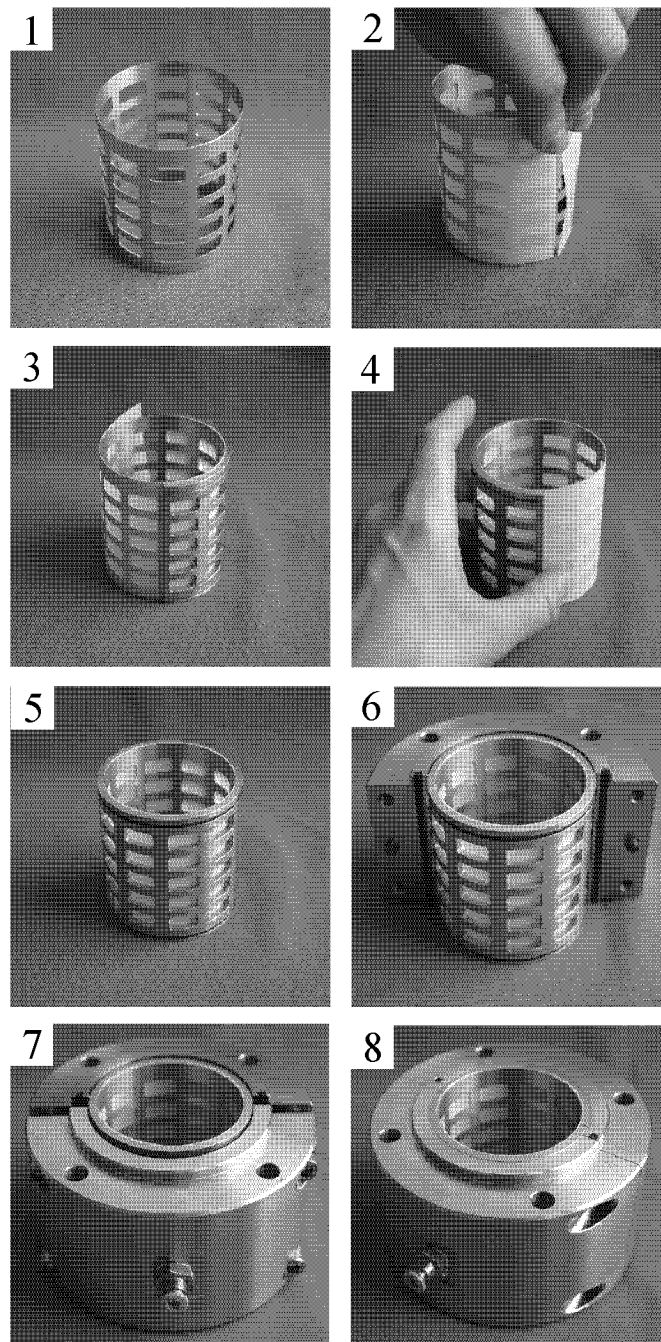


Figure A.3.: Assembling of open mesh fabric to head of DESM device.

# Curriculum Vitae

Nadina Müller-Fischer



## Personal data

date of birth 18 November 1977  
place of birth Zurich  
citizen of Switzerland

## Education

11/2006 Ph.D. exam leading to title Dr. sc. ETH Zurich  
06/2003 - 12/2006 Ph.D. student  
Laboratory of Food Process Engineering  
ETH Zurich, Switzerland  
05/2003 Dipl. Lm.-Ing. ETH  
10/1997 - 05/2003 Studies of Food Engineering at ETH Zurich  
Diploma thesis: "Vacuum whipping: the influence of reduced  
pressure on the microstructure of continuously produced foams"  
Laboratory of Food Process Engineering  
ETH Zurich, Switzerland  
08/1990 - 01/1997 High School in Zürich-Wiedikon, Switzerland  
08/1984 - 07/1990 Primary School in Uitikon, Switzerland

## Work experience and internships

- from 01/2007 Project leader Nutrition Solutions, Bühler AG, Uzwil
- 06/2003 - 12/2006 Research assistant at ETH Zurich  
Laboratory of Food Process Engineering  
Topic: "Dynamically enhanced membrane foaming"
- 03/2002 - 04/2002 Scientific project at ETH Zurich,  
Laboratory of Food Process Engineering  
Topic: "Continuous production of vacuum-whipped foams"
- 07/2001 - 10/2001 Scientific project at ETH Zurich,  
Laboratory of Food Process Engineering  
Topic: "Batchwise vacuum whipping: feasibility study"
- 07/2000 - 12/2000 Internship with Givaudan AG  
Flavor performance group, R&D department
- 08/1997 - 10/1997 Internship with Waid hospital  
Dietary kitchen